Hidden Physics at the Neutrino Frontier: Tridents, Dark Forces, and Hidden Particles

MATHEUS HOSTERT

Hidden Physics at the Neutrino Frontier

Tridents, Dark Forces, and Hidden Particles

Matheus Hostert

A Thesis presented for the degree of
Doctor of Philosophy

Institute for Particle Physics Phenomenology
Department of Physics
Durham University
United Kingdom

September 2019

Hidden Physics at the Neutrino Frontier

Tridents, Dark Forces, and Hidden Particles

Matheus Hostert

Submitted for the degree of Doctor of Philosophy

September 2019

Abstract: The unexplained origin of neutrino masses suggests that these neutral and weakly interacting particles might provide a portal to physics beyond the Standard Model. In view of the growing prospects in experimental neutrino physics, we explore new theoretical models and experimental searches that can shed light on the existence of low-scale particles with very small couplings to ordinary matter. Our efforts highlight a vast landscape of models where neutrino physics offers our best chance of discovering such hidden sectors. Along the way, we revisit the Standard Model physics of neutrino trident production with a modern calculation and explore its phenomenology at neutrino facilities. As shown here, this type of rare neutrino scattering process can probe unexplored anomaly-free extensions of the Standard Model with a complementary, and often more powerful, search strategy to to the well-known searches in neutrino-electron scattering. As to new models, we propose a novel neutrino mass model resembling the inverse seesaw, where neutrino mixing stands as the most prominent portal to dark sectors and dark matter. In our *dark neutrino* model, neutrino masses are generated radiatively, with the vector, scalar, and neutrino phenomenology displaying an unique interplay. Later, we devise new methods to search for these dark neutrinos using neutrino-electron scattering data, aiming to discriminate among new physics explanations of the MiniBooNE anomalous results. Finally, we discuss light and heavy conventional sterile neutrinos in the context of νSTORM, an entry-level neutrino factory for precision neutrino physics.

Dedicated to

Bárbara, Humberto and Luciana.

Contents

List of Figures

Declaration

The work in this thesis is based on research carried out in the Department of Physics at Durham University. No part of this thesis has been submitted elsewhere for any degree or qualification. This thesis is partly based on joint research leading to the articles below.

- Ref. [1]: *"Neutrino trident scattering at near detectors"*, P. Ballett, M. Hostert, S. Pascoli, Y. F. Perez-Gonzalez, Z. Tabrizi, R. Z. Funchal, arXiv:1807.10973, J. High Energ. Phys. (2019) 2019: 119.

- Ref. [2]: *"Neutrino Masses from a Dark Neutrino Sector below the Electroweak Scale"*, P. Ballett, M. Hostert, S. Pascoli, arxiv:1903.07590, PRD99 (2019) 091701.

- Ref. [3]: *"Dark Neutrinos and a Three Portal Connection to the Standard Model"*, P. Ballett, M. Hostert, S. Pascoli, arxiv:1903.07589, to be published presently.

- Ref. [4]: *"Z' in neutrino scattering at DUNE"*, P. Ballett, M. Hostert, S. Pascoli, Y. F. Perez-Gonzalez, Z. Tabrizi, R. Z. Funchal, arXiv:1902.08579, PRD100 (2019) 055012

- Ref. [5]: *"Testing New Physics Explanations of MiniBooNE Anomaly at Neutrino Scattering Experiments"*, C. Argüelles, M. Hostert, Y. Tsai, arXiv:1812.08768, to be published presently.

Acknowledgements

I would like to thank my supervisor Silvia Pascoli for her guidance and for her vision as a supervisor. I am lucky to have been your student and to have had the opportunities you gave me. I am also greatly thankful to Peter Ballett, from whom I have learned physics on the blackboard and in research, and how to make sense of any of it. Thank you both for your patience.

Carlos Argüelles, Pedro Machado and Renata Zukanovich Funchal, thank you for the inspiration and support. My collaborators Yuber Perez Gonzalez, Zahra Tabrizi and Yu-Dai Tsai, thank you for all the hard work that made this thesis possible.

Looking further back, I also want to thank Débora Peres Menezes and Marcus Benghi Pinto for introducing me to scientific research so early in my career. Nuclear physics and symmetry ideas that at the time seemed so foreign to me, are now a recurrent aspect of my own research.

To all friends with whom I shared this adventure in Durham, you have made this place unforgettable. Special thanks go to Andrew Cheek, Kristian Moffat, Andres Olivares-del-Campo, Alexis Plascencia, Jack Richings and Julia Stadler for their immense encouragement and lasting friendship.

To my family, thank you for supporting my decisions and for being unconditional allies. I will be forever grateful for the education of my mother, and for the advice and partnership of my father. Bê, you have always been the *best*.

Madeline, your support and sense of humour have been truly out of this world. A heartfelt thanks for being such a great partner and for filling life with laughter.

"Light seeking light, doth light of light beguile.
So, ere you find where light in darkness lies,
Your light grows dark by losing of your eyes"

— Berowne in *Love's Labour's Lost*

Preface

These are exciting times in high-energy physics. The Standard Model (SM), our most powerful and well-tested theory of particles and their interactions, triumphs across the experimental landscape and proves to be much more robust than anticipated. Yet, once confronted with some of the simplest questions about the Universe, it provides unsatisfactory answers, and to our great frustration, little theoretical guidance on what may lie beyond. While there is no guarantee that some of the theoretical questions we ask are indeed "good" ones, we may rely on two indirect experimental evidence to claim the SM is incomplete: neutrino masses and the existence of dark matter in our Universe. These two unexplained observations suggest the existence of new neutral particles, calling not only for extended particle content but also for novel symmetries. It makes the series of negative results in particle physics all the more thrilling. Uncertain moments like the one we live are frequent in the history of physics. For many times we saw established theoretical expectations and increasingly fine-tuned models making way for elegant theories like Special Relativity, new particles such as the neutrino and for new ideas like spontaneous symmetry breaking (SSB). In practice, of course, such grandiose endeavours are reduced to much less noble but no less important efforts. The frequency of negative results and the need to over-constrain our models make the search for new physics a true exercise in patience. Nevertheless, it is in a persistent and curious spirit that this thesis stands.

Studying neutrinos in the laboratory is notoriously difficult due to their neutral and weakly interacting nature. Although a lot has been learned about their properties, the recent advances on the experimental side, such as the advent of liquid argon time projection chambers, allows us to study neutrino interactions to unprecedented levels of detail. This is the case for the large scale experiments planned for the near future, namely the Deep Underground Neutrino Experiment (DUNE) [6] and HyperKamiokande [7]. These multi-

kiloton projects will put the three neutrino oscillation paradigm to stringent tests, and their near detectors will provide vast amount of data on neutrino interactions. Therefore, given the frequency of surprises in the field of neutrino physics, it is all the more timely to explore such experimental efforts to their fullest and identify what new physics may surface from future data.

One interesting avenue for beyond the SM physics at neutrino experiments, marked by low energies but large exposures, is the existence of feebly-interacting light particles, *e.g.*, *dark* interactions or *hidden* particles. This possibility will be the main motivation for the current thesis, forcing us to consider processes with small SM backgrounds and creative experimental searches. Hidden particles of their own, neutrinos are the only singlets under the broken symmetry of the SM and provide a unique portal to additional neutral particles. Nevertheless, theoretical models that are strongly connected to the neutrino sector at low scales are hard to come by, and most often neutrino experiments cannot compete with the precision achieved with charged particles. In this thesis, we both study and propose models where neutrinos offer our best chance of discovery. For isntance, rare semi-leptonic neutrino scattering processes can serve as the most sensitive probes of light new gauge bosons from well-known anomaly-free gauge symmetries. One such scattering channel is neutrino tridents production, a process we revisit both in the SM and in new physics models, clarifying discrepancies in the literature in a modern approach. For new models we introduce a novel class of self-consistent low-scale hidden sectors that explain neutrino masses and can be tested at current and upcoming neutrino experiments. These models make use of portal couplings to a hidden sector enriched by a new Abelian symmetry. The combination of a new force with neutrino mixing yields a plethora of low-energy signatures that escape current searches for heavy neutral leptons, dark photons and scalars, and is able to explain several longstanding experimental anomalies.

We start the thesis with a reminder of the main features and limitations of the SM, motivating the models we pursue in the chapters that follow. In Chapter 2, we concentrate on the theoretical basis and current status of neutrino physics. Chapter 3 is entirely dedicated to neutrino trident production, and is a testimony to the level of precision achieved in current and future generation neutrino experiments. As an application of this rare process, we will see in Chapter 4 how such signatures probe new gauge interactions

much weaker than those in the SM ($g \lesssim 10^{-3}$). In Chapter 5, we build a new model for neutrino masses that can be tested below the Electroweak scale, and briefly discuss its novel phenomenology. This model has also great implications for short-baseline results, such as the observation of low-energy electron-like events at MiniBooNE. We study this in Chapter 6, proposing a new analysis to search for this kind of signature in neutrino-electron scattering measurements. In Chapter 7, we shift our focus to a new type of neutrino beam offering sub-percent precision in the neutrino flux. We study short-baseline oscillations and sterile neutrinos in the context of such an experiment. Finally, Chapter 8 contains our concluding remarks.

Chapter 1

The Standard Model and Beyond

1.1 The Standard Model

The Standard Model (SM) of particle physics is a Yang-Mills theory [8] of strong, weak and electromagnetic (EM) particle interactions based on an $SU(3) \times SU(2) \times U(1)$ local gauge symmetry. The first remarkable aspect of the theory is in the fact that it relies on the same idea that explains Maxwell's equations, the principle of gauge invariance. In this way, it is hard to pin down the official conception of the SM, although widely associated with the works of Sheldon L. Glashow [9], Steven Weinberg [10] and Abdus Salam [11]. Unconcerned with quarks and the strong force, they proposed a spontaneously broken $SU(2) \times U(1)$ local gauge symmetry for leptons, which already reflected most of what we know about the electroweak (EW) interactions nowadays. In fact, the spontaneous broken symmetry that was used already predicted the existence of a charged massive vector boson, the $W^{\pm}$, a neutral massive vector boson, the Z, and of a massless generator of the unbroken $U(1)_{\mathrm{EM}}$ group, the photon γ. Beyond unifying the weak and EM forces, the breaking through the Higgs mechanism [12–14] implied that an additional scalar particle, the Higgs boson H, had to exist. This last prediction was experimentally validated after the discovery of a neutral scalar boson at the LHC in 2012 [15, 16], the last SM particle to be experimentally observed.

The strong force had a much richer and more turbulent history. The quark model, developed by Murray Gell-Mann and George Zweig [17,18] in 1964, had great success in explaining the growing number of hadronic resonances found by experiments. However, it was not until

	Q_L^α	L^α	$\overline{u_R^\alpha}$	$\overline{d_R^\alpha}$	$\overline{e_R^\alpha}$	H	G	W	B
$SU(3)_c$	**3**	**1**	$\overline{\mathbf{3}}$	$\overline{\mathbf{3}}$	**1**	**1**	**8**	**1**	**1**
$SU(2)_L$	**2**	**2**	**1**	**1**	**1**	**2**	**1**	**3**	**1**
$U(1)_Y$	1/3	-1	$-4/3$	2/3	2	1	0	0	1

Tab. 1.1. The representation of the left-handed Weyl fields, the complex scalar and gauge bosons under each gauge group of the SM. For $U(1)_Y$, the charge is shown instead. All fermions carry a flavour index $\alpha = e, \mu$ or τ.

asymptotic freedom was discovered in non-Abelian gauge theories [19, 20] that quantum chromodynamics (QCD) was really born. QCD is an $SU(3)$ local gauge theory describing the interaction of quarks and gluons, and is vastly different from any other theory we will encounter in this thesis. Its uniqueness is best exemplified through color confinement, the property that colored particles must always be present in bound colorless states, called hadrons. For QCD, confinement is guaranteed below the scale $\Lambda_{\text{QCD}} \approx 250$ MeV, below which strong processes are non-perturbative. This is to be contrasted with asymptotic freedom, where the strong interactions between quarks and gluons become asymptotically weaker at higher energies. The presence of new degrees of freedom other than quarks and gluons at low energies, namely the hadrons, is a clear evidence of a phase transition and makes QCD a unique topic within the SM. At times we will refer to known results in this theory, but it usually has little bearings on electroweak physics.

1.1.1 Fields and Symmetries

We now set out for a more precise definition of the SM field content, discussing some details of local gauge invariance. All fermion fields in the SM are Weyl fields of either definite left-handed (LH) or right-handed (RH) chirality. An equivalent statement is that SM fields are eigenvectors of γ_5: $\gamma_5 \psi_R = \psi_R$ for RH, and $\gamma_5 \psi_L = -\psi_L$ for LH fields. This is an important feature that allows us to work with 2 component Weyl spinors and makes explicitly manifest the chiral nature of weak interactions. The LH field content and their representation under the different gauge groups is shown in Table 1.1. Note that only LH particles transform non-trivially under $SU(2)_L$. Also shown is the Higgs field H, a complex scalar field, doublet under $SU(2)$. As we will see in the next section, H is responsible for the breaking of $SU(2)_L \times U(1)_Y \to U(1)_{\text{EM}}$. From the observed EM charges Q_{EM}, the

$SU(2)_L$ isospin T_3, and by virtue of the Gell-Mann-Nishijima formula [21, 22]

$$Q_{\mathrm{EM}} = T_3 + \frac{Y}{2}, \tag{1.1.1}$$

the hypercharge Y of each SM field is fixed. The *local* gauge transformation of the matter fields are given by

$$\psi \to \exp\{ig\theta^a(x)T^a\}\psi, \tag{1.1.2}$$

where g is the gauge coupling constant, a counts the number of generators T^a, and $\theta^a(x)$ are arbitrary parameters that depend on space-time coordinates x^μ. To achieve local gauge invariance, we require the following gauge fields associated with each group:

$$SU(3)_C : \{G_1(x), \cdots, G_8(x)\}, \quad SU(2)_L : \{W_1(x), W_2(x), W_3(x)\}, \quad U(1)_Y : B(x), \tag{1.1.3}$$

corresponding to the eight gluons, the $SU(2)$ gauge fields and the hypercharge field. Note that the number of gauge fields matches the number of generators in each group, *e.g.* for $SU(N)$ there are N^2-1 generators. For the original $SU(2)\times U(1)$ theory, this implied that in addition to the charged gauge fields, which explained Fermi's theory for beta decays, and the observed massless photon, there must have been an additional neutral gauge field corresponding to some linear combination of W^3 of $SU(2)_L$ and B of $U(1)_Y$. This striking prediction was in fact first confirmed by Gargamelle through the observation of accelerator neutrinos scattering into final states with no charged leptons [23].

The generators of a given symmetry group equipped with commutators form a Lie Algebra, obeying $[T^a, T^b] = if^{abc}T_c$, with f^{abc} being the group structure constant. In the special case $f^{abc} = 0$, the generators commute and the group is said to be Abelian, like in the case of $U(1)_Y$. Otherwise, the group is non-Abelian and the theory displays a much richer underlying dynamics. The SM is a non-Abelian theory, since its symmetry group contains direct products of two $SU(N)$ groups with $N > 1$. We now illustrate how to build a gauge-invariant Yang-Mills Lagrangian, like that of the SM. Take an a-dimensional Yang-Mills theory and define $\boldsymbol{\theta} = T^a\theta^a$ and $U = e^{ig\boldsymbol{\theta}}$. We can now perform gauge transformations on the relevant matter fields ψ, gauge fields $\boldsymbol{A}_\mu = T_a A_\mu(x)^a$ and derivatives of matter fields as follows

$$\psi \to U\psi, \quad \boldsymbol{A}_\mu \to U\boldsymbol{A}_\mu U^{-1} - \frac{i}{g}(\partial_\mu U)U^{-1}, \quad \partial_\mu\psi \to U\partial_\mu\psi + \psi(\partial_\mu U). \tag{1.1.4}$$

As we can see, the last term is not invariant due to the local character of the gauge transformations. To preserve gauge invariance, a covariant derivative, transforming as $D_\mu \to U D_\mu U^{-1}$, now replaces the ordinary derivative. It is defined as

$$D_\mu = \partial_\mu + ig\boldsymbol{A}, \quad \text{such that} \quad D_\mu\psi \to U D_\mu \psi, \implies \overline{\psi} i \not{D} \psi \to \overline{\psi} i \not{D} \psi. \tag{1.1.5}$$

The invariant term above is the fermion kinetic term. Beyond fermion propagation, it is the main way to describe fermion-gauge interactions in the SM. In particular, the full covariant derivative in the SM is given by

$$D_\mu = \partial_\mu + ig\, W^a_\mu \tau_a + i\frac{Y}{2} g'\, B_\mu + i\frac{g_s}{2}\, G^b_\mu \lambda_b, \tag{1.1.6}$$

where $\tau_a = \sigma_a/2$ are the generators built from Pauli matrices acting on the doublets of $SU(2)_L$, and λ_b the generators built from the Gell-Mann matrices acting on the triplet representations of $SU(3)_c$. This also fixes the notation for the gauge couplings in the SM. Finally, the gauge invariant kinetic terms for the gauge bosons are

$$\mathscr{L}_{\text{gauge}} = -\frac{1}{4} G^a_{\mu\nu} G^{\mu\nu}_a - \frac{1}{4} W^a_{\mu\nu} W^{\mu\nu}_a - \frac{1}{4} B_{\mu\nu} B^{\mu\nu}, \tag{1.1.7}$$

where $F^a_{\mu\nu} = \partial_\mu F^a_\nu - \partial_\nu F^a_\mu - g_F f^{abc} F_{b\,\mu} F_{c\,\nu}$ with g_F the relevant gauge coupling. The kinetic term in Abelian theories concern only the propagation of gauge bosons, however, for non-Abelian groups the term proportional to g_F in $F^a_{\mu\nu}$ introduces interactions among the gauge bosons proportional to g and g^2. Therefore, a non-Abelian theory is already an interacting theory without the addition of any matter fields.

1.1.2 Spontaneous Symmetry Breaking

So far we have only discussed the gauge and fermionic content of the SM. The scalar sector is, in fact, quite special. The only scalar particle, the Higgs boson, is responsible for spontaneously breaking $SU(2)_L \times U(1)_Y$ to $U(1)_{\text{EM}}$ after it acquires a non-zero vacuum expectation value (vev). This introduces a mass scale in the theory which, apart from dimensionless couplings, sets the scale of EW physics. Note that because it is a scalar particle, a non-zero vev does not violate the symmetries of space-time, namely Lorentz invariance. The Higgs is a complex scalar field and a doublet under $SU(2)_L$, and so we

can write

$$H = \frac{1}{\sqrt{2}} \begin{pmatrix} G_1^+ + iG_2^+ \\ h^0 + iG_3^0 \end{pmatrix} = \frac{e^{iG_a\tau^a}}{\sqrt{2}} \begin{pmatrix} 0 \\ h \end{pmatrix}. \tag{1.1.8}$$

The Higgs Lagrangian reads

$$\mathscr{L}_{\text{Higgs}} \supset (D^\mu H)^\dagger (D_\mu H) - V(H), \quad \text{with} \quad V(H) = \mu^2 H^\dagger H + \lambda \left(H^\dagger H\right)^2, \tag{1.1.9}$$

where μ^2 has mass dimension 2, being the only dimensionful parameter in the SM. If $\mu^2 < 0$, minimizing the potential $V(H)$ requires $\langle 0| H |0\rangle = \left(0,\ v/\sqrt{2}\right)^T$, where $v^2 = -\mu^2/\lambda$ is the vev chosen to lie in the real and neutral direction. We now can then expand around the true vacuum of the theory by redefining the fields $G_a \to G_a/v$ and $h \to h + v$. At this point, a rewriting of the potential reveals the mass and interactions of every component of the scalar doublet. Note, however, that it contains no mass terms for G_1, G_2 and G_3. These are the Nambu-Goldstone bosons of the theory, and although they are massless, they do possess interactions with the scalar and gauge boson fields. One way to understand their role is to perform an $SU(2)_L \times U(1)_Y$ gauge transformation in our Lagrangian such that the resulting Higgs doublet reads

$$H \to e^{-iG_a\tau^a/v} H = \frac{1}{\sqrt{2}} \begin{pmatrix} 0 \\ h + v \end{pmatrix}. \tag{1.1.10}$$

This transformation must also be applied to the gauge fields, fixing the gauge. This particular choice is rather convenient and is known as the unitary gauge. We then find

$$\begin{aligned} \mathscr{L}_{\text{Higgs}} \supset & -\frac{1}{2} m_h^2 h^2 - \lambda v h^3 - \frac{\lambda}{4} h^4 \\ & + M_{\text{W}}^2 W_\mu^\dagger W^\mu \left[1 + \frac{2h}{v} + \frac{h^2}{v^2}\right] + \frac{M_{\text{Z}}^2}{2} Z_\mu Z^\mu \left[1 + \frac{2h}{v} + \frac{h^2}{v^2}\right], \end{aligned} \tag{1.1.11}$$

where $m_h = \sqrt{2\lambda}\, v = 125.18 \pm 0.16$ GeV [24]. Most importantly, after SSB, the Higgs kinetic term has given us three massive and one massless vector bosons, defined as

$$W_\mu^\pm = \frac{1}{\sqrt{2}} \left(W_\mu^1 \mp i W_\mu^2\right), \quad Z_\mu = c_{\text{W}} W_\mu^3 - s_{\text{W}} B_\mu, \quad A_\mu = c_{\text{W}} B_\mu - s_{\text{W}} W_\mu^3. \tag{1.1.12}$$

where s_{W} (c_{W}) is the sine (cosine) of the weak angle, defined by $c_{\text{W}} = g/\sqrt{g^2 + g'^2}$. These fields correspond to the mediators of the weak charged-current (CC) interactions ($M_{\text{W}} = gv/2 = 80.387 \pm 0.016$ GeV [24]), of the weak neutral-current (NC) interactions ($M_{\text{Z}} = M_{\text{W}}/c_{\text{W}} = 91.1876 \pm 0.0021$ GeV [25]) and the massless photon A_μ, mediator of the unbroken

EM interactions. Their interactions with the Higgs boson are also shown in the triple and quadruple vertex terms above. The interactions with matter are obtained from the fermion kinetic terms, where the charged, neutral and electromagnetic currents are defined and written as

$$\mathscr{L}_{\rm NC} = e\, J^\gamma_\mu A^\mu + \frac{g}{c_{\rm W}}\, J^Z_\mu Z^\mu, \quad J^\gamma_\mu = \overline{\psi} Q_{\rm EM} \gamma_\mu \psi, \quad J^Z_\mu = \overline{\psi}\gamma_\mu \left[\left(\frac{T_3}{2} - Q_{\rm EM} s^2_{\rm W} \right) - \frac{T_3}{2}\gamma^5 \right] \psi,$$

$$\mathscr{L}_{\rm CC} = \frac{g}{\sqrt{2}} \left(J^+_\mu W^{\mu\,+} + J^-_\mu W^{\mu\,-} \right), \quad J^+_\mu = \frac{1}{2}\overline{\psi}_u \gamma_\mu \left(1 - \gamma^5 \right) \psi_d + \text{h.c.}, \tag{1.1.13}$$

where $\psi \in \{\nu_L, e_L, u_L, d_L, e_R, u_R, d_R\}$, and $\psi_{u,\,d}$ denoting fermions with $T_3 = \pm 1/2$. From the weak currents we note two important aspects: *i)* weak interactions indeed violate parity with a $V - A$ structure, *ii)* charged-current interactions are purely LH as they should be since no RH fields are charged under $SU(2)_L$. After SSB, only the EM current is conserved $\partial^\mu J^\gamma_\mu = 0$.

In the discussion above, we fixed the gauge of the SM to simplify the EW Lagrangian. This is not necessary and, in fact, another possibility is to keep all terms involving the Nambu-Goldstone fields G_a and eliminate off-diagonal kinetic terms of the type $Z_\mu \partial^\mu G_3$ by introducing the following gauge breaking Lagrangian to the SM

$$\mathscr{L}_{\rm R_\xi} = -\frac{\left(\partial_\mu A^\mu\right)^2}{2\xi_\gamma} - \frac{\left(\partial_\mu Z^\mu + \xi_Z M_Z G^0_3\right)^2}{2\xi_Z} - \frac{\left|\partial_\mu W^{\mu\,-} + i\xi_W M_W G^-\right|^2}{2\xi_W}. \tag{1.1.14}$$

This is known as the R_ξ gauge, where the explicit dependence on the gauge breaking parameters ξ serves as a useful diagnostic of gauge invariance in physical observables. The Lorentz gauge is recovered for $\xi = 0$ and the Feynman-'t Hooft gauge with $\xi = 1$. This method to fix the gauge played an important role in the development of the SM. First introduced by Ludvig Fadeev and Victor Popov [26], this provided a recipe to perform calculations in gauge theories without the ambiguity of the gauge symmetry. In practice, one must also add unphysical ghost fields to guarantee the unitarity of the theory. These only appear in loop processes and we will not encounter them again in this thesis. An additional advantage of fixing the gauge in this way is that it allows us to trace the Nambu-Goldstone degrees of freedom. The pseudo-scalar fields $G^\pm$ and G_3 end up behaving very similarly to the $W^\pm$ and Z gauge bosons. In fact, at high-energies it can be shown that the Nambu-Goldstone bosons are equivalent to the longitudinal polarization states of their respective gauge bosons [27,28]. This is known as the Nambu-Goldstone boson equivalence

theorem, and it turns out to be very important to understand processes like $W_L\,W_L$ and $Z_L\,Z_L$ scattering. At very high-energies and without the Higgs boson, such processes grow indefinitely ($\sigma \propto s$), spoiling the unitarity of the S-matrix. The fact that this problem was solved by including contributions from h exchange provided a no-lose theorem for the LHC: either the Higgs boson would be discovered, or new physics must appear to unitarize these processes.

1.1.3 Fermion Masses

The EW sector is also responsible for the generation of fermion masses in the SM. As noted before, all LH fermions in the SM are $SU(2)_L$ doublets, just like the Higgs. This allows us to construct the so-called Yukawa terms,

$$\mathscr{L}_{\text{Yukawa}} = y^e_{\alpha\,\beta}\left(\overline{L}^{\alpha} H\right) e^{\beta}_R + y^u_{\alpha\,\beta}\left(\overline{Q}^{\alpha}_L \tilde{H}\right) u^{\beta}_R + y^d_{\alpha\,\beta}\left(\overline{Q}^{\alpha}_L H\right) d^{\beta}_R + \text{ h.c.}, \tag{1.1.15}$$

where we defined the charge-parity (CP) conjugated Higgs field $\tilde{H} = i\sigma_2 H^* = (h^0 + iG^0_3,\ G^-_1 - iG^-_2)^T$ and included all three families of fermions by promoting $y^{\psi} \to \mathbf{Y}^{\psi}$ to a 3×3 matrix. . After SSB, these interaction terms endow charged-leptons and quarks with a dirac mass term of the form

$$m_{\psi}\overline{\psi}\psi = m_{\psi}\left(\overline{\psi}_L\psi_R + \overline{\psi}_R\psi_L\right), \quad \text{with} \quad m_{\psi} = \frac{y_{\psi}\,v}{\sqrt{2}}, \tag{1.1.16}$$

where $\psi_{L,\,R} = P_{L,\,R}\,\psi = (1 \mp \gamma_5)\,\psi/2$ are the chiral projections of the fermion field ψ.

In the quark sector, the Yukawa matrix is off-diagonal and the different generations mix. The physical quark masses are found after rotating the up and down quarks, left and right, as $u^{\alpha}_{L,\,R} = \left(V^u_{L,\,R}\right)^*_{\alpha i}\,u^i_{L,\,R}$ and $d^{\alpha}_{L,\,R} = \left(V^d_{L,\,R}\right)^*_{\alpha i}\,d^i_{L,\,R}$. The diagonal mass matrix is then $\mathbf{m}^{u,\,d} = \mathbf{V}^{u,\,d}_L \mathbf{y}_{u,\,d} \mathbf{V}^{u,\,d\,\dagger}_R v/\sqrt{2}$. Note that after this procedure we cannot help but introduce mixing in the charged current. This defines the Cabbibo-Kobayashi-Maskawa (CKM) matrix [29, 30], $\mathbf{V}_{\text{CKM}} = \mathbf{V}^u_L \mathbf{V}^{d\,\dagger}_L$. The CKM matrix is nearly diagonal, so the mixing between quark flavour and mass eigenstates is small. From the unitarity of the rotation matrices, neutral currents remain invariant

$$\sum_{\alpha,\,\beta}\overline{\psi}^{\alpha}_L\,\Gamma^{\mu}\,\psi^{\beta}_L = \sum_{i,\,j}\overline{\psi}^{i}_L\,\left(\sum_{\alpha,\,\beta}(V_L)_{\alpha i}(V^*_L)_{\beta j}\right)\,\Gamma^{\mu}\,\psi^{j}_L = \sum_{i,\,j}\overline{\psi}^{i}_L\,\Gamma^{\mu}\,\psi^{j}_L, \tag{1.1.17}$$

where Γ^{μ} are the neutral-current couplings and gamma matrices. Crucially, Γ^{μ} has no

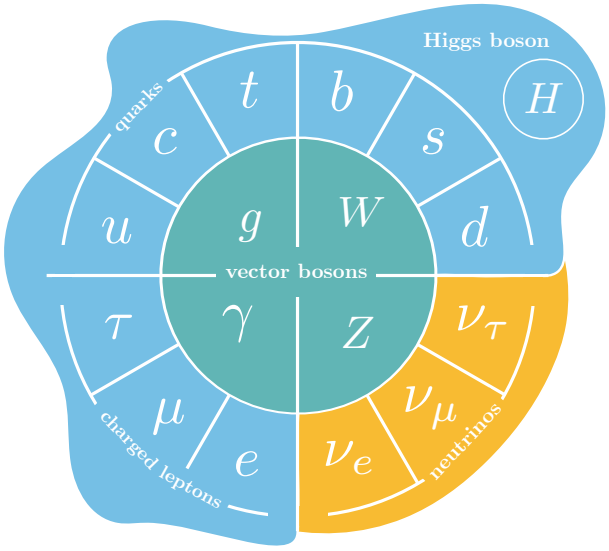

Fig. 1.1. Artistic rendering of the particles in the Standard Model.

flavour dependence and so the SM forbids flavour changing neutral currents (FCNC). This mechanism was first proposed by Glashow, Illiopoulous and Maiani to explain why decays of the type $K^0 \to \mu\mu$ were unobserved. Famously referred to as the GIM mechanism, this relies on the flavour universal nature of SM neutral currents and on the unitarity of the CKM. As we will see, this mechanism also plays an important role in the neutrino sector and in many extensions of the SM.

Summarizing, the SM particles are illustrated in Fig. 1.1 and the full SM Lagrangian is simply

$$\mathscr{L}_{\text{SM}} = \mathscr{L}_{\text{gauge}} + \mathscr{L}_{\text{Higgs}} + \mathscr{L}_{\text{Yukawa}} + \sum_{\alpha,\Psi} \overline{\Psi^\alpha} i \not{D} \Psi^\alpha, \tag{1.1.18}$$

where α is a flavour index and $\Psi \in \{L, Q_L, e_R, u_R, d_R\}$. We saw how a single parameter with massive dimensions in the scalar potential of the SM leads to SSB. This is then "propagated" to the rest of the SM through the Higgs kinetic terms and Yukawa couplings. At this point it is possible to appreciate two problems with the SM mass generation mechanism. Firstly, it implies that all Yukawa couplings are just parameters to be inferred from the measured masses of particles. That is, the SM makes no statements and provides no explanations as to why the Yukawas that we observe in nature are what they are. This is known as the flavour puzzle and is equivalent to asking what explains the different observed fermion masses. This problem is aggravated when we consider that neutrinos do have masses and that the leptonic mixing is drastically different from the one in the quark sector. This leads us to the second problem with the SM mass generation. The SM

predicts exaclty massless neutrinos in the absence of ν_R fields. This is perhaps the biggest motivation for studying neutrino physics at present.

Before moving on to more speculative topics, a few comments are in order. EW SSB seems to be, as far as we know, a real phenomenon. It explains why the symmetries of the SM were so well hidden the first place: true symmetries of Nature seem to not be shared by the vacuum. While the evidence for EW SSB comes mainly from studying fundamental particles, its consequences do not concern only particle physics. EW physics helps us understand the past and future of our own Universe. In the early Universe, at hight temperatures, it is expected that the EW symmetry is restored [31–33]. If this is the case, the EW phase transition provides a unique test of the Higgs mechanism and points to a completely different Universe from our own, where finite temperature effects and non-perturbative physics play a major role. In addition, we have no reason to expect the vacuum structure of the Universe to be as simple as describe above. After all, the stability of our own vacuum is not even guaranteed within the SM [34, 35]. Radiative corrections to the Higgs self-coupling λ alter the shape of the scalar potential and imply we may live in a local, rather than global, minimum of the potential. For these reasons, studying the Higgs sector, confirming that it generates all fermion masses in the SM and why it seemingly fails to do so in the case of the neutrino are all questions worth pursuing.

1.2 Evidence for Beyond the Standard Model Physics

The most important aspects and building blocks of the SM have been laid out above. Now, a different question will concern us: is this theory sufficient to explain fundamental particles and their interactions? In this section we will list what we believe to be the most important hints and evidence that this is not the case. We have already stumbled upon a few problems of the SM, but even before that one must already suspect that the SM is not a final theory. It does not explain gravity. This tells us that the SM should be treated as an effective theory valid up until the Planck mass $M_{\rm Pl} = (\hbar c/2G_{\rm Newton})^{1/2} \approx 10^{19}$ GeV, where the effects of gravity are expected to be large [1]. This very fact already brings us to one of the most debated evidence for beyond the Standard Model (BSM) physics.

[1] This is a naive expectation based on the observation that the Schwarzschild radius $\ell_s = 2G_{\rm Newton}m/c^2$ and the Compton wavelength $\ell_c = h/mc$ of a particle become comparable at $m \approx M_{\rm Pl}$.

The hierarchy problem The lack of evidence for new physics at the LHC can be argued to be more than just unfortunate. If no new physics is indeed present between the EW and the Planck scale, then the cut-off of the SM, beyond which the effective field theory is no longer valid, is $\Lambda = M_{\rm Pl}$. This implies that unless symmetries are at play, terms of dimensions d are suppressed by, or are of the order of Λ^{4-d}. However, in the SM $m_h^2 \ll \Lambda^2$, suggesting a fine-tuning of many orders of magnitude. Quantum corrections to the Higgs mass, $m_h^2 = m_{\rm bare}^2 + \delta m_h^2$, are dominated by the top quark and go as $\delta m_h^2 = y_t^2 \Lambda^2 / 8\pi^2$. This quadratically divergent result implies that to obtain the observed light Higgs mass, whatever new physics that may appear at the scale Λ (possibly even below $M_{\rm Pl}$) must cancel the fermion loops to order m_h^2/Λ^2. In other words, the matching condition for the renormalization of m_h^2 parameter becomes fine-tuned to order m_h^2/Λ^2 in the presence of such cut-off. Supersymmetric theories are notorious candidates to solve this problem, but so far we are yet to find any evidence for them. One may argue that indeed there exists a "desert" between the EW and the Planck scale, and that some miraculous mechanism is at play in quantum gravity that may solve the fine-tuning problem. In that case, a solution to all following items in this list must be found at that scale, or somewhere outside the realm of particle physics.

The strong-CP problem The QCD Lagrangian admits the following field-strength contraction term

$$\mathscr{L} \supset \frac{\theta \alpha_s}{8\pi} G^a_{\mu\nu} \tilde{G}^{\mu\nu}_a, \quad \text{where} \quad \tilde{G}^a_{\mu\nu} = \frac{\epsilon_{\mu\nu\rho\sigma}}{2} G^{a\,\rho\sigma}. \tag{1.2.1}$$

This can be shown to be a surface term (a total divergence in the action) and can be neglected in perturbative calculations. Nevertheless, this term induces CP violation in the strong sector via non-perturbative effects, leading to a large electric dipole moment for free neutrons [36], which is orders of magnitude above the experimental upper limits [37]. The most popular scenario to explain the smallness of θ is the Peccei-Quinn symmetry [38], a global chiral $U(1)$. The breaking of this symmetry leads to the prediction of a pseudo-Nambu-Goldstone boson, the axion.

Matter-antimatter asymmetry The observed baryon asymmetry of the Universe contradicts the standard Cosmology, which assumes that matter and anti-matter were created

in equal amounts in the Big Bang. A good measure of this effect is $\eta_B = (n_B - n_{\overline{B}})/n_\gamma$, where the difference between the number density of baryons and anti-baryons is normalized to the photon number density n_γ, rendering η_B insensitive to the expansion of the Universe. This is measured to be extremely small, $\eta_B \approx 6 \times 10^{-10}$ with baryons being the dominant component. The SM does not contain enough source of CP violation to explain this phenomenon. Popular scenarios to explain this are EW baryogenesis and leptogenesis. The latter relies on the CP violation from the lepton sector, which is later translated into a baryon asymmetry through non-perturbative spharelon processes that violate total $B + L$ number. This is relevant for neutrino physics, since heavy right-handed neutrinos may realise leptogenesis.

Dark matter In the 1930's, Fritz Zwicky measured the velocity dispersion of galaxies in the Coma cluster [39], and applied the virial theorem to show that the matter inferred from its luminosity was insufficient to hold the cluster together. Alongside the pioneering work of Vera Rubin on galaxy rotation curves in the 70's [40], these observations showed that the gravitational potential in astrophysical scales is much deeper than the one extrapolated from luminous matter. Already at the time, astronomers would refer to the source of this additional gravitational influence as Dark Matter (DM). As astrophysics and cosmology evolved, concrete evidence for DM continued to build up. Now, it is present at a variety of scales, from the precise measurements of the cosmic microwave background (CMB) [41], the matter distribution in galaxy cluster mergers [42], and the observed large scale structure of the Universe [43]. In fact, from the CMB power spectrum we can infer the DM density today as [41]

$$\Omega_{\rm DM} h^2 = 0.1200 \pm 0.0012, \tag{1.2.2}$$

with $\Omega_{\rm DM} = \rho_{\rm DM}/\rho_c$ the energy density of DM in units of the critical density $\rho_c \approx 10^{-26}$ kg/m^3, and $h = H_0/(100 \text{ km s}^{-1}/\text{Mpc}^{-1}) = 0.674 \pm 0.005$ the scaled Hubble expansion rate. This is roughly five times larger than the density of baryons, understood as all other non-relativistic matter. The latter is also measured through the relative abundances of light elements during Big Bang Nucleosynthesis (BBN) [44], where DM plays no role, and provides further evidence for the non-baryonic nature of DM.

The nature of DM is not yet understood and many possibilities are under investigation. Modified gravity models explain local astrophysical observations, but struggle to explain

all CMB datasets and X-ray observations of mergers of galaxy clusters [45]. Primordial black holes [46] have also been put forward as DM candidates and have triggered great interest due to their connection to the detection of gravitational waves. However, the most popular hypothesis at this point remains that DM is made of new particles. This new state better be neutral, to have evaded our detection, and sufficiently long-lived, so that it may linger until today after its production in the early Universe. The fluid of such particles would have to display negligible pressure and viscosity, and to have been created cold so as to help form clumpy structures in the Universe through its gravitational pull. This points us to a particle that is massive, collisionless and, yet, very abundant today. Most notably, DM models have often focused on the possibility of a weakly-interacting massive particle (WIMP). In this paradigm, DM particles, denoted as χ in this context, are produced in the early Universe through its weak interactions with the SM plasma. At later times, approximately at temperatures of the order of the DM mass m_χ, DM production stops and annihilation into SM particles dominates. As the Universe cools and expands, the DM gas is diluted and annihilation is no longer effective, *freezing-out* the DM population at around $T \approx m_\chi/20$. In particular, the relic density obtained in this mechanism is of the order $\Omega_\chi H_0^2 \approx 0.1\,\mathrm{pb}/\sigma$, where σ stands for the thermally averaged cross section of χ annihilation into SM particles. The fact that $\sigma \approx 1$ pb allows to reproduce the current DM density and is of the order of typical weak cross sections (as in mediated by weak bosons) is known as the WIMP-miracle. WIMP DM is a collisionless and thermal candidate, although DM candidates that are non-thermal, or collisionless, or both exist.

Neutrino masses One of the most important evidence for BSM physics is the fact that neutrinos have non-zero masses. This comes from the plethora of measurements of neutrino oscillations and flavour conversions, which we study in the next chapter. Put simply, neutrino oscillation data requires at least two non-degenerate massive neutrinos. Although one might argue that this is solved by the mere addition of at least two RH singlet states to the SM, this simple extension would require additional theoretical ingredients and experimental confirmation. For instance, such states would be the only SM particle to admit a Majorana mass term of the type $M\,\overline{\nu_R^c}\nu_R$, and unless new symmetries are introduced, there is no reason to expect that M is exactly zero. Therefore, neutrino masses are the first evidence of physics beyond the SM observed in controlled laboratory

conditions.

1.3 Portals to Beyond the Standard Model

While we lack a single compelling evidence for the direct detection of a new particle, we can interpret many of the problems outlined above as evidence for new states. The existence of DM and neutrino masses, in particular, suggests (but does not require) that these new states may be a new sector of electromagnetically neutral particles, secluded to their own dark sector. Here, the SM provides little guidance on their masses or symmetries. For this reason, many possibilities to such models exist. We can be guided by experimental anomalous results, by increased elegance in our theories, or by complete agnosticism. In this section we follow take a stronger preference for the latter approach, and set out to discuss the many possibilities through which secluded states may couple to the SM. Much of what we discuss here narrows down the scope of the models we will work with throughout this thesis.

Dark sectors arise in theories where new states, say dark matter particles, are secluded and are not charged under the SM group. These particles may have simple or complicated dynamics in their lair, but their only connection to our SM world is through small *portal couplings* [47–49]. This hypothesis is compelling because it explains why a large fraction of the Universe is invisible to us (in the form of dark states), and why the SM appears so self-contained. The modular and hidden aspect of this point of view is indeed frightening, but this is is not the first time we have encountered it. When Wolfgang Pauli proposed the existence of the neutrino to explain the continuous spectra of electrons from beta decays, he had in fact stumbled upon a key player of a new hidden sector. Initially, in Pauli's own words, this particle was believed to be "impossible to detect." It was later clear that this may not be the case if the 4-fermion theory for beta decays by Enrico Fermi was correct. We now know that to be true, where the fact that the neutrino had escaped detection up until that point is explained by the smallness of the fermi coupling constant [24]

$$\frac{G_F}{\sqrt{2}} = \frac{g^2}{8M_{\rm W}^2} = 1.1663787(6) \times 10^{-5}\ \text{GeV}^{-2}. \tag{1.3.1}$$

In this case, the neutrino represents the hidden sector, and the weak interactions the small portal couplings to it. In fact, to study such hidden sector, the smallness of G_F had to

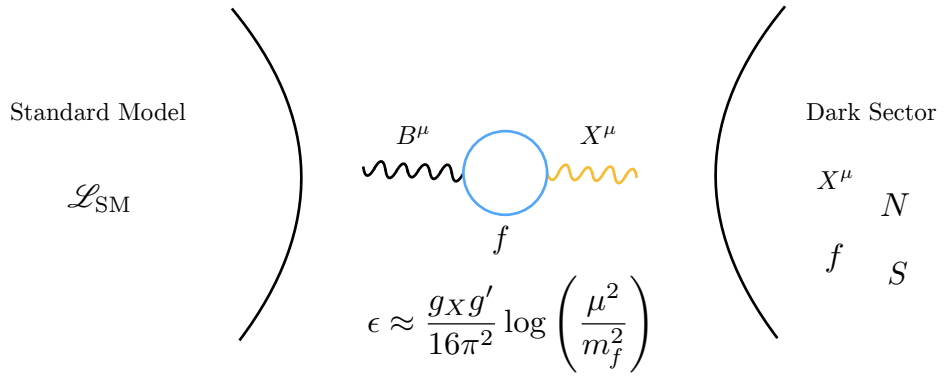

Fig. 1.2. A possibility for a portal between the Standard Model and a dark sector. Fermions f charged under both the hypercharge group and a new $U(1)$ group generate kinetic mixing at loop level between B^μ and the new boson X^μ. In the approximate formula for ϵ, μ^2 stands for the renormalization scale and g_X to the gauge coupling of the new $U(1)$.

be overcome with large-exposure experiments at low energies, The first direct detection of neutrinos, by an experiment performed by Cowan and Reiness in 1956, was achieved by placing a detector just a few meters away from a nuclear reactor. Of course, this was not enough to understand the whole physical picture of the weak interactions. As it turns out, G_F is only an artefact of the effective theory proposed by Fermi, and its smallness is due to the large masses of the weak bosons.

With this familiar analogy, we may hope that the problems in the previous sections may be solved in a similar way. Of course, the smallness of portal couplings may not always be due to the large mediator masses. It may arise from a mere accident of the theory, if one believes in such things, from large separation of scales, or from other mechanisms. One realization of small couplings is nicely exemplified by kinetic mixing. In theories with heavy fermions charged both under a new $U(1)$ group and hypercharge, the low energy effects of the new $U(1)$ come in through loop-diagrams like those shown in Fig. 1.2. The loop suppression then explains why ϵ, the kinetic mixing parameter, is small, typically of the order of $\epsilon \lesssim 10^{-2}$.

To understand the possible links between dark sectors and the SM, we would like to understand all possible ways in which dark and SM particles can interact. One way to tackle this question is to build effective field theories, where one studies all operators which are allowed by the content and symmetries of the SM. The idea is to construct

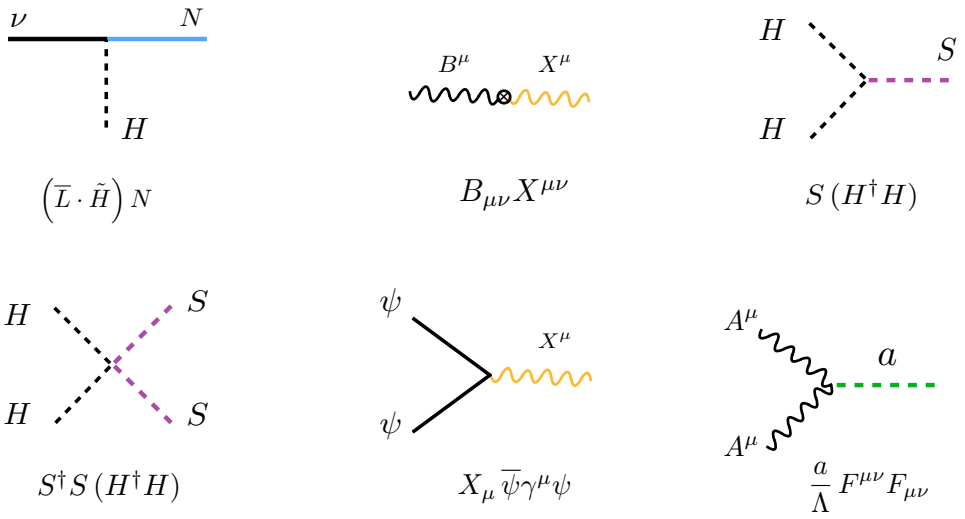

Fig. 1.3. Diagramatic representation of all portal couplings discussed here. From left to right, the top row shows the neutrino, vector and $d = 4$ Higgs portal. The bottom row shows the super-renormalizable $d = 3$ Higgs portal, the fermionic portal and the non-renormalizable pseudo-scalar portal.

a series of $d > 4$ operators in $1/\Lambda^{d-4}$, where Λ is the scale of the new physics. This approach thrives on its generality, but can become complicated very quickly with growing d. Most importantly, the scale Λ is assumed to be large, so that all new degrees of freedom have been integrated out of the theory. This is suitable for extensions involving particles which are very heavy, but the series is no longer well defined for new physics that is light and kinematically accessible at our experiments. In this case, the kinematics of the new particles play a role, forcing us to write down the field content and symmetry group of the new physics. This is the approach we describe in what follows.

We would like our SM extensions to follow specific guiding principles and organize them in a meaningful way. One way to do so is to study all the low-dimension neutral operators that the SM has to offer. In contrast to effective field theories, we want renormalizable operators with $d < 4$ and that are preferably gauge invariant. As it turns only a few such operators exist, which we usually refer to as *portals*. We dedicate this section to presenting these, as well as the most popular operators that have also been associated with portal couplings, but that are not renormalizable or gauge-invariant.

Neutrino portal Arguably the most motivated portal, this $d = 5/2$ operator can be written as

$$\left(\overline{L}^\alpha\cdot\tilde{H}\right). \tag{1.3.2}$$

Any fermion field which couples to this operator acquires a coupling to SM neutrinos. This typically induces off-diagonal mass terms in the Lagrangian, leading to mixing between the new species and all massive neutrinos in the broken phase of the SM. The new particle is then commonly referred to as *heavy neutral lepton* or right-handed neutrino, though its chirality is a matter of convention. The smallness of this coupling is usually associated to a difference of scales between the EW vev, and the new mass scales of the heavy neutral lepton. We will study such a model in detail in the next chapter.

Vector portal Any new vector particle X^μ from an Abelian gauge group may couple to the $d = 2$ field strength of the SM hypercharge

$$B_{\mu\nu}, \tag{1.3.3}$$

through its own field strength tensor $X^{\mu\nu}$. The resulting term, $B_{\mu\nu}X^{\mu\nu}$, is a off-diagonal kinetic term for the massive bosons and is sometimes called the *kinetic mixing* operator. This may arise from heavy fermion loops that are integrated out, or through the simultaneous presence of the two Abelian groups across all scales [2]. To work in a basis of physical states with diagonal kinetic terms, where the propagators are in their standard form, one usually performs a field redefinition. If much lighter than the EW scale, the new vector particle couples primarily to the EM current, hence the name dark photon. If heavy, it can also couple to the NC and is therefore referred to as a dark Z. Models with the term

$$Z_\mu X^\mu, \tag{1.3.4}$$

also appear in the literature, where it is said that *mass-mixing* between the new vector particle and the SM Z exists. This term is not gauge invariant, but may arise in the broken phase of BSM theories with additional doublet scalars, like in two-Higgs-doublet models (2HDM). In this case, several charged degrees of freedom typically appear and experimental constraints tend to be more severe.

Higgs portal New scalar particles can couple to the $d = 2$ bilinear

$$H^\dagger H, \tag{1.3.5}$$

[2] Such possibility is clearly incompatible with Grand unification at the highest scales, but this remains, after all, a hypothesis.

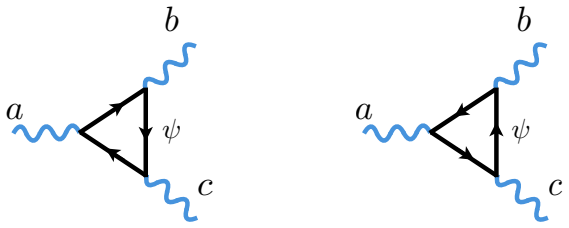

Fig. 1.4. Anomalous triangle diagrams. The fermion loop is reversed on the right.

the only renormalizable portal with no free Lorentz or spinor indices. In this case there are two possibilities for a scalar to couple to the SM, depending on its charges. We can write $H^\dagger H\, S^\dagger S$ for a charged, or $H^\dagger H\, S$ for a singlet complex scalar. The latter term is the only super-renormalizable operator connecting the SM fields to new physics which is allowed. Beyond important consequences for EW SSB, these operators typically inherit the Higgs couplings to matter fields, and may be hard to search for due to the smallness of the SM Yukawa couplings. Remarkably, this extension can also have consequences to the hierarchy problem, as the new scalar also contributes to the Higgs self-energy [50].

Fermionic currents A whole set of (EM) neutral operators in the SM come from the fermionic currents

$$J^\mu = \overline{\Psi}\gamma^\mu\Psi, \tag{1.3.6}$$

where $\Psi \in \{Q_L, L, u_R, d_R, \ell_R\}$. These are not gauge invariant, in general, and will generally require new gauge symmetries to be useful as a portal to the dark sector. The SM currents can be associated with new conserved charges, which in turn may be regarded as a global or promoted to a local gauge symmetry. In the latter case, the new conserved charge is said to be gauged under a local symmetry and additional gauge bosons are introduced, potentially massive. Here, we must also require that it be anomaly-free. This means that the symmetry must be conserved not only classically, but also at loop level. Various types of anomalies exist, but of most interest in gauge extensions of the SM are the chiral gauge anomalies. These can be calculated from the amplitudes of the triangle diagrams shown in Fig. 1.4, and are proportional to

$$\mathrm{Tr}\left[(T^a T^b + T^b T^a)T^c\right], \tag{1.3.7}$$

where T^a is the group generator corresponding to the gauge boson and in the relevant representation. Here, we take only left-handed particles and anti-particles running in the loop. The simplest case is the one of the $[U(1)]^3$ chiral anomaly, where it reduces to the requirement that $\sum_\psi Q_\psi^3 = 0$ for all fermions ψ charged under the Abelian group. In the SM, baryon number B, lepton number L and the individual lepton number L_α are all accidentally conserved quantities. Non-perturbative effects, however, violate B and L_α, and these quantities are no longer conserved [3]. Nevertheless, $B - L$ and the combinations $L_\alpha - L_\beta$ are preserved in these processes and can be taken to be a *global* symmetry of the SM. It is only when gauging these symmetries that one realizes that $B - L$ is, in fact, violated by the chiral triangle diagrams and $L_\alpha - L_\beta$ remains anomaly-free. We explore these leptphilic currents in Abelian extensions of the SM in Chapter 4.

The above exhausts the minimal possibilities for SM portals that lead to renormalizable operators to new physics. Nevertheless, for completeness, we will also comment on a well-motivated non-renormalizable operator that is also frequently discussed in the context of light new physics.

Pseudo-scalar The Peccei-Quinn solution to the strong-CP problem predicts the existence of a new pseudo-scalar a, the axion. This is the pseudo-Nambu-Goldstone boson from the breaking of the global $U(1)_{\rm PQ}$ *axial* symmetry at a scale f_a. Such particle would then acquire couplings to gauge bosons and SM fermions ψ as in

$$c_1 \frac{a}{f_a} G^a_{\mu\nu}\widetilde{G}^{\mu\nu}_a + c_2 \frac{a}{f_a} W^a_{\mu\nu}\widetilde{W}^{\mu\nu}_a + c_3 \frac{a}{f_a} B_{\mu\nu}\widetilde{B}^{\mu\nu} + \sum_\psi c_4^\psi \frac{\partial_\mu a}{f_a}\overline{\psi}\gamma^\mu\gamma^5\psi, \tag{1.3.8}$$

where c_i are model-dependent couplings and are typically linear dependent. Axion particles from models that solve the strong-CP problem, commonly referred to as the QCD axions, are not the only possibility. In fact, light pseudo-scalar from the breaking of new symmetries at higher energies provide a well-motivated target for study and go under the name axion-like-particle (ALP). In this case, the relation between the ALP mass and its couplings is less restricted.

[3] Beyond the SM, L_α is already violated at tree-level by the small observed neutrino masses.

Chapter 2

Current Aspects of Neutrino Physics

This chapter is dedicated to studying some important and more technical aspects of neutrino physics for the rest of the thesis. We start by reviewing some of the most popular models to explain non-zero neutrino masses beyond the SM. This will be useful to introduce neutrino masses and mixing, with which we can comment on neutrino oscillations in vacuum and in matter. We then move on to discuss the usual approach to studying neutrinos in the laboratory, focusing on accelerator experiments. We will find that it is hard to ignore the strong force in many of the most important neutrino cross sections.

2.1 Mass Mechanisms

Understanding the theoretical origins of neutrino mass and mixing is a worthwhile but ambitious task. The possibilities are endless and the high-scale dynamics, typical of many neutrino mass models, is hard to test in the laboratory. Presently, it is fair to say there are more neutrino mass models than ways to test them. Nonetheless, many of these models possess similar features and just a couple of low energy observables are sufficient to probe a large class of models. These models may rely on the seesaw mechanism, on radiative effects or in extended scalar sectors. On top of that, new symmetries and fundamental forces may also be at play, making the theories more predictive. We will now explore a small fraction of this model space.

We have already alluded to the first possibility to introduce light neutrino masses in the SM. All that is needed are at least two RH neutrino fields, singlets under all SM symmetries. We shall refer to them as N^α, where α is their generation index. This may be chosen to be $\alpha = e, \mu, \tau$ or any combination of two of these. The full new neutrino mass Lagrangian then becomes

$$\mathscr{L}_{\nu-\text{mass}} = \overline{N}^\alpha i\partial\!\!\!/ N_\alpha - y^\nu_{\alpha\beta}\left(\overline{L}^\alpha \widetilde{H}\right) N^\beta - \left(y^\nu_{\alpha\beta}\right)^* \overline{N^\beta}\left(\widetilde{H}^T L^\alpha\right) - M_{\alpha\beta}\overline{N^c}^\alpha N^\beta, \qquad (2.1.1)$$

where $N^c = C\overline{N}^T$ with C the charge conjugation matrix ($C = i\gamma^2\gamma^0$ in the Dirac and Weyl representation). The middle terms endow neutrinos with Dirac masses, but the last one is a new ingredient. This is the Majorana mass matrix for the new RH neutrinos, and it is allowed by the symmetries of the model. It does, however, violate any $U(1)$ symmetry associated with the fields N, as

$$N \to e^{i\theta} N \implies \overline{N^c} N \to e^{2i\theta}\overline{N^c} N. \qquad (2.1.2)$$

So if N are assigned lepton number, then the accidental global symmetries of the SM $B-L$ and L are violated by the Majorana mass term. If we insist and set $L(N) = 0$, then the Dirac mass term will, instead, explicitly break these global symmetries. This interesting observation, together with the fact that gauging $B - L$ leads to an anomaly-free theory with three RH neutrinos, has led proposals of Dirac neutrino mass models with gauged and unbroken $B - L$ [51]. On top of that, the scale of the entries in $\mathbf{M}$ is not set by the Higgs vev and, therefore, may be wildly different from the EW scale. We may argue that it has to be small, since in the limit that all $M_{\alpha\beta} \to 0$, the SM symmetry is enhanced and the theory is said to be technically natural in the t'Hooft sense. Regardless of our argument to prevent this term, one thing is clear, a purely Dirac neutrino mass model has to deal with the fact that the neutrino Yukawas are extremely small $y^\nu/y^t \approx 10^{-12}$. If the arbitrariness of Yukawa couplings in the SM already made us uncomfortable, this SM extension dramatically worsens the picture. Of course, we may be tempted to ignore the flavour puzzle and just stop here. This solution, however, as underwhelming as it is, is not unique. Many other models for neutrino masses exist and, while we cannot rule all of them out, it is worthwhile to study the alternatives.

In the same way that the N particles admitted a Majorana mass term, we may wonder if the SM may also provide a similar term for the LH states. Clearly $SU(2)\times U(1)$ invariance

forbids any renormalizable operator that would give rise to this operator before SSB, but at $d = 5$, we can write the so-called Weinberg operator

$$\mathscr{L}_{d=5} = \frac{c_{\alpha\beta}}{\Lambda}\left(\overline{L^c}\widetilde{H}^*\right)\left(\widetilde{H}^\dagger L\right) \to \frac{c_{\alpha\beta}}{\Lambda}\frac{v^2}{2}\overline{\nu_L^c}^\alpha \nu_L^\beta \tag{2.1.3}$$

where we go from the unbroken to the broken phase. This operator is, in fact, the only $d = 5$ operators allowed in the SM effective field theory (SMEFT). The fact that the lowest dimension non-renormalizable operator in the SMEFT gives neutrino masses is, yet again, another indication that neutrino masses point towards BSM physics. Unfortunately, assuming the coefficients to be $\mathcal{O}(1)$ and saturating the upper bound on the sum of neutrino masses $m_\nu \lesssim 0.1$ eV, we are led to conclude that $\Lambda \approx 10^{14}$ GeV, eerily close to the Planck scale. There is, however, no reason to expect the couplings of the theory to be large and for the mass mechanism to be simple. Technical naturalness, for instance, is commonly invoked to claim that the mass mechanism may reside at low scales, where we trade unreachable energies for tiny couplings. We will shortly see all tree-level UV-completions to the Weinberg operator. Of course, neutrino masses need not be tree-level effects, and loop-induced mechanisms for generating Dirac or Majorana neutrino masses are also important. In this case, the smallness of neutrino masses is explained through loop suppression factors. We come back to these issues in Section 2.1.1.

The mass term induced by Eq. (2.1.3) turn out to be of the Majorana kind. Testing this hypothesis is extremely difficult because of the smallness of m_ν. Any process containing lepton number violation (LNV), the hallmark of Majorana neutrinos, will be suppressed by m_ν^2/E^2, where E is the typical energy involved. Another way to understand this is that any process where the operator above is important must be sensitive to the effects of neutrino mass, which we have yet to measure. Curiously, this holds also for neutrino oscillations. In that case, one might also worry about additional phases that appear in the Majorana case, but these can be shown to drop out. Currently, the most promising search for the Majorana nature of neutrinos is neutrinoless double-beta decay ($0\nu\beta\beta$), $(A, Z) \to (A, Z+2) + e^- + e^-$. This process is only allowed if neutrinos are Majorana, and should be contrasted with double-beta decays ($2\nu\beta\beta$), where two neutrinos are present in the final state.

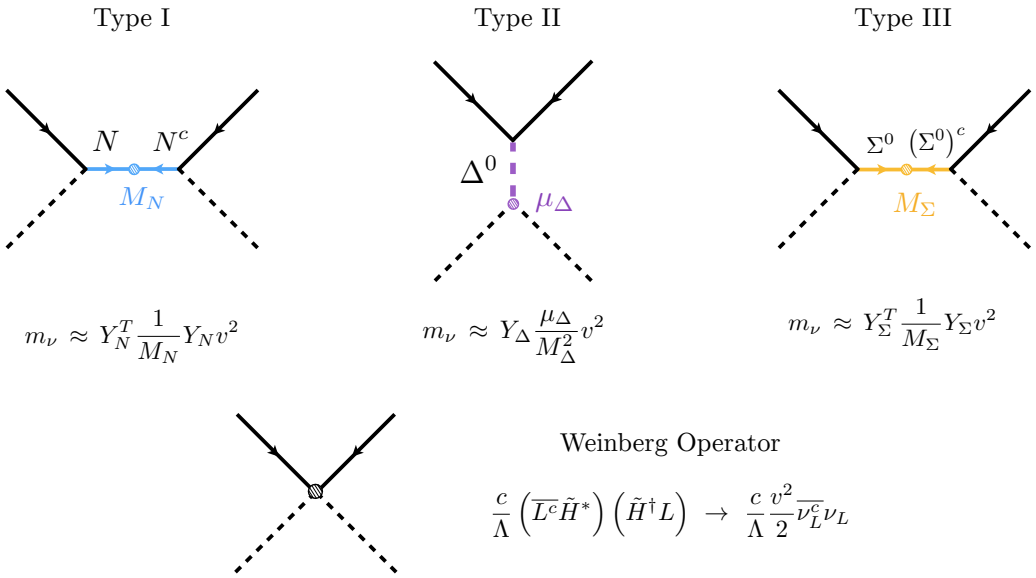

Fig. 2.1. The tree-level UV completions (top) of the $d = 5$ Weinberg operator (bottom) with their respective contributions to light neutrino masses.

2.1.1 Conventional Seesaw Mechanisms

There exist only three ways to UV complete the Weinberg operator at tree-level. These correspond to introducing a new fermion which is a singlet of $SU(2)_L$, a new scalar that transforms as a triplet of $SU(2)_L$ or a new fermion that also transforms as a triplet. These models are usually referred to as the Type I [52–55], Type II [56–60] and Type III [61] seesaw mechanism, respectively. They are shown in Fig. 2.1 and we discuss each one individually below.

Type I The Lagrangian for this extension is precisely the one in Eq. (2.1.1). For convenience, let us work in the single generation case. We collect all mass terms into a single mass matrix of the form

$$-\mathscr{L}_{\nu-\text{mass}} \supset \frac{1}{2}\begin{pmatrix}\overline{\nu_L} & \overline{N^c}\end{pmatrix}\begin{pmatrix}0 & m\\ m & M_N\end{pmatrix}\begin{pmatrix}\nu_L^c\\ N\end{pmatrix} + \text{h.c.}, \tag{2.1.4}$$

where $m = y_N^\nu v/\sqrt{2}$ and M_N is the Majorana mass for N. Diagonalizing this mass matrix with a simple rotation $R(\theta)$, we find

$$m_{1,2} = \frac{M_N \pm \sqrt{M_N^2 - 4m^2}}{2}, \quad \text{with} \quad \tan 2\theta = \frac{2m}{M_N}. \tag{2.1.5}$$

In the so-called seesaw limit ($m \ll M_N$), this simplifies to

$$m_1 \approx -\frac{m^2}{M_N} = \frac{(y_N^\nu v)^2}{2M_N}, \quad m_2 \approx M_N \quad \text{with,} \quad \theta \approx \frac{m}{M_N}, \tag{2.1.6}$$

where the seesaw mechanism is in action: the large separation of scales between m and M_N explains the smallness of the light neutrino masses m_1. Saturating the upper bound on neutrino masses $m_1 \approx 0.1$ eV, we can infer that

$$(y_N^\nu)^2 \approx 3 \times 10^{-15} \left(\frac{M_N}{\text{GeV}}\right), \qquad \theta^2 \approx 10^{-10} \left(\frac{M_N}{\text{GeV}}\right)^{-1}. \tag{2.1.7}$$

Again, we conclude that the scale of new physics for couplings of $\mathcal{O}(1)$ lies at $M_N \approx 10^{15}$ GeV, in this case with very small mixing angles between the light states and the flavour N. Of course, this is only a naive scaling and becomes more complicated in the full three generation case [62]. Nevertheless, it shows that heavy neutrinos at reasonably low scales are a reachable candidate to realise the seesaw mechanism, provided we are comfortable with small values for y_N^ν.

Type II In the presence of a scalar $\mathbf{\Delta}$, triplet under $SU(2)$, we can write

$$-\mathscr{L}_{\nu-\text{mass}} \supset y_\Delta^\nu \, \overline{L^c} i\sigma_2 \mathbf{\Delta} L, \quad \text{with} \quad \mathbf{\Delta} = \begin{pmatrix} \Delta^+/\sqrt{2} & \Delta^{++} \\ \Delta^0 & -\Delta^+/\sqrt{2} \end{pmatrix}, \tag{2.1.8}$$

where new charged scalars are appear. The scalar potential acquires the term

$$-V(H,\Delta) \supset \mu_\Delta H^T \, i\sigma_2 \mathbf{\Delta} H + M_\Delta^2 \, \text{Tr}\Big\{\mathbf{\Delta}^\dagger \mathbf{\Delta}\Big\}, \tag{2.1.9}$$

and is in general much more complicated. One can show that the neutral component acquires a vev $\langle \Delta^0 \rangle \approx \mu_\Delta v^2 / M_\Delta^2$, where we ignored additional mixing terms between the Higgs and the new scalar degrees of freedom [63]. This vev, then gives neutrinos mass through Eq. (2.1.8), which interestingly, is linear in the neutrino Yukawa and suppressed by the typical mass scale of Δ

$$m_1 \approx y_\Delta^\nu \frac{\mu_\Delta \, v^2}{M_\Delta^2}. \tag{2.1.10}$$

The field $\mathbf{\Delta}$, in fact, carries lepton number $L = 2$, and so the LNV parameter μ_Δ being small is a technically natural choice. In this model, the vev of Δ^0 is constrained to be very low, $\langle \Delta^0 \rangle \lesssim 5$ GeV, as $\mathbf{\Delta}$ contributes to the EW gauge boson masses through its kinetic

term Tr $\left[(D_\mu \mathbf{\Delta})^\dagger (D^\mu \mathbf{\Delta})\right]$. Finally, we can see for $m_1 \approx 0.1$ eV, we get

$$y^\nu_\Delta \approx \left(\frac{1\text{eV}}{\mu_\Delta}\right)\left(\frac{M}{1\,\text{TeV}}\right)^2, \tag{2.1.11}$$

suggesting a clear target for experimental searches around at EW scale.

Type III The fermionic triplet couples to the doublets through

$$-\mathscr{L}_{\nu-\text{mass}} \supset y^\nu_\Sigma \overline{L}\mathbf{\Sigma}H, \quad \text{with} \quad \mathbf{\Sigma} = \begin{pmatrix} \Sigma^0 & \Sigma^+/\sqrt{2} \\ \Sigma^-/\sqrt{2} & -\Sigma^0 \end{pmatrix}. \tag{2.1.12}$$

In this case, the scalar sector may remain unchanged and the field Σ^0 behaves very similarly to the field N in the Type I seesaw. Analogously to the Type I, we can write

$$m_1 \approx \frac{(y^\nu_\Sigma v)^2}{2M_\Sigma}. \tag{2.1.13}$$

This model is much less explored in the literature, but its phenomenology is quite rich. The term related to charged-leptons in Eq. (2.1.12) induces charged-lepton mixing, and leads to rare processes such as $\mu \to e\gamma$ and $\mu \to eee$ already at tree-level, contrary to the Type-I seesaw where they appear at one loop.

2.1.2 Low-Scale Seesaw Variants

All of the previous models may be searched for at low or high energy ranges, but for large Yukawa couplings, are regarded as high-scale solutions to the neutrino problem. Exceptions to this arise in constructions where additional symmetry arguments are at play. Most famous are the Inverse Seesaw (ISS) [64, 65] and the Linear Seesaw (LSS) [66–68], where the lightness of neutrino masses is explained by an approximate conservation of lepton number, and the Extended Seesaw (ESS) [69–71], where new hierarchies appear in the heavy sector. All these extensions arise from introducing additional neutral fermions to the Type I seesaw particle content. In particular, in the single generation case, the most general mass matrix we can construct with the new fermions N and S is given by [72]

$$-\mathscr{L}_{\nu-\text{mass}} \supset \frac{1}{2}\begin{pmatrix} \overline{\nu_L} & \overline{N} & \overline{S} \end{pmatrix}\begin{pmatrix} 0 & m & \epsilon \\ m & \mu' & \Lambda \\ \epsilon & \Lambda & \mu \end{pmatrix}\begin{pmatrix} \nu^c_L \\ N^c \\ S^c \end{pmatrix} + \text{h.c.} \tag{2.1.14}$$

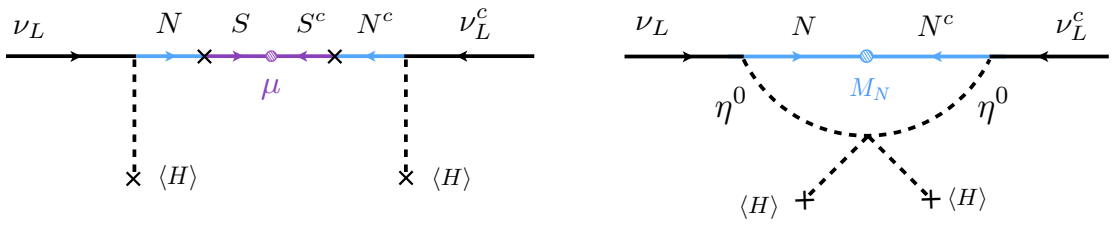

Fig. 2.2. On the left, the inverse seesaw flavour diagram for Majorana neutrino masses. On the right, the flavour diagram for the scotogenic mode. Arrows represent lepton number.

Note that lepton number, defined as $L = L_e + L_\mu + L_\tau + L_N + L_S$, is violated by μ, μ' and ϵ if we assign, as usual, $L_N = -L_S$. From the diagonalization of this mass matrix, we learn that

$$m_1 = \frac{\mu m^2 - 2\epsilon m\Lambda + \epsilon^2\mu'}{\Lambda^2 - \mu\mu'}. \tag{2.1.15}$$

Therefore, we see that if all LNV parameters are set to zero, neutrino masses vanish. In the same way, if we set $\epsilon, \mu \to 0$, then we also get vanishing neutrino masses, at tree level. This accidental cancellation is very peculiar, and will be realised in the model introduced in Chapter 5. As it turns out, μ' breaks lepton number, and so radiative corrections can be large, responsible for the light neutrino masses in this case.

The ISS model can be recovered in the limit $\Lambda \gg m \gg \mu \gg \mu', \epsilon$. Now, the smallness of neutrino masses are controlled by the LNV parameter μ, which is small due to approximate conservation of L, and suppressed by $1/\Lambda^2$, realising the seesaw mechanism. In this way, the additional neutrino states combine into a pseudo-Dirac pair, with a mass of $m_{2,3} \approx \Lambda \mp (\mu + \mu')/2$. These type of models predict small LNV, but the new heavy fermions will reside at much smaller scales while mainting the Yukawa couplings large. The LSS is another special case where $\Lambda \gg m \gg \epsilon \gg \mu', \mu$. In this case the light neutrino mass is *linear* in m and suppressed by ϵ/Λ^2.

In the ESS limit, $\mu' \gg \Lambda, m \gg \mu, \epsilon$, LNV is large and the light neutrino masses are suppressed by the scale μ'. The seesaw, in this case, happens both for light and intermediate neutrinos, and so light new fermions are typical predictions of the model, of interest to the literature on scale sterile neutrinos.

2.1.3 Radiative Masses

A further possibility to generate the Weinberg operator is that Majorana neutrino masses arise from higher-order diagrams in perturbation theory. Since in the SM L is an accidental symmetry, neutrino masses vanish at all orders, but this may not be the case in a generic SM extension. For instance, neutrino masses may arise at n loops, in which case a naive estimate for the scale of new physics is

$$\frac{c}{\Lambda} \approx \left(\prod_{i}^{\#\text{ of vertices}} g_i \right) \left(\frac{1}{4\pi} \right)^{2n} \frac{1}{M}, \tag{2.1.16}$$

where g_i stand for the new couplings of the theory and M is a new mass scale. The loop suppression factor is of interest since it lowers the scale Λ without the need for small couplings or large masses. Many models for radiative neutrino masses exist, where typically new particles are introduced together with a new symmetry that prevents any of the mechanisms discussed previously to take place.

The most illustrative example is perhaps the *scotogenic* model [73], sometimes also referred to as the radiative seesaw. Here, new SM singlet fermions N are introduced together with η, a copy of the Higgs doublet with $\eta = (\eta^+, \eta^0)^T$ and $Y_\eta = Y_H = 1$. To forbid tree-level masses, an additional Z_2 discrete symmetry is introduced, under which all new states are odd ($N \to -N$ and $\eta \to -\eta$) and all SM particles are even (*e.g.*, $L \to L$). In the single generation case, the new fermion mass terms are

$$-\mathscr{L}_{\nu-\text{mass}} \supset \frac{M_N}{2} \overline{N^c} N + \left[y^N \left(\overline{L}\, \widetilde{\eta} \right) N \,+\, \text{h.c.} \right], \tag{2.1.17}$$

where the Yukawa term $(\overline{L}\widetilde{H})N$ is not allowed by virtue of the Z_2 symmetry. The scalar potential now contains

$$V(H, \eta) \supset m_\eta^2 \eta^\dagger \eta + \frac{\lambda'}{2} \left[\left(H^\dagger \eta \right)^2 + \left(\eta^\dagger H \right)^2 \right], \tag{2.1.18}$$

where $m_\eta^2 > 0$ and $\eta^0 = (\eta_R + i\eta_I)/\sqrt{2}$ acquires no vev. After SSB, we end up with an additional neutral scalar η_R and neutral pseudo-scalar η_I of masses $m^2_{R,\,I} = m_\eta^2 \pm \lambda' v^2/2$. The one-loop neutrino masses are then given by

$$m_1 = \frac{1}{2} \left(\frac{y^N}{4\pi} \right)^2 M_N \left[\frac{m_R^2}{m_R^2 - M_N^2} \ln \left(\frac{m_R^2}{M_N^2} \right) - \frac{m_I^2}{m_I^2 - M_N^2} \ln \left(\frac{m_I^2}{M_N^2} \right) \right]. \tag{2.1.19}$$

In this case, we can see the loop suppression and the new Yukawas. To find what mass scale

appears in the denominator, we may choose a limit. For $M_N \gg m_\eta$, we find $m_1 \propto \lambda' v^2/M_N$ up to loop factors and the Yukawas, while for $M_N \ll m_\eta$, we have $m_1 \propto \lambda' v^2 M_N/m_\eta^2$. The diagram on the right in Fig. 2.2 explicitly shows how this dependence comes about.

Note that due to the Z_2 symmetry, N and η^0 define a dark sector, with the lightest particle being a DM candidate. Despite the absence of the neutrino portal operator in this case, neutrino mixing between light states and the flavour N is generated at one loop. In addition, the $\eta^\pm$ provides a strong connection between the SM and the dark sector. Many models for radiative neutrino masses display similar features to these, where new dark states often solve the neutrino and DM puzzle at the same time. This connection is explored in more detail in Chapter 5. Beyond one loop, neutrino mass models have been studied up to three-loop level [74].

2.2 Neutrino Mixing

Now that we have a series of concrete models to generate neutrino masses, we would like to understand the consequences of massive neutrinos at low energies and how we learned about their mass. For our current purposes, we will focus purely on the $SU(2)$ breaking operator for Majorana and Dirac neutrino masses

$$\mathscr{L}^{\mathrm{M}}_{\nu-\mathrm{mass}} = \frac{M_{\alpha\beta}}{2}\overline{\nu_L^c}^{\alpha}\nu_L^{\beta} + \text{h.c.}, \qquad \mathscr{L}^{\mathrm{D}}_{\nu-\mathrm{mass}} = \frac{y^{\nu}_{\alpha\beta}v}{\sqrt{2}}\,\overline{\nu_L}^{\alpha}N^{\beta} + \text{h.c.}, \tag{2.2.1}$$

where the former Lagrangian describes purely Majorana neutrinos, and the latter describes purely Dirac neutrinos with the addition of three N states to the SM. We will work with only three N states for simplicity, any number greater than two is analogous. Similarly to the quark sector, we would like to diagonalize these mass matrices and find the relevant mixing matrix. We proceed with the two cases in parallel and start by rotating all fields independently with unitary matrices

$$\begin{aligned} \nu_L^{\alpha} &\to U^{\nu}_{\alpha k}\nu_L^k, \qquad & N^{\alpha} &\to V^{\nu}_{\alpha k}N^k \\ e_L^{\alpha} &\to U^{e}_{\alpha k}e_L^k, \qquad & e_R &\to V^{e}_{\alpha k}e^k, \end{aligned} \tag{2.2.2}$$

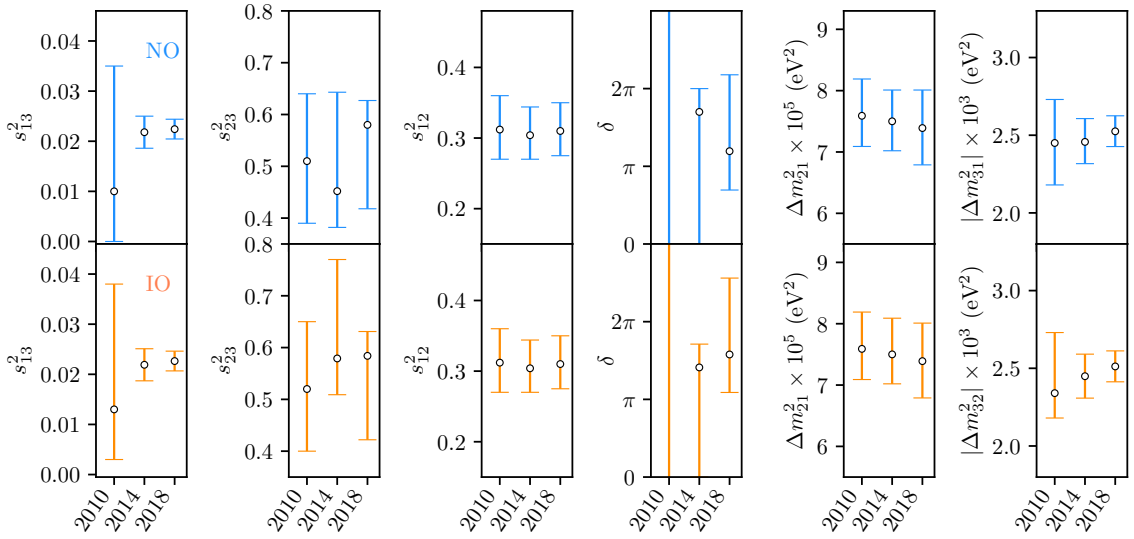

Fig. 2.3. The neutrino oscillation global-fit results in 2010 [77], 2014 [78] and 2018 [79]. We show the best-fit point, together with the 3σ regions for normal ordering (NO) and inverted ordering (IO).

where U (V) rotates LH (RH) fields. From Eq. (2.2.1), it is clear that the diagonalization is slightly different in the two cases. The diagonal mass matrices are

$$\mathbf{M} \to \hat{\mathbf{M}} = \mathbf{U}^{\nu\,T}\mathbf{M}\mathbf{U}^{\nu}, \qquad \mathbf{Y} \to \hat{\mathbf{Y}} = \mathbf{U}^{\nu\,\dagger}\mathbf{Y}\mathbf{V}^{\nu}, \tag{2.2.3}$$

where $\mathbf{M}$ and $\mathbf{Y}$ are diagonal matrices [1]. The CC Lagrangian defines lepton mixing through the Pontecorvo-Maki-Nakagawa-Sakata (PMNS) matrix [75, 76]

$$\overline{e_L}^{\alpha}\gamma_{\mu}P_L\nu_L^{\alpha} \to \overline{e_L}^{k}P_L\,(U_{\rm PMNS})_{kj}\,\nu_L^{j}, \qquad \mathbf{U}_{\rm PMNS} = \mathbf{U}^{e\,\dagger}\mathbf{U}^{\nu}. \tag{2.2.4}$$

At this point, we can identify the charged-lepton fields e^k with their gauge basis (*i.e.*, their flavour and mass basis coincide $\alpha \sim k$) and define the LH flavour neutrino field $\widehat{\nu}^{\alpha} = (U_{\rm PMNS})_{\alpha j}\,\nu_L^j$. This is the relevant field for all neutrino CC interactions, but it does not have a well-defined mass. For simplicity, we will now adopt the notation $\widehat{\nu}^{\alpha} \equiv \nu^{\alpha}$.

The PMNS mixing matrix is responsible for neutrino mixing and its entries are model dependent, arising from the flavour structure of the neutrino Yukawas and Majorana

[1] Note that in the Dirac case, the mass matrix $\mathbf{Y}$ is diagonalized by its singular value decomposition, and in the Majorana case we assumed $\mathbf{M}$ to be complex *symmetric* and the special case of Takagi factorization applies.

masses. In the general case, it is parametrized by

$$U_{\rm PMNS} = \begin{pmatrix} 1 & 0 & 0 \\ 0 & c_{23} & s_{23} \\ 0 & -s_{23} & c_{23} \end{pmatrix} \begin{pmatrix} c_{13} & 0 & s_{13}e^{-i\delta} \\ 0 & 1 & 0 \\ -s_{13}e^{-i\delta} & 0 & c_{13} \end{pmatrix} \begin{pmatrix} c_{12} & s_{12} & 0 \\ -s_{12} & c_{12} & 0 \\ 0 & 0 & 1 \end{pmatrix} D, \tag{2.2.5}$$

where $c_{ij} = \cos\theta_{ij}$ and $s_{ij} = \sin\theta_{ij}$ are the cosine and sine of the mixing angles to be measured from oscillation data. The matrix $D = \text{diag}\{1, e^{i\alpha_2/2}, e^{i\alpha_3/2}\}$ contains additional phases that are physical when neutrinos are Majorana. As we will see in the next section, oscillation data can shed light on all mixing angles, mass-squared differences $m^2_{ij} = m^2_i - m^2_j$, and on the CP-violating phase δ. Neutrino oscillations are insensitive, however, to any Majorana phases.

Immense efforts to measure all parameters in the PMNS have been carried out in the past 26 years. In Fig. 2.3, we show the relative precision reported by a global-fit to neutrino oscillation data, comparing the data release from after the Neutrino conferences of 2010 [77], 2014 [78] and 2018 [79]. All three mixing angles and two mass-squared splittings have been succesfully measured to at least 3σ, with the exception of the CP-violating phase δ, which is still largely unknown. Another interesting development is our knowledge of the mass ordering. This is a measurement of the sign of $\Delta m^2_{3\ell}$, where $\ell = 1$ for normal ordering (NO) and $\ell = 2$ for inverted ordering (IO). While currently the global-fit in Ref. [79] displays a mild preference for NO ($\Delta\chi^2 = 4.7$), future measurements are needed. For Δm^2_{21}, this sign is known, as it strongly impacts the matter potential of solar neutrinos.

2.2.1 Neutrino Oscillations

Neutrino oscillations arise when a superposition of neutrino mass eigenstates is produced, propagates macroscopic distances and scatters inside a detector. Given sufficiently long baselines, neutrino flavour transitions may always occurs due to mixing, but for a non-trivial dependence on baseline distances, coherence must be preserved throughout the process. In this section, we will make these statements more precise and derive the standard formula for the oscillation probability $P(\nu_\alpha \to \nu_\beta)$ in vacuum (matter effects are discussed in Section 2.2.2). This exercise can be done in multiple ways and most often derivations rely on plane-wave neutrino states. This approach leads to correct expressions for $P(\nu_\alpha \to \nu_\beta)$ in virtually all cases of interest, but it is a rather poor conceptual

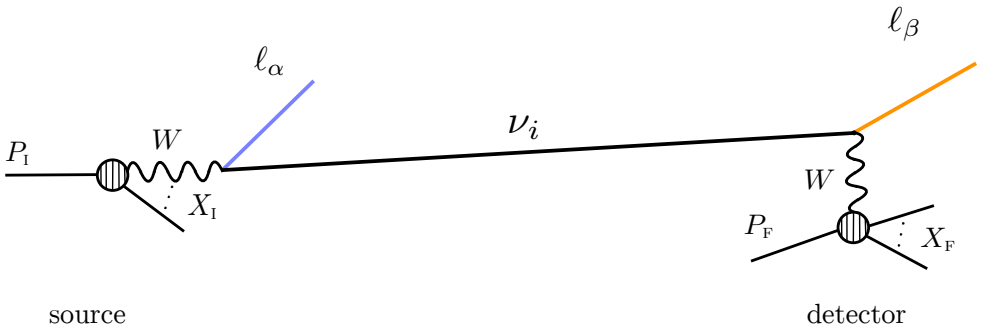

Fig. 2.4. The usual set-up of an oscillation experiment. We show the source, where a process $P_\mathrm{I} \to \nu_\alpha\, X_\mathrm{I}$ happens (note that $P_\mathrm{I} = \ell_\alpha$ is allowed and that P_I may be a scattering process), and the detector, where $\nu_\beta\, P_i \to \ell_\beta\, X_\mathrm{f}$.

description of oscillations and relies on unphysical assumptions. Instead, we will derive the oscillation formula from a quantum mechanical wave packet approach, and encounter a few conditions for oscillations to happen. More sophisticated treatments in Quantum Field Theory (QFT), often called the *external* wave packet approach, have been known for some time [80–82], and their results have been shown to be directly mapped onto the *internal* wave packet approach [83] we discuss here. Nonetheless, neutrino oscillations are notorious for being conceptually confusing and the correct method to compute such processes is still debated in the literature [84]. We may seek consolation in the fact that a few aspects are common to all approaches, for instance, the ultra-relativistic nature of the mass states through expansions of $\sqrt{m^2+p^2}$ and the need for momentum uncertainties in the initial and final neutrino processes.

Our setup typical of neutrino oscillations experiments and is represented in Fig. 2.4. We will first discuss the role of production and detection processes, and then later study the oscillations *per se*. Initially, a neutrino flavour state ν_β is produced in a CC reaction at the source, $P_\mathrm{I} \to \nu_\beta X_\mathrm{I}$. More precisely, a state $|f\rangle$ is produced,

$$|f\rangle = \hat{S}\,|P_\mathrm{I}\rangle\,, \quad \hat{S} \approx \hat{1} - i\int \mathrm{d}^4x\, H^{\mathrm{CC}}_{\mathrm{int}}(x), \tag{2.2.6}$$

where $\hat{S}$ is the S-matrix operator approximated to first order in weak coupling and

$$H^{\mathrm{CC}}_{\mathrm{int}}(x) = \sqrt{2}G_F \sum_\alpha \overline{\nu}_\alpha(x)\gamma^\mu P_L \ell_\alpha(x)\, J_\mu(x) \;+\; \mathrm{h.c.}, \tag{2.2.7}$$

is the interaction Hamiltonian between the neutrino current and the current $J_\mu(x)$ that describes the transition $P_\mathrm{I} \to X_\mathrm{I}$. After ℓ_α and the final particles interact with the medium,

$|f\rangle$ is projected out onto the state $\langle \ell_\alpha,\, X_{\rm I}|f\rangle$, which ought to ensure that the neutrino state produced is a superposition of massive states weighed by the PMNS matrix elements $U^*_{\alpha i}$ and other kinematic factors. Note that this may differ from the usual definition of a flavour state $|\nu^\alpha\rangle = U^*_{\alpha i}\,|\nu_i\rangle$, which can be misleading in this situation as these do have a definite mass and do not span a Fock space (for a recent and illuminating discussion on this issue, see Ref. [85]). We want to work instead with the eigenstates of the free Hamiltonian, which are the ones with a definite mass and that can easily be evolved in time. With this in mind, we define the following amplitude

$$A_{\alpha k}(\vec{p},h)^P \equiv \langle \nu_k(\vec{p},h), \ell_\beta, X_{\rm I}|\,\hat{S}\,|P_{\rm I}\rangle\,, \quad \text{with} \quad A_{\alpha k}(\vec{p},h) = U^*_{\alpha k} M_{\alpha k}(\vec{p},h), \tag{2.2.8}$$

where we factored out a mixing angle in the definition of $M_{\alpha k}$ and made the helicity index h explicit. By virtue of the completeness relation with massive neutrino eigenstates, we can insert the identity in $\langle \ell_\alpha,\, X_{\rm I}|f\rangle$ and define a *normalized* neutrino flavour state as

$$|\nu_\alpha\rangle^P = N_P \sum_{k,h} \int \mathrm{d}^3p\, A^P_{\alpha k}(\vec{p},h)\,|\nu_k(\vec{p},h)\rangle\,, \quad N_P^{-2} = \sum_{k,h}\int \mathrm{d}^3p\,\left|A^P_{\alpha k}(\vec{p},h)\right|^2. \tag{2.2.9}$$

An analogous discussion holds for the detection process $\nu_\beta\, P_{\rm F} \to \ell_\beta\, X_{\rm F}$, where a detection flavour state $|\nu_\alpha\rangle^D$ with an amplitude for detection $A_{\alpha k}(\vec{p},h)^D$ can be defined. Before we move on to a discussion about oscillations, we want to emphasize two points. First, the normalization of the flavour state is a clear sign that we are working in a quantum mechanical description. To compute probabilities, we rely on normalized states. In a QFT description, however, the normalization is not necessary, but neither is the concept of $P_{\rm I} \to X_{\rm I}$ in the first place. There, the full process $P_{\rm I}\,P_{\rm F} \to X_{\rm I}\,X_{\rm F}\,\ell_\alpha\,\ell_\beta$ in Fig. 2.4 can be compute directly through the use of long-distance propagators. If the production, propagation and detection parts of the amplitude squared factorize, an object analogous to the oscillation probability can be extracted. This factorization is implicitly assumed in our calculation. Secondly, the decay rate of the $P_{\rm I}$ particle can be computed as

$$\left|A^P\right|^2 = \left|\langle \nu_\alpha(\vec{p},h), \ell_\beta, X_{\rm I}|\,\hat{S}\,|P_{\rm I}\rangle\right|^2 = \sum_{k,h}|U_{\alpha k}|^2 \int \mathrm{d}^3p\,\left|M^P_{\alpha k}(\vec{p},h)\right|^2, \tag{2.2.10}$$

and it becomes evident that the decay rate is given by the *incoherent* sum of the decay rate into different massive neutrinos. No interference is present as the states $|\nu_k\rangle$ are assumed to be orthonormal to each other. This remains true in the QFT description [82].

Now, one is left to compute the functions $M_{\alpha k}$. This is a rather involved process, but one can show that the form of these functions resemble simple wave packets [83]. In doing so, many approximations are necessary, in particular, that of ultra-relativistic neutrinos. More precisely, the most relevant assumptions are *i)* flipped-helicity terms ($h = +1$ for neutrinos), suppressed by m_k^2/E_k^2, are ignored, *ii)* all neutrinos travel in the same direction, $\vec{p} \to p$, and *iii)* the production and detection processes are not sensitive to the neutrino mass differences, amounting to replacing $M_{\alpha k} \approx M_\alpha$. Under these assumptions, we are justified to take normalized gaussian wave packets for production and detection flavour states as an *ansatz*,

$$|\nu_\alpha\rangle^i = \sum_k U_{\alpha k}^* \int \mathrm{d}p\, \psi_k^i(p)\ |\nu_k(p)\rangle\,, \quad \psi_k^i(p) = \left(2\pi\, \sigma_p^{i\,2}\right)^{-1/4} \exp\left[-\frac{(p-p_k)^2}{4\sigma_p^{i\,2}}\right], \quad (2.2.11)$$

with σ_p^i being the spread around the central momenta p_k and $i = P, D$.

Now that the flavour states are written in terms of the eigenstates of the free Hamiltonian, we know how to evolve them and how to write the flavour transition amplitude after a time t and distance L

$$\begin{aligned} A(\nu_\alpha \to \nu_\beta) &= \left\langle \nu_\beta^D \right| e^{-i\hat{E}t + i\hat{P}L} \left| \nu_\alpha^P \right\rangle \\ &= N \sum_k U_{\alpha k}^* U_{\beta k} \int \mathrm{d}p \exp\left[-iE_k(p)t + ipL - (p-p_k)^2/4\sigma_p^2\right], \end{aligned} \quad (2.2.12)$$

where $E_k(p) = \sqrt{p^2 + m_k^2}$ and N is a normalization factor coming from the normalization of the wave packets and a single integral over p. We have also defined the global uncertainty on momentum $\sigma_p^{-2} = \left(\sigma_p^P\right)^{-2} + \left(\sigma_p^D\right)^{-2}$. This may also be related to the global uncertainty on production and detection positions through $\sigma_x \sigma_p \approx 1/2$. Finally, to integrate over the remaining p integral, we can Taylor expand around the central wave packet momentum

$$E_k(p) \approx E_k + v_k(p - p_k), \quad \text{with} \quad v_k = \left.\frac{\partial E_k(p)}{\partial p}\right|_{p=p_k} = \frac{p_k}{E_k}, \quad E_k = \sqrt{p_k^2 + m_k^2}. \quad (2.2.13)$$

Performing the final integral over p, integrating over t (an unmeasured quantity) and squaring the amplitude, one obtains a formula for the oscillation probability

$$P(\nu_\alpha \to \nu_\beta) = \sum_{k,j} U_{\alpha k}^* U_{\alpha j} U_{\beta k} U_{\beta j}^*\, e^{-2\pi i L/L_{kj}^{\mathrm{osc}}}\, P_{kj}^{\mathrm{coh}}\, P_{kj}^{\mathrm{loc}}, \quad (2.2.14)$$

where we defined

$$P_{kj}^{\rm loc} = \exp\left(-2\pi^2\xi^2\left(\frac{\sigma_x}{L_{kj}^{\rm osc}}\right)^2\right), \quad P_{kj}^{\rm coh} = \exp\left(\frac{L\left|\Delta m_{kj}^2\right|^2}{16E^2\sigma_x}\right), \tag{2.2.15}$$

with the important scales of the problem identified as

$$L_{kj}^{\rm osc} = \frac{4\pi E}{\Delta m_{kj}^2}, \quad p_k \approx E - (1-\xi)\frac{m_k^2}{2E}, \quad E_k \approx E + \xi\frac{m_k^2}{2E}, \tag{2.2.16}$$

with ξ measuring the deviation from ultra-relativistic behaviour. The factors $P_{kj}^{\rm coh}$ and $P_{kj}^{\rm loc}$ are related to the coherence of the propagating wave packets and the localization of the source (or detector), respectively.

For most applications, $P_{kj}^{\rm coh} = P_{kj}^{\rm loc} = 1$, and one recovers the standard oscillation formula. A more useful way of writing it is

$$\begin{aligned} P(\nu_\alpha \to \nu_\beta) = \delta_{\alpha\beta} &- 2\sum_{k>j} {\rm Re}\left\{U_{\alpha k}^* U_{\alpha j} U_{\beta k} U_{\beta j}^*\right\}\left[1 - \cos\left(\frac{\Delta m_{kj}^2 L}{2E}\right)\right] \\ &- 2\sum_{k>j} {\rm Im}\left\{U_{\alpha k}^* U_{\alpha j} U_{\beta k} U_{\beta j}^*\right\}\sin\left(\frac{\Delta m_{kj}^2 L}{2E}\right). \end{aligned} \tag{2.2.17}$$

Note that for very small distances, $L/E \to 0$, no oscillations happen, $P(\nu_\alpha \to \nu_\beta) = \delta_{\alpha\beta}$. For very large $L/E \to \infty$, the oscillatory arguments are large and the oscillations are averaged out, although flavour transitions are still allowed.

2.2.2 Matter Effects

Neutrinos are neutral particles and their rare interactions allow them to propagate through matter without losing energy in collisions with the medium particles. Nevertheless, in a similar fashion to photons, neutrinos undergo coherent forward scattering, acquiring an effective refractive index in the presence of a medium. In contrast to photons, which undergo Compton scattering, neutrinos are only charged under the weak force and undergo CC and NC interactions. Therefore, matter effects are present whenever the medium displays a net weak charge, provided by neutrons, protons and electrons in the case of the Earth. The weakness of these interactions at low energies, however, implies that matter effects are only important when neutrinos have transversed sufficiently large distances or are in a sufficiently dense environment. In addition, for such effects to be observable in the flavour evolution of neutrinos, different neutrino flavour fields must exhibit different

interactions with the medium. In the SM, this is possible only due to the CC interactions that are exclusively present between electron-neutrinos and electrons in the medium.

We will now comment on the impact of matter in the flavour evolution, and derive the neutrino interaction potential. We want to avoid the complications from the previous discussion due to coherence and focus on the effects of matter. We merely note that similar conditions to the ones we found in the previous section apply for oscillation probabilities in matter to be well-defined, and with this caveat we proceed with a plane-wave picture of the flavour evolution. By applying the same momentum approximation and assuming neutrinos to be relativistic, we can write the Schröedinger equation in matrix form as

$$i\frac{\mathrm{d}}{\mathrm{d}x}\left|\nu_\alpha\right\rangle = \left[U\frac{\hat{m}^2}{2E}U^\dagger + \hat{V}(x)\right]\left|\nu_\alpha\right\rangle, \tag{2.2.18}$$

where we used $H_0\left|\nu_\alpha\right\rangle \approx U\left[p\hat{1} + \hat{m}^2/2p\right]U^\dagger\left|\nu_\alpha\right\rangle$ and $t \approx x$. Here, $\hat{V}(x)$ is a matrix containing the interaction potential of each neutrino flavour with the background. Note that $\hat{V}(x)$ depends on the density profile of matter particles. Solving this equation is a much more complicated task than in the vacuum case and analytical solutions are only known in specific cases, such as when the matter density is constant. In general, this may be solved numerically for a given choice of $\hat{V}(x)$, although several perturbative expansions exist. In this sense, the problem reduces to finding the appropriate potential and solving Eq. (2.2.18).

The neutrino matter potential arises from finite temperature and finite density corrections to the neutrino dispersion relation. The derivation of the potential following the approach of Refs. [86,87] can easily be modified to early Universe physics and to exotic astrophysical media such as supernovae and environments with large magnetic fields. The dispersion relation arises from

$$\det\{\not{k} - \Sigma\} = 0, \tag{2.2.19}$$

ensuring non-trivial solutions to the Dirac equation $(\not{k} - \Sigma)\nu_L = 0$, with k^μ the neutrino four-momentum and Σ its self-energy. For LH neutrino states ν_L, we can write the neutrino self-energy in the most general form and make explicit the background dependent contribution as [88]

$$\Sigma = m - \left(a_L\not{k} + b_L\not{u} + c_L[\not{k},\not{u}]\right)P_L. \tag{2.2.20}$$

where u is the 4-velocity of the medium, a_L, b_L and c_L are scalar functions of Lorentz

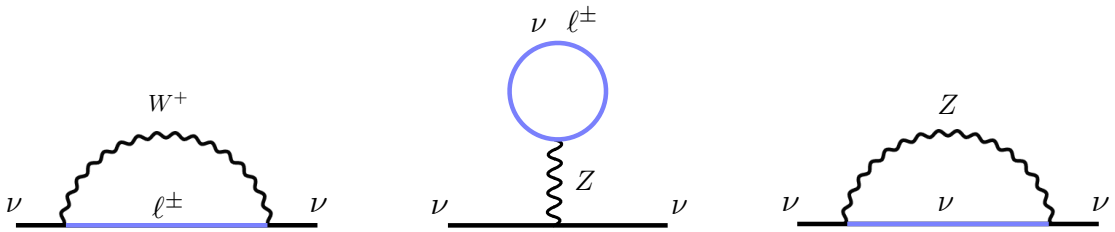

Fig. 2.5. Finite temperature and density corrections to the neutrino self-energy. These can be used to infer the effective matter potential for neutrinos.

invariants $w = k\cdot u$ and $\kappa = (w^2 - k^2)^{1/2}$, and m is the vacuum neutrino mass. The presence of the medium introduces a preferential frame, namely the rest frame of the medium with $u = (1, 0, 0, 0)$. Also note that in vacuum, only terms proportional to $\not{k}$ exist, and the pole of the neutrino propagator is unchanged. To lowest order in $g^2/m_{\rm W}^2$, only b_L contributes and it is proportional to the medium particle-antiparticle asymmetry. Higher order terms of the form $g^2/m_{\rm W}^4$ [89] complicate the picture, but can be safely neglected in the Earth, for instance. The neutrino self-energy is, in fact, a gauge-dependent quantity, and the physical observables of interest are the dispersion relations, $(1 - a_L)(w - \kappa) - b_L = 0$ for neutrinos and $(1 - a_L)(w + \kappa) - b_L = 0$ for antineutrinos. To lowest order, however, the dispersion relations are much simpler,

$$w \approx \kappa + \frac{m^2}{2\kappa} + V_{\rm eff}, \quad V_{\rm eff} = -b_L, \tag{2.2.21}$$

where we defined the effective potential, which for ultra-relativistic neutrinos arises precisely from the difference between the total and kinetic energy $V_{\rm eff} = w - \kappa$. This also shows us how to calculate the neutrino refractive index $n = \kappa/w$.

Now the problem reduces to computing Σ in finite temperature field theory. For most applications of thermal mass calculations, replacing vacuum propagators by the thermal propagators from the real-time formalism is sufficient. In particular, the fermion thermal propagator of interest is

$$S(P) = (\not{p} + m)\left[\frac{1}{P^2 - m^2 + i\epsilon} + i2\pi\delta(P^2 - m^2) f(P)\right], \tag{2.2.22}$$

with $f(P) = \{\exp\left[(|P\cdot u| - \mathrm{sgn}(P\cdot u)\,\mu_f)/T\right] + 1\}^{-1}$ is the occupational number of the fermions in the thermal bath of temperature T and chemical potential μ_f. Similar expressions exist for bosonic propagators. Finally, as an example, explicit computation of the

tadpole self-energy contribution in Fig. 2.5 yields

$$\Sigma = -i\frac{g^2}{16c_{\rm W}^2}\int\frac{{\rm d}^4P}{(2\pi)^4}\gamma^\mu P_L\, iS(P+K)\,\gamma^\nu\, P_L\, iD_{\mu\nu}(P), \quad D_{\mu\nu} = \frac{-g_{\mu\nu}+\frac{P_\mu P_\nu}{M_Z^2}}{P^2-M_Z^2+i\epsilon}. \quad (2.2.23)$$

By explicit computation in the rest frame of the medium, the potential for neutrinos of flavour α on a zero-temperature background of protons, neutrons and electrons is

$$\begin{aligned} V_\alpha^e =& -\frac{G_F}{\sqrt{2}}\left(1-4s_{\rm W}^2-2\delta_{\alpha e}\right)\left(N_e-N_{\overline{e}}\right), \\ V_\alpha^p =& \frac{G_F}{\sqrt{2}}\left(1-4s_{\rm W}^2\right)\left(N_p-N_{\overline{p}}\right), \\ V_\alpha^n =& -\frac{G_F}{\sqrt{2}}\left(N_n-N_{\overline{n}}\right), \end{aligned} \quad (2.2.24)$$

where $N_f = 2\int {\rm d}^3P f(P)/(2\pi)^3$ are the number density of the background particles. For antineutrino an overall minus sign is introduced. Note the total ν_e potential is the only one where CC interactions contribute, and so it is the sole responsible for non-trivial flavour evolution in Eq. (2.2.18). One may wonder about radiative corrections to these potentials in the SM and whether additional flavour non-universality can be achieved through the difference in charged-lepton masses. These effects, however, are known to be extremely small in the SM [90], where $\left(V_\tau - V_\mu\right)/V_e \approx 5\times 10^{-5}$ for a neutral unpolarized medium like the Earth.

2.3 Neutrinos in the Laboratory

To find a source of neutrinos, all we have to do is to look for environments where the weak force is prominently manifested. Natural candidates are nuclear reactors, having played a crucial role in the discovery of the neutrino. Fortunately, the list does not stop there. Abundant neutrino sources include the Sun, the atmosphere, the Big-Bang, particle accelerators and more violent astrophysical environments such as supernovae, active galactic nuclei and others. In this thesis, we will focus mostly on accelerator neutrinos.

Accelerator experiments typically produce neutrinos with energies of a few GeV to achieve $\mathcal{O}(1)$ oscillation phases $\Delta m^2_{\rm atm}L/E$ within thousands of km. Drastically different energy regimes are impractical either due to diluted fluxes at longer baselines ($\Phi \propto 1/L^2$), or due to thresholds to produce muons in CC interactions ($E_\nu > m_\ell + m_\ell^2/2m_{\mathcal{H}}$ in reactions of the type $\nu_\ell\mathcal{H} \to \ell^\pm\mathcal{H}'$). Proton beams with multi-GeV energies are used to produce

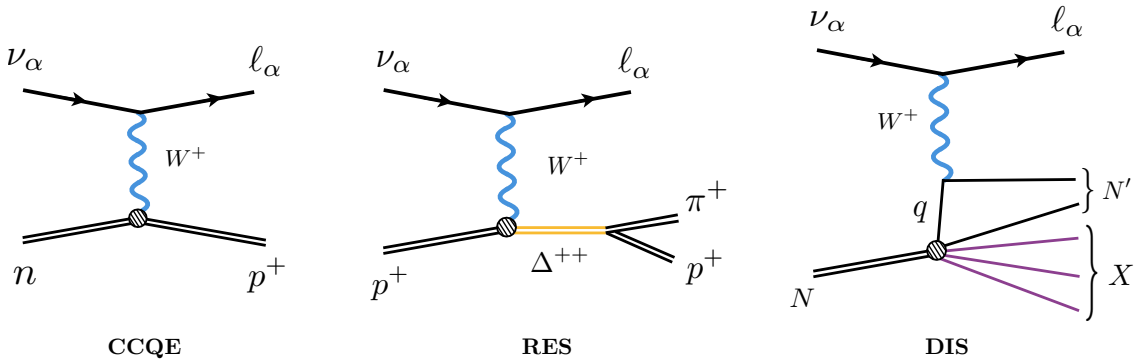

Fig. 2.6. The CC neutrino-nucleon scattering relevant for GeV neutrinos.From left to right, the CC quasi-elastic (CCQE), resonant (RES) and deep-inelastic scattering (DIS) regimes. Analogous diagrams exist for NC scattering.

neutrinos through the following steps: the protons are directed onto a dense target, the charged mesons produced in the proton-on-target collisions are focused with magnetic fields into a decay pipeline, and charged particles are absorbed further down the line. This allows the mesons to decay into neutrinos, most often through $\pi^\pm \to \overset{(-)}{\nu}_\mu \mu^\pm$. These experiments produce neutrinos within a wide range of energies, giving rise to wide-band beams. The shape and normalization of the neutrino flux produced are hard to model due to hadro-production and focusing uncertainties [91]. This comes mainly from the difficulty in describing hadron-nucleus interactions, their attenuation in propagation and, ultimately, by lack of data. In this way, the expected neutrino event rate in neutrino detectors inherits two sources of uncertainties which are difficult to disentangle: the unoscillated flux spectra and the neutrino-matter cross sections.

For oscillation physics, however, one is only interested in disentangling uncertainties in the event rate and the effects of oscillations. One effective method to achieve this is to build near detectors, where unoscillated rate is measured, as well as far detectors, where oscillations have developed. By definition, near detectors have to be limited by the systematics of the experiment, and so require a large number of neutrino interactions. These are dominated by the processes shown in Fig. 2.6 and their NC analogues. Because these processes are often subject to large nuclear effects (see below), other cleaner probes, such as neutrino-lepton scattering offer a better probe of the weak interactions in isolation. This argument will be essential when we search for *stronger than weak* neutrino interactions (new interactions with 4-Fermi coupling constants with $G_X > G_F$).

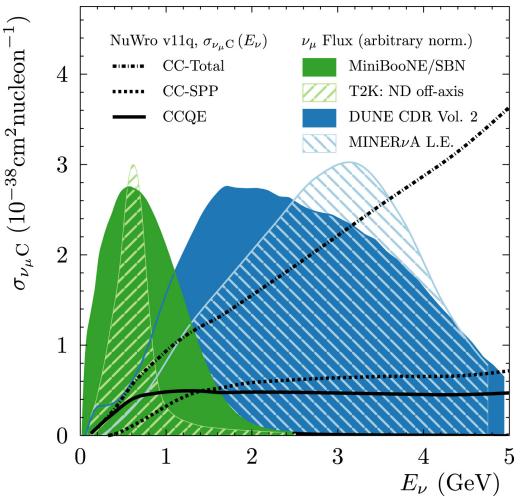

Fig. 2.7. Figure from Ref. [92] showing the NuWro prediction for $\nu_\mu - ^{12}C$ cross section per nucleon for CCQE scattering, CC single pion production (CC-SPP, dominated by RES diagrams), and for total CC scattering (including DIS). Overlaid are some of the neutrino fluxes of MINERνA, MiniBooNE, SBN, T2K off-axis and a projection for DUNE.

2.3.1 Interactions and Challenges

Despite interacting exclusively through the weak force, when the neutrino scatters on a target nucleus, the visible final states are subject to the influence of the nuclear force. Opting for dense materials with large nuclei is preferred for oscillation physics, but as more precision is required in oscillation measurements, more control over the nuclear effects is needed. The near and far measurements of the neutrino flux helps in reducing systematics, but the neutrino flux at the near site is different from the oscillated flux at the far site, both in shape and in flavour composition. In this way, understanding how nuclear effects and neutrino cross sections depend on neutrino energy E_ν and neutrino flavour is of great importance. Let us comment on a few examples. Even in the crudest approximation for a nucleus, that of a $T = 0$ Fermi gas of free protons and neutrons, nucleon final states are Pauli blocked and the occupation number of these fermions suppresses the total cross section. For realistic nuclei, these nucleons also display Fermi motion with momenta in the rest frame of the nucleus, $|p_N| \lesssim 250$ MeV, that are comparable to the incoming neutrino energy. On their way out of the nucleus, struck nucleons may also exchange EM charge, knock-out additional particles or be absorbed by the nuclear medium. The importance of nuclear effects is perhaps most famously illustrated by the measurement of the CC quasi-elastic (CCQE) process by the MiniBooNE [93] experiment. MiniBooNE is an accelerator experiment where a neutrino flux with an average energy of $\langle E_\nu \rangle \approx 800$ MeV is directed

towards a detector filled with mineral oil, made mostly of CH molecules. A disagreement of 20% was observed between the MC prediction and the data, unless the axial mass M_A was set to be ≈ 1.32 GeV, much larger than the world-average of $M_A = 1.03 \pm 0.02$ GeV. This was later understood as a missing contribution from two-particle two-hole meson exchange currents (where the neutrino interacts with a nucleon pair, rather than with an individual nucleon), shown to be as large as 30% of the CCQE cross section used by the experiment [94].

The most common interactions of neutrino with the nucleons in the detector are displayed in Fig. 2.6. Below $\lesssim 1$ GeV, CCQE scattering is most common, but at larger energies the resonant (RES) contributions start to become more important. The decay of the intermediate resonance is also affected by the nuclear medium and this has to be implemented in a nuclear model-dependent way, such as in the so called microscopical models. Another approach is that of macroscopic models, where one makes use of hypotheses such as the partially conserved axial current (PCAC) to relate the neutrino cross sections with the meson-nucleus cross section [2]. The PCAC relation for neutrino scattering holds only for the $q^2 = (k_1 - k_2)^2 \to 0$ limit, where the incoming neutrino momenta k_1 is parallel to the outgoing lepton momenta k_2. This is a good approximation of the cross section at large energies, but breaks down at low energies, where it is very often used [95]. For larger neutrino energies $E_\nu \gtrsim 3$ GeV, the deep-inelastic scattering (DIS) regime start to dominate. Here, the cross section calculations are much more reliable, although nuclear effects are still in place (see Ref. [96], for instance). Past neutrino scattering experiments such as NuTeV, CCFR and CHARM operated at neutrino energies in the tens and hundreds of GeV, and provided the most precise measurements of the neutrino DIS cross sections to date. All the processes we just discussed are now implemented in several neutrino event generators, the most popular being GENIE [97], GiBUU [98], NEUT [99] and NuWro [100]. Different neutrino-nucleus cross section models are implemented in these generators, but one typically relies on tuning to pre-existing data to make predictions. For illustration, in Fig. 2.7 we show the NuWro predictions for CC cross sections, overlaid on neutrino fluxes in current and future accelerator experiments.

[2] PCAC is the result of the spontaneous breaking of the chiral symmetry $SU(2)_L \times SU(2)_R$ in the quark sector. Because this symmetry is explicitly broken by quark masses, the pion is massive (although quite light compared to the η meson, for instance) and therefore the pseudo-Golstone boson of the theory.

Chapter 3

Neutrino Trident Production

Neutrino trident scattering is a rare process hiding at the level of a per million of the CCQE event rates. This process was the object of study of experiments back in the 80's and 90's, but the high beam luminosity achieved at current neutrino experiments and expected at future facilitites (typically beyond 10^{21} protons on target), the relatively large fiducial masses of high-Z materials (typically 100 ton) of modern detectors, and improved particle identification (PID) capabilities allows us to return to this topic at lower energies ($E_\nu =$ few GeV) with a refreshed approach. We refine previous calculations of the trident cross section, pointing out subtleties about the Equivalent Photon Approximation, and develop a dedicated Montecarlo for neutrino trident events. Our phenomenological analysis is a first assessment of the capabilities of current and future near detectors to measure several trident channels with improved precision, or for the very first time.

3.1 History of Neutrino Trident Production

Trident events are processes predicted by the SM as the result of (anti)neutrino-nucleus scattering with the production of a charged lepton pair [101–105], $\overset{(-)}{\nu}_\alpha + \mathcal{H} \to \overset{(-)}{\nu}_{\alpha \text{ or } \kappa(\beta)} + \ell^-_\beta + \ell^+_\kappa + \mathcal{H}$, $\{\alpha, \beta, \kappa\} \in \{e, \mu, \tau\}$[1] where $\mathcal{H}$ denotes a hadronic target. Depending on the (anti)neutrino and charged lepton flavours in the final-state, the process will be mediated by the Z^0 boson, W boson or both. Coherent interactions between (anti)neutrinos and the atomic nuclei are expected to dominate these processes as long as the momentum

[1] Throughout the manuscript we will consider α, β, κ as flavour indexes.

transferred Q is significantly smaller than the inverse of the nuclear size [101]. For larger momentum transfers diffractive elastic and deep-inelastic scattering become increasingly relevant [106]. Although this process exists for all combinations of same-flavour or mixed flavour charged-lepton final-states, to this day only the ν_μ-induced dimuon mode, $\overset{(-)}{\nu}_\mu + \mathcal{H} \to \overset{(-)}{\nu}_\mu + \mu^+ + \mu^- + \mathcal{H}$, has been observed. The first measurement of this trident signal performed by CHARM II [107] is also the one with the largest statistics: 55 signal events in a beam of neutrinos and antineutrinos with $\langle E_\nu \rangle \approx 20$ GeV. Other measurements by CCFR [108] and NuTeV [109] at larger energies soon followed.

As the measurement of trident events may provide a sensitive test of the weak sector [110] as well as placing constraints on physics beyond the SM [108, 111–116] it is relevant to investigate how to probe it further at current and future neutrino experiments. Atmospheric neutrinos, for instance, may provide a feasible measurement of the dimuon channel, as pointed out in Ref. [114][2]. Other trident modes were also recognized to be relevant by the authors of Ref. [106] who calculated the cross sections for trident production in all possible flavour combinations and estimated the number of events expected for the DUNE and SHiP experiments. They used the Equivalent Photon Approximation (EPA) [117] to compute the cross section in the coherent and diffractive regimes of the scattering. The EPA, however, is known to breakdown for final state electrons [101, 118, 119] leading, as we will demonstrate here, to an overestimation of the cross section that in some cases is by more than 200%.

3.2 Cross Section at Low Energies

In this section we consider neutrino trident production in the SM, defined as the process where a (anti)neutrino scattering off a hadronic system $\mathcal{H}$ produces a pair of same-flavour or mixed flavour charged leptons

$$\overset{(-)}{\nu}_\alpha(k_1) + \mathcal{H}(P) \to \overset{(-)}{\nu}_{\alpha'}(k_2) + \ell^-_\beta(p_-) + \ell^+_\kappa(p_+) + \mathcal{H}(P'), \tag{3.2.1}$$

where $\beta(\kappa)$ corresponds to the flavour index of the negative (positive) charged lepton in both neutrino and antineutrino cases. Neutrino trident scattering can be divided into three

[2]The authors of Ref. [114] have performed the full calculation of the trident process and made their code publicly available.

regimes depending on the nature of the hadronic target: coherent, diffractive elastic and deep inelastic, when the neutrino scatters off the nuclei, nucleons and quarks, respectively. At the energies relevant for neutrino oscillation experiments, the deep inelastic scattering contribution amounts at most to 1% of the total trident production cross section [106] and we will not consider it further. At larger energies, this regime may become important, especially if the production of on-shell vector bosons becomes kinematically accessible.

The cross section for trident production has been calculated before in the literature, both in the context of the $V - A$ theory [101–103] and in the SM [110], while the EPA treatment was developed in Refs. [117–119]. Most calculations have focused on the coherent channels [101–103, 110, 117] but the diffractive process has been considered in [101, 102]. More recently, calculations using the EPA have been performed for coherent scattering with a dimuon final-state [112], and for all combinations of hadronic targets and flavours of final-states in [106]. While the EPA is expected to agree reasonably well with the full calculation for coherent channels with dimuon final-states, the assumptions of this approximation are invalid for the coherent process with electrons in the final-state [101, 118, 119]. For this reason, we perform the full $2 \to 4$ calculation without the EPA in a manner applicable to any hadronic target, following a similar approach to Refs. [101, 102]. Our treatment of the cross section allows us to quantitatively assess the breakdown of the EPA in both coherent and diffractive channels for all final-state flavours, an issue we come back to in Sec. 3.2.2.

We write the total cross section for neutrino trident production off a nucleus $\mathcal{N}$ with Z protons and $(A - Z)$ neutrons as the sum

$$\sigma_{\nu\mathcal{N}} = \sigma_{\nu\mathrm{c}} + \sigma_{\nu\mathrm{d}}\,, \tag{3.2.2}$$

where $\sigma_{\nu\mathrm{c}}$ ($\sigma_{\nu\mathrm{d}}$) is the coherent (diffractive) part of the cross section. The relevant diagrams for these processes in the coherent or diffractive regimes involve the boson Z^0, W or both mediators, depending on the particular mode. In the four-point interaction limit, depicted in Fig. 3.1, these reduce to only two contributions[3], one where the photon couples to the negatively and one to the positively charged lepton. In Table 3.1, we present the processes we will consider in this thesis as well as the SM contributions present in each. Although our formalism applies also to processes with final-state τ leptons, the increased threshold

[3] An additional diagram involving a $WW\gamma$ vertex has also been neglected, since it is of order $1/M_W^4$.

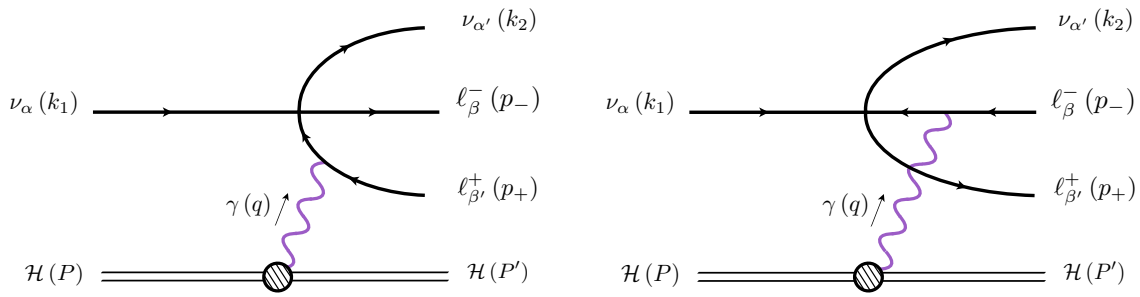

Fig. 3.1. Diagrams contributing to the neutrino trident process in the four-point interaction limit of the Standard Model.

and their suppressed cross section makes them irrelevant for the experiments of interest in this study and we do not consider them further. The trident amplitude for a coherent (X = c) or diffractive (X = d) scattering regime can be written as

$$i\mathcal{M} = \mathrm{L}^\mu(\{p_i\}, q)\,\frac{-ig_{\mu\nu}}{q^2}\,\mathrm{H}^\nu_{\mathrm{X}}(P, P')\,, \tag{3.2.3}$$

where $\{p_i\} = \{k_2, p_-, p_+\}$ is the set of outgoing leptonic momenta. $\mathrm{L}^\mu(\{p_i\}, q)$ is the total leptonic amplitude

$$\mathrm{L}^\mu \equiv -\frac{ieG_F}{\sqrt{2}}[\bar{u}(k_2)\gamma^\tau(1-\gamma_5)u(k_1)] \times \bar{u}(p_-)\left[\gamma_\tau(V - A\gamma_5)\frac{1}{(\not{q} - \not{p}_+ - m_+)}\gamma^\mu \right.$$
$$\left. +\gamma^\mu\frac{1}{(\not{p}_- - \not{q} - m_-)}\gamma_\tau(V - A\gamma_5)\right] v(p_+)\,, \tag{3.2.4}$$

and $\mathrm{H}^\nu_{\mathrm{X}}(P, P')$ is the total hadronic amplitude

$$H^\nu_{\mathrm{X}} \equiv \langle \mathcal{H}(P)|J^\nu_{\mathrm{E.M.}}(q^2)|\mathcal{H}(P')\rangle\,, \tag{3.2.5}$$

with $q \equiv P - P'$ denoting the transferred momentum, m_+ (m_-) the positively (negatively) charged lepton mass and $J^\nu_{\mathrm{E.M.}}(q^2)$ the electromagnetic current for the hadronic system $\mathcal{H}$ (a nucleus or a nucleon). The flavour indices have been ommitted from the vector V and axial A couplings, determined by $V \equiv g_V^{\alpha'}\delta_{\alpha\alpha'}\delta_{\beta\beta'} + \delta_{\alpha'\beta'}\delta_{\alpha\beta}$ and $A \equiv g_A^{\alpha'}\delta_{\alpha\alpha'}\delta_{\beta\beta'} + \delta_{\alpha'\beta'}\delta_{\alpha\beta}$ in accordance to Eq. (3.2.1) and shown in Table 3.1.

We can write the differential cross section as

$$\frac{\mathrm{d}^2\sigma_{\nu\mathrm{X}}}{\mathrm{d}Q^2\mathrm{d}\hat{s}} = \frac{1}{32\pi^2(s - M^2_{\mathcal{H}})^2}\frac{\mathrm{H}^{\mu\nu}_{\mathrm{X}}\mathrm{L}_{\mu\nu}}{Q^4}\,, \tag{3.2.6}$$

where $s = (k_1 + P)^2$, $\hat{s} \equiv 2\,(k_1 \cdot q)$, $Q^2 = -q^2$ and $M_{\mathcal{H}}$ is the mass of the hadronic target.

Trident channel	SM Contributions	V	A
$\nu_\mu\,\mathcal{H} \to \nu_\mu\,\mu^-\mu^+\,\mathcal{H}$	CC + NC	$1/2 + 2\,s_{\rm W}^2$	$1/2$
$\nu_\mu\,\mathcal{H} \to \nu_\mu\,e^-e^+\,\mathcal{H}$	NC	$-1/2 + 2\,s_{\rm W}^2$	$-1/2$
$\nu_\mu\,\mathcal{H} \to \nu_e\,e^+\mu^-\,\mathcal{H}$	CC	1	1
$\nu_e\,\mathcal{H} \to \nu_e\,e^-e^+\,\mathcal{H}$	CC + NC	$1/2 + 2\,s_{\rm W}^2$	$1/2$
$\nu_e\,\mathcal{H} \to \nu_e\,\mu^-\mu^+\,\mathcal{H}$	NC	$-1/2 + 2\,s_{\rm W}^2$	$-1/2$
$\nu_e\,\mathcal{H} \to \nu_\mu\,\mu^+e^-\,\mathcal{H}$	CC	1	1

Tab. 3.1. Neutrino trident processes considered in this thesis. Antineutrino induced channels are analogous.

We have also introduced the hadronic tensor $\mathrm{H}_{\rm X}^{\mu\nu}$

$$\mathrm{H}_{\rm X}^{\mu\nu} \equiv \overline{\sum_{\rm spins}} \left(\mathrm{H}_{\rm X}^{\mu}\right)^* \mathrm{H}_{\rm X}^{\nu}. \tag{3.2.7}$$

The two scattering regimes in which the hadronic tensor is computed will be discussed in more detail in Sec. 3.2.1. The leptonic tensor, $\mathrm{L}^{\mu\nu}$, integrated over the phase space of the three final-state leptons, $\mathrm{d}^3\Pi\,(k_1+q;\{p_i\})$, and merely summed over final and initial spins is given by

$$\mathrm{L}^{\mu\nu}(k_1,q) \equiv \int \mathrm{d}^3\Pi\,(k_1+q;\{p_i\}) \left(\sum_{\rm spins} \left(\mathrm{L}^{\mu}\right)^* \mathrm{L}^{\nu}\right). \tag{3.2.8}$$

We can use $\mathrm{L}^{\mu\nu}$ to define two scalar functions, one related to the longitudinal ($\mathrm{L_L}$) and the other to the transverse ($\mathrm{L_T}$) polarization of the exchanged photon

$$\mathrm{L_T} = -\frac{1}{2}\left(g^{\mu\nu} - \frac{4Q^2}{\hat{s}^2}k_1^\mu k_1^\nu\right)\mathrm{L}_{\mu\nu}, \quad \text{and} \quad \mathrm{L_L} = \frac{4Q^2}{\hat{s}^2}k_1^\mu k_1^\nu \mathrm{L}_{\mu\nu}\,. \tag{3.2.9}$$

This allows us to write the differential cross section as a sum of a longitudinal and a transverse contribution [120] as follows

$$\frac{\mathrm{d}^2\sigma_{\nu\rm X}}{\mathrm{d}Q^2\mathrm{d}\hat{s}} = \frac{1}{32\pi^2}\frac{1}{\hat{s}\,Q^2}\left[h_{\rm X}^{\rm T}(Q^2,\hat{s})\,\sigma_{\nu\gamma}^{\rm T}(Q^2,\hat{s}) + h_{\rm X}^{\rm L}(Q^2,\hat{s})\,\sigma_{\nu\gamma}^{\rm L}(Q^2,\hat{s})\right], \tag{3.2.10}$$

where we have defined two functions for the flux of longitudinal and transverse virtual photons

$$h_{\rm X}^{\rm T}(Q^2,\hat{s}) \equiv \frac{2}{(E_\nu M_{\mathcal{H}})^2}\left[k_{1\mu}k_{1\nu} - \frac{\hat{s}^2}{4Q^2}\,g_{\mu\nu}\right]\mathrm{H}_{\rm X}^{\mu\nu}, \quad \text{and} \tag{3.2.11a}$$

$$h_{\rm X}^{\rm L}(Q^2,\hat{s}) \equiv \frac{1}{(E_\nu M_{\mathcal{H}})^2}\,k_{1\mu}k_{1\nu}\,\mathrm{H}_{\rm X}^{\mu\nu}\,, \tag{3.2.11b}$$

and two leptonic neutrino-photon cross sections associated with them[4]

$$\sigma^{\mathrm{T}}_{\nu\gamma}(Q^2,\hat{s}) = \frac{\mathrm{L_T}}{2\hat{s}}\,, \quad \text{and} \quad \sigma^{\mathrm{L}}_{\nu\gamma}(Q^2,\hat{s}) = \frac{\mathrm{L_L}}{\hat{s}}\,. \tag{3.2.12}$$

The kinematically allowed region in the $(Q^2,\hat{s})$ plane can be obtained by considering the full four-body phase space, as in [101–103]. The limits for such physical region are given by

$$Q^2_{\mathrm{min}} = \frac{M_{\mathcal{H}}\hat{s}^2}{2E_\nu(2E_\nu M_{\mathcal{H}}-\hat{s})}, \qquad Q^2_{\mathrm{max}} = \hat{s} - m_L^2, \tag{3.2.13a}$$

$$\hat{s}_{\mathrm{min}} = \frac{E_\nu}{2E_\nu + M_{\mathcal{H}}}\left[m_L^2 + 2E_\nu M_{\mathcal{H}} - \Delta\right] \qquad \hat{s}_{\mathrm{max}} = \frac{E_\nu}{2E_\nu + M_{\mathcal{H}}}\left[m_L^2 + 2E_\nu M_{\mathcal{H}} + \Delta\right], \tag{3.2.13b}$$

with $m_L \equiv m_+ + m_-$, and

$$\Delta \equiv \sqrt{(2E_\nu M_{\mathcal{H}} - m_L^2)^2 - 4M_{\mathcal{H}}^2 m_L^2}\,.$$

Let us emphasize that Eq. (3.2.10) is an exact decomposition, and does not rely on any approximation of the process. In the following section, we will show how to calculate the flux functions $h^{\mathrm{T}}_{\mathrm{X}}$ and $h^{\mathrm{L}}_{\mathrm{X}}$ from Eq. 3.2.11 in different scattering regimes. The total cross section for the process can then be computed by finding $\sigma^{\mathrm{L}}_{\nu\gamma}$ and $\sigma^{\mathrm{T}}_{\nu\gamma}$ from Eqs. (3.2.4), (3.2.8) and (3.2.9) and integrating over all allowed values of Q^2 and $\hat{s}$. Note that $\sigma^{\mathrm{L}}_{\nu\gamma}$ and $\sigma^{\mathrm{T}}_{\nu\gamma}$ are universal functions for a given leptonic process and need only to be computed once.

3.2.1 Hadronic Scattering Regimes

Depending on the magnitude of the virtuality of the photon, $Q = \sqrt{-q^2}$, the hadronic current can contribute in different ways to the trident process. Thus, given the decomposition in Eq. (3.2.10), the change in the hadronic treatment translates to computing the flux factors $h^{\mathrm{T}}_{\mathrm{X}}$ and $h^{\mathrm{L}}_{\mathrm{X}}$ for each scattering regime. From those flux factors, $\sigma_{\nu\mathrm{c}}$ and $\sigma_{\nu\mathrm{d}}$ can be calculated.

[4]Note that we include a factor of 1/2 in $\sigma^{\mathrm{T}}_{\nu\gamma}$ to match the polarization averaging of the on-shell cross section: $\sigma^{\mathrm{on-shell}}_{\nu\gamma} = \frac{1}{2\hat{s}}\left(\sum_r (\epsilon^\mu_r)^* \epsilon^\nu_r\, \mathrm{L}_{\mu\nu}\right)\big|_{Q^2=0} = \frac{1}{4\hat{s}}\left(-g^{\mu\nu}L_{\mu\nu}\right)\big|_{Q^2=0} = \frac{\mathrm{L_T}}{2\hat{s}}\big|_{Q^2=0} = \sigma^{\mathrm{T}}_{\nu\gamma}(0,\hat{s})$.

Coherent Regime ($\mathrm{H}_{\mathrm{c}}^{\mu\nu}$)

In the coherent scattering regime the incoming neutrino interacts with the whole nucleus without resolving its substructure. For this to occur frequently, we need small values of Q. Despite the relatively large neutrino energies in contemporary neutrino beams, this is still allowed for trident.

In this regime, the hadronic tensor $\mathrm{H}_{\mathrm{c}}^{\mu\nu}$ for a ground state spin-zero nucleus of charge Ze can be written in terms of the nuclear electromagnetic form factor $F(Q^2)$, discussed in more detail in Appendix B, as

$$\mathrm{H}_{\mathrm{c}}^{\mu\nu} = 4Z^2e^2 \left|F(Q^2)\right|^2 \left(P^\mu - \frac{q^\mu}{2}\right)\left(P^\nu - \frac{q^\nu}{2}\right). \tag{3.2.14}$$

In this case the vertex is spin-independent and $F(Q^2)$ describes the electric charge distribution in the nucleus. In general, and for more complex nuclei, magnetic scattering is also possible, and magnetic form factors would be present. In fact, the current problem is analogous to elastic electron scattering on nuclei, and benefits from the literature and data in that topic (see Ref. [121] for a thorough review). From Eq. 3.2.11, we find that the transverse and longitudinal flux functions for the coherent regime are

$$h_{\mathrm{c}}^{\mathrm{T}}(Q^2,\hat{s}) = 8Z^2e^2\left(1 - \frac{\hat{s}}{2E_\nu M} - \frac{\hat{s}^2}{4E_\nu^2 Q^2}\right)|F(Q^2)|^2\,, \tag{3.2.15a}$$

$$h_{\mathrm{c}}^{\mathrm{L}}(Q^2,\hat{s}) = 4Z^2e^2\left(1 - \frac{\hat{s}}{4E_\nu M}\right)^2|F(Q^2)|^2\,, \tag{3.2.15b}$$

where E_ν is the energy of the incoming neutrino and M is the nuclear mass. For a fixed value of $\hat{s}$ in the physical region, the $h_{\mathrm{c}}^{\mathrm{T}}$ flux function becomes zero at Q_{min} while the longitudinal component does not. This different behaviour can be seen explicitly in their definitions, Eqs. (3.2.15), as the terms in the parenthesis in $h_{\mathrm{c}}^{\mathrm{T}}$ cancel each other at Q_{min}. This does not occur for $h_{\mathrm{c}}^{\mathrm{L}}$ since the physical values of $\hat{s}$ are always smaller than $E_\nu M$ in this hadronic regime. Due to this fact, Q_{min}, which according to Eq. (3.2.13a) depends on both the neutrino energy and target material, can be approximated to

$$Q_{\mathrm{min}} \approx \frac{\hat{s}}{2E_\nu},$$

which only depends on the incoming neutrino energy. On the other hand, as Q becomes large, the flux functions $h^{T,L}$ become quite similar, $h_{\mathrm{c}}^{\mathrm{T}} \approx 2h_{\mathrm{c}}^{\mathrm{L}}$, and favour small values of $\hat{s}$. After some critical value of the virtuality Q, $h_{\mathrm{c}}^{\mathrm{T,L}}$ become negligible due to the nuclear

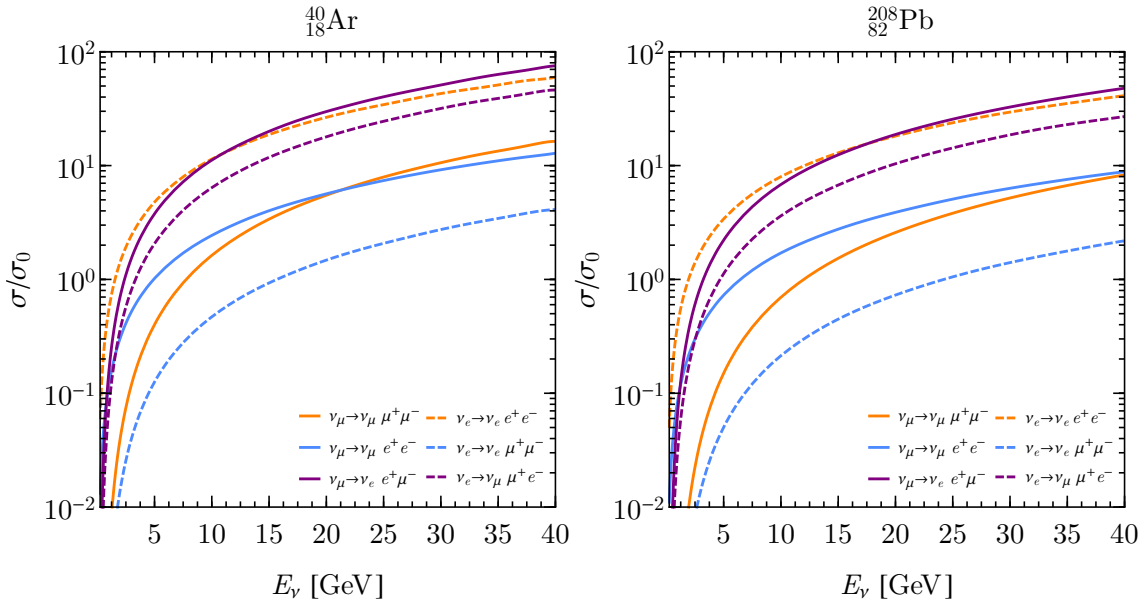

Fig. 3.2. Cross sections for coherent neutrino trident production on ^{40}Ar (left) and ^{208}Pb (right) normalized to $\sigma_0 = Z^2\, 10^{-44}$ cm^2. The full (dashed) lines correspond to the scattering of an incoming ν_μ (ν_e) produced by the NC (light-blue), CC (purple), and CC+NC (orange) SM interactions.

form factor. The Q value at which this happens depends on the target material, but not on the incoming neutrino energy. For instance, in the case of an Ar target the flux functions basically vanish for $Q \gtrsim 250$ MeV. The knowledge of the nuclear form factor and its shape in Q^2, therefore, has a significant impact on the total cross section. Here, we use a Woods-Saxon form factor described in more detail in Appendix B. Our form factor leads to a difference of 12% on the total cross section of coherent dimuon tridents if compared to the more recent Ref. [122].

The final cross sections for coherent neutrino trident production on Argon can be seen in Fig. 3.2. Despite thresholds being important for the behaviour of these cross sections for GeV neutrino energies, we can see that mixed channels quickly become the most important due to their CC nature. At large energies one can then rank the cross sections from largest to smallest as CC, CC+NC, and NC only channels. Nevertheless, one must be aware of the fact that the cross sections are dominated by low Q^2 even at large energies, leading to large effects due to the final-state lepton masses as discussed in [106].

Diffractive Regime ($\mathrm{H}_{\mathrm{d}}^{\mu\nu}$)

At larger Q^2, the neutrino interacts with the individual nucleons of the nucleus. In this diffractive (or incoherent elastic) regime $\mathrm{H}_{\mathrm{d}}^{\mu\nu}$ is given by the sum of the contributions of the two types of nucleons: protons (N = p) and neutrons (N = n), so

$$\mathrm{H}_{\mathrm{d}}^{\mu\nu}(P,P') = Z\,\mathrm{H}_{\mathrm{p}}^{\mu\nu}(P,P') + (A-Z)\,\mathrm{H}_{\mathrm{n}}^{\mu\nu}(P,P')\,, \tag{3.2.16}$$

where each $\mathrm{H}_{\mathrm{N}}^{\mu\nu}$ is the square of the matrix element of the nucleon electromagnetic current summed over final and averaged over initial spins. Neglecting second class currents, the matrix elements take the form

$$\langle \mathrm{N}(P')|\, J^{\mu}_{\mathrm{E.M.}}(Q^2)\,|\mathrm{N}(P)\rangle = e\,\overline{u}_{\mathrm{N}}(P')\left[\gamma^{\mu}F_1^{\mathrm{N}}(Q^2) - i\frac{\sigma^{\mu\nu}q_{\nu}}{2M_{\mathrm{N}}}F_2^{\mathrm{N}}(Q^2)\right]u_{\mathrm{N}}(P)\,, \tag{3.2.17}$$

with $F_{1,2}^{\mathrm{N}}(Q^2)$ the Dirac and Pauli form factors, respectively. The hadronic tensors are then given by [123]

$$\mathrm{H}_{\mathrm{N}}^{\mu\nu} = e^2\left[4\,H_1^{\mathrm{N}}(Q^2)\left(P^{\mu}-\frac{q^{\mu}}{2}\right)\left(P^{\nu}-\frac{q^{\nu}}{2}\right) - H_2^{\mathrm{N}}(Q^2)\left(Q^2 g^{\mu\nu}+q^{\mu}q^{\nu}\right)\right]\,, \tag{3.2.18}$$

where the $H_1^{\mathrm{N}}(Q^2)$ and $H_2^{\mathrm{N}}(Q^2)$ form factors, functions of $F_{1,2}^{\mathrm{N}}(Q^2)$, are given in Appendix B. The flux functions in the diffractive regime can then be calculated as

$$h_{\mathrm{N}}^{\mathrm{T}}(Q^2,\hat{s}) = 8\,e^2\left[\left(1-\frac{\hat{s}}{2E_{\nu}M_{\mathrm{N}}}-\frac{\hat{s}^2}{4E_{\nu}^2Q^2}\right)H_1^{\mathrm{N}}(Q^2)+\frac{\hat{s}^2}{8E_{\nu}^2M_{\mathrm{N}}^2}H_2^{\mathrm{N}}(Q^2)\right]\,, \tag{3.2.19a}$$

$$h_{\mathrm{N}}^{\mathrm{L}}(Q^2,\hat{s}) = 4e^2\left[\left(1-\frac{\hat{s}}{4E_{\nu}M_{\mathrm{N}}}\right)^2 H_1^{\mathrm{N}}(Q^2)-\frac{\hat{s}^2}{16E_{\nu}^2M_{\mathrm{N}}^2}H_2^{\mathrm{N}}(Q^2)\right]\,. \tag{3.2.19b}$$

In the case of the proton, the flux functions $h_{\mathrm{p}}^{\mathrm{T,L}}$ have some unique features given the presence of both electric and magnetic contributions. Specifically, the transverse function is non-zero at $Q = Q_{\mathrm{min}}$ for a fixed $\hat{s}$, due to the additional term proportional to H_2^{p}. Indeed, for large values of $\hat{s}$, the H_2^{p} term dominates the transverse function. An opposite behaviour occurs for the longitudinal component. There, the H_1^{p} term dominates over the second term for all physical values of $\hat{s}$, Q, and for any incoming neutrino energy. On the other hand, the flux functions of the neutron, which have only the magnetic moment contribution, have somewhat different characteristics. While $h_{\mathrm{n}}^{\mathrm{T}}$ behaves similarly to $h_{\mathrm{p}}^{\mathrm{T}}$, that is, it is dominated by the second term for large values of $\hat{s}$, $h_{\mathrm{n}}^{\mathrm{L}}$ is zero at Q_{min} due to the exact cancellation between the $H_{1,2}^{\mathrm{n}}$ terms. This cancellation is not evident from Eq.

(3.2.19b); however, simplifying the longitudinal component for the neutron case, one finds

$$h_{\mathrm{n}}^{\mathrm{L}}(Q^2,\hat{s}) = 4e^2\left(1+\frac{Q^2}{4M_{\mathrm{n}}^2}\right)\frac{Q^2}{4M_{\mathrm{N}}^2}\left(1-\frac{\hat{s}}{2E_\nu M_{\mathrm{N}}}-\frac{\hat{s}^2}{4E_\nu^2 Q^2}\right)\left|F_2^{\mathrm{n}}(Q^2)\right|^2,$$

which is zero for $Q = Q_{\min}$. Also, this shows why $h_{\mathrm{p}}^{\mathrm{L}}$ does not vanish at $Q_{\min}$ since there we have the additional contribution of the electric component.

When the neutrino interacts with an individual nucleon inside the nucleus, one must be aware of the nuclear effects at play. One such effect is Pauli blocking, a suppression of neutrino-nucleon interactions due to the Pauli exclusion principle. Modelling the nucleus as an ideal Fermi gas of protons and neutrons, one can take Pauli blocking effects into account by requiring that the hit nucleon cannot be in a state which is already occupied [104]. This requirement is implemented in our calculations by a simple replacement of the differential diffractive cross section

$$\frac{\mathrm{d}^2\sigma_{\nu\mathrm{d}}}{\mathrm{d}Q^2\mathrm{d}\hat{s}} \to f(|\vec{q}|)\,\frac{\mathrm{d}^2\sigma_{\nu\mathrm{d}}}{\mathrm{d}Q^2\mathrm{d}\hat{s}},$$

where $|\vec{q}|$ is the magnitude of the transferred three-momentum in the lab frame. In particular, following [104], assuming an equal density of neutrons and protons, we have

$$f(|\vec{q}|) = \begin{cases} \dfrac{3}{2}\dfrac{|\vec{q}|}{2\,k_F} - \dfrac{1}{2}\left(\dfrac{|\vec{q}|}{2\,k_F}\right)^3, & \text{if } |\vec{q}| < 2\,k_F\,, \\ 1, & \text{if } |\vec{q}| \geq 2\,k_F\,, \end{cases} \tag{3.2.20}$$

where k_F is the Fermi momentum of the gas, taken to be 235 MeV. This is a rather low value of k_F and the assumption of equal density of neutrons and protons must be taken with care for heavy nuclei. We refrain from trying to model any additional nuclear effects as we believe that this is the dominant effect on the total diffractive rate, particularly when requiring no hadronic activity in the event. The net result is a reduction of the diffractive cross section by about 50% for protons and 20% for neutrons. Unless clearly stated otherwise, we always include Pauli blocking in our calculations.

Our final cross sections for this regime can be seen in Fig. 3.3. One can clearly see that the neutron contribution is subdominant, and that, up to factors of Z^2, the proton one is comparable to the coherent cross section. Note that now the typical values of Q^2 are much larger than in the coherent regime and the impact of the final-state lepton masses is much smaller.

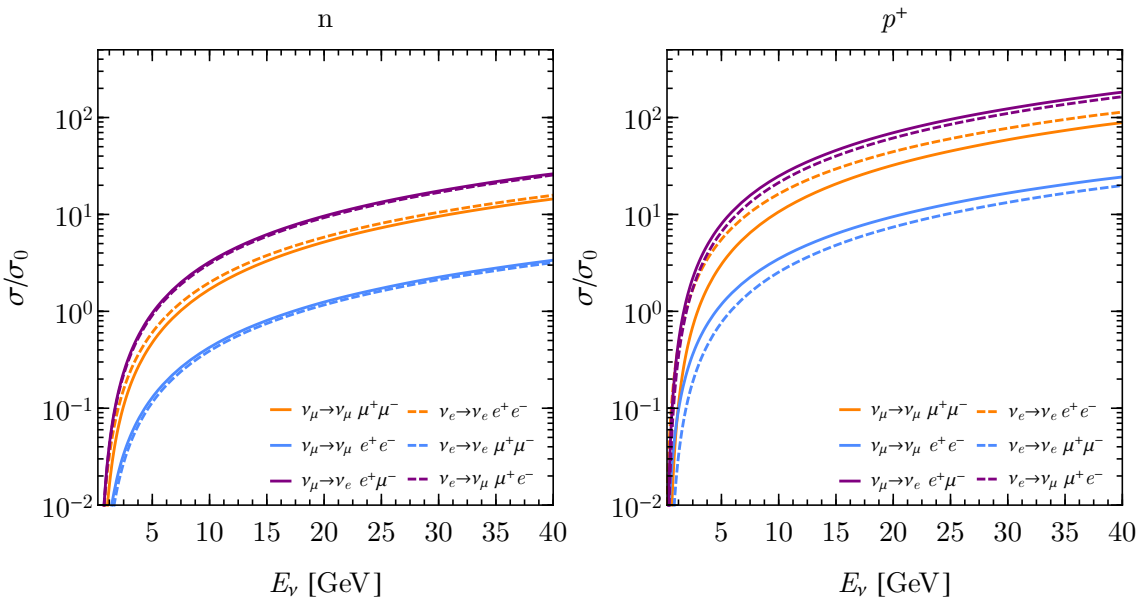

Fig. 3.3. Cross sections for diffractive neutrino trident production on neutrons (left) and protons (right), including Pauli blocking effects as described in the text, normalized to $\sigma_0 = 10^{-44}$ cm^2. The full (dashed) lines correspond to the scattering of an incoming ν_μ (ν_e) produced by the NC (light-blue), CC (purple), and CC+NC (orange) SM interactions.

3.2.2 Breakdown of the EPA

In order to understand the breakdown of the EPA in the neutrino trident case, let us first remind briefly the reader about the Weizsäcker–Williams method of equivalent photons in Quantum Electrodynamics (QED) [124, 125], and the main reason for its validity in that theory. The EPA, first introduced by E. Fermi [126], is based on a simple principle: when an ultra-relativistic particle P_i approaches a charged system C_s, like a nucleus, it will perceive the electromagnetic fields as nearly transverse, similar to the fields of a pulse of radiation, *i.e.*, as an on-shell photon. Therefore, it is possible to obtain an approximate total cross section for the inelastic scattering process producing a set of final particles P_f, $\sigma_{\rm t}(P_i + C_s \to P_f + C_s)$, by computing the scattering of the incoming particle with a real photon integrated over the energy spectrum of the off-shell photons,

$$\sigma_{\rm t}(P_i + C_s \to P_f + C_s) \approx \int dP(Q^2, \hat{s})\, \sigma_\gamma(P_i + \gamma \to P_f; \hat{s}, Q^2 = 0), \tag{3.2.21}$$

where the photo-production cross section for the process $P_i + \gamma \to P_f$, $\sigma_\gamma(P_i + \gamma \to P_f; \hat{s}, Q^2 = 0)$, depends on the center-of-mass energy of the P_i–photon system, $\sqrt{\hat{s}}$. Here $dP(Q^2, \hat{s})$ corresponds to the energy spectrum of the virtual photons, that is, the probability of emission of a virtual photon with transferred four-momentum Q^2 resulting in an center-

of-mass energy $\sqrt{\hat{s}}$. For trident scattering off a nuclear target, this probability can be approximated by [112, 117]

$$dP(Q^2, \hat{s}) = \frac{Z^2 e^2}{4\pi^2} |F(Q^2)|^2 \, \frac{d\hat{s}}{\hat{s}} \, \frac{dQ^2}{Q^2} \, . \tag{3.2.22}$$

A crucial fact in QED is that the cross section $\sigma_\gamma^{\rm QED}(P_i + \gamma \to P_f; \hat{s}, 0)$ is inversely proportional to $\hat{s}$,

$$\sigma_\gamma^{\rm QED}(P_i + \gamma \to P_f; \hat{s}, 0) \propto \frac{1}{\hat{s}} \, .$$

We see clearly that small values of $\hat{s}$ and consequently of the transferred four-momentum Q^2 dominate the cross section. Hence, the on-shell contribution is much more significant than the off-shell one, so the EPA will be valid and give the correct cross section estimate for any QED process.

Now, let us consider the case of neutrino trident production. In this case, the equivalent-photon cross section in the four-point interaction limit has a completely opposite dependence on the center-of-mass energy; it is *proportional* to $\hat{s}$,

$$\sigma_\gamma^{\rm FL}(P_i + \gamma \to P_f; \hat{s}, 0) \propto G_{\rm F}^2 \, \hat{s} \, .$$

This dependence is a manifestation of the unitarity violation in the Fermi theory. Therefore, we can see that for weak processes larger values of $\hat{s}$, and, consequently, larger values of Q^2 are more significant [118, 119]. The EPA is then generally not valid for the neutrino trident production, as the virtual photon contribution dominates over the real one. Nevertheless, one may wonder if there is a situation in which the EPA can give a reasonable estimate for a neutrino trident process. As noticed in the early literature [118, 119], the presence of the nuclear form factor introduces a cut in the transferred momentum which, in turn, makes the EPA applicable for the specific case of the dimuon channel in the coherent regime. Let us discuss this in more detail.

Recalling our exact decomposition, Eq. (3.2.10), it is necessary to consider two assumptions for implementing the EPA [118]:

1. The longitudinal polarization contribution to the cross section can be neglected, i.e., $\sigma_{\nu\gamma}^{\rm L}(Q^2, \hat{s}) \approx 0$;

2. The transverse polarization contribution to the cross section can be taken to be

on-shell, i.e., $\sigma^{\rm T}_{\nu\gamma}(Q^2,\hat{s}) \approx \sigma^{\rm T}_{\nu\gamma}(0,\hat{s})$.

Assuming for now that these approximations hold, we can find a simplified expression for the coherent neutrino-target process, described by Eqs. (3.2.10) and (3.2.15), in terms of the photon-neutrino cross section[5]:

$$\sigma_{\rm EPA} = \frac{Z^2e^2}{4\pi^2}\int_{m_L^2}^{\hat{s}_{\rm max}} \frac{d\hat{s}}{\hat{s}}\,\sigma^{\rm T}_{\nu\gamma}(0,\hat{s}) \int_{(\hat{s}/2E_\nu)^2}^{Q^2_{\rm max}} \frac{|F(Q^2)|^2}{Q^4}\left[Q^2(1-y) - M_{\mathcal{H}}^2 y^2\right] dQ^2\,, \quad (3.2.23)$$

where we introduced the fractional change of the nucleus energy y, defined as $\hat{s} = (s - M_{\mathcal{H}}^2)y$, and the integration limits can be obtained from (3.2.13) after considering that $m_L^2 \ll E_\nu M_{\mathcal{H}}$. Keeping only the leading terms in the small parameter y [117], we recover the EPA applied to the neutrino trident case

$$\sigma_{\rm EPA} = \int \sigma^{\rm T}_{\nu\gamma}(0,\hat{s})\, dP(Q^2,\hat{s})\,, \quad (3.2.24)$$

where $dP(Q^2,\hat{s})$ is given in Eq. (3.2.22). The EPA in the form of Eq. (3.2.24) has been used in trident calculations for the coherent dimuon channel [112] as well as for coherent mixed- and electron-flavour trident modes and diffractive trident modes [106]. Using our decomposition, we can explicitly compute both $\sigma^{\rm L}_{\nu\gamma}$ and $\sigma^{\rm T}_{\nu\gamma}$ and verify if the EPA conditions are satisfied for any channel and, if they are not, quantify the error introduced by making this approximation. For that purpose, we will compare the results of the full calculation, Eq. (3.2.10), with the EPA results, Eq. (3.2.24), by computing the following ratios in the physical region of the $(Q,\hat{s})$ plane,

$$\frac{\sigma^{\rm L}(Q^2,\hat{s})\, h_{\rm c}^{\rm L}(Q^2,\hat{s})}{\sigma^{\rm T}(Q^2,\hat{s})\, h_{\rm c}^{\rm T}(Q^2,\hat{s})}\,, \quad \frac{\sigma^{\rm T}_{\nu\gamma}(Q^2,\hat{s})}{\sigma^{\rm T}_{\nu\gamma}(0,\hat{s})}\,. \quad (3.2.25)$$

The first ratio in Eq. (3.2.25) will indicate where the longitudinal contribution can be neglected compared to the transverse one; while, the second ratio will show where the transverse contribution behaves as an on-shell photon.

As an illustration of the general behaviour, we show in Fig. 3.4 those ratios of cross sections for an incoming ν_μ of fixed energy $E_\nu = 3$ GeV colliding coherently with an ^{40}Ar target, for the dielectron (left panels), mixed (middle panels) and dimuon (right panels) channels. On the top panels of Fig. 3.4 we see that the longitudinal component can be neglected for $Q \lesssim m_\alpha$, for the dielectron and dimuon channels, $\alpha = e, \mu$, while in the mixed case there

[5] An analogous expression can be obtained for the diffractive regime from Eq. (3.2.19).

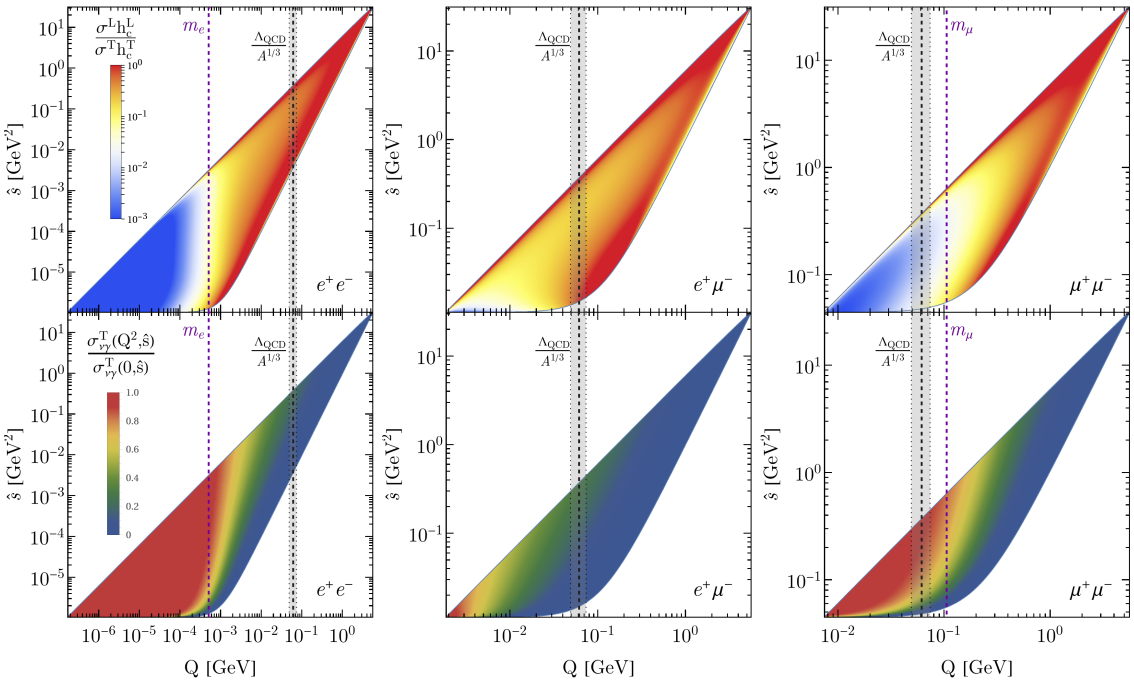

Fig. 3.4. Comparison between the full calculation of the trident production coherent cross section and the EPA in the kinematically allowed region of the $(Q, \hat{s})$ plane for an incoming ν_μ with fixed energy $E_\nu = 3$ GeV colliding with an ^{40}Ar target. The left, middle and right panels correspond to the dielectron, mixed and dimuon final-states, respectively. The top panels correspond to the comparison between the longitudinal and transverse contributions while the bottom ones show the ratio between the transverse cross sections computed for an specific value of Q with the cross section for an on-shell photon. The thick black dashed lines correspond to the cut in the Q^2 integration at $\Lambda^2_{\rm QCD}/A^{2/3}$, and the shadowed region around these lines account for a variation of 20% in the value of this cut. The purple dashed lines are for $Q = m_\alpha$, $\alpha = e, \mu$ for the unmixed cases.

is a much less pronounced hierarchy between the transverse and longitudinal components. On the bottom panels we have the comparison between on-shell and off-shell transverse photo-production cross sections. Again, we find that the EPA is only valid for $Q \lesssim m_\alpha$ for the dielectron and dimuon channels. For the mixed case, there is only a very small region in $Q < 10^{-2}$ GeV for which the off-shell transverse cross section is comparable to the on-shell one. This relative suppression of the off-shell cross section can be understood by noticing that Q enters the lepton propagators, suppressing the process for $Q \gtrsim m_\alpha$. For mixed channels it is then the smallest mass scale (m_e) that dictates the fall-off of the matrix element in Q, whilst the heaviest mass (m_μ) defines the phase space boundaries, rendering most of this phase space incompatible with the EPA assumptions.

These results explicitly show that the EPA is, in principle, not suitable for any neutrino trident process as it can overestimate the cross section quite substantially by treating the

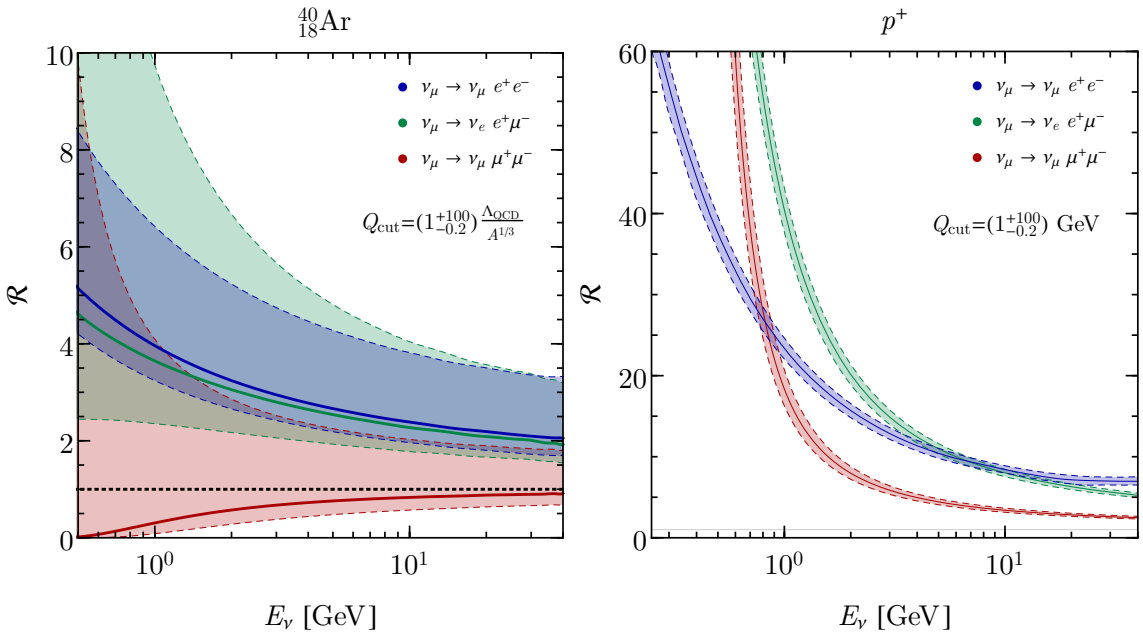

Fig. 3.5. Ratio $\mathcal{R}$ of the trident cross section calculated using the EPA to the full four-body calculation. Left panel: Ratio in the coherent regime on ^{40}Ar. The full curves correspond to the central value of $Q_{\rm cut}$, and the upper (lower) boundary corresponds to a choice 100 times larger (20% smaller). Right panel: Ratio in the diffractive regime for scattering on protons, where the full curves corresponds to the central value of 1.0 GeV, and the upper (lower) boundary corresponds to a choice 100 times larger (20% smaller); we have taken the lower limit in the integration on Q to match the choice of the coherent regime and we do not include Pauli blocking in these curves. A guide to the eye at $\mathcal{R} = 1$ is also shown.

photo-production cross section at large Q^2 as on-shell. However, as previously mentioned, in the coherent regime the nuclear form factor introduces a strong suppression for large values of Q^2. In general, this dominates the behaviour of the cross sections for values of Q^2 smaller than the purely kinematic limit, $Q^2_{\rm max}$, and of the order of $\Lambda_{\rm QCD}/A^{1/3} \approx 0.06$ GeV for coherent scattering on ^{40}Ar. In the dimuon case, the latter scale happens to be smaller than the charged lepton masses, implying that the region where the EPA breaks down is heavily suppressed due to the nuclear form factor. The same cannot be said about coherent trident channels involving electrons, as the nuclear form factor suppression happens for much larger values of Q than the EPA breakdown. Furthermore, for diffractive scattering the nucleon form factors suppress the cross sections only for much larger Q values, $Q \approx 0.8$ GeV. The effective range of integration then includes a significant region where the EPA assumptions are invalid, leading to an overestimation of the diffractive cross section for every process regardless of the flavours of their final-state charged leptons.

In some calculations, artificial cuts have been imposed on the range of Q^2, affecting the

validity of the EPA. In Ref. [106], it is claimed that to avoid double counting between different regimes, an artificial cut must be imposed, lowering the upper limit of integration in Q^2. Ref. [106] chooses a value of $Q^{\rm cut}_{\rm max} = \Lambda_{\rm QCD}/A^{1/3}$ in the coherent regime (black thick dashed lines in Fig. 3.4), and $Q^{\rm cut}_{\rm min} = \max\left(\Lambda_{\rm QCD}/A^{1/3}, \hat{s}/2E_\nu\right)$ and $Q^{\rm cut}_{\rm max} = 1.0$ GeV in the diffractive regime. We believe that no such cut is required on physical grounds[6], and their presence will impact the EPA cross section quite dramatically. Let us first consider the dimuon case in the coherent regime, where the EPA assumptions hold reasonably well in the relevant parts of phase space. By introducing a value for $Q^{\rm cut}_{\rm max}$ we would be decreasing the total relevant phase space for the process, reducing the total cross section. Therefore, despite the EPA tendency to overestimate the cross section in this channel, an artificial cut in Q^2 can actually lead to an underestimation of the cross section. In the electron channels, where the EPA breakdown is much more dramatic, we can expect that the overestimation of the cross section by the EPA is reduced by the cut $Q^{\rm cut}_{\rm max}$. In fact, one way to improve the EPA for the dielectron channel is to artificially cut on the Q^2 integral around the region where the approximation breaks down [127]. This cut does then improve the coherent EPA calculation by decreasing the overestimation of the cross section. However, an energy independent cut cannot provide a good estimate of the cross section over all values of E_ν. To illustrate our point and to quantify the errors induced by the EPA, we show on the left panel of Fig. 3.5 the ratio $\mathcal{R}$ of the trident cross section calculated using the EPA with an artificial cut at $Q^2_{\rm cut}$, as performed in [106], to the full calculation used in this work as a function of the incoming neutrino energy:

$$\mathcal{R} = \frac{\sigma_{\rm EPA}(E_\nu)|_{Q_{\rm cut}}}{\sigma_{\rm 4PS}(E_\nu)}\,. \tag{3.2.26}$$

In this plot we vary the artificial cut on Q^2 around the choice of [106] (shown as the central dashed line) in two ways. First we reduce it by 20%, and then increase it by a large factor, recovering the case with no Q^2 cut. From this, our conclusions about the validity of the approximation are confirmed, and it becomes evident that the trident coherent cross section is very sensitive to the choice of $Q^2_{\rm cut}$. In particular, the EPA with all the assumptions that lead to Eq. (3.2.24) and the absence of a Q^2 cut can lead to an overestimation of all trident channels, including the dimuon one. Once the cut is implemented, however,

[6] It should be noted that the coherent and diffractive regimes have different phase space boundaries and that the form factors should guarantee their independence.

the approximation becomes better for the dimuon channel, but still unacceptable for the electron ones. It is also clear that an energy independent cut cannot give the correct cross section at all energies. This is particularly troublesome for detectors subjected to a neutrino flux covering a wide energy range such as the near detectors for DUNE and MINOS or MINERνA. Moreover, Eq. (3.2.24) fails at low energies, and generally, overestimates the coherent cross sections by at least 200%. At these energies, one must be wary of the additional approximations in Eq. (3.2.24) regarding the integration limits and the small y limit.

On the right panel of Fig. 3.5 we illustrate what happens in the diffractive regime, where the nucleon form factors impact the cross section at much larger values of Q^2 and have a slower fall-off. We see that the diffractive cross section is dramatically overestimated over the full range of E_ν considered and for any trident mode. The discrepancy is particularly important for $E_\nu \lesssim 5$ GeV and larger than in the coherent regime by at least an order of magnitude[7]. We also see that the cuts on Q^2 impact the EPA calculation much less dramatically, and that its use is unlikely to yield the correct result.

Given these problems with both coherent and diffractive cross section calculations due to the breakdown of the EPA for trident production, in what follows we will use the complete four-body calculation.

3.2.3 Coherent Versus Diffractive Scattering in Trident Production

Let us now comment on the significance of the coherent and diffractive contributions to the total cross for the different trident channels. In Fig. 3.6 we present the ratio of the coherent and the diffractive scattering cross sections to the total cross section for an ^{40}Ar target for an incoming ν_μ (left) and ν_e (right) neutrino. We can see that the coherent regime dominates at all neutrino energies when there is an electron in the final-state, especially in the dielectron case. This can be explained by noting that the Q^2 necessary to create an electron pair is smaller than the one needed to create a muon; thus, coherent scattering is more likely to occur for this mode. Conversely, as one needs larger momentum

[7]There are some differences in the treatment of the hadronic system between the EPA calculation in [106] and the one presented here. However, these differences are of the order 10% to 20%. Note also that we do not implement any Pauli blocking when calculating $\mathcal{R}$ to avoid ambiguities over the choice of the range of Q^2.

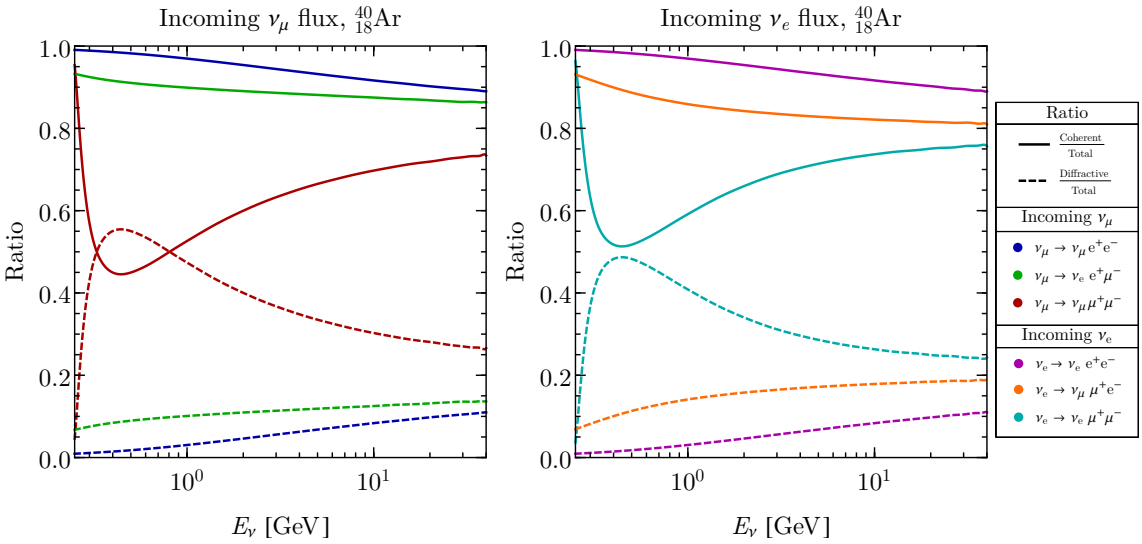

Fig. 3.6. On the left (right) panel we show the ratio of the coherent (full lines) and the diffractive (dashed lines) contributions to the total trident cross section for an incoming flux of $\nu_\mu(\nu_e)$ as a function of E_ν for an ^{40}Ar target.

transferred to produce a muon (either accompanied by an electron or another muon) the diffractive regime becomes more likely in these modes, as we can explicitly see in Fig. 3.6. Because of this effect the diffractive contribution is $\lesssim 10\%$, except for the dimuon channel where it can be between 30 and 40% in most of the energy region. Furthermore, when we compare the two incoming types of neutrinos, we see that for an incoming ν_μ the diffractive contribution is larger than the coherent one in the range 0.3 GeV $\lesssim E_\nu \lesssim$ 0.8 GeV, while for an incoming ν_e this never happens. This difference can be explained by the fact that CC and NC contributions are simultaneously present for the scattering of an initial ν_μ creating a muon pair, whereas for an initial ν_e creating a muon pair, we will only have the NC contribution, see Table 3.1.

An important difference between the coherent and diffractive regimes will be in their hadronic signatures in the detector. Neutrino trident production is usually associated with zero hadronic energy at the vertex, a feature that proved very useful in reducing backgrounds in previous measurements. Whilst this is a natural assumption for the coherent regime, it need not be the case in the diffractive one. In fact, in the latter it is likely that the struck nucleon is ejected from the nucleus in a significant fraction of events with Q exceeding the nuclear binding energy [8]. Since the dominant diffractive contribution comes from scattering on protons, these could then be visible in the detector if their

[8] The peak of our diffractive Q^2 distributions happens at around $Q \approx 300$ MeV, much beyond the typical binding energy for Ar (see Appendix C). Without Pauli suppression, however, we expect this value to drop.

energies are above threshold. On the other hand, the struck nucleon is subject to many nuclear effects which may significantly affect the hadronic signature, such as interactions of the struck nucleon in the nuclear medium as well as reabsorption. Our calculation of Pauli blocking, for example, shows large suppressions ($\sim 50\%$) precisely in the low Q^2 region, usually associated with no hadronic activity. This then raises the question of how well one can predict the hadronic signatures of diffractive events given the difficulty in modelling the nuclear environment. We therefore do not commit to an estimate of the number of diffractive events that would have a coherent-like hadronic signature, but merely point out that this might introduce additional uncertainties in the calculation, especially in the $\mu^+\mu^-$ channel where the diffractive contribution is comparable to the coherent one. Finally, from now on we will refer to the number of trident events with no hadronic activity as coherent-like, where this number can range from coherent only to coherent plus all diffractive events.

3.3 Trident Events in LAr Detectors

In this section we calculate the total number of expected trident events for some present and future LAr detectors with different fiducial masses, total exposures and beamlines.

3.3.1 Event Rates

The total number of trident events, $N_{\rm X}^{\Psi}$, expected for a given trident mode at any detector is written as

$$N_{\rm X}^{\Psi} = \text{Norm} \times \int dE_\nu \, \sigma_{\nu \rm X}(E_\nu) \frac{d\phi_\nu(E_\nu)}{dE_\nu} \epsilon(E_\nu) \,, \tag{3.3.1}$$

where $\sigma_{\nu \rm X}$ can be the trident total ($\rm X = \mathcal{N}$), coherent ($\rm X = c$) or diffractive ($\rm X = d$) cross sections for a given mode, ϕ_ν is the flux of the incoming neutrino and $\epsilon(E_\nu)$ is the efficiency of detection of the charged leptons. In the calculations of this section, we assume an efficiency of 100%[9]. Two features of the cross sections are important for the event rate calculation: threshold effects, especially for channels involving muons in the final-state, and cross section's growth with energy. In particular, we expect higher trident event rates for experiments with higher energy neutrino beams.

[9]See Appendix C for a discussion on the detection efficiencies for trident events and backgrounds.

We start our study with the three detectors of the SBN program, one of which, μBooNE, is already installed and taking data at Fermilab. These three LAr time projection chamber detectors are located along the Booster Neutrino Beam line which is by now a well-understood source, having the focus of active research for over 15 years. Although the number of trident events expected in these detectors is rather low, they may offer the first opportunity to develop search techniques and learn more about background processes to tridents in LAr. After that we study the proposed near detector for DUNE. This turns out to be the most important LAr detector for trident production since it will provide the highest number of events in both neutrino and antineutrino modes. Finally, having in mind the novel flavour composition of neutrino beams from muon facilities, we investigate trident rates at a 100 t LAr detector for the νSTORM project. This last facility could offer a very well understood neutrino beam with as many electron neutrinos as muon antineutrinos from muon decays, creating new possibilities for trident scattering measurements.

The SBN Program The SBN Program at Fermilab is a joint endeavour by three collaborations ICARUS, μBooNE and SBND to perform searches for eV-sterile neutrinos and study neutrino-Ar cross sections [128]. SBND has the shortest baseline (110 m) and therefore the largest neutrino fluxes. The largest detector, ICARUS, is also the one with the longest baseline (600 m) and consequently subject to the lowest neutrino fluxes. The ratio between the fluxes at the different detectors are $\phi_{\mu\text{BooNE}}/\phi_{\text{SBND}} = 5\%$ and $\phi_{\text{ICARUS}}/\phi_{\text{SBND}} = 3\%$. The neutrino beam composition is about 93% of ν_μ, 6% of $\overline{\nu}_\mu$ and 1% of $\nu_e + \overline{\nu}_e$.

Considering the difference in fluxes and the total number of targets in each of these detectors, one can estimate the following ratios of trident events: $N^{\Psi}_{\mu\text{BooNE}}/N^{\Psi}_{\text{SBND}} \sim 8\%$ and $N^{\Psi}_{\text{ICARUS}}/N^{\Psi}_{\text{SBND}} \sim 10\%$. Unfortunately, since the fluxes are peaked at a rather low energy ($E_\nu \lesssim 1$ GeV), where the trident cross sections are still quite small ($\lesssim 10^{-42}$ cm^2) we expect very few trident events produced. The exact number of trident events for those detectors according to our calculations is presented in Tab. 3.2. For each trident channel the first (second) row shows the number of coherent (diffractive) events. As expected, less than a total of 20 events across all channels can be detected by SBND, and a negligible rate of events is expected at μBooNE and ICARUS.

Channel	SBND	μBooNE	ICARUS	DUNE ND	νSTORM ND
$\nu_\mu \to \nu_e e^+ \mu^-$	10	0.7	1	2844 (235)	159
	1	0.08	0.1	369 (33)	18
$\overline{\nu}_\mu \to \overline{\nu}_e e^- \mu^+$	0.4	0.02	0.04	122 (2051)	23
	0.04	0.003	0.004	16 (262)	3
$\nu_e \to \nu_\mu e^- \mu^+$	0.05	0.003	0.004	22 (7)	9
	0.008	0.0005	0.0008	5 (1)	2
$\overline{\nu}_e \to \overline{\nu}_\mu e^+ \mu^-$	0.005	0.0003	0.0005	5 (14)	–
	0.001	0.0001	0.0001	1 (3)	–
Total $e^\pm \mu^\mp$	10	0.7	1	2993 (2307)	191
	1	0.1	0.1	391 (299)	23
$\nu_\mu \to \nu_\mu e^+ e^-$	6	0.4	0.7	913 (58)	73
	0.2	0.04	0.02	57 (5)	3
$\overline{\nu}_\mu \to \overline{\nu}_\mu e^- e^+$	0.2	0.01	0.02	34 (695)	9
	0.01	0.001	0.002	2 (41)	0.5
$\nu_e \to \nu_e e^- e^+$	0.2	0.01	0.02	50 (13)	32
	0.01	0.001	0.002	4 (1)	2
$\overline{\nu}_e \to \overline{\nu}_e e^+ e^-$	0.02	0.001	0.002	10 (34)	–
	0.0009	0.0001	0.0002	1 (2)	–
Total $e^+ e^-$	6	0.4	0.7	1007 (800)	114
	0.2	0.0	0.02	64 (49)	6
$\nu_\mu \to \nu_\mu \mu^+ \mu^-$	0.4	0.03	0.04	271 (32)	9
	0.3	0.03	0.04	135 (14)	5
$\overline{\nu}_\mu \to \overline{\nu}_\mu \mu^- \mu^+$	0.01	0.001	0.001	14 (177)	2
	0.01	0.0009	0.001	7 (93)	1
$\nu_e \to \nu_e \mu^+ \mu^-$	0.002	0.0001	0.0001	1 (0.5)	0.4
	0.001	0.0001	0.0001	0.5 (0.2)	0.2
$\overline{\nu}_e \to \overline{\nu}_e \mu^+ \mu^-$	0.0002	0.0000	0.0000	0.3 (0.9)	–
	0.0001	0.0000	0.0000	0.1 (0.3)	–
Total $\mu^+ \mu^-$	0.4	0.0	0.0	286 (210)	11
	0.3	0.0	0.0	143 (108)	6

Tab. 3.2. Total number of **coherent** (top row) and **diffractive** (bottom row) trident events expected at different LAr experiments for a given channel. The numbers in parentheses are for the antineutrino running mode, when present. We assume detector efficiencies of 100%. For the νSTORM ND, we take a fiducial mass of 100t of LAr.

DUNE Near Detector The DUNE experiment will operate with neutrino as well as antineutrino LBNF beams produced by directing a 1.2 MW beam of protons onto a fixed target [129, 130]. The design of the near detector is not finalised, but the current designs favour a mixed technology detector combining a LAr TPC with a larger tracker module.

In this work, we will assume that DUNE ND is a LAr detector located at 574 m from the target with a fiducial mass of 50 t [131]. As the trident event rate scales with the density of the target, any tracker module will not significantly influence the total event rate, and does not feature in our estimates; although, its presence is assumed to improve reconstruction of final-state muons. Our estimates can be easily scaled for the final design by using Eq. (3.3.1).

For the first 6 years of data taking (3 years in the neutrino plus 3 years in the antineutrino mode) the collaboration expects 1.83×10^{21} POT/year with a plan to upgrade the beam after the 6th year for 2 extra years in each beam mode with double exposure, making a total of $1.83 \times (3 + 2 \times 2) \times 10^{21}$ POT for each mode [132]. We will assume the total 10-year exposure in our calculations.

The number of trident events for DUNE ND can be found in Tab. 3.2. The numbers in parentheses correspond to antineutrino beam mode. Note that although the trident cross sections are the same for neutrinos and antineutrinos, the fluxes are a bit lower for the antineutrino beam, as a consequence we predict a lower event rate for this beam [10]. Due to the much higher energy and wider energy range of the neutrino fluxes at DUNE ND, as compared to the SBN detectors, DUNE can observe a considerable number of trident events, about 300 times the number of trident events expected for SBND just in the neutrino mode. Moreover, the subdominant component of each beam mode will also contribute to the signal. For example, we expect to observe 2051 trident events in the $\overline{\nu}_\mu \to \overline{\nu}_e e^- \mu^+$ channel in the antineutrino mode. However, we also expect 235 events in the $\nu_\mu \to \nu_e e^+ \mu^-$ channel produced by the subdominant component of ν_μ in the antineutrino beam. We have considered 100% detection efficiency here, however, we will see in Sec. 3.4 that after implementing hadronic vetos, detector thresholds and kinematical cuts to substantially reduce the background we expect an efficiency of about 47%-65% on coherent tridents, depending on the channel (see Tab. 3.4).

The mixed flavour trident channel is the one with the highest statistics (more than 6000 events adding neutrino and antineutrino beam modes), 11% of which are produced by diffractive scattering. The dielectron channel comes next with a total of a bit more than 1900 events, 5% of which are produced by diffractive scattering. Although the dimuon

[10] A similar difference will apply to the processes constituting the background to the trident process, although there is an additional suppression in many channels due to the lower antineutrino cross sections.

channel is the less copious one, with only about 750 events produced, almost 34% of these events are produced by a diffractive process. This can be understood by recalling our discussions in Sec. 3.2.3.

Finally, we note that a dedicated high-energy run at DUNE has been mooted, to be undertaken after the full period of data collecting for the oscillation analysis. Thanks to the higher energies of the beam, this has the potential to see a significant number of neutrino tridents, provided it can collect enough POTs.

νSTORM In this section we study the trident rates for a possible LAr detector for the proposed νSTORM experiment [133, 134]. The νSTORM facility is based on a neutrino factory-like design and has the goal to search for sterile neutrinos and study neutrino nucleus cross sections [135]. Although this proposal is in its early days, νSTORM has the potential to make cross section measurements with unprecedented precision. In its current design, 120-GeV protons are used to produce pions from a fixed target with the pions subsequently decaying into muons and neutrinos. The muons are captured in a storage ring and during repeated passes around the ring they decay to produce neutrinos. Consequently, the storage ring is an intense source of three types of neutrino flavours: ν_μ from π^+ and K^+ decays, which will be more than 99% of the total flux, ν_e and $\overline{\nu}_\mu$ from recirculated muon decays which will comprise less than 1% of the total flux. An important point, however, is that the neutrinos coming from the pion and kaon decays can be separated by event timing from the ones produced by the stored muons. This distinction allows the ν_μ flux to be studied almost independently from the $\overline{\nu}_\mu$ and ν_e flux. In addition, it implies after the initial flash of meson-derived events, that the flux consists of as many electron neutrinos as muon antineutrinos. We will assume a LAr detector for νSTORM at a baseline of 50 m with 100 t of fiducial mass with an exposure of 10^{21} POT. The neutrino fluxes, assuming a central μ^+ momentum of 3.8 GeV/c in the storage ring, are taken from Ref. [134].

In Tab. 3.2, we show the results of our calculations for νSTORM. More than 97% of the events from the incoming ν_μ are from pion decays and only less than 3% from kaon decays. Since we only consider the decay of mesons with positive charges and we expect neutral and wrong charge contamination to be small, we do not have trident events from incoming $\overline{\nu}_e$. The total number of mixed flavour, dielectron and dimuon channel events is, respectively,

214, 120 and 17, much less than what can be achieved at the larger neutrino energies available at the DUNE ND. The novel flavour structure of the beam does enhance the contribution of ν_e induced tridents with respect to the $\overset{(-)}{\nu}_\mu$ ones, but this contribution only becomes dominant for the e^+e^- tridents in the muon decay events. Finally, we emphasize that the experimental design parameters for νSTORM are far from definite. Increasing the energy of stored muons and the size of the detector are both viable options which could significantly enhance the rates we present.

3.4 Backgrounds to Tridents in LAr

The study of any rare process is a struggle against both systematic uncertainties in the event rates and unavoidable background processes. True dilepton signatures are naturally rare in neutrino scattering experiments, but with modest rates of particle misidentification a non-trivial background arises. In this section we estimate the background to trident processes in LAr and its impact on the trident measurement. We perform our analysis only for DUNE ND, in neutrino and antineutrino mode, but our results are expected to be broadly applicable to other LAr detectors. We have generated a sample of 1.1×10^6 background events using GENIE [136] for incident electron and muon flavour neutrinos and antineutrinos. It is worth noting, however, that this event sample will in fact be smaller than the total number of neutrino interactions expected in the DUNE ND. Our goal, therefore, will be to demonstrate that with modest analysis cuts background levels can be suppressed significantly such that they become comparable to or smaller than the signals we are looking for. In the absence of events that satisfy our background definition, we argue that the frequency of that type of event is less than one in 1.1×10^6 interactions of the corresponding initial neutrino.

To account for misreconstruction in the detector, we implement resolutions as a gaussian smear around the true MC energies and angles. We assume relative energy resolutions as $\sigma/E = 15\%/\sqrt{E}$ for e/γ showers and protons, and $6\%/\sqrt{E}$ for charged pions and muons. Angular resolutions are assumed to be 1° for all particles (proton angles are never smeared in our analysis). The detection thresholds are a crucial part of the analysis, since for many channels one ends up with very soft electrons. We take thresholds to be 30 MeV for muons and e/γ showers kinetic energy, 21 MeV for protons and 100 MeV for $\pi^\pm$ [130].

Background Candidates

We focus on three final-state charged lepton combinations: $\mu^+\mu^-$, $\mu^\pm e^\mp$ and e^+e^-. Genuine production of these states is possible in background processes, but usually rare, deriving from meson resonances or other prompt decays. The majority of the background is expected to be from particle misidentification (misID). We assume that protons can always be identified above threshold and that neutrons leave no detectable signature in the detector. In addition, we require no charge ID capabilities from the detector and assume that the interaction vertex can always be reconstructed. Under these assumptions, we have incorporated three misidentifications which will affect our analysis, and give our naive estimates for their rates in Tab. 3.3. Any other particle pairs are assumed to be distinguishable from each other when needed. Of great importance is the misID rate for μ/π. Because the typical energy deposition in the detector, dE/dx, is very similar between pions and muons, these are indistinguishable if the particle escapes the detector. If the pion interacts, however, it may be identified. The pion interaction length in LAr is taken to be around 1m, and travelling a distance of around $\lesssim$ 3m would occur in $\sim$ 10% of cases. Increasing this misID rate has a large impact, increasing the number of backgrounds events to dimuon tridents. Additional possibilities to control backgrounds from pion production are tightening cuts on the opening angle of the dimuon pair or increasing the detector volume (see Ref. [122] for a more recent discussion on this issue).

	γ as $e^\pm$	γ as e^+e^-	$\pi^\pm$ as $\mu^\pm$
Rate	5%	10% (w/ vertex) 100% (no vertex + overlapping)	10%

Tab. 3.3. Assumed misID rates for various particles in a LAr detector. We take these values to be constant in energy.

The requirement of no hadronic activity helps constrain the possible background processes, but one is still left with significant events with invisible hadronic activity and other coherent neutrino-nucleus scatterings. These are then reduced by choosing appropriate cuts on physical observables, exploring the discrepancies between our signal and the background. In our GENIE analysis, we include all events that have final-states identical to trident, or that could be interpreted as a trident final-state considering our proposed misID scenarios. Our dominant sources of background for $\mu^+\mu^-$ tridents are ν_μ-initiated charged-current

events with an additional charged pion in the final-state (ν_μCC1$\pi^\pm$). For e^+e^- tridents, the most important processes are neutral current scattering with a π^0 (NCπ^0), while for mixed $e^\pm\mu^\mp$ tridents, the ν_μ-initiated charged-current events with a final-state π^0 (CCπ^0) dominate the backgrounds. In each case, the pion is misidentified to mimic the true trident final-state. Other relevant topologies include charm production, CCγ and ν_eCC$\pi^\pm$. For a detailed discussion of these backgrounds processes we refer the reader to Ref. [1].

Estimates for the DUNE ND

In this section we provide estimates for the total background for each trident final-state for the DUNE ND. The number of total inclusive CC interactions in the 50 t detector due to neutrinos of all flavours is calculated to be 5.18×10^8. We scale our background event numbers to match this, and argue that one has to reach suppressions of order $10^{-6} - 10^{-5}$ to have a chance to observe trident events. Whenever our cuts remove all background events from our sample, we assume the true background rate is one event per 1.1×10^6 ν interactions and scale it to the appropriate number of events in the ND, applying the misID rate whenever relevant. Within our framework, this provides a conservative estimate as the true background is expected to be smaller.

Our estimates are shown in Table 3.4. We start with the total number of background candidates N_B^{misID}, using only the naive misID rates shown in Table 3.3. These are much larger than the trident rates we expect, by at least 2 orders of magnitude. Next, we veto any hadronic activity at the interaction vertex, obtaining N_B^{had}. We emphasize that this veto also affects the diffractive tridents in a non-trivial way, and therefore we remain agnostic about the hadronic signature of these. Finally, one can look at the kinematical distributions of coherent trident in Appendix C and try to estimate optimal one dimensional cuts for the DUNE ND based on the kinematics of the final-state charged leptons. This is a simple way to explore the striking differences between the peaked nature of our signal and the smoother background. In a real experimental setting it is desirable to have optimization methods for isolating signal from background, preferably with a multivariate analyses. However, even in our simple analysis, cutting on the small angles to the beamline and the low invariant masses of our trident signal can achieve the desired background suppressions. For the $\mu^+\mu^-$ tridents we show the effect of our cuts in Fig. 3.7. The cuts are defined to

be $m^2_{\mu^+\mu^-} < 0.2$ GeV^2, $\Delta\theta < 20°$, $\theta_\pm < 15°$. The kinematics is very similar in the other trident channels, with slightly less forward distributions for electrons. For the e^+e^- channel we take $m^2_{e^+e^-} < 0.1$ GeV^2, $\Delta\theta < 40°$ and $\theta_\pm < 20°$. The asymmetry between the positive and negative charged leptons is visible in the distributions, where the latter tends to be more energetic. This feature was not explored in our cuts, as it is not significant enough to further improve background discrimination. In the mixed flavour tridents, however, one sees a much more pronounced asymmetry. The muon tends to carry most of the energy and be more forward than the electron, which can make the search for this channel more challenging due to the softness of the electron in the high energy event. Nevertheless, the low invariant masses and forward profiles can still serve as powerful tool for background discrimination, provided the event can be well reconstructed. We assume that is the case here and use the following cuts on the background: $m^2_{e^\pm\mu^\mp} < 0.1$ GeV^2, $\Delta\theta < 20°$, $\theta_e < 40°$ and $\theta_\mu < 20°$. When performing kinematical cuts, we also include the effects of detection thresholds after smearing. For a discussion on the impact of these thresholds on the trident signal see Appendix C.

The resulting signal efficiencies due to our cuts and thresholds are shown in the last two columns of Table 3.4. One can see that these are all $\approx 50\%$ or greater for our coherent samples, whilst all background numbers remain much below the trident signal. The diffractive samples are also somewhat more affected by our cuts than the coherent ones. If one is worried about the contamination of coherent events by diffractive ones, then the kinematics of the charged leptons alone can help reduce this, independently of the hadronic energy deposition of the events. For instance, in the case where all $\mu^+\mu^-$ diffractive events appear with no hadronic signature, then after our cuts the diffractive contribution is reduced from 41% to 15% of the total trident signal. This reduction is, however, also subject to large uncertainties coming from nuclear effects. In summary, the set of results above are encouraging, suggesting that the signal of coherent-like trident production is sufficiently unique to allow for its search at near detectors despite naively large backgrounds.

Finally, we comment on some of the limitations of our analysis. The low rate of trident events calls for a more careful evaluation of other subdominant processes that could be easily

[11] Despite the fact that many diffractive events will likely deposit hadronic energy in the detector, we quote the efficiency of our cuts on diffractive events with no assumptions on their hadronic signature.

Channel	$\mathbf{N}_{\mathrm{B}}^{\mathrm{misID}}/\mathbf{N}_{\mathrm{CC}}$	$\mathbf{N}_{\mathrm{B}}^{\mathrm{had}}/\mathbf{N}_{\mathrm{CC}}$	$\mathbf{N}_{\mathrm{B}}^{\mathrm{kin}}/\mathbf{N}_{\mathrm{CC}}$	$\epsilon_{\mathrm{sig}}^{\mathrm{coh}}$	$\epsilon_{\mathrm{sig}}^{\mathrm{dif}}$ [11]
$e^{\pm}\mu^{\mp}$	$1.67\ (1.62) \times 10^{-4}$	$2.68\ (4.31) \times 10^{-5}$	$4.40\ (3.17) \times 10^{-7}$	0.61 (0.61)	0.39 (0.39)
$e^{+}e^{-}$	$2.83\ (4.19) \times 10^{-4}$	$1.30\ (2.41) \times 10^{-4}$	$6.54\ (14.1) \times 10^{-6}$	0.48 (0.47)	0.21 (0.21)
$\mu^{+}\mu^{-}$	$2.66\ (2.73) \times 10^{-3}$	$10.4\ (9.75) \times 10^{-4}$	$3.36\ (3.10) \times 10^{-8}$	0.66 (0.67)	0.17 (0.16)

Tab. 3.4. Reduction of backgrounds at the DUNE ND in neutrino (antineutrino) mode and its impact on the signal for each distinguishable trident final-state. $\mathbf{N}_{\mathrm{B}}^{\mathrm{misID}}$ stands for total backgrounds to trident after only applying misID rates, $\mathbf{N}_{\mathrm{B}}^{\mathrm{had}}$ are the backgrounds after the hadronic veto, and $\mathbf{N}_{\mathrm{B}}^{\mathrm{kin}}$ reduce the latter with detection thresholds and kinematical cuts (see text for the cuts chosen). These quantities are normalized to the total number of CC interactions in the ND $\mathbf{N}_{\mathrm{CC}}$ (flavour inclusive). We also show the impact of our detection thresholds and kinematical cuts on the trident signal via efficiencies for coherent only ($\epsilon_{\mathrm{sig}}^{\mathrm{coh}}$) and diffractive only samples ($\epsilon_{\mathrm{sig}}^{\mathrm{dif}}$). We do not cut on the hadronic activity of diffractive events.

be overlooked. For channels involving electrons, it is possible that de-excitation photons and internal bremsstrahlung become a source of background, as these also produce very soft EM showers, none of which are implemented in GENIE. The question of reconstruction of these soft EM showers, accompanied either by a high energy muon or by another soft EM shower also would have to be addressed, especially in the latter case where a trigger for these soft events would have to be in place. A more complete analysis is also needed for treating the decay products of charged pions and muons produced in neutrino interactions, as well as rare meson decay channels (like the Dalitz decay of neutral pions $\pi^0 \to \gamma e^+ e^-$). Cosmic ray events are not expected to be a problem due to the requirement of a vertex and a correlation with the beam for trident events. Perhaps even more exotic processes, such as the production of three final-state charged leptons ($\nu_\alpha(\overline{\nu}_\alpha) + \mathcal{H} \to \ell_\alpha^-(\ell_\alpha^+) + \ell_\beta^+ + \ell_\beta^- + \mathcal{H}'$), can also become relevant. For instance, radiative trimuon production [137] can potentially serve as a background to dimuon tridents if one of the muons is undetected. Similarly, μee production would fake a dielectron (mixed) trident signature if the muon (an electron) is missed. We are not aware of any estimates for the rate of these processes at the DUNE ND, but we note that their rate can be comparable to trident production at energies above 30 GeV [138]. Improvements on our analysis should come from the collaboration's sophisticated simulations, allowing for a better quantification of hadronic activity, more realistic misID rates and more accurate detector responses.

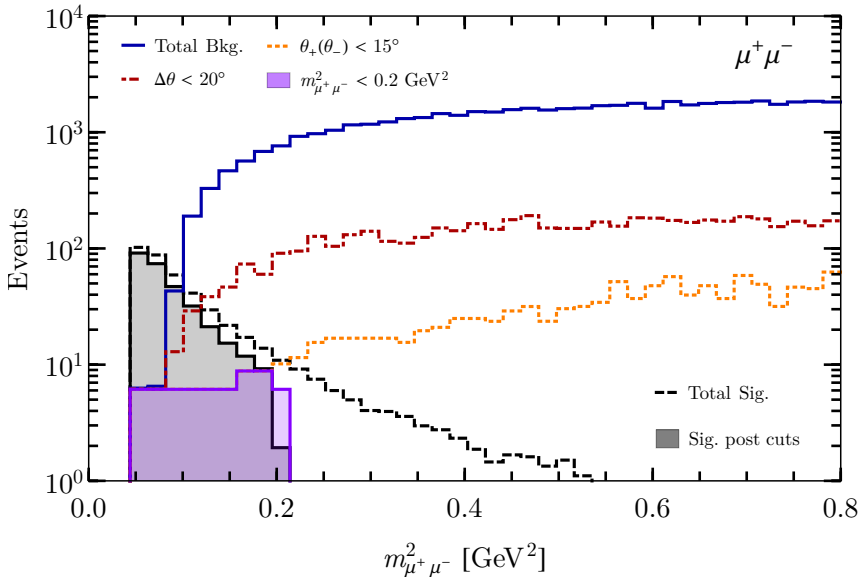

Fig. 3.7. Signal and background distributions in invariant mass. The total background events (blue) include the misID rates in table Table 3.3. We apply consecutive cuts on the background, starting with cuts on the separation angle $\Delta\theta$ (red), both charged lepton angles to the beamline (θ_+ and θ_-) (orange) and the invariant mass $m^2_{\mu^+\mu^-}$. We show the signal samples before and after all the cuts in dashed black and filled black, respectively.

3.5 Overview

Neutrino trident events are predicted by the SM, however, only $\overline{\nu}_\mu$ initiated dimuon tridents have been observed in small numbers, typically fewer than 100 events. This will change in the near future thanks to the current and future generations of precision neutrino scattering and oscillation experiments, which incorporate state-of-the-art detectors located at short distances from intense neutrino sources. Our calculation of the neutrino trident cross section holds for all flavours and hadronic targets, and with it we provided estimates for the number and distributions of events at 5 current and future neutrino detectors: five detectors based on the new LAr technology (SBND, μBooNE, ICARUS, DUNE ND and νSTORM ND). The search for tridents, however, need not be exclusive to near detectors of accelerator neutrino experiments. As pointed out by the authors of Ref. [114], atmospheric neutrino experiments can also look for these processes, benefiting from the increase of the cross section at large energies. Extending our formalism to DIS regimes would also be interesting and straightforward for larger energies.

The DUNE ND is the future detector with the highest neutrino trident statistics, more than 6000 mixed events, 11% produced by diffractive scattering, more than 1900 dielectron events, 5% produced by diffractive scattering and about 750 dimuon events, almost 34%

of those produced by a diffractive process. Making use of our efficiencies (see Table 3.4), assuming an ideal background rejection and neglecting systematic uncertainties, we quote the statistical uncertainty on the coherent-like flux averaged cross section for the DUNE ND. We do this for coherent only events and, in brackets, for coherent plus diffractive events, yielding

$$\frac{\delta\langle\sigma^{e^\pm\mu^\mp}\rangle}{\langle\sigma^{e^\pm\mu^\mp}\rangle} = 1.8\%\,(1.6\%), \quad \frac{\delta\langle\sigma^{e^+e^-}\rangle}{\langle\sigma^{e^+e^-}\rangle} = 3.4\%\,(3.3\%) \quad \text{and} \quad \frac{\delta\langle\sigma^{\mu^+\mu^-}\rangle}{\langle\sigma^{\mu^+\mu^-}\rangle} = 5.5\%\,(5.1\%).$$

In this optimistic framework we expect the true statistical uncertainty on coherent-like tridents to lie between the two numbers quoted, depending on how many diffractive events contribute to the coherent-like event sample. This impressive precision would provide unprecedented knowledge of the trident process. We emphasize, however, that given these small values, the trident cross section will likely be dominated by systematic uncertainties from detector response and backgrounds which are not modeled here.

Chapter 4

New Fundamental Forces at DUNE

Novel interactions in the neutrino sector have been proposed for a variety of reasons, including as a potentially observable effect in the neutrino oscillation probabilities (see *e.g.* [139]), as a way of ameliorating tension introduced by sterile neutrinos in the early universe [140–147], and as a possible explanation of anomalous results at short baseline [5, 148, 149]. Models which introduce new interactions between neutrinos and matter have been discussed in simplified settings [150–152], via Effective Field Theory [116, 153] and specific UV complete models [154] (see also [155] for a neutrinophilic Z' study at the DUNE ND). One class of models restricts the new interactions to leptons. This arises most naturally in settings with a gauged subgroup of lepton number, with most attention given to the anomaly free subgroups $L_\alpha - L_\beta$ for $\alpha, \beta \in \{e, \mu, \tau\}$ [156, 157]. Such leptophilic interactions must satisfy strong constraints from processes involving charged-leptons [158], but in the case of a gauged $L_\mu - L_\tau$ symmetry, neutrino processes have been found to be particularly competitive [159].

In this chapter, we study potential constraints which can be placed on a general set of leptophilic Z' models in the two most likely scattering channels for this type of BSM at the near detector of DUNE: $\nu - e$ scattering and $\nu\ell\ell$ trident scattering. During ten years of running, a 75-t near detector subjected to the intense neutrino beam at the Long-Baseline Neutrino Facility (LBNF) will provide tens of thousands of $\nu - e$ scattering events. The cross section for this process is theoretically well understood and can therefore be a sensitive

probe of BSM physics. Additionally, this process has received special interest due to its potential in reducing systematic uncertainties in the neutrino flux [160,161], an undertaking which can be affected by new physics. Despite not being a purely leptonic process, neutrino trident production can also be measured with reasonable precision at DUNE, where we have seen in the previous chapter that hundreds of coherent and diffractive trident events are expected at the ND. We study the neutral current channels with dielectron or dimuon final states, pointing out how the new physics contribution impacts the non-trivial kinematics of these processes. The main advantage in such measurements lies on the flavour structure of dimuon tridents, which can be used to constrain otherwise difficult to test models, such as the one where a new force is associated to the $L_\mu - L_\tau$ gauge symmetry [159].

Although these processes can place stringent bounds on many classes of mediators, many scenarios are already heavily constrained through other experimental work. A recent study of several different $U(1)_X$ models using $\nu - e$ scattering was presented in Ref. [162], where data from past $\nu - e$ experiments CHARM-II, GEMMA and TEXONO has been used to put bounds on the couplings and masses of general Z's. Novel charged particles are typically constrained to be very massive, leading to little enhancement of the charged current neutrino scattering rates. In particular, charged scalars have been considered in $\nu\ell\ell$ trident scattering in Ref. [115], where it is found that trident measurements can provide competitive bounds on charged scalars, albeit only in simplified theoretical settings. The requirement of doubly charged scalars or the connection to neutrino masses introduced by the typical UV completions of such models dilutes the relevance of the trident bounds. Neutral scalars are viable, but also present challenging UV completions. Novel Z' interactions in $\nu\ell\ell$ trident scattering with dimuon final states have been studied in Ref. [159], where it was shown to be a promising channel to probe a $L_\mu - L_\tau$ gauge symmetry. This model was revisited in Refs. [113] and [163], where the effects of kinetic mixing and the possibility of a measurement by T2K was alluded to. Finally, neutrino trident scattering with atmospheric neutrinos was shown to be sensitive to this model as well as to simplified scalar models in [164]. It should be noted, however, that as it was shown in the previous chapter the Equivalent Photon Approximation (EPA) discussed in several recent studies [113, 115] for the calculation of the trident cross section leads to intolerably large errors in the predictions for the $\nu\ell\ell$ scattering channels in the SM. For this reason, we calculate this process without making this approximation.

4.1 Leptophilic Z' Models

Since we are interested in models where the novel neutral currents are present only in the lepton sector, let us consider explicitly a $\mathrm{U}(1)_{Z'}$ extension of the SM whose Lagrangian is given by

$$\mathscr{L} \supset -g' Z'_\mu \left[Q^{\mathrm{L}}_\alpha \, \overline{L^\alpha_L} \gamma^\mu L^\alpha_L + Q^{\mathrm{R}}_\alpha \, \overline{\ell^\alpha_R} \gamma^\mu \ell^\alpha_R + \sum_{\mathrm{N}} Q_{\mathrm{N}} \, \overline{N_R} \gamma^\mu N_R \right], \tag{4.1.1}$$

where L_α (ℓ_α) represents the leptonic SU(2) doublet (singlet) of flavour $\alpha \in \{e, \mu, \tau\}$, and we included N right-handed neutrinos with charges Q_{N} under the new symmetry for completeness. Thus, we have $7 + \mathrm{N}$ new parameters to characterize the couplings between the new boson and the lepton sector, one gauge coupling g' and $6{+}N$ charges $\{Q^{\mathrm{L}}_\alpha, Q^{\mathrm{R}}_\alpha, Q_{\mathrm{N}}\}$. Below the scale of the Electroweak Symmetry Breaking (EWSB), the relevant interaction terms in the Lagrangian are given by

$$\mathscr{L} \supset - g' Z'_\mu [Q^{\mathrm{L}}_\alpha \, \overline{\nu_\alpha} \gamma^\mu P_{\mathrm{L}} \nu_\alpha + \frac{1}{2} \, \overline{\ell_\alpha} \gamma^\mu (Q^{\mathrm{V}}_\alpha - Q^{\mathrm{A}}_\alpha \gamma^5) \ell_\alpha + \sum_{\mathrm{N}} Q_{\mathrm{N}} \, \overline{N_R} \gamma^\mu N_R], \tag{4.1.2}$$

where $Q^{\mathrm{V}}_\alpha \equiv Q^{\mathrm{L}}_\alpha + Q^{\mathrm{R}}_\alpha$ and $Q^{\mathrm{A}}_\alpha \equiv Q^{\mathrm{L}}_\alpha - Q^{\mathrm{R}}_\alpha$. We note that the right-handed singlets could modify the form of the neutrino interaction in Eq. (4.1.2) by introducing a right-chiral current. The details of this would depend on the relationship between these chiral states and the flavour-basis neutrino ν_α. However, in practice our Lagrangian is fully general, as the polarization effects in the neutrino beam ensure that only the left-handed charge is relevant for light-neutrino scattering experiments.

The Lagrangian in Eq. (4.1.1) contains all of the terms necessary for this analysis. However, when it comes to assigning specific charges to the particles, a few wider model-building considerations are worthy of discussion. In the SM, any non-vectorial symmetry would forbid the Yukawas responsible for the charged-lepton mass terms post-ESWB; similarly, possible negative implications for neutrino mass generation are expected. The precise implementation of the neutrino mass mechanism is highly model dependent, but neutrino gauge charges are not compatible with many usual realizations[1]. Furthermore, the novel gauge boson Z' will also require a mass generation mechanism, and indeed this could be achieved via the means of symmetry breaking. Although each of these is an important aspect of model building, their resolution can be expected to have little impact on the

[1] If neutrino masses are thought of as coming from a Weinberg operator, it is clear that the leptonic doublet must be uncharged under any unbroken $\mathrm{U}(1)'$ group.

phenomenology of neutrino scattering, and we will not pursue them here. Anomaly freedom of our new symmetry, however, is a more pertinent concern. It has been shown that an anomalous group can always be made anomaly free via the introduction of exotically charged sets of fermions which can be given arbitrarily large masses [165]. Yet these novel fermionic states necessarily introduce effects at low-scales, which in some cases can strongly affect the phenomenology of the model [166]. Therefore, while it seems likely that mass generation can be addressed with the addition of new particles which do not interfere with neutrino scattering phenomenology, anomaly freedom is more pernicious. For this reason we will briefly discuss how anomaly freedom will dictate the types of leptonic symmetries that we consider in the remainder of this work.

Anomaly freedom. The most general anomaly-free symmetries compatible with the SM were first deduced in the context of Grand Unification Theories (GUT) [167,168]. More recently, an atlas of all anomaly-free $U(1)$ extensions of the SM with flavour-dependent charges has been provided by Ref. [169]. Interestingly, the only anomaly-free subgroups of the SM with renormalisable Yukawa sector are leptophilic: the lepton-family number differences $L_\alpha - L_\beta$ $(\alpha, \beta = e, \mu, \tau)$ [156, 157]. The popular $B - L$ symmetry is in fact anomalous unless right-handed SM singlets are added with the appropriate charges. This is well motivated by the necessity of neutrino mass generation but remains a hypothesis, as not all models of neutrino mass require novel fermionic content. For the sake of discussion, we follow a similar logic and consider the most general anomaly free subgroups of the SM accidental leptonic symmetries allowing for an arbitrary number of right-handed fermionic singlets. These would presumably be associated with the neutrino mass generation mechanism, but we impose no specific relations in this regard due to the significant model-building freedom. The anomaly conditions for a leptophilic model with right-handed neutrinos are given below [170] [2]

$$\mathrm{SU}(2)_{\mathrm{W}}^2 \times \mathrm{U}(1)_{\mathrm{Z}'} \quad \sum_\alpha Q_\alpha^{\mathrm{L}} = 0, \tag{4.1.3a}$$

$$\mathrm{U}(1)_{\mathrm{Y}}^2 \times \mathrm{U}(1)_{\mathrm{Z}'} \quad \sum_\alpha \left[\frac{1}{2} Q_\alpha^{\mathrm{L}} - Q_\alpha^{\mathrm{R}}\right] = 0, \tag{4.1.3b}$$

$$\mathrm{U}(1)_{\mathrm{Y}} \times \mathrm{U}(1)_{\mathrm{Z}'}^2 \quad \sum_\alpha \left[(Q_\alpha^{\mathrm{L}})^2 - (Q_\alpha^{\mathrm{R}})^2\right] = 0, \tag{4.1.3c}$$

[2] Notice that $\mathrm{U}(1)_{\mathrm{Z}'}^3$ together with gauge-gravity conditions imply that the number of right-handed states must be at least $N = 3$.

$$\mathrm{U(1)}^3_{\mathrm{Z}'} \quad \sum_\alpha \left[2(Q^{\mathrm{L}}_\alpha)^3 - (Q^{\mathrm{R}}_\alpha)^3\right] - \sum_{\mathrm{N}} Q^3_{\mathrm{N}} = 0, \tag{4.1.3d}$$

$$\text{Gauge-Gravity} \quad \sum_\alpha \left[2Q^{\mathrm{L}}_\alpha - Q^{\mathrm{R}}_\alpha\right] - \sum_{\mathrm{N}} Q_{\mathrm{N}} = 0. \tag{4.1.3e}$$

In the absence of new N_R particles ($Q_{\mathrm{N}} = 0$) and assuming that $Q^{\mathrm{L}}_\alpha = Q^{\mathrm{R}}_\alpha$, that is considering vector couplings, we find the three well-known discrete solutions for the Eqs. (4.1.3): the antisymmetric pairs $L_\alpha - L_\beta$, $\alpha, \beta = \{e, \mu, \tau\}$, $\alpha \neq \beta$. As far as anomalies are concerned, all three pairs are equal, but frequently focus falls on $L_\mu - L_\tau$, which has no coupling to electrons and correspondingly weaker constraints. If we reconsider these conditions with charged right-handed neutrinos, we find a one dimensional continuous family of potential symmetries which can be consistently gauged. We can parametrise this as

$$\varrho(L_\alpha - L_\beta) + \vartheta(L_\beta - L_\lambda), \quad \text{with} \quad 3\varrho\,\vartheta(\vartheta - \varrho) = \sum_{\mathrm{N}} Q^3_{\mathrm{N}}. \tag{4.1.4}$$

What we have shown is that linear combinations of the $(L_\alpha - L_\beta)$ choice of charges yield an anomaly free scenario provided N right-handed neutrinos respecting Eq. (4.1.4) are added to the theory. We have checked that the "anomaly-free atlas" in [171] contains a subset of these solutions, which are more general.

The above conclusions are based on the assumption of vectorial charge assignments. In the SM, this requirement is a consequence of the origin of mass assuming a chargeless Higgs. However, in non-minimal models this requirement could be relaxed. Even with this extra freedom, not all charge assignments are allowed: for example, a purely chiral $U(1)'$ cannot satisfy Eq. (4.1.3c) without additional matter charged under the SM gauge group. The axial-vector case, however, does have further solutions: we find that the same one-dimensional family of charges is allowed as for the vectorial gauge boson — in this case, the charges apply to the left-handed fields and the right-handed ones have the opposite charges. In such a model the leptonic mass generation mechanism would necessarily be more complicated than in the SM, but such a possibility is not excluded. UV completions of an axial-vector Z' have been presented in [172, 173], however, these generally introduce extra bounds that are expected to be stronger than neutrino scattering bounds (see *e.g.* [166, 174]). For this reason, we only comment on the consequences of an axial-vector case in our calculations, but do not develop any particular model or constraint.

Kinetic mixing. The symmetries of our SM extensions allow for kinetic mixing between the Z' and the SM gauge bosons [175–177]

$$\mathscr{L}_{\text{mix}} = -\frac{\varepsilon}{2} F_{\kappa\rho} F'^{\kappa\rho}, \tag{4.1.5}$$

where $F_{\kappa\rho}$ and $F'^{\kappa\rho}$ are the field strength tensors of the hypercharge and the Z' boson, respectively. The presence of such coupling introduces a very rich phenomenology and has been explored in great detail in the literature [49]. In this work, we choose to focus on the less constrained possibility of vanishing tree-level kinetic mixing. In this case, kinetic mixing is still radiatively generated due to the presence of particles charged under both the SM and the new $U(1)$ group. As well as the SM particle content, additional particles present in the UV theory may also contribute to kinetic mixing, but we will neglect these contributions in this study as they are highly model dependent [3]. We compute ε between the Z' and the SM *photon*, and find the one-loop result to be finite for any $\varrho(L_\alpha - L_\beta) + \vartheta(L_\beta - L_\lambda)$ gauge group, with divergences cancelling between families. In particular, for the $L_\mu - L_\tau$ model our result is in agreement with Refs. [163, 178]

$$\varepsilon(q^2) = \frac{eg'}{2\pi^2} \int_0^1 \mathrm{d}x\, x(1-x) \ln \frac{m_\mu^2 - x(1-x)q^2}{m_\tau^2 - x(1-x)q^2} \xrightarrow{q^2 \to 0} \frac{eg'}{12\pi^2} \ln \frac{m_\mu^2}{m_\tau^2}. \tag{4.1.6}$$

Note that the finiteness of the one-loop result has important consequences for the leptophilic theories we consider. As pointed out in Ref. [158], the finiteness of ε implies that one is able to forbid tree-level kinetic mixing, albeit in a model dependent manner. This happens, for instance, when embedding the new leptophilic $U(1)$ group in a larger non-abelian group G, which is completely independent from the SM sector. This choice of one-loop generated kinetic mixing should be seen as a conservative choice; in the absence of cancellation between tree and loop-level kinetic mixing, this yields the least constrained scenario for an $L_\mu - L_\tau$ model. Additional constraints from first-family leptons are now relevant [176, 179], especially $\nu - e$ scattering measurements, where the strength of the constraint makes up for the loop suppression in the coupling. For neutrino trident scattering, one can safely ignore loop-induced kinetic mixing contributions in the calculation since these are either smaller than the tree-level new physics contribution or yield very weak bounds compared to other processes.

[3] The authors of Ref. [178] have calculated the contribution to kinetic mixing in the $L_\mu - L_\tau$ model from a pair of scalars with opposite charges. These are typically subdominant, provided the mass hierarchy between the two scalars is not much larger than that of the charged leptons.

We emphasize that if accompanied by a consistent mechanism for the generation of the Z' mass terms and leptonic Yukawa terms, the models we consider constitute a UV complete extension of the SM. The treatment of such scenarios lies beyond the scope of this work, but we note that if their scalar sectors are light enough they can also yield rich phenomenology at low scales [180].

4.2 Signatures of Leptonic Neutral Currents

When a neutrino impinges on a detector it has only two options for BSM scattering via a leptophilic mediator. In the simplest scenario, the neutrino interacts via the new mediator with the electrons of the detection medium. In this case, there is a tree-level $\nu - e$ scattering process which would be expected to show the clearest signs of new physics. For scattering off a hadron, however, the leptophilic nature of the mediator means that the first tree-level contribution will necessarily come from a diagram which also includes at least one additional SM mediator. Any neutrino-hadron scattering process can be embellished with the new boson to create a BSM signature. In general, the final states of these processes will be either identical to the original un-embellished process (perhaps with missing energy) or it will have an extra pair of leptons in the final state. These neutrino trilepton production processes, which we will refer to as tridents for simplicity, can be subdivided into four types:

- $\ell\ell\ell$ trident: $\mathcal{H} + \nu_\alpha \to \mathcal{H}' + \ell_\alpha^- + \ell_\beta^+ + \ell_\beta^-$
- $\nu\ell\ell$ trident: $\mathcal{H} + \nu_\alpha \to \mathcal{H} + \nu_\beta + \ell_\gamma^+ + \ell_\delta^-$
- $\nu\nu\ell$ trident: $\mathcal{H} + \nu_\alpha \to \mathcal{H}' + \ell_\alpha^- + \nu_\beta + \overline{\nu}_\beta$
- $\nu\nu\nu$ trident: $\mathcal{H} + \nu_\alpha \to \mathcal{H} + \nu_\alpha + \nu_\beta + \overline{\nu}_\beta$

We note that these processes all occur in the SM, and so the hunt for new physics will necessarily be competing against a background of genuine SM events. Moreover, for final states with missing energy in the form of neutrinos, isolating a BSM signal would necessarily rely on spectral measurements and other backgrounds have the potential to be large. In particular, the trident production of $\nu\nu\nu$ and $\nu\nu\ell$ will be seen as contributions to the neutral-current (NC) elastic and charged-current quasi-elastic (CCQE) processes,

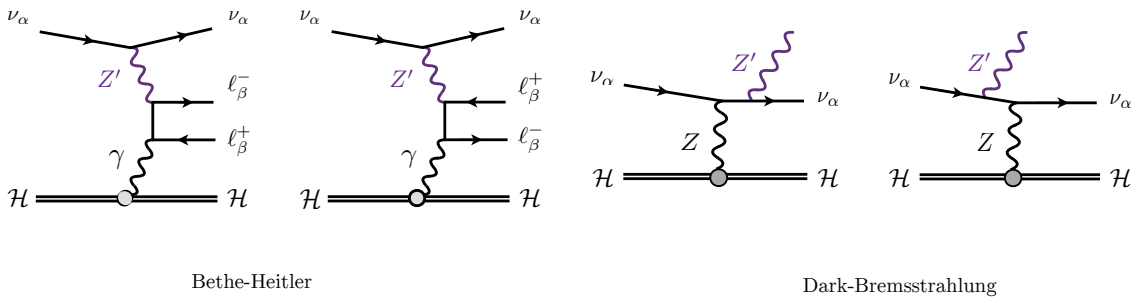

Fig. 4.1. The BSM contributions to neutrino trident production considered in our calculation. The diagrams on the left are referred to as Bether-Heitler contributions due to their resemblance to pair-production. On the right, we show diagrams with a radiative-like Z' emission, which allows for the production of on-shell Z' particles, which subsequently decays into a charged-lepton pair.

and we expect backgrounds to be insurmountable (see *e.g.* Ref. [181] for new physics contributions to CCQE processes). The $\ell\ell\ell$ channels, on the other hand, are expected to have a much more manageable SM background. Trimuon production, for instance, has been measured in the past and provides a multitude of kinematical observables in the final state [182, 183]. The SM rate for this channel contains radiative photon diagrams as well as hadronic contributions [184–186], whilst for leptophilic neutral bosons, the dominant contributions comes from a weak process with initial and final state radiation of a Z', making it a less sensitive probe of light new physics. Finally, the $\nu\ell\ell$ production, the most discussed trident signature in the literature, has already been observed in the dimuon channel [107, 108, 187]. This channel is by far the most important trident process for our study, as the leptonic subdiagrams contain only weak vertices in the SM.

4.2.1 Neutrino Trident Scattering

In the $\nu\ell\ell$ neutrino trident scattering, an initial neutrino scatters off a hadronic target producing a pair of charged leptons in the process. Since we focus solely on neutral current processes and on flavour conserving new physics, no mixed flavour tridents are relevant and we can write

$$\mathcal{H}(P) + \nu_\alpha(p_1) \to \mathcal{H}(P') + \nu_\alpha(p_2) + \ell_\beta^-(p_3) + \ell_\beta^+(p_4).$$

In the SM this process receives CC and NC contributions when $\alpha = \beta$, and is a purely NC process if $\alpha \neq \beta$. The BSM contributions to trident production we consider are shown in

Fig. 4.1. Beyond computing the Bethe-Heitler (BH) contributions considered previously, we show that radiative contributions to these processes are generally small. Using the Narrow-Width-Approximation (NWA), we compute the cross section for the radiation of a Z' particle from a neutrino-nucleus interaction, which can then promptly decay to an $\ell^+\ell^-$ pair. We call these contributions Dark-Bremsstrahlung (DB) processes for their similarity with electron brehmsstrahlung in QED. We now discuss the two amplitudes individually.

Bethe-Heitler. The BH amplitude can be written as follows

$$\mathcal{M}_{\rm BH} = \frac{\mathrm{L}_\mu \, \mathrm{H}^\mu_{\rm EM}}{Q^2}\,, \tag{4.2.1}$$

where $Q^2 \equiv -q^2 = (P - P')^2$ is the momentum transfer and $\mathrm{H}^\mu_{\rm EM}$ the hadronic amplitude for coherent or diffractive electromagnetic scattering

$$\mathrm{H}^\mu_{\rm EM} \equiv \langle \mathcal{H}(P)|J^\nu_{\rm EM}(q^2)|\mathcal{H}(P')\rangle\,. \tag{4.2.2}$$

For the details on the treatment of the hadronic amplitude, see the previous chapter. The leptonic amplitude for NC scattering L_μ reads

$$\begin{aligned}\mathrm{L}_\mu \equiv -\frac{ieG_F}{\sqrt{2}}[\bar{u}(p_2)\gamma^\tau(1-\gamma_5)u(p_1)]\bar{u}(p_4)\Bigg[&\gamma_\tau(\hat{V}_{\alpha\beta} - \hat{A}_{\alpha\beta}\gamma_5)\frac{1}{(\not{q} - \not{p}_3 - m_3)}\gamma_\mu \\ &+ \gamma_\mu\frac{1}{(\not{p}_4 - \not{q} - m_4)}\gamma_\tau(\hat{V}_{\alpha\beta} - \hat{A}_{\alpha\beta}\gamma_5)\Bigg]v(p_3)\,.\end{aligned} \tag{4.2.3}$$

In writing the equation above, we have introduced effective vector and axial couplings containing SM and BSM contributions

$$\hat{V}_{\alpha\beta} = g_V^{\ell_\beta} + \delta_{\alpha\beta} + \frac{Q^L_\alpha Q^V_\beta}{2\sqrt{2}G_F}\frac{(g')^2}{K^2 + M^2_{Z'}}, \quad \hat{A}_{\alpha\beta} = g_A^{\ell_\beta} + \delta_{\alpha\beta} + \frac{Q^L_\alpha Q^A_\beta}{2\sqrt{2}G_F}\frac{(g')^2}{K^2 + M^2_{Z'}}\,, \tag{4.2.4}$$

where $K^2 = -(p_1 - p_2)^2$ and $g_V^{\ell_\beta}$'s ($g_A^{\ell_\beta}$'s) are the SM vector (axial) couplings. Note the dependence on the positive kinematic variable K^2 in the BSM contribution, which can lead to a significant peaked behaviour in the cross section. To avoid numerical difficulties, we have modified the phase space treatment proposed in [188, 189], as shown in Appendix A.

Dark-Bremsstrahlung. Due to the small decay width of the Z' ($\Gamma \propto g'^2 M_{Z'}$), one can obtain an estimate for its resonant production using the NWA. In the true narrow-width limit, this process reduces to a 3-body phase space calculation and does not interfere with

the BH amplitude [4]. Our DB amplitude for $\nu_\alpha(k_a) + \mathrm{A}(k_b) \to \nu_\alpha(k_1) + Z'(k_2) + \mathrm{A}(k_3)$ reads

$$\mathcal{M}_{\mathrm{DB}} = g' Q_\alpha^L \frac{G_F}{\sqrt{2}} J_\mu \mathrm{H}_{\mathrm{W}}^\mu, \tag{4.2.5}$$

where $\mathrm{H}_{\mathrm{W}}^\mu$ is the weak hadronic current (see Appendix B) and

$$J_\mu = \overline{u}(k_1) \left[\gamma^\alpha \frac{\not{k}_1 + \not{k}_2}{(k_1+k_2)^2} \gamma_\mu + \gamma_\mu \frac{\not{k}_a - \not{k}_2}{(k_a-k_2)^2} \gamma^\alpha \right] (1-\gamma^5) u(k_2)\, \epsilon_\alpha^*(k_2), \tag{4.2.6}$$

where $\epsilon_\alpha^*(k_2)$ is the polarization vector of the Z'. The previous amplitude can then be squared and integrated over phase-space for the total DB cross section. The different charged lepton final states can then be imposed with their respective branching ratios (BR). As a final remark, we note that the typical decay lengths of the new boson are typically below 1 cm for the parameter space of interest, such that their decay is indeed prompt.

From the previous discussions it is clear that the contributions to the total cross section at the lowest order in g' come from the interference between the BSM and the SM BH diagrams, and from the DB. The latter, however, contains an extra power of G_{F} and is expected to be subdominant with respect to the BH interference. Our results for the individual flux integrated cross sections are shown in Fig. 4.2 for the $\mu^+\mu^-$ and in Fig. 4.3 for the e^+e^- trident channels. We show the BH contributions as well as the DB one normalized by the SM trident cross section. All cross sections are flux integrated using the 62.4 GeV p^+ DUNE flux described in Section 4.3.1. For generality, we do not include the BR factors in the DB contributions, and so the green lines only apply for $\mu^+\mu^-$ tridents if $M_{Z'} > 2m_\mu$ and would suffer additional suppression due to the BR. In each figure we show two panels, one for vector couplings and one for axial-vector couplings. This is interesting from a purely computational point of view, as it shows explicitly the BH cross section scaling with the $M_{Z'}$ in the two cases. Whilst the scaling is similar for dielectron tridents, it differs significantly between the vector and axial-vector cases of the dimuon cross section. This suggests the presence of mass suppression effects in the BH process. We do not investigate this further, but note that there are large cancellations between the two BH diagrams in Fig. 4.1 which are only present for vector-like couplings.

[4] We note that despite the fact that interference terms between resonant and non-resonant contributions vanish in the narrow-width limit, the errors induced by the NWA can no longer be shown to be of the order of $\Gamma_{Z'}/M_{Z'}$ [190]. Nevertheless, we do not expect a more careful evaluation of the resonant contribution to change our conclusions.

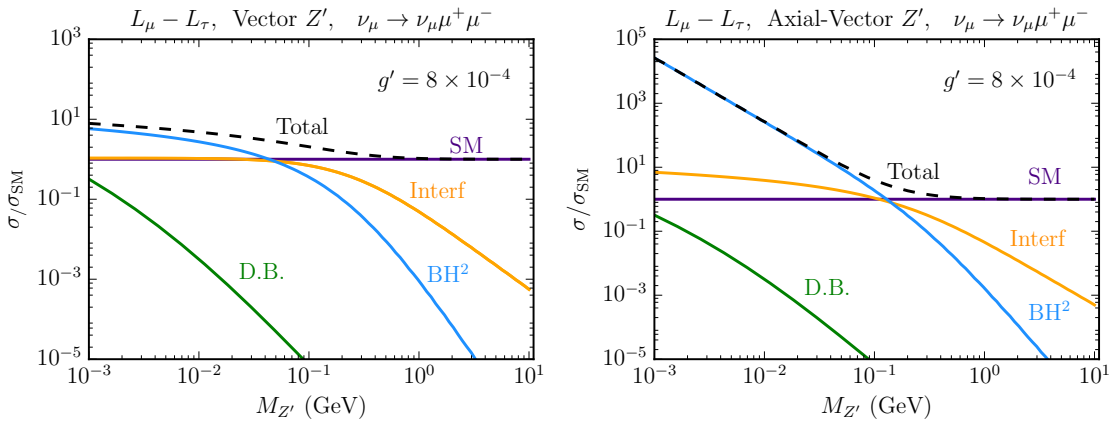

Fig. 4.2. Flux integrated cross sections normalized to the flux integrated SM trident cross section for dimuon production. On the left (right) panel we show the vector (axial-vector) Z' case. We separate the different contributions: SM only, interference between SM and BSM Bethe-Heitler contributions (interf) and BSM Bethe-Heither only (BH^2). The Dark-Bremsstrahlung (DB) cross section is also shown, but does not take the branching ratio into final state charged leptons into account.

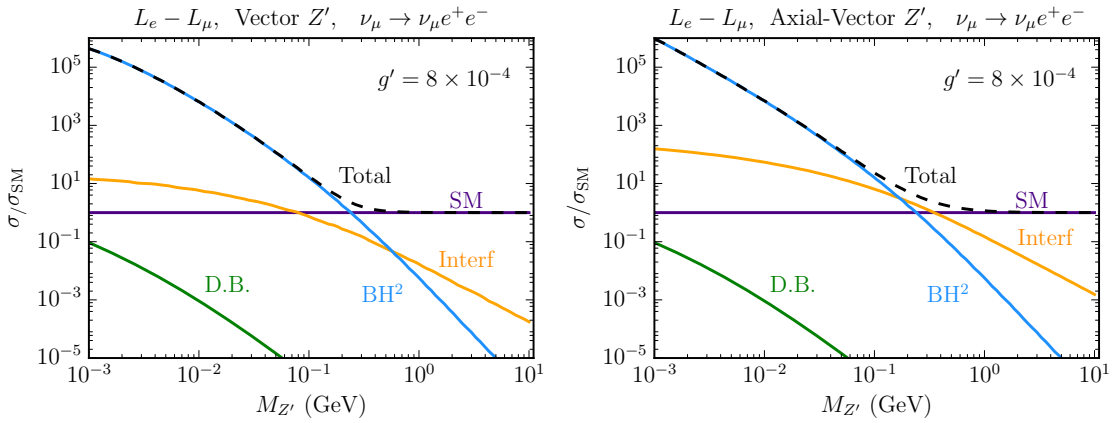

Fig. 4.3. Same as Fig. 4.2 but for the e^+e^- trident channel.

Finally, a cautionary remark on the axial-vector case. Despite the large enhancement present in the axial-vector case, we note that this is likely an artifact of our simplified model approach. In an UV-completion, additional particles might contribute to the process, and these quadratic enhancements as a function of $1/M_{Z'}^2$ are expected to be regulated at some model dependent scale. It is beyond the scope of this work to build such a model, and so for the sake of simplicity and concreteness, we only perform sensitivity studies for the vector model, where these enhancements are less problematic.

The Equivalent Photon Approximation

We now comment on the EPA for neutrino trident production. This approximation is known to perform quite badly for the SM neutrino trident production cross section. One may wonder, however, if the EPA gets better or worse when computing our BSM cross sections. Naturally, it would be most inadequate for the resonant-like cross sections, since the photon propagator and the strong $1/Q^4$ behaviour is absent. However, if one focuses on the BH contributions, a marginal improvement of the accuracy of the approximation is seen as one lowers the mass of the Z' mediator. In the SM, the $\nu - \gamma$ cross sections scale as a typical weak cross section, $\sigma_{\nu\gamma} \propto G_{\rm F}^2 \hat{s}$, where $\hat{s}$ is the square of the center of mass energy of the $\nu - \gamma$ system. On the other hand, if the cross section is dominated by the BSM BH contributions, then as we take the limit of small Z' masses, it scales more similarly to a QED cross section, $\sigma_{\nu\gamma} \propto 1/\hat{s}$. This behaviour, however, is only present at low masses and only for the BSM contribution. Since we are interested in regions of the parameter space where BSM and SM cross sections are of similar size, then we expect the total cross section to have a behaviour which is a combination of the two. As a sanity check, we numerically verified that for parameter space points where the BSM contributions are of the same order as the SM cross section, the improvement in the accuracy of the EPA is still not satisfactory. For instance, the ratio between the EPA prediction and the full calculation for the dimuon channel assuming a $Q_{\rm max} = (140\ {\rm MeV})/A^{1/3}$ goes from $\approx 30\%$ in the SM to $\approx 60\%$ for $g' = 8 \times 10^{-4}$ and $M_{Z'} = 5$ MeV. For this reason, we only use the full $2 \to 4$ calculation in what follows.

Trident Kinematical Distributions

The impact of new physics on the total cross section for trident production has been explored in the previous section. It is then natural to ask what the impact of new physics is on the kinematics of trident production which are, especially in the case of the invariant mass and angular variables, of utmost importance for background reduction. In this section we show how the new physics can alter the distributions of these important variables. All results that follow have been obtained using trident events produced by our dedicated Monte Carlo (MC). Smearing and selection cuts have been applied as detailed in Sec. 4.3.

The variables of interest in background reduction are the charged lepton invariant mass

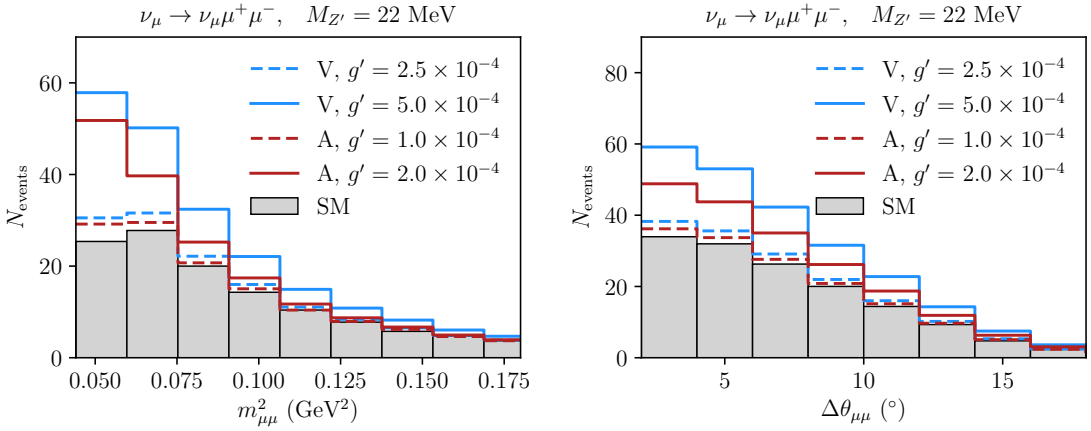

Fig. 4.4. Distribution of the number of neutrino trident events as a function of the invariant mass of the dimuon pair (left) and their separation angle (right) at the DUNE ND. The distributions were produced using the DUNE 120 GeV p^+ neutrino beam and have been smeared as described in Section 4.3.1. For the new physics, we plot the case of a vector (V), $Q^L = Q^R$, and axial-vector (A), $Q^L = -Q^R$, Z' assuming Q^L_α to be given by $L_\mu - L_\tau$.

$m^2_{\ell\ell} = (p_3 + p_4)^2$ and their separation angle $\Delta\theta_{\ell\ell}$. The invariant mass can be experimentally inferred from the energy of each charged-lepton and their separation angle, and so heavily relies on the experimental resolution to such parameters. In Fig. 4.4 we show the dimuon invariant mass spectrum between $4m^2_\mu$ and 0.2 GeV^2, and the dimuon separation angle between 2° and 18° for a light vector boson with $M_{Z'} = 22$ MeV. We show the results for the dielectron channel in Fig. 4.5. The light new physics here enhances these distributions at low values of these parameters. We show our results for two types of mediators, vector and axial-vector leptophilic bosons. Comparing the couplings necessary to produce similar BSM enhancements of the number of events, we see that axial-vector bosons lead to larger enhancements with smaller couplings. In particular, it leads to greater spectral distortions for the Z' mass shown.

4.2.2 Neutrino-Electron Scattering

Neutrino-electron scattering has long been a valuable probe of both the SM and potential new physics [162, 191–193]. It is important to note that in the presence of novel leptophilic currents, experiments searching for e^+e^- tridents would also observe anomalous $\nu - e$ event rates. In fact, given the larger statistics present in the $\nu - e$ scattering sample, this channel is expected to provide the leading constraints in our scenarios with tree-level couplings to electrons.

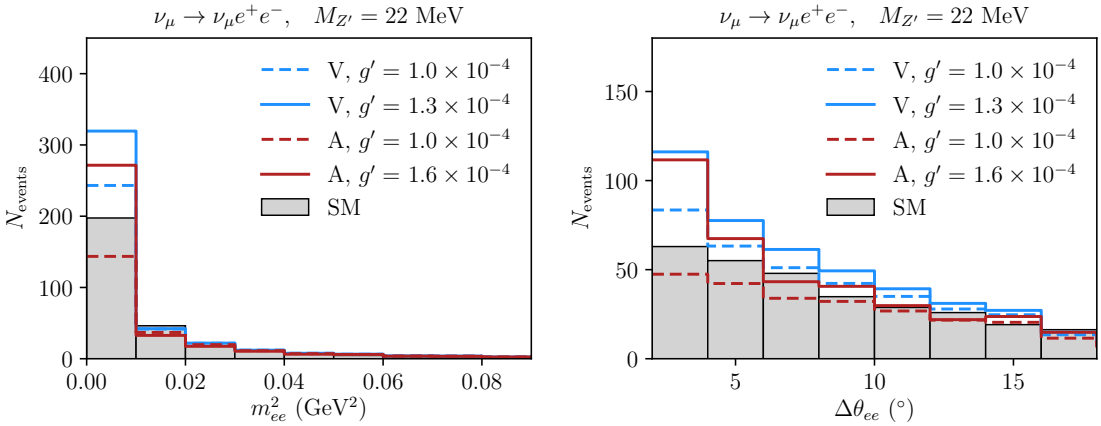

Fig. 4.5. Same as Fig. 4.4 but for e^+e^- trident events. In all cases we assume Q^L_α to be given by $L_e - L_\mu$.

In order to compute the $\nu - e$ cross section in the presence of the new leptophilic interactions we need to consider an analogous modification of the NC scattering amplitude

$$\mathcal{M}_{\nu_\alpha - \mathrm{e}} = -\frac{G_F}{\sqrt{2}} \left[\bar{u}(k_2)\gamma^\mu(1-\gamma_5)u(k_1)\right] \left[\bar{u}(p_2)\gamma_\mu(C^{\mathrm{V}}_\alpha - C^{\mathrm{A}}_\alpha\gamma_5)u(p_1)\right], \tag{4.2.7}$$

where the vector (C_V) and axial (C_A) effective couplings include both the SM and BSM contributions

$$C^{\mathrm{V}}_\alpha = -\frac{1}{2} + 2s^2_{\mathrm{W}} + \delta_{\alpha e} + \frac{Q^{\mathrm{V}}_e Q^{\mathrm{L}}_\alpha}{2\sqrt{2}G_F} \frac{(g')^2}{M^2_{Z'} + 2m_e T_e}, \tag{4.2.8a}$$

$$C^{\mathrm{A}}_\alpha = -\frac{1}{2} + \delta_{\alpha e} + \frac{Q^{\mathrm{A}}_e Q^{\mathrm{L}}_\alpha}{2\sqrt{2}G_F} \frac{(g')^2}{M^2_{Z'} + 2m_e T_e}, \tag{4.2.8b}$$

with, as usual, $s_{\mathrm{W}} \equiv \sin\theta_{\mathrm{W}}$, being θ_{W} the weak angle and T_e is the kinetic energy of the recoil electron. The loop-induced kinetic mixing in the $L_\mu - L_\tau$ model also induces a $\nu - e$ coupling

$$C^{\mathrm{V}}_\alpha = -\frac{1}{2} + 2s^2_{\mathrm{W}} + \delta_{\alpha e} + \frac{1}{\sqrt{2}G_F} \frac{g'\, e\, \varepsilon(q^2)}{M^2_{Z'} + 2m_e T_e}. \tag{4.2.9}$$

The differential cross section is then given by

$$\frac{d\sigma_{\nu_\alpha - e}}{dT_e} = \frac{2m_e G_F^2}{\pi} \left[\left(C^{\mathrm{L}}_\alpha\right)^2 + \left(C^{\mathrm{R}}_\alpha\right)^2 \left(1 - \frac{T_e}{E_\nu}\right)^2 - C^{\mathrm{L}}_\alpha C^{\mathrm{R}}_\alpha\, m_e \frac{T_e}{E^2_\nu} \right]. \tag{4.2.10}$$

where the left and right handed constants are given by

$$C^{\mathrm{L}}_\alpha \equiv \frac{1}{2}\left(C^{\mathrm{V}}_\alpha + C^{\mathrm{A}}_\alpha\right) \qquad \text{and} \qquad C^{\mathrm{R}}_\alpha \equiv \frac{1}{2}\left(C^{\mathrm{V}}_\alpha - C^{\mathrm{A}}_\alpha\right).$$

For antineutrino scattering one obtains the cross section by exchanging $C^{\mathrm{L}}_\alpha \leftrightarrow C^{\mathrm{R}}_\alpha$.

The kinetic energy of the outgoing electron is bounded by kinematics and the energy

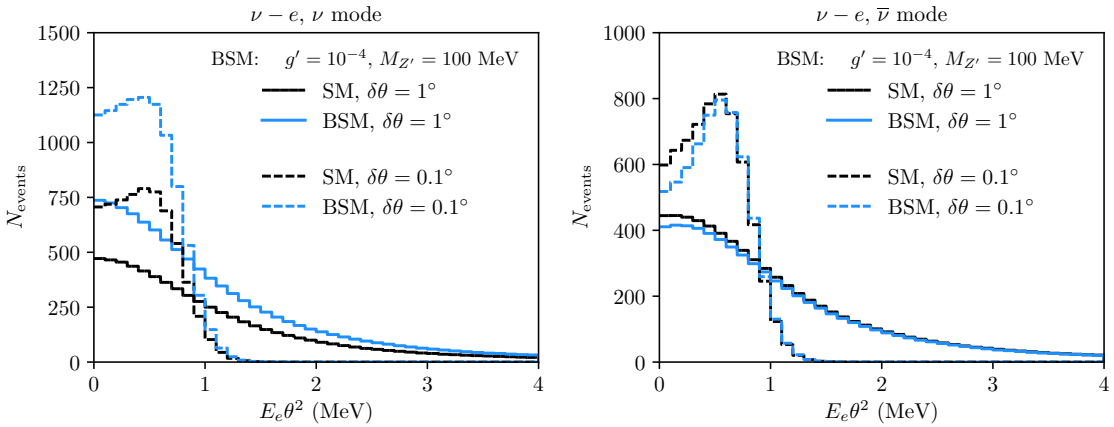

Fig. 4.6. Number of $\nu - e$ scattering events in the DUNE ND as a function of $E_e\theta^2$ for the neutrino (left) and antineutrino (right) beams from the 120 GeV p^+ configuration. We show the prediction in the SM and in a vector $L_e - L_\mu$ Z' model for two angular resolutions $\delta\theta$. The electron kinetic energy threshold is taken to be 600 MeV and the energy resolution is fixed at $\sigma/E = 15\%/\sqrt{E}$.

resolution of the detector, which effectively sets a threshold energy T_{th} such that

$$T_{\text{th}} \leq T_e \leq T_{\text{max}}, \tag{4.2.11}$$

with $T_{\text{max}} = 2E_\nu^2/m_e + 2E_\nu$, the maximum kinetic energy attainable. We define the effective total cross section for an initial neutrino energy E_ν as

$$\sigma_{\text{eff}}(E_\nu, T_{\text{th}}) = \int_{T_{\text{th}}}^{T_{\text{max}}} \frac{d\sigma}{dT_e}\, dT_e. \tag{4.2.12}$$

This definition also ensures that the enhancement due to very light mediators becomes constant at around $\sqrt{2m_eT_{\text{th}}}$, as discussed in Ref. [162]. This is a consequence of the detector threshold and of the 2-body kinematics of the process. Finally, electroweak radiative corrections have been computed in the SM [194, 195], but will not be included here. Since they correspond to a change of a few percent we do not expect them to affect very much our results.

Neutrino-Electron Scattering Kinematical Distributions

The angle between the scattered electron and the neutrino beam direction, θ, is related to the electron energy as

$$1 - \cos\theta = m_e \frac{1-y}{E_e},$$

where $y \equiv T_e/E_\nu$ is the inelasticity ($T_{\rm th}/E_\nu < y < 1$) and $E_e = T_e + m_e$ is the outgoing electron energy. This implies that at $\mathcal{O}(\text{GeV})$ neutrino energies, the electron recoil is very forward and obey $E_e\theta^2 < 2m_e$, up to detector resolution. For this reason, we choose to analyse our results in terms of $E_e\theta^2$. In this case, the differential cross section becomes

$$\frac{d\sigma_{\nu_\alpha - e}}{d(E_e\theta^2)} = \frac{E_\nu}{2m_e}\frac{d\sigma_{\nu_\alpha - e}}{dT_e}\bigg|_{T_e = E_\nu(1-\frac{E_e\theta^2}{2m_e})} . \tag{4.2.13}$$

This distribution is particularly important for suppressing the background. Given the kinematics explained above, $E_e\theta^2$ must be smaller than $2m_e$ for $\nu - e$ scattering, while it is often much larger for neutrino-nucleon scattering, the dominant background (See Section 4.3.1). We show in Fig. 4.6 the expected $\nu - e$ event distribution as a function of $E_e\theta^2$ for the SM and a light Z' case, in the neutrino and anti-neutrino modes at the DUNE ND. As expected, the signal is extremely forward and the final distribution is highly sensitive to the angular resolution $\delta\theta$ of the detector. At a conservative value of $\delta\theta = 1^\circ$, little information about the true distribution is left, and a significant portion of the signal lies in a region where $E_e\theta^2 > 2m_e$. Therefore, shape information may improve the search for a light new physics only when the angular and energy resolutions of the detector are well understood.

4.2.3 Interference Effects

Since for $\nu - e$ scattering and neutrino trident production there exists a SM contribution, we expect the experimental sensitivity to new physics to be dominated by the interference between SM and BSM contributions. We now argue what kind of interference one can expect in each one of these processes.

For neutrino trident production we follow Ref. [196] and separate the differential cross section as

$$d\sigma = \hat{V}^2\, d\sigma_{\rm V} + \hat{V}\hat{A}\, d\sigma_{\rm V-A} + \hat{A}^2\, d\sigma_{\rm A}, \tag{4.2.14}$$

where we dropped the flavour indices in $\hat{V}$ and $\hat{A}$ from (4.2.4) for simplicity. This allows us to write the interference between the SM and the vector new physics as

$$d\sigma_{\rm INT} = \frac{Q^L_\alpha Q^V_\beta}{2\sqrt{2}G_F}\frac{(g')^2}{K^2 + M^2_{Z'}}\left(2\, C^{\rm SM}_{\rm V}\, d\sigma_{\rm V} + C^{\rm SM}_{\rm A}\, d\sigma_{\rm V-A}\right). \tag{4.2.15}$$

Depending on the region of phase space considered, the term proportional to $d\sigma_{\rm V-A}$ can

be of similar size to $d\sigma_{\rm V}$. However, $d\sigma_{\rm V-A}$ changes sign as a function of the angular variables or energies, leading to small integrated cross sections (typically two orders of magnitude smaller than the integral of the $d\sigma_{\rm V}$ term). Ignoring this term, one can then completely predict the type of interference in trident production. For $\nu_\mu \to \nu_\mu \mu^+ \mu^-$ trident production, for instance, $C_{\rm V}^{\rm SM} > 0$ and the second generation charge appears squared, leading to constructive interference in all cases. For $\nu_\mu \to \nu_\mu e^+ e^-$ trident events, on the other hand, $C_{\rm V}^{\rm SM} < 0$. If the first and second generation charges come in with opposite signs, then the interference is still constructive, otherwise destructive interference happens. The same considerations also apply to antineutrino scattering if one ignores the $d\sigma_{\rm V-A}$ term. Finally, the axial-vector case is completely analogous taking $V \leftrightarrow A$ in Eq. (4.2.15).

For $\nu - e$ scattering analytical expressions can easily be used [162]. Taking $C_L^{\rm SM} = -1/2 + s_{\rm W}^2 \sim -1/4$ and $C_L^{\rm SM} = s_{\rm W}^2 \sim 1/4$ we have

$$\frac{d\sigma_{{\rm INT}\,\nu_\mu - e}}{dT_e} \sim -\frac{\sqrt{2} m_e G_F}{4\pi} \frac{g'^2}{m_{Z'}^2 + 2 m_e T_e} \left(-1 + (1-y)^2\right) \tag{4.2.16a}$$

$$\frac{d\sigma_{{\rm INT}\,\bar{\nu}_\mu - e}}{dT_e} \sim -\frac{\sqrt{2} m_e G_F}{4\pi} \frac{g'^2}{m_{Z'}^2 + 2 m_e T_e} \left(1 - (1-y)^2\right). \tag{4.2.16b}$$

Since $y < 1$, the interference term for $\nu_\mu - e$ is always positive (constructive), and for $\bar{\nu}_\mu - e$ it is always negative (destructive).

4.3 DUNE Sensitivities

Having studied the behaviour of neutrino trident production and neutrino-electron scattering cross sections in the presence of light new bosons, we now apply our results in sensitivity studies for the DUNE ND. As discussed in Section 4.1, we limit our studies to $L_e - L_\mu$ and $L_\mu - L_\tau$ models with vector gauge bosons. We start with a discussion on the experimental details, highlighting the challenges of backgrounds and laying out our statistical methods in Section 4.3.1. Then we show our main results in Sections 4.3.2 and 4.3.3, comparing our sensitivity curves to the leading bounds in the parameter space of the leptophilic models from other experiments.

4.3.1 Analysis Techniques

The LBNF is expected to produce an intense beam of neutrinos and antineutrinos from a 1.2 MW proton beam colliding against a fixed target [197]. The DUNE ND, where the number of neutrino interactions is the largest, is expected to be located at a distance of 574 m from the target. Despite its design not being final yet [198, 199], we focus on the possibility of a 75-t fiducial mass Liquid Argon (LAr) detector. Regarding the neutrino fluxes, we now concentrate on the option of a beam from 120 GeV protons with 1.1×10^{21} POT per year. The LBNF could also provide higher or lower energy neutrinos depending on the proton energy, target and focusing system used. We explore other possibilities shown in Table 4.1 and we take the flux files provided in Ref. [200, 201]. We assume that the experiment will run 5 years in neutrino and another 5 years in antineutrino mode. The final exposure, therefore, will vary with beam designs, and is equal to a total of 11×10^{22} POT in the case of 120 GeV protons. To generate neutrino scattering events, we use our own dedicated MC, Gaussian smearing the true MC energies and angles as a proxy for the detector effects during reconstruction. We assume an energy resolution of $\sigma/E = 15\%/\sqrt{E}$ ($\sigma/E = 6\%/\sqrt{E}$) for e/γ showers (muons) and angular resolutions of $\delta\theta = 1^\circ$ for all particles [130].

An interesting addition to the design of the DUNE ND would be a magnetized high-pressure Gaseous Argon (GAr) tracker placed directly behind the LAr module [202]. The lower thresholds for particle reconstruction and the presence of a magnetic field is expected to improve event reconstruction and reduce backgrounds to neutrino-electron scattering and neutrino trident production. We note that despite the relatively small fiducial mass of such a GAr module, $\lesssim 1$ tonne, it would still provide a sizeable number of these rare leptonic neutrino scattering processes.

With the intense flux at DUNE and the large number of POT, the $\nu - e$ scattering measurement will not be statistically limited, with order 10^4 events in the DUNE ND after a few years. Systematics from the beam and detector are then the limiting factor for the sensitivity to new physics in this measurement. Current work on neutrino flux uncertainties shows that normalization uncertainties can be reduced to the order of 5% [203–205], with similar projections for DUNE [197]. The electron energy threshold also plays a role in the new physics search. In particular, for new light bosons the enhancement at very

Design	Mode	$\mu^+\mu^-$ trident	e^+e^- trident	$\nu - e$ scattering	POTs/year
62.4 GeV p^+	ν	36.5	92.7	7670	1.83×10^{21}
	$\overline{\nu}$	27.3	73.4	4620	1.83×10^{21}
80 GeV p^+	ν	42.0	102	8380	1.4×10^{21}
	$\overline{\nu}$	33.0	84.3	5320	1.4×10^{21}
120 GeV p^+	ν	47.6	110	8930	1.1×10^{21}
	$\overline{\nu}$	40.7	97.6	6450	1.1×10^{21}
ν_τ app optm	ν	210	321	24900	1.1×10^{21}
	$\overline{\nu}$	156	243	14700	1.1×10^{21}

Tab. 4.1. The SM rates for neutrino trident production and neutrino-electron scattering per year at the 75-t DUNE ND after kinematical cuts.

low momentum transfer $2T_e m_e$ has a cut-off at the minimum electron recoil energy (see Eq. (4.2.12)). This implies that the experiment is no longer sensitive to the Z' mass below $\sqrt{2T_{\rm th} m_e}$. In our analysis, we assume a realistic overall normalization systematic uncertainty of 5% and a $\nu - e$ scattering electron kinetic energy threshold of 600 MeV.

Lowering systematic uncertainties on the flux is challenging given the large hadroproduction and focusing uncertainties at the LBNF beam. Here, improvements on the experimental side in determining the neutrino flux will be extremely valuable (see *e.g.* Ref. [206]). If one is searching for novel leptophilic neutral currents, hadronic processes and inverse muon decay measurements are available, but these are limited either by theoretical uncertainties or by statistics, and might not be applicable in the whole energy region of interest. As to the electron energy, assuming a threshold as low as 30 MeV would be safe for electron detection, but at these low energies backgrounds can be incredibly challenging due to the overwhelming π^0 backgrounds. Increasing this threshold to 600 MeV, however, has little impact in our sensitivities and is only 200 MeV below the threshold used in the most recent MINERνA analysis [160], where good reconstruction is important for measuring the flux. For e^+e^- and $\mu^+\mu^-$ tridents, we refrain from increasing the analysis thresholds from a naive 30 MeV. This is certainly an aggressive assumption but it is necessary if e^+e^- tridents are to be measured, since these events are quite soft (see Appendix C). Thresholds for $\mu^+\mu^-$ tridents are much less important since the events are generally more energetic than their dielectron analogue.

Backgrounds ($\nu_\mu \to \nu_\mu \ell^+ \ell^-$) We now discuss the individual sources of backgrounds to neutrino trident production. A pair of charged leptons is very rarely produced in neutrino

interactions, usually coming from heavy resonance decays [187, 207–210]. Since our signal is mostly coming from coherent interactions with nuclei, cuts in the hadronic energy deposition in the detector $E_{\rm had}$, often large in heavy meson production processes, can help reduce backgrounds. Coherent and diffractive production of mesons is an exception to this, in particular pion production [211–214], which is the main background to trident due to particle mis-identification (misID). Muons are known to be easily spoofed by charged pions, making CC ν_μ interactions with $\pi^\pm$ in the final state (CC1π) one of the largest contributions to the backgrounds of $\mu^+\mu^-$ tridents. Similarly, NC π^0 production stands as the leading background to e^+e^- tridents when the photons are misIDed as two electrons, or if one of the photons pair converts and the other escapes detection. In Appendix C, we have shown that the $\mu^+\mu^-$ and e^+e^- pairs produced in trident have small separation angles ($\Delta\theta$), possess small invariant masses ($m^2_{\ell\ell}$) and that both charged leptons are produced with small angles with respect to the neutrino beam ($\theta_\pm$). With simplified misID rates, we used the GENIE [136] event generator to show that simple kinematical cuts can reduce backgrounds significantly, achieving a significance of $S_{\mu\mu}/\sqrt{B_{\mu\mu}} \sim 44$ and $S_{ee}/\sqrt{B_{ee}} \sim 17.3$ for the DUNE ND in neutrino mode, where S and B stand for signal and background, respectively. In our current analysis we implement the same kinematical cuts, which are as follows: $m^2_{\mu\mu} < 0.2$ GeV^2, $\theta_\pm < 15^\circ$ and $\Delta\theta < 20^\circ$ for the $\mu^+\mu^-$ channel, and $m^2_{ee} < 0.1$ GeV^2, $\theta_\pm < 20^\circ$ and $\Delta\theta < 40^\circ$ for the e^+e^- one. We impose these cuts again in our signal analysis, and point out that the new physics enhancement happens precisely in this favourable kinematical region, (see Section 4.2.1). The degree with which the experiment will be able to reduce backgrounds will rely on reconstruction properties of the signal and background final states. In particular, the detector containment of the charged-lepton pairs, as well as pions and photons, is crucial for momentum and invariant mass reconstruction, and so a detector simulation is desirable. Since we do not aim to develop a full experimental analysis and since the DUNE ND design is still under debate, we present our results with no backgrounds in Fig. 4.9 and vary the total background rate in Fig. 4.10, all the while applying the cuts above. This illustrates the impact of worse detector performance in background rejection.

Backgrounds ($\nu-e$) For neutrino-electron scattering, backgrounds will arise from either the genuine production of an electron or via the misID of particle showers in the detector,

both in the absence of observable hadronic energy deposition. The former scenario happens mostly by the CC interactions of the flux suppressed ν_e states present in the beam. The main contribution will be from CCQE interactions where the struck nucleon is invisible either for being below threshold or due to nuclear re-absorption. The misID of a photon initiated EM shower for an electron one is expected to be rare in LAr, where the first few cm of the showers can be used to separate electrons and photons by their characteristic dE/dx. However, the large NC rates for the production of single photons and π^0 can become a non-negligible background. For instance, coherent NC π^0 production leaves no observable hadronic signature and may look like a single electron if one of the photons is mis-identified and the other escapes detection. Finally, after misID happens, the signal can still look unique in its kinematical properties. In particular, $E_e\theta^2$ cuts can dramatically reduce backgrounds due to the forwardness of our signal (see e.g. [160, 215]).

Statistics. In order to assess the potential of DUNE to discover new physics, we perform a sensitivity analysis using a χ^2 test with a pull method for systematic uncertainties. Our goal is to assess when DUNE would be able to rule out the SM, and so we generate BSM events and fit the SM prediction to it. Our χ^2 function is defined as

$$\chi^2 = \min_{\alpha}\left[\frac{(N_{\rm BSM} - (1+\alpha)N_{\rm SM} - (\alpha+\beta)N_{\rm BKG})^2}{N_{\rm BSM}} + \left(\frac{\alpha}{\sigma_{\rm norm}}\right)^2 + \left(\frac{\beta}{\sigma_{\rm BKG}}\right)^2\right], \quad (4.3.1)$$

where the number of events for the BSM case is given by $N_{\rm BSM}$, the SM number of events is $N_{\rm SM}$ and the number of background events is $N_{\rm BKG}$. The nuisance parameters α and β, with their uncertainties $\sigma_{\rm norm}$ and $\sigma_{\rm BKG}$, take into account normalization uncertainties from the flux and detector, and uncertainties on the background prediction, respectively. For the DUNE ND, we assume $\sigma_{\rm norm} = 5\%$ and $\sigma_{\rm BKG} = 10\%$. These systematics will likely be dominated by flux normalization uncertainties, and can only be measured with interactions that do not depend on the leptophilic BSM physics.

4.3.2 $L_e - L_\mu$

New vector bosons with couplings to the first and second generation leptons can be probed very effectively in neutrino experiments by meausuring the $\nu - e$ scattering rate. This has been recognized in the literature [158, 162, 216], where bounds from various experiments, including CHARM-II [217], TEXONO [218–220] and Borexino [221] have been derived

on these bosons. Curiously, the bound calculated from the CHARM-II data has been pointed out by Ref. [158] to be too optimistic. The uncertainty on the neutrino flux is a real hindrance for these measurements which has not been taken into account when these bounds were computed. This is particularly important for measurements with large statistics, and for this reason we do not show the CHARM-II bound here. The measurement of $\overline{\nu}_e - e$ scattering at TEXONO, on the other hand, is statistically limited, and the bound it places on this class of models can safely ignore the flux systematics. This turns out to provide the strongest limit in a large region of the $L_e - L_\mu$ parameter space. Trident bounds can be obtained for this model, but due to their lower statistics and more involved kinematics, are subdominant.

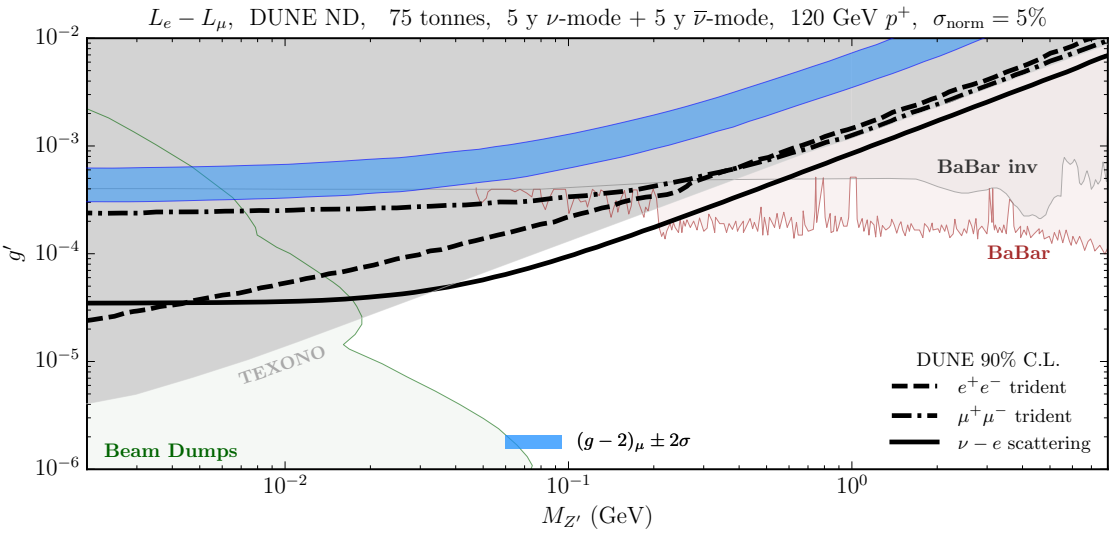

Fig. 4.7. The DUNE ND neutrino scattering sensitivities to the $L_e - L_\mu$ Z' at 90% C.L. The solid line shows the $\nu - e$ scattering sensitivity, followed by the dielectron trident in dashed line, and the dimuon trident in dot-dashed line. The coloured regions are excluded by other experiments, where we highlight the neutrino-electron scattering measurements at reactor experiments [218–220], searches at the BaBar e^+e^- collider [222, 223] and beam dump experiments [158].

We show our results for the DUNE ND in Fig. 4.7. Our results are for the combined $\nu + \bar{\nu}$ modes and do not include backgrounds. The opposite charges between the first and second families implies constructive interference between the SM and BSM contributions for neutrino scattering, contrary to what happens in a $B-L$ model, for instance. Therefore, the strongest bounds on this model can be obtained at DUNE in neutrino mode. It is clear, however, that the degree with which DUNE can probe unexplored parameter space is a question of how much the uncertainties on the flux can be lowered. To illustrate this

effect, we vary the normalization systematics on the right panel of Fig. 4.8, going from a conservative 10% to an aggressive 1% uncertainty. The effect of changing the thresholds is very small, being most important in a region already probed by other experiments. Different beam designs seem to have only a small impact on the sensitivity, as shown on the left panel of Fig. 4.8.

Since we show the bounds obtained from the neutrino and antineutrino runs combined, it is not possible to see the effects of destructive interference. If only channels with destructive interference were available, however, it would have been possible to allow for cancellations between the total interference and the square of the BSM contributions in certain regions of parameter space at the level of the total rate. The region where this cancellation happens depends strongly on the neutrino energies involved and on the integrated phase space of the recoiled electron. In that case, one expects that the sensitivity to the lowest new physics couplings comes, in fact, from the search for a deficit of $\nu - e$ scattering events, as opposed to the constructive interference case where an excess of events is always produced. We note that this has no significant impact on the sensitivity of a leptophilic Z', but might provide crucial information about the nature of the Z' charges in case of detection.

The trident bounds we obtain are not competitive for this model despite the fact that the trident cross sections receive similar enhancements to that of $\nu - e$ scattering. This is due to two reasons: the low number of events and the non-trivial kinematics of trident processes. Since the neutrino is essentially scattering off virtual charged leptons produced in the Coulomb field of the nucleus, it has to typically transfer more energy to the system than it would in a scattering off real particles in order to produce visible signatures. This remark also helps us to explain the behaviour of the sensitivity curves at the lowest masses. Whilst $\nu - e$ scattering cross sections become insensitive to the boson mass at $\sqrt{2m_e T_{\rm th}}$, the trident cross sections do not. This behaviour is most dramatic in the e^+e^- tridents, but is also present in the $\mu^+\mu^-$ one. This is a consequence of the 4-body phase space kinematics, where now the momentum transfer through the Z' propagator is no longer trivially related to the final state particle energies, as in $2 \to 2$ processes. It should be noted, however, that both the dimuon and the dielectron trident rates become nearly independent of $M_{Z'}$ below the muon and the electron mass, respectively, where only a logarithmic dependence is expected [159]. DUNE can also probe this class of models in

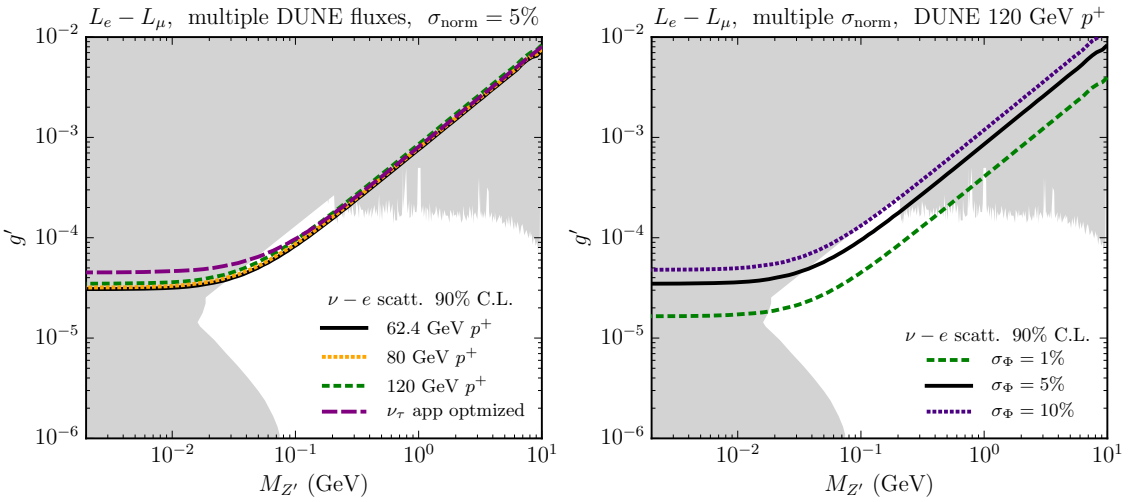

Fig. 4.8. The $\nu - e$ scattering sensitivity to the $L_e - L_\mu$ model at 90% C.L. On the left panel we show the sensitivity using different choices for the neutrino flux, and on the right we use the neutrino beam from 120 GeV protons and vary the normalization systematic uncertainty from an aggressive 1% to a conservative 10%.

a different way. In the context of long range forces in neutrino oscillation experiments and with the same choice of charges, Ref. [224] places competitive bounds in this model with Super-Kamiokande data and makes projections for DUNE. The matter potential created by the local matter density modifies the dispersion relation of the neutrinos with lepton non-universal charges, leading to very competitive bounds in our region of interest. Similar considerations have also been explored in the context of high-energy astrophysical neutrinos [225]. Other experimental searches have been conducted at electron beam dumps. This technique consists of producing the Z' boson at the target via radiative processes such as $e + A \to e + A + Z'$, and look for the visible decays of the boson in the detector. In this model, the decay products are mostly e^+e^- states and the bounds are only applicable at appreciably small values of g' and $M_{Z'}$, where the lifetime of the Z' is sufficiently large. Probing the large mass region, on the other hand, requires high-energy experiments. In that regime, the strongest bounds come from searches at the e^+e^- collider BaBar. These come about in two ways: looking for the visible decay products of a Z' produced radiatively or in heavy meson decays [222], or exploring the BR into invisible final states [223].

4.3.3 $L_\mu - L_\tau$

In this section we evaluate the DUNE ND sensitivity to the presence of a light vector Z' charged under $L_\mu - L_\tau$. Beyond being anomaly free, this choice of charges allows for

positive contributions to the anomalous magnetic moment of the muon, $a_\mu = (g-2)_\mu$, as discussed in Refs. [176,179,226–228]. This quantity is well known for a $\sim 3.7\sigma$ discrepancy between the experimental measurement [229] and the theory predictions [230, 231]. If future efforts to measure it [232] confirm this disagreement and if theoretical uncertainties are better controlled in the next few years, then constraining new physics scenarios that could contribute to a_μ is of utmost importance.

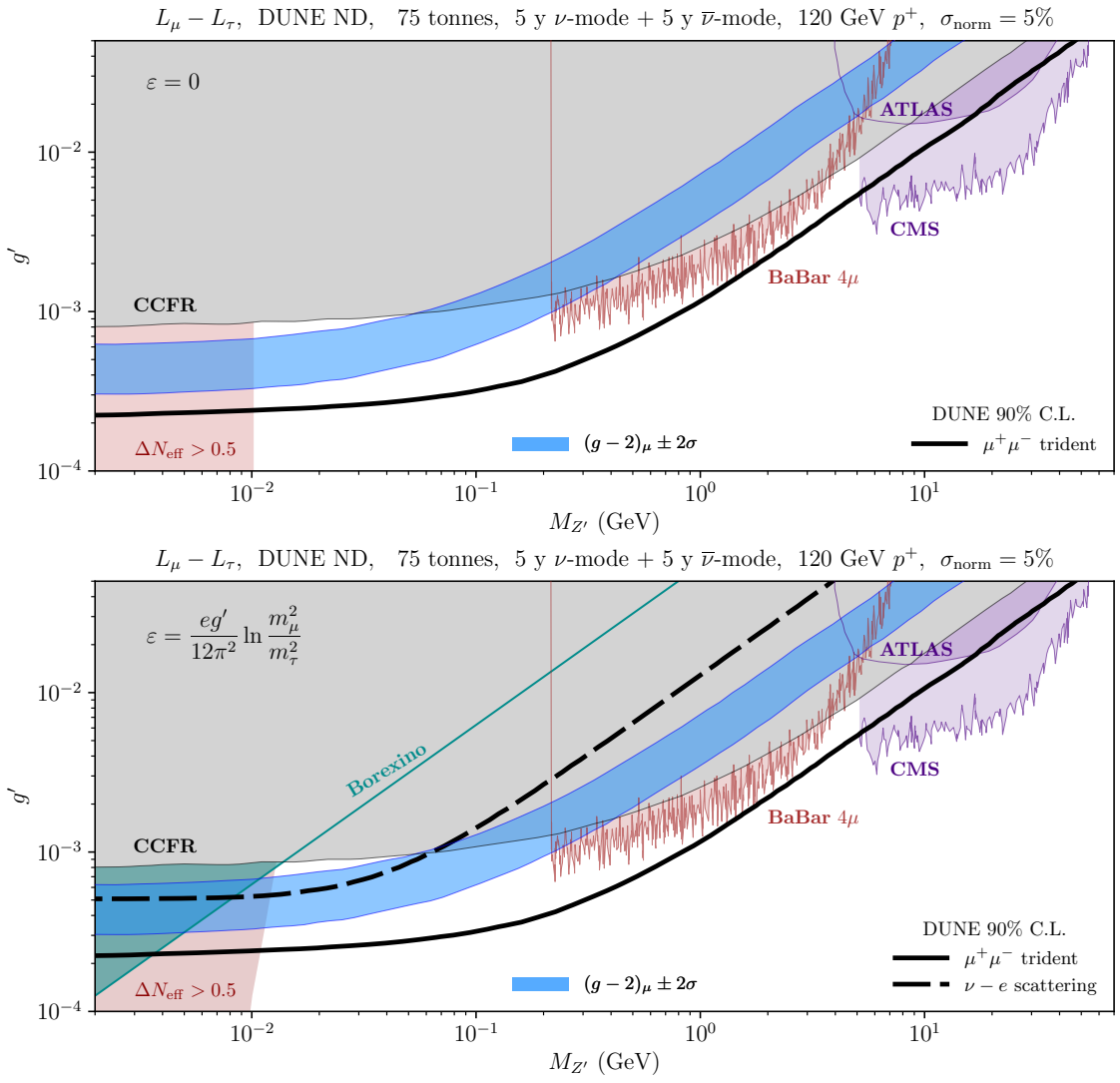

Fig. 4.9. The DUNE ND neutrino scattering sensitivities for $L_\mu - L_\tau$ at 90% C.L. The upper panel shows the case with no kinetic mixing, and the lower panel the case with the loop-induced mixing. Bounds from neutrino-electron scattering apply only to the latter. We also show bounds from BaBar [233], LHC [234], Borexino [113] and from the neutrino trident production measurement at CCFR [108,159]. Recent cosmological bounds for the two kinetic mixing cases derived in Ref. [178] are also shown.

This model can significantly impact neutrino trident production of a muon pair. In fact, the leading bound in this parameter space for masses $M_{Z'} \lesssim 200$ MeV comes from the

CCFR measurement of the same neutrino trident channel [108]. CCFR observed 37.0 ± 12.4 events, extracting a measurement of the trident cross section of $\sigma_{\rm CCFR}/\sigma_{\rm SM} = 0.82 \pm 0.28$. Curiously, the measurement by CHARM-II [107] provides weaker constraints on this model despite seeing a larger number of trident events, namely 55 ± 16 events in total, most likely due to the 1σ upward fluctuation of the measurement: $\sigma_{\rm CHARM-II}/\sigma_{\rm SM} = 1.58 \pm 0.57$. Other important bounds from $\nu - e$ scattering have also been obtained using the kinetic mixing parameter generated at one-loop. The strongest of which uses data from Borexino [113], and are only relevant for the low mass region $M_{Z'} \lesssim 20$ MeV.

At DUNE, both of these measurements are possible, allowing to constrain this model in different ways. We show our results in Fig. 4.9, without including backgrounds. In this scenario, DUNE would be able to cover all the 2σ region compatible with the $(g-2)_\mu$ measurement only with the $\mu^+\mu^-$ trident events. For the low mass region, measuring the $\nu - e$ scattering rate can provide a complementary probe of this region, depending most strongly on the systematic uncertainties DUNE can achieve. We note that analysis thresholds used for $\nu - e$ scattering have little impact on the sensitivity in the region of interest. Our conclusion that DUNE can cover all of the $(g-2)_\mu$ region holds provided backgrounds are kept below the SM signal rate. This can be seen when we include backgrounds with different assumption on the right panel of Fig. 4.10. Finally, different assumption for the beam design have little impact on the sensitivity, as show on the left panel of Fig. 4.10.

Apart from neutrino scattering, dedicated searches for resonances decaying into $\mu^+\mu^-$ in four muon final states have been performed at BaBar [233], looking for $e^+e^- \to \mu^+\mu^- Z'(\to \mu^+\mu^-)$. At the LHC, the $Z \to 4\mu$ measurement performed by the ATLAS collaboration [234] was used to derive a constraint in the $L_\mu - L_\tau$ parameter space in Ref. [159]. Recently, the CMS collaboration performed a dedicated search for a resonance between $M_{Z'} = 5$ and 70 GeV, significantly improving previous constraints at large masses [235]. Big Bang Nucleosynthesis bounds were studied in [176, 228], and shown to constrain the mass of the boson to be $M_{Z'} \gtrsim 5$ MeV. Recently, additional constraints from Cosmology were derived given that the presence of very light Z' bosons changes the evolution of the early Universe [178]. In particular, the decays and inverse decays induced by the new leptophilic interactions can modify the neutrino relativistic degrees of freedom, requiring

$M_{Z'} \gtrsim 10$ MeV in order for $\Delta N_{\rm eff} < 0.5$ for the case with no kinetic mixing. The authors of Ref. [178] also found that an additional Z' boson can alleviate the tension in the different measurements of the Hubble parameter. Let us stress here that all these bounds will be complementary to possible future constraints that can be obtained by the DUNE program, as shown in Fig. 4.9.

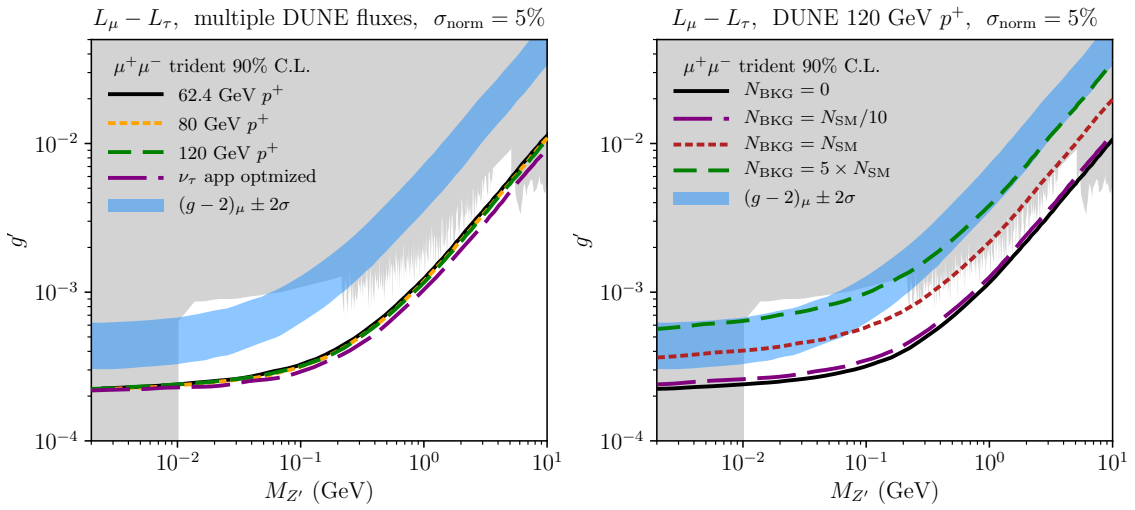

Fig. 4.10. The dimuon neutrino trident sensitivity to the $L_\mu - L_\tau$ model with no kinetic mixing at 90% C.L. On the left panel we show the sensitivity using different choices for the neutrino flux, and on the right we use the neutrino beam from 120 GeV protons and scale the background with respect to the total number of SM trident events after cuts.

4.4 Overview

Although the next generation neutrino oscillation experiments are primarily designed for making precision measurements of the neutrino mixing parameters, the unprecedented fluxes and large detectors will allow for many non-minimal new physics searches. In this work, we have considered the physics potential of the DUNE ND for constraining the existence of an additional anomaly-free $U(1)$ gauge group giving rise to a Z' boson which only couples to leptons — a form of a purely leptophilic neutral current. Specifically, we have considered the anomaly free scenarios with charges associated to the lepton number difference $L_\alpha - L_\beta$. Focusing on the two most promising neutrino scattering processes, $\nu - e$ and $\nu\ell\ell$ trident scattering, we have computed expected sensitivity curves for the DUNE ND for a variety of charge assignments.

In performing our sensitivity studies as a function of the coupling and mass of the Z'

boson, we have remained as faithful as possible to the real experimental conditions of a LAr detector. Our main results rely on the realistic assumptions of flux uncertainties of 5% and feasible exposures. To avoid large backgrounds, we have also implemented kinematical cuts on the neutrino trident sample, and a kinetic energy threshold of 600 MeV for $\nu - e$ scattering events. The parameter space which can be probed by $\nu - e$ scattering in the $L_e - L_\mu$ scenario is at least two times better than the e^+e^- and almost twenty times better than the $\mu^+\mu^-$ trident channels, specially for the lower mass region. In this case, the DUNE ND would improve only slightly on previous $\nu - e$ scattering bounds, especially at around $M_{Z'} \sim 100$ MeV. We do not expect e^+e^- trident measurements at DUNE to improve our coverage of the $L_e - L_\mu$ Z' parameter space, but note this process has a distinct dependence on $M_{Z'}$ if compared to $\nu - e$ scattering.

If the light vector Z' is charged under $L_\mu - L_\tau$, we have found that the dimuon trident measurement could provide the leading bound in this parameter space. This is particularly interesting as these models can also explain the discrepancy between the measurement of the anomalous magnetic moment of the muon and its SM prediction. We expect that DUNE will be able to fully explore the $(g-2)_\mu$ motivated parameter space provided backgrounds are kept under control. The robustness of our results is tested against different choices of neutrino fluxes, where we find that despite the larger rates at higher neutrino energies and the larger BSM enhancement at lower energies, the sensitivities are very similar.

Improvements to the experimental sensitivities we have displayed in Figs. 4.7 and 4.9 can be achieved by reducing uncertainties on the neutrino flux and detection. From the experimental side, novel detection techniques suitable to rare neutrino events are currently under discussion, such as the magnetized HPgTPC [202] and the Straw Tube Tracker [236, 237]. Together with improved analysis techniques, these will help to improve upon our projections for the sensitivity of DUNE to new physics that might be hiding at light masses and small couplings.

Chapter 5

A Light Dark Neutrino Sector

5.1 Neutrinos and Dark Sectors

The most important evidence that the Standard Model (SM) of particle physics is incomplete are neutrino masses and mixing, and the presence of DM in the Universe. Both call for extensions of the SM and the possible existence of dark sectors which do not partake in SM interactions, or do so with extremely weak couplings while displaying strong "dark" interactions [47–49]. Such sectors might exist at relatively light scales below the electroweak one, being within reach of present and future non-collider experiments. In this chapter, we propose a new neutrino model with a hidden $U(1)'$ gauge symmetry under which no SM fields are charged, see Fig. 5.1. We introduce new SM-neutral fermions, ν_D and an additional sterile neutrino N. The symmetry is subsequently broken by the vacuum expectation value (vev) of a complex dark scalar Φ, which gives mass to the new gauge boson. For concreteness, we restrict the scale of the breaking to be below the electroweak one. The interest in such *dark neutrinos* ν_D arises from their novel dark interactions which may "leak" into the SM sector via neutrino mixing, where they offer a variety of phenomenological and cosmological consequences.

Models with heavy neutrinos which are not completely sterile and might participate in new gauge interactions have been studied in several contexts, including $B - L$, $L_\mu - L_\tau$ and left-right symmetric models [238–246], but here we focus on the possibility of a symmetry under which no SM fields are charged [247–249]. New heavy neutral fermions that feel such hidden forces, such as ν_D, are referred to as *dark neutrinos*, since they define a

dark sector separate from the SM. Nevertheless, the dark interactions “leak" into the SM sector via neutrino mixing, where they may dominate [250, 251]. Models of this type have been invoked to generate large neutrino non-standard interactions [154, 252], generate new signals in DM experiments [250,253–256], weaken cosmological and terrestrial bounds on eV scale sterile neutrinos [140–143, 145–147, 257], and as a potential explanation of anomalous short-baseline results at the MiniBooNE [258, 259] and/or LSND [260, 261] experiments with new degrees of freedom at the MeV/GeV scale [5, 148, 149, 262–265].

Our model presents all the three renormalizable portals to the SM. The Yukawa interactions between the leptonic doublet and N, and between N and ν_D induce neutrino mixing. The gauge symmetry allows a cross-coupling term in the potential between the Higgs and the real part of the scalar, inducing mixing between the two after symmetry breaking. The broken gauge symmetry implies the existence of a light hidden gauge boson X_μ, which mediates the dark neutrino interactions and generically kinetically mixes with the SM hypercharge. The set-up is self-consistent and combines the three portals into a unified picture that exhibits significantly different phenomenology with respect to each portal taken separately, as we discuss. The interplay of the different portal degrees of freedom leads to novel signatures which would have escaped searches performed to date, and that can explain long-standing anomalies. For the latter, we focus on the MiniBooNE anomaly as discussed in Ref. [149] (see also [148]) and on new neutrino scattering signatures at neutrino experiments [5]. We also reconsider the possibility to explain the discrepancy between the prediction and measurement of the anomalous magnetic moment of the muon (Δa_μ) [229] via kinetic mixing [227, 266].

An interesting feature of the model is the generation of neutrino masses at loop-level. This requires only two key features of our setup, namely a light Z' and neutrino mixing, but not the vector and scalar portals. For this reason, we discuss it later in Section 5.3.2.

In its minimal form, the model is not anomaly-free. We discuss how this can be cured and propose a minor extension that introduces additional dark sector neutral fermions charged under the new symmetry [47, 48]. Neutrinos, we argue, may be a window into such dark sectors, bridging the puzzles of neutrino masses and DM [73, 144, 267–275]. We briefly outline the key features of a DM extension and leave a more detailed analysis to future work.

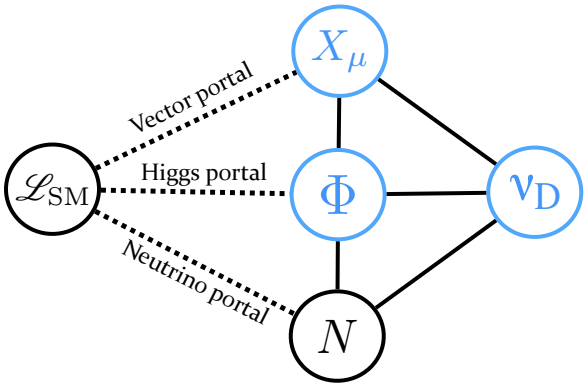

Fig. 5.1. Schematic representation of our dark neutrino model. The dark neutrino, ν_D and the complex scalar Φ are the only fields charged under the new $\mathrm{U}(1)'$ gauge symmetry. The new vector boson X_μ acquires a mass after spontaneous symmetry breaking, and N remains a complete singlet.

	$\mathrm{SU}(3)_c$	$\mathrm{SU}(2)_L$	$\mathrm{U}(1)_Y$	$\mathrm{U}(1)_X$
N	**1**	**1**	0	0
ν_D	**1**	**1**	0	Q
Φ	**1**	**1**	0	Q

Tab. 5.1. The additional field content of our model. N and ν_D are left-handed fermions while φ is a complex scalar. Although this field content implies $U(1)_X$ is anomalous, remedies which do not affect mass generation are discussed in Section 5.2.3.

5.2 Interplay of Multiple Portals

We extend the SM gauge group with a new abelian gauge symmetry $U(1)'$ with associated mediator X_μ and introduce three new singlets of the SM gauge group: a complex scalar Φ, and two left-handed fermions $\nu_{D,L} \equiv \nu_D$ and $N_L \equiv N$. As shown in Table 5.1, the scalar Φ and the fermion ν_D are equally charged under the new symmetry, and N is neutral with respect to all gauge symmetries of the model. For simplicity, we restrict our discussion to a single generation of hidden fermions. The relevant terms in the gauge-invariant Lagrangian are

$$\begin{aligned}\mathscr{L} \supset (D_\mu \Phi)^\dagger (D^\mu \Phi) - V(\Phi, H) + \mathscr{L}_{\rm kinetic} + \overline{N} i\partial\!\!\!/ N + \overline{\nu_D} i\gamma^\mu \left(\partial_\mu - i g' X_\mu\right) \nu_D \\ - \left[y_\nu^\alpha (\overline{L_\alpha} \cdot \widetilde{H}) N^c + \frac{\mu'}{2} \overline{N} N^c + y_N \overline{N} \nu_D^c \Phi + \text{h.c.} \right],\end{aligned} \tag{5.2.1}$$

where $L_\alpha \equiv (\nu_\alpha^T, \ell_\alpha^T)^T$ the SM leptonic doublet of flavour $\alpha = e, \mu, \tau$ and $\widetilde{H} \equiv i\sigma_2 H^*$ is the charge conjugate of the SM Higgs doublet. We write y_ν^α for the L_α–N Yukawa coupling, y_N for the ν_D–N one, and μ' for the Majorana mass of N, which is allowed by the SM and the new gauge interaction, although it breaks lepton number by 2 units.

The minimisation of the scalar potential $V(\Phi, H)$ leads the neutral component of the fields H and Φ to acquire vevs v_h and v_φ, respectively. The latter also generates a mass for both the new gauge boson X_μ and the real component of the scalar field φ. Although v_φ is arbitrary, we choose it to be below the electroweak scale, $v_\varphi < v_h$, as we are interested in building a model testable at low scales.

Neutrino portal In the neutral fermion sector and after symmetry breaking, two Dirac mass terms are induced with $m_D \equiv y_\nu^\alpha v_h/\sqrt{2}$ and $\Lambda \equiv y_N v_\varphi/\sqrt{2}$. It is useful to consider the form of the neutrino mass matrix in the single generation case to clarify its main features. For one active neutrino ν_α ($\alpha = e, \mu, \tau$), it reads

$$\mathscr{L}_{\text{mass}} \supset \frac{1}{2}\begin{pmatrix}\overline{\nu}_\alpha & \overline{N} & \overline{\nu_D}\end{pmatrix}\begin{pmatrix}0 & m_D & 0\\ m_D & \mu' & \Lambda\\ 0 & \Lambda & 0\end{pmatrix}\begin{pmatrix}\nu_\alpha^c\\ N^c\\ \nu_D^c\end{pmatrix} + \text{h.c.} \tag{5.2.2}$$

The form of this matrix appears in Inverse Seesaw (ISS) [64, 65] and in Extended Seesaw (ESS) [70, 71] models. In fact, it is the same matrix discussed in the so-called Minimal ISS [276], with the difference that in our case its structure is a consequence of the hidden symmetry. After diagonalisation of the mass matrix, the two heavy neutrinos, ν_h with $h = 4, 5$, acquire masses

$$m_{4,5} = \frac{\mu' \mp \sqrt{\mu'^2 + 4(\Lambda^2 + m_D^2)}}{2}. \tag{5.2.3}$$

Assuming that $m_D \ll \Lambda$, we focus on two interesting limiting cases.

In the *ISS-like* limit, where $\Lambda \gg \mu'$ and the two heavy neutrinos are nearly degenerate, we have

$$\begin{aligned} &m_5 \simeq -m_4 \simeq \Lambda\ , \qquad m_5 - |m_4| = \mu'\ , \qquad U_{\alpha 5} \simeq U_{\alpha 4} \simeq \frac{m_D}{\sqrt{2}\Lambda}\ , \\ &U_{Di} \simeq \frac{m_D}{\Lambda}, \qquad U_{D5} \simeq U_{D4} \simeq \frac{1}{\sqrt{2}}\ , \qquad U_{N5} \simeq U_{N4} \simeq \frac{1}{\sqrt{2}}\ . \end{aligned} \tag{5.2.4}$$

In the *ESS-like* case, $\Lambda \ll \mu'$, one neutral lepton remains very heavy and mainly in the completely neutral direction N, and the other acquires a small mass via the seesaw mechanism in the hidden sector. We find

$$m_4 \simeq -\frac{\Lambda^2}{\mu'}\ , \qquad m_5 \simeq \mu'\ , \qquad U_{\alpha 4} \simeq U_{\alpha 5}\sqrt{\frac{m_5}{|m_4|}} \simeq \frac{m_D}{\Lambda}\ ,$$

$$U_{Di} \simeq \frac{m_D}{\Lambda}, \qquad U_{N5} \simeq U_{D4} \simeq 1 \ , \qquad U_{D5} \simeq U_{N4} \simeq \frac{\Lambda}{\mu'} \ . \tag{5.2.5}$$

From the discussion above, it is clear that the masses of Z' and φ' are typically above the heavy neutrino ones, unless we are in the ESS-like regime.

The Yukawa terms in Eq. (5.2.1) induce *neutrino mixing* between the active (light) and heavy (sterile, dark) neutrinos. In this model, similarly to the ISS and the ESS cases, this mixing can be much larger than the typical values required in type-I seesaw extensions to explain neutrino masses, making its phenomenology more interesting. The determinant of the mass matrix in Eq. (5.2.2) is zero, and so light neutrino masses vanish at tree-level and do not constrain the values of the active-heavy mixing angles. This, however, is no longer the case at one-loop level, as light neutrino masses emerge through radiative corrections from diagrams involving the φ' and Z' degrees of freedom [2].

Scalar portal The symmetries of the model allow us to write the following scalar potential

$$V(\Phi, H) = - m_\Phi^2 |\Phi|^2 + \lambda_\Phi |\Phi|^4 - m_H^2 H^\dagger H + \lambda_H (H^\dagger H)^2 + \lambda \, (H^\dagger H) |\Phi|^2, \tag{5.2.6}$$

where we identify λ as the scalar portal coupling [277], responsible for mixing in the neutral scalar sector. We parametrize the scalar fields as

$$H = \frac{1}{\sqrt{2}} \begin{pmatrix} G_1^+ + i G_2^+ \\ h + i G^0 \end{pmatrix} \qquad \text{and} \qquad \Phi = \frac{\varphi + i G_\varphi}{\sqrt{2}},$$

where all component fields are real. Minimising the potential, we find

$$v_\varphi^2 = \frac{\lambda_H \, m_\Phi^2 - \lambda \, m_H^2/2}{\lambda_H \lambda_\Phi - \lambda^2/4}, \qquad\qquad v_h^2 = \frac{\lambda_\Phi \, m_H^2 - \lambda \, m_\Phi^2/2}{\lambda_H \lambda_\Phi - \lambda^2/4}, \tag{5.2.7}$$

such that the new degrees of freedom around the minimum are found by performing the transformations $\varphi \to \varphi + v_\varphi$ and $h \to h + v_h$. The new potential is then

$$\begin{aligned} V(\Phi, H) = & \, \varphi^2 \left(\lambda_\Phi v_\varphi^2 \right) + h^2 \left(\lambda_H v_h^2 \right) + \varphi h \left(\lambda \, v_\varphi v_h \right) \\ & + \varphi^2 h \left(\frac{\lambda v_h}{2} \right) + \varphi h^2 \left(\frac{\lambda v_\varphi}{2} \right) + \varphi^3 \left(\lambda_\Phi v_\varphi \right) + h^3 \left(\lambda_H v_h \right) \\ & + \varphi^4 \left(\frac{\lambda_\Phi}{4} \right) + h^4 \left(\frac{\lambda_H}{4} \right) + \varphi^2 h^2 \left(\frac{\lambda}{4} \right) \\ & + V_{\text{Goldstone}} + \text{constants}, \end{aligned} \tag{5.2.8}$$

where $V_{\text{Goldstone}}$ contains terms related to the Goldstone bosons. The physical mass basis of scalar fields comes from the diagonalisation

$$\begin{pmatrix} h & \varphi \end{pmatrix} \begin{pmatrix} \lambda_H v_h^2 & \frac{\lambda}{2} v_h v_\varphi \\ \frac{\lambda}{2} v_h v_\varphi & \lambda_\Phi v_\varphi^2 \end{pmatrix} \begin{pmatrix} h \\ \varphi \end{pmatrix} = \begin{pmatrix} h' & \varphi' \end{pmatrix} R(\theta) \begin{pmatrix} \lambda_H v_h^2 & \frac{\lambda}{2} v_h v_\varphi \\ \frac{\lambda}{2} v_h v_\varphi & \lambda_\Phi v_\varphi^2 \end{pmatrix} R(-\theta) \begin{pmatrix} h' \\ \varphi' \end{pmatrix}, \tag{5.2.9}$$

where

$$R(-\theta) = \begin{pmatrix} \cos\theta & \sin\theta \\ -\sin\theta & \cos\theta \end{pmatrix}, \quad \tan 2\theta \equiv \frac{\lambda v_h v_\varphi}{\lambda_H v_h^2 - \lambda_\Phi v_\varphi^2}. \tag{5.2.10}$$

The masses of the physical fields are

$$\frac{m^2_{\varphi',h'}}{2} = \frac{\lambda_\Phi v_\varphi^2 + \lambda_H v_h^2}{2} \pm \frac{\sqrt{(\lambda_\Phi v_\varphi^2 - \lambda_H v_h^2)^2 + \lambda^2 v_h^2 v_\varphi^2}}{2} \tag{5.2.11}$$

so that φ' is the lightest state and h' is mostly in the Higgs direction. To summarise, we have now the physical basis $(h'\,\varphi')$, which is a superposition of the flavour states $(h\,\varphi)$. This is what we refer to as scalar mixing. Note as well that the mass matrix is diagonal when we set the portal coupling λ to zero.

Vector portal Similarly, mixing also arises in the neutral vector boson sector from the kinetic Lagrangian [175]

$$\mathscr{L}_{\text{kinetic}} = -\frac{1}{4} B_{\mu\nu} B^{\mu\nu} - \frac{1}{4} W^a_{\mu\nu} W_a^{\mu\nu} - \frac{1}{4} X_{\mu\nu} X^{\mu\nu} - \frac{\sin\chi}{2} B_{\mu\nu} X^{\mu\nu}, \tag{5.2.12}$$

where $X^{\mu\nu}$ is the field strength tensor for X_μ and the last term is always allowed but introduces non-canonical kinetic terms for the gauge bosons. This operator may be removed with a field redefinition, resulting in three mass eigenstates $(A,\, Z^0,\, Z')$, corresponding to the photon, Z^0-boson and the hypothetical Z'-boson. The full transformation to go from off-diagonal flavour basis to the physical basis is

$$\begin{pmatrix} B^\mu \\ W^\mu \\ X^\mu \end{pmatrix} = \begin{pmatrix} 1/\cos\chi & 0 & 0 \\ 0 & 1 & 0 \\ -\tan\chi & 0 & 1 \end{pmatrix} R^y(\chi) R^z(\theta_W) R^x(\beta) \begin{pmatrix} A^\mu \\ Z^\mu \\ Z'^\mu \end{pmatrix}. \tag{5.2.13}$$

where $R(\theta)^i$ is the rotation matrix around the axis i, and

$$\mu^2 = \frac{(g')^2 v_\varphi^2}{c_W^2 M_W^2}, \qquad \tan 2\beta = \frac{2 s_W s_\chi c_\chi}{c_\chi^2 - s_W^2 s_\chi^2 - \mu^2}. \tag{5.2.14}$$

The physical masses are

$$\frac{m_Z^2}{\left(M_Z^{\rm SM}\right)^2} = 1 + s_W t_\chi t_\beta, \quad \frac{m_{Z'}^2}{\left(M_Z^{\rm SM}\right)^2} = 1 - \frac{s_W t_\chi}{t_\beta}. \tag{5.2.15}$$

For a light Z' ($\mu \to 0$), the Z' coupling to SM fermions f to first order in the small parameter χ is given by

$$\mathscr{L} \supset -(e\, q_f\, c_W)\chi\, \overline{f}\gamma^\mu f\, Z'_\mu\ , \tag{5.2.16}$$

with q_f the fermion electric charge.

The values of χ and λ are arbitrary and could be expected to be rather large. As such, we treat them as free parameters within their allowed ranges. Here, we merely note that with our current minimal matter content, χ and λ receive contributions at loop level from the $(\overline{L}_\alpha \cdot \widetilde{H})N^c$ and $\overline{N}\nu_D^c\Phi$ terms, which are necessarily suppressed by neutrino mixing ($\chi \propto g'e|U_{\alpha h}|^2$ and $\lambda \propto |U_{\alpha h}|^2$). These values constitute a lower bound and larger values should be expected in a complete model.

5.2.1 Neutrino Interactions in the Mass Basis

We now provide the neutrino interactions in the model in the mass basis. The interaction Lagrangia reads

$$\mathcal{L}_I = +\,\overline{\nu_i}\gamma^\mu \left((C_Z)_{ij}P_{\rm L} - (C_Z)^*_{ij}P_{\rm R}\right)\nu_j Z_\mu + \overline{\nu_i}\gamma^\mu \left((C_{Z'})_{ij}P_{\rm L} - (C_{Z'})^*_{ij}P_{\rm R}\right)\nu_j Z'_\mu, \tag{5.2.17}$$

$$-\,\overline{\nu_i}\left((\Delta_h)_{ij}P_{\rm R} + (\Delta_h)^*_{ij}P_{\rm L}\right)\nu_j h - \overline{\nu_i}\left[i(\Delta_h)^*_{ij}P_{\rm L} - i(\Delta_h)_{ij}P_{\rm R}\right]\nu_j G_h, \tag{5.2.18}$$

$$-\,\overline{\nu_i}\left((\Delta_\varphi)_{ij}P_{\rm R} + (\Delta_\varphi)^*_{ij}P_{\rm L}\right)\nu_j \varphi - \overline{\nu_i}\left[i(\Delta_\varphi)_{ij}P_{\rm R} - i(\Delta_\varphi)^*_{ij}P_{\rm L}\right]\nu_j G_\varphi. \tag{5.2.19}$$

The new matrices of coefficients for the gauge bosons are given by

$$(C_Z)_{ij} = \frac{m_Z}{2}\left[\left(\sum_{\alpha=e}^{\tau} U^*_{\alpha i}U_{\alpha j}\right)\frac{c_\omega}{v} - U^*_{Di}U_{Dj}\frac{s_\omega}{v_\varphi}\right], \tag{5.2.20}$$

$$(C_{Z'})_{ij} = \frac{m_{Z'}}{2}\left[\left(\sum_{\alpha=e}^{\tau} U^*_{\alpha i}U_{\alpha j}\right)\frac{s_\omega}{v} + U^*_{Di}U_{Dj}\frac{c_\omega}{v_\varphi}\right]. \tag{5.2.21}$$

The matrices for the scalar interactions are

$$(\Delta_h)_{ij} = \sum_{\alpha=e}^{\tau}\frac{y_\nu^\alpha}{2\sqrt{2}}\left(U^*_{\alpha i}U^*_{Nj} + U^*_{\alpha j}U^*_{Ni}\right), \tag{5.2.22}$$

$$(\Delta_\varphi)_{ij} = \frac{y_\varphi}{2\sqrt{2}}\left(U^*_{Ni}U^*_{Dj} + U^*_{Nj}U^*_{Di}\right). \tag{5.2.23}$$

Two useful identities between the coupling constants which are used in the calculaton of the radiative mass are

$$C_Z \hat{m} C_Z^{\mathrm{T}} = C_{Z'} \hat{m} C_{Z'}^{\mathrm{T}} = 0. \tag{5.2.24}$$

A consequence of spontaneous symmetry breaking is the existence of relationships between gauge bosons and scalar couplings,

$$\begin{aligned} \Delta_h &= c_\omega \left(\frac{C_Z \hat{m} + \hat{m} C_Z^{\mathrm{T}}}{m_Z} \right) + s_\omega \left(\frac{C_{Z'} \hat{m} + \hat{m} C_{Z'}^{\mathrm{T}}}{m_{Z'}} \right), \\ \Delta_\varphi &= -s_\omega \left(\frac{C_Z \hat{m} + \hat{m} C_Z^{\mathrm{T}}}{m_Z} \right) + c_\omega \left(\frac{C_{Z'} \hat{m} + \hat{m} C_{Z'}^{\mathrm{T}}}{m_{Z'}} \right). \end{aligned} \tag{5.2.25}$$

In the presence of scalar mixing ($\lambda \neq 0$ in the scalar potential), we must also relate these to the physical coupling matrices of h' and φ'. This takes the form of an additional rotation, shifting $\omega \to \omega' \equiv \omega - \theta$,

$$\begin{aligned} \Delta' &= c_{\omega'} \left(\frac{C \hat{m} + \hat{m} C^{\mathrm{T}}}{m_Z} \right) + s_{\omega'} \left(\frac{D \hat{m} + \hat{m} D^{\mathrm{T}}}{m_{Z'}} \right), \\ \Omega' &= -s_{\omega'} \left(\frac{C \hat{m} + \hat{m} C^{\mathrm{T}}}{m_Z} \right) + c_{\omega'} \left(\frac{D \hat{m} + \hat{m} D^{\mathrm{T}}}{m_{Z'}} \right), \end{aligned} \tag{5.2.26}$$

where

$$s_\omega = -s_\beta \frac{m_{Z'}}{c_{\mathrm{W}} M_{\mathrm{W}}} \qquad \text{and} \qquad c_\omega = c_\beta \frac{m_Z}{c_{\mathrm{W}} M_{\mathrm{W}}}, \tag{5.2.27}$$

which satisfy the expected relation $s_\omega^2 + c_\omega^2 = 1$ and $m_Z^0 = gv/(2c_W)$

5.2.2 Portal Phenomenology

The interplay between portal couplings and the heavy neutrinos ν_h ($h = 4, 5$) leads to a distinct, and possibly richer, phenomenology to what is commonly discussed in the presence of a single portal. We present here some of the most relevant signatures, devolving a longer study to future work.

Heavy neutrino searches The strongest bounds on heavy neutrinos in the MeV–GeV mass range come from peak searches in meson decays [278–280] and beam dump experiments [281–286] looking for visible ν_h decays. These, however, can be weakened if the ν_h decays are sufficiently different from the case of “standard" sterile neutrinos with SM interactions suppressed by neutrino mixing. We now discuss how this may happen, depending on the mass hierarchy of the two heavy neutrinos and the values of neutrino

and kinetic mixing. For concreteness, we focus on specific benchmark points (BP) that illustrate the key features. In the ISS-like regime, we take $m_4/m_5 = 99\%$ and choose $m_4 \simeq m_5 = 100$ MeV. If χ is negligible, we have that ν_h decays as in the standard sterile case via SM interactions. This is because the $\nu_5 \to \nu_4 \bar{\nu}_\alpha \nu_\alpha$ decay is phase-space suppressed ($\Gamma_{\nu_5 \to \nu_4 \nu\nu} \propto \mu'^5$), and because Z' mediated decays into three light neutrinos are negligible for small mixing, as $\Gamma_{\nu_h \to \nu\nu\nu} \propto |U_{\alpha h}|^6 m_h^5/m_{Z'}^4$. If χ is sizeable, on the other hand, new visible decay channels dominate, specifically $\nu_4 \to \nu_\alpha e^+ e^-$ for this BP. The corresponding decay rate is given by

$$\Gamma(\nu_4 \to \nu_\alpha e^+ e^-) \approx \frac{1}{2} \frac{e^2 \chi^2 g'^2 |U_{\alpha 4}|^2}{192\pi^3} \frac{m_4^5}{m_{Z'}^4}. \tag{5.2.28}$$

Depending on the value of χ and m'_Z this decay can be much faster than in the SM, implying stronger constraints on the neutrino mixing parameters as discussed in Ref. [287]. For heavier masses, additional decay channels, e.g. $\nu_4 \to \nu_\alpha \mu^+ \mu^-$, would open. A feature of the model is that such channel would have the same BR as the electron one, albeit phase space suppressed. No two-body decays into neutral pseudoscalars arise due to the vector nature of the gauge coupling, unless mass mixing is introduced (see [288] for a thorough discussion of the decay products of a dark photon). We consider also a BP in the ESS-like regime. We take $m_4 = m_5/10$. In this case, ν_5 decays into 3 ν_4 states very rapidly. The subsequent decays of ν_4 would proceed as discussed above and would be much slower than the ν_5 one, given the hierarchy of masses and the further suppression due to neutrino and/or kinetic mixing.

For large χ, peak searches and bounds on lepton number violation (LNV) from meson and tau decays may be affected [289, 290]. Despite simply relying on kinematics, we note that in peak searches the strict requirement of a single charged track in the detector [279] would, in fact, veto a large fraction of new physics events if ν_h decays promptly into $\nu_\alpha e^+ e^-$, for instance. In addition, LNV meson and tau decays would need to be reconsidered as the intermediate on-shell ν_h could decay dominantly via the novel NC interactions and the $\ell\pi$ and ℓK final states would be absent.

Dark photon searches Bounds on the vector portal come from several different processes [158, 291]. Electroweak precision data and measurements of the $g-2$ of the muon and electron constrain our model [292]. Major efforts at collider and beam dump experi-

ments led to strong constraints on dark photons by searching for the production and decay of these particles. Such bounds, however, depend on the lifetime of the Z' and on its branching ratio (BR) into charged particles. In our model, the Z' decays invisibly into heavy fermions if $m_{Z'} > 2m_4$ and into light neutrinos otherwise. In the latter case, constraints would be much weaker than usually quoted with only mono-photon searches [223] applying. In the former case, however, new signatures arise, where the subsequent decay of ν_h leads to multi-lepton/multi-meson events, potentially with displaced vertices and providing a very clean experimental signature. Notably, if the Z' decays into ν_h states that subsequently decay sufficiently fast within the detector, even the “invisible decay" bounds will be weakened.

Revisiting Δa_μ The above possibility opens the option to explain the discrepancy between the theoretical prediction [230,231] and the experimental value [229] of the $(g-2)$ of the muon via kinetic mixing. For instance, a 1 GeV Z' with $\chi = 2.2 \times 10^{-2}$ can explain a_μ. Taking ν_4 around 400 MeV (800 MeV) and $m_5 > m_{Z'}$, then the Z' would decay into 2 ν_4 ($\nu_4\nu_\alpha$) immediately. For the quoted value of the kinetic mixing and the largest neutrino mixing allowed, these heavy fermions would further decay into e^+e^- and $\mu^+\mu^-$ pairs plus missing energy with sub-meter decay lengths. This region of the χ parameter space is constrained only by the BaBar e^+e^- collider searches for visible [222] and invisible decays [223] of a standard dark photon. Both of these searches would veto the three-body decays of ν_4, opening up a large region of parameter space (see Ref. [293] for a similar discussion in an inelatic DM model). Resonance searches still constrain the Z' BR into e^+e^- and $\mu^+\mu^-$ which are proportional to χ^2, providing a weak upper bound. In order to shorten the lifetime of ν_4, we can increase mixing with the tau neutrino in order to avoid constraints from neutrino scattering. A detailed analysis to identify the viable parameter space is required and will be done elsewhere.

Fake rare meson decays The ν_h states can fake leptonic decays of charged mesons $M^\pm$ and charged leptons $\ell^\pm$ through the decay chains $M^\pm \to \ell^\pm_\alpha\,(\nu_h \to \nu\,\ell^+_\beta\,\ell^-_\beta)$ and $\ell^\pm_\alpha \to \ell^\pm_\beta\,\nu\,(\nu_h \to \nu\,\ell^+\,\ell^-)$. If the decays of ν_h are prompt, these could mimic rare SM 5-body decays, setting stringent constraints on $\Gamma_{M^\pm\to\ell^\pm_\alpha\nu_h} \propto |U_{\alpha h}|^2$. Measurements compatible with the SM prediction exist for pions [294,295] and kaons [296–298], where the

BR are of the order of 10^{-8}, and for muons [299] and taus [300], where the BR are around 10^{-5}. This type of signature can also lead to displaced vertices and are complementary to peak searches.

Neutrino scattering The presence of a light vector mediator and kinetic mixing can also enhance neutrino scattering cross sections. For a hadronic target Z, the active neutrinos may upscatter electromagnetically into ν_h, which subsequently decays into observable particles ($\nu_\alpha\, Z \to (\nu_h \to \nu\, \ell_\beta^+\, \ell_\beta^-)\, Z$). Beyond explaining MiniBooNE, see below, such upscattering signatures can also produce exotic final states in neutrino detectors such as $\mu^+\mu^-$, $\tau^+\tau^-$ and multi-meson final states.

MiniBooNE low energy excess The above signatures with $\ell^\pm = e^\pm$ have been invoked as an explanation of the excess of electron-like low energy events at MiniBooNE in Ref. [149], where a good fit to energy and angular data is achieved with a similar model containing a single heavy neutrino with $m_4 = 140$ MeV, $m_{Z'} = 1$ GeV and $\chi^2 = 5 \times 10^{-6}$. There, the prompt decays of ν_4 were achieved by requiring large mixing with the tau flavour. In a ESS-like limit of our current model, ν_4 would be dominantly produced via upscattering, decaying into $\nu_\alpha e^+ e^-$ inside the detector. A dedicated analysis to understand the resulting energy and angular distribution is underway.

Dark scalar searches For the scalar portal, the coupling λ is rather weakly bound by electroweak precision data and the measurement of the Higgs invisible decay at the level of $\lambda \lesssim 0.1$ [301]. For processes involving λ, the physical observables are suppressed by mass insertions due to the nature of the Higgs interaction. Nevertheless, if φ' decays to ν_h states, this scalar may also lead to multi-lepton signatures inherited from ν_h decays, potentially also in the form of displaced vertices.

In the limiting case of a neutrinophilic model ($\chi = \lambda = 0$), the vector and scalar particles present a challenge for detection. Nonetheless, if light, they can be searched for in meson decays [302, 303] and at neutrino experiments [155].

Finally, the faster decays of ν_h and its self-interactions can help ameliorate tensions with cosmological observations. We do not comment further on this, but note that great effort has been put into accommodating eV scale sterile neutrinos charged under new forces

with cosmological observables [140–143, 146, 257, 304] (see also Ref. [178] for an interesting discussion where the Z' decay to neutrinos leads to an altered expansions history of the Universe). We note that an eV sterile neutrino with relatively large mixing could be easily accommodated in our ESS framework. The eV neutrino would be mainly in the ν_D direction and would have strong hidden gauge interactions.

5.2.3 Dark Matter

Given the presence of a dark sector, we can ask if the model can accommodate a DM candidate. This can be achieved introducing new fermions that do not mix with the neutrinos, in order to preserve their stability. A minimal solution would be to introduce a fermionic field ψ_L which has $U(1)'$ charge 1/2. The different charges of ψ, ν_D and N would forbid neutrino mixing. A Majorana mass term $\psi_L^T C^\dagger \psi_L$ would emerge after hidden-symmetry breaking leading to a Majorana DM candidate.

Another minimal realisation has the advantage of being anomaly free. Following Ref. [275], we introduce a pair of chiral fermion fields ψ_L and ψ_R, and charge only the latter under the $U(1)'$ symmetry with the same charge as ν_D. This choice ensures anomaly cancellation, and allows us to write $y_\psi \overline{\psi_L} \psi_R \Phi^\dagger$, which after hidden-symmetry breaking yields a Dirac mass m_ψ. In order to avoid $\psi_R - \nu_D$ and $\psi_L - N$ mixing, an additional $\mathbb{Z}_2$ symmetry may be imposed, under which all particles have charge $+1$, except for ψ_L and ψ_R, which have charge -1. In general, this setup leads to the following mass matrix for the DM fermions

$$-\mathscr{L}_{\text{DM}-\text{mass}} = \frac{1}{2}\begin{pmatrix}\overline{\psi_R^c} & \overline{\psi_L}\end{pmatrix}\begin{pmatrix}0 & m_D^\psi \\ m_D^\psi & \mu_\psi\end{pmatrix}\begin{pmatrix}\psi_R \\ \psi_L^c\end{pmatrix} + \text{h.c.}, \tag{5.2.29}$$

where μ_ψ is the arbitrary Majorana mass term for ψ_L and $m_D^\psi = y_\psi v_\varphi/\sqrt{2}$ the Dirac mass term. Two limiting cases then appear:

$\mu_\psi \gg m_D^\psi$ This is nothing more than the Type-I Seesaw being realised in the DM sector. In this case, $m_{\psi_1} \approx (m_D^\psi)^2/\mu_\psi$ and $m_{\psi_2} \approx \mu_\psi$. Since μ_ψ is arbitrary, we can set it to be much larger than m_D^ψ. In this case, ψ_1 is our DM candidate, and it can be rather light. For instance, for $y_\psi = 1$, $v_\varphi = 4$ GeV, we find

$$m_{\psi_1} \approx 20\,\text{MeV}\left(\frac{400\,\text{GeV}}{\mu_\psi}\right). \tag{5.2.30}$$

The mixing is $\tan 2\theta = 2m_D^\psi/\mu_\psi$, such that the physical states are $\psi_1 \approx \psi_R - \theta\psi_L$ and $\psi_1 \approx \theta\psi_R + \psi_L$. In this case, ψ_1 interacts most strongly via the dark force, while the interactions of ψ_2 are suppressed by θ.

$\mu_\psi \ll m_D^\psi$ In this case, we realise a pseudo-Dirac DM scenario. Now, $m_{\psi_1} \approx m_D^\psi - \mu_\psi/2$ and $m_{\psi_2} \approx m_D^\psi + \mu_\psi/2$. In this case, the mixing is $\tan 2\theta = 2m_D^\psi/\mu_\psi$ is large, such that $\theta \to \pi/2$. Differently from inelastic DM models, both ψ_1 and ψ_2 feel the dark force with the same strength. As an example, if the heavy neutrinos remain at the GeV scale, and we ignore the scalar particle, we can reproduce the correct relic density with $g' = 4\pi$, $m_{Z'} = 1$ GeV, $m_\psi \approx 80$ MeV and $|U_{\mu h}| \approx 10^{-2}$, remaining in allowed parameter space and within reach of indirect detection searches that may be performed at DUNE [275].

If the scalar and vector portal couplings are small in such scenarios, DM interacts mainly with neutrinos. Direct detection bounds are then evaded, since interactions with matter are loop-suppressed. Indirect detection, on the other hand, is more promising as DM annihilation into neutrinos would dominate. For instance, take the mass of ψ to be smaller than the masses of the Z', φ' and of both heavy neutrinos. In this case, the DM annihilation is directly into light neutrinos via $\psi\overline{\psi} \to \nu_i\nu_i$. This yields a mono-energetic neutrino line that can be looked for in large volume neutrino [305, 306] or direct detection experiments [256]. Alternatively, if m_ψ is larger than the mass of any of our new particles, then the annihilation may be predominantly into such states via $\psi\overline{\psi} \to XX$, where $X = \varphi', Z'$ or ν_h, which subsequently decay to light neutrinos. In this secluded realisation [307], the search strategy for DM can be very different since the neutrino spectrum from such annihilation is continuous [272]. Nevertheless, neutrino-DM interactions are expected to be large and can be searched for in a variety of ways [274, 308–311].

5.3 Neutrino Portal and Mass Generation

In this section, we discuss the generation of neutrino masses in our dark neutrino model. Crucially, the new gauge symmetry forbids Majorana mass terms for the ν_D states and, after symmetry breaking, leads to a mass matrix similar to the one in the so-called minimal radiative ISS [276]. As such, this symmetry-enhanced seesaw predicts vanishing light neutrino masses at tree-level. Here, we show that it induces their radiative generation

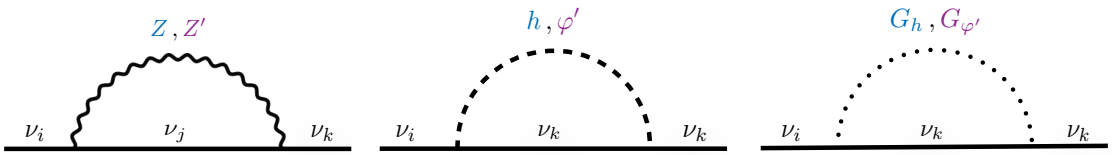

Fig. 5.2. The three contributions to the neutrino self-energy arising from novel bosons in the theory.

via one-loop diagrams involving the new scalar and vector particles [248, 276, 312]. After identifying the range of heavy neutrino parameters required to explain the observed light neutrino masses, we point out interesting phenomenological consequences.

Let us emphasize the fact that in Eq. (5.2.2), the zeros in the ν_D-ν_D and ν_α-ν_D entries are enforced by the $U(1)'$ symmetry, differently from LSS and ISS models, in which these are generically assumed to be nonzero and small due to the quasi-preservation of lepton number. Here, lepton number violation (LNV) may be large, as the μ' term breaks it by 2 units. Alternatively, it can be small and technically natural, leading to quasi-degenerate heavy neutrinos, see below. The specific form of the mass matrix in Eq. 5.2.2 implies vanishing light neutrino masses at tree level, as its determinant is zero [72, 276]. This feature holds to all orders in the seesaw expansion [72,313,314]. The light neutrino masses, however, are not protected by any symmetry and arise from radiative corrections (for a review of radiative neutrino mass models see, *e.g.*, Ref. [315]).

5.3.1 Radiative Corrections

We now show that our model generically leads to the generation of light neutrino masses at one loop. The calculation of the radiative mass term follows Refs. [316, 317] with the addition of the loops with the new boson and scalar particles shown in Fig. 5.2. The self-energy of the Majorana neutrino fields is given by

$$\Sigma_{ij}(\not{q}) = \not{q} P_{\rm L}\Sigma^{\rm L}_{ij}(\not{q}) + \not{q} P_{\rm R}\Sigma^{\rm L^*}_{ij}(\not{q}) + P_{\rm L}\Sigma^{\rm M}_{ij}(q^2) + P_{\rm R}\Sigma^{\rm M*}_{ij}(q^2).$$

Using the on-shell renormalization scheme, the renormalized mass matrix for the light neutrinos, massless at tree level, emerges at one-loop and is given by [317]

$$m_{ij}^{\text{one-loop}} = \text{Re}\left[\Sigma_{ij}^{\text{M}}(0)\right], \quad i,j < 4. \tag{5.3.1}$$

The self energy can be decomposed as

$$\Sigma_{ij}^{\text{M}}(0) = \Sigma_{ij}^{Z}(0) + \Sigma_{ij}^{h}(0) + \Sigma_{ij}^{G_h}(0) \; + \; \Sigma_{ij}^{Z'}(0) + \Sigma_{ij}^{\varphi'}(0) + \Sigma_{ij}^{G_\varphi}(0), \tag{5.3.2}$$

where Σ^{Z,h,G_h} come from the SM particles, Z^0, the Higgs and the associated Goldstone boson, respectively, and $\Sigma^{Z',\varphi',G_\varphi}$ are the new terms present in our model, mediated by the new gauge boson and new scalar components. From it, we write the 3×3 light neutrino mass matrix

$$m_{ij} = \frac{1}{4\pi^2}\sum_{k=4}^{5}\left[C_{ik}C_{jk}\frac{m_k^3}{m_Z^2}F(m_k^2, m_Z^2, m_h^2) \; + \; D_{ik}D_{jk}\frac{m_k^3}{m_{Z'}^2}F(m_k^2, m_{Z'}^2, m_{\varphi'}^2)\right], \tag{5.3.3}$$

where we defined coupling matrices corresponding to the SM and new physics interaction terms assuming $\chi = \lambda = 0$:

$$C_{ik} \equiv \frac{g}{4c_W}\sum_{\alpha=e}^{\tau} U_{\alpha i}^* U_{\alpha k} \quad \text{and} \quad D_{ik} \equiv \frac{g'}{2} U_{Di}^* U_{Dk}. \tag{5.3.4}$$

Equivalent expressions can be found for non-vanishing portal couplings, but considering experimental constraints we find that these do not play a role in the neutrino mass generation. It is possible to show that in general $\sum_k m_k C_{ik} C_{jk} = 0$ and $\sum_k m_k D_{ik} D_{jk} = 0$ for any i, j. By virtue of the latter property, the loop function can be written as

$$F(a,b,c) \equiv \frac{3\,\ln(a/b)}{a/b - 1} + \frac{\ln(a/c)}{a/c - 1}. \tag{5.3.5}$$

Turning off the g' gauge coupling, we recover the expression for the Type-I seesaw case [316]:

$$m_{ij} = \frac{\alpha_W}{16\pi}\sum_{\alpha,\beta=e}^{\tau} U_{\alpha i}^* U_{\beta j}^* U_{\alpha 5} U_{\beta 5}\frac{m_5}{m_W^2}\left(m_5^2 F(m_5^2, m_Z^2, m_h^2) - m_4^2 F(m_4^2, m_Z^2, m_h^2)\right). \tag{5.3.6}$$

These SM corrections to neutrino masses also arise in the Minimal ISS model [72, 276]. In the latter, however, no explanation is provided as to why they dominate neutrino masses. Moreover, if we restrict the discussion to scales well below the electroweak one, $m_5 \ll 10$ GeV, bounds on the mixing angles severely constrain the parameter space viable to generate the observed values of the masses.

For a light Z', the second term in Eq. 5.3.3 dominates

$$m_{ij} \simeq \frac{g'^2}{16\pi^2} U_{Di}^* U_{Dj}^* U_{D5}^2 \frac{m_5}{m_{Z'}^2} \left(m_5^2 F(m_5^2, m_{Z'}^2, m_{\varphi'}^2) - m_4^2 F(m_4^2, m_{Z'}^2, m_{\varphi'}^2) \right) . \tag{5.3.7}$$

We notice that the resulting mass matrix has only one nonzero eigenvalue. This suggests that a typical prediction of our model is a normal ordering mass spectrum, in which m_3 is given by this radiative mechanism and m_2 has another origin, for example the loops mediated by the SM gauge bosons or by additional particle content. Our simplifying assumption of one generation of hidden fermions is by no means necessary and more generations of new fermions are possible, leading to a much richer structure for the light neutrino mass matrix. The additional μ' terms would not be constrained and could be at different scales, while the Λ terms arise from the $U(1)'$ breaking and are therefore constrained to be at/below v_φ. Therefore, the full model could present a combination of relatively light Majorana ν_h, mainly in dark direction, some very heavy nearly-neutral neutrinos and pseudo-Dirac pairs at intermediate scales. A discussion of this extension is beyond our scope, but we note that it has interesting consequences for both the heavy and light neutrino mass spectra and mixing structure.

Working in a single family case, we derive expressions for Eq. 5.3.7 in the seesaw limit for both the ISS and ESS-like scenarios. In the ISS-like regime and assuming $m_{Z'}, m_{\varphi'} \ll \Lambda$, Eq. (5.3.7) simplifies to

$$m_3 \simeq \frac{g'^2}{8\pi^2} \frac{m_D^2}{m_{Z'}^2} \mu' \left(3 \ln \frac{m_{Z'}^2}{\Lambda^2} + \ln \frac{m_{\varphi'}^2}{\Lambda^2} - 4 \right) , \tag{5.3.8}$$

while for $m_{Z'}, m_{\varphi'} \gg \Lambda$ it reduces to

$$m_3 \simeq \frac{g'^2}{16\pi^2} \frac{m_D^2}{\Lambda^2} \mu' \left(3 + \frac{m_{\varphi'}^2}{m_{Z'}^2} \right) . \tag{5.3.9}$$

As it can be expected, neutrino masses are controlled by the LNV parameter μ' and are enhanced with respect to the SM contribution by a factor of $(m_Z/m_{Z'})^2$ in the former, or $(m_Z/\Lambda)^2$ in the latter case.

For the ESS-like regime, taking $m_{Z'}, m_{\varphi'} \ll \mu'$, the light neutrino mass is approximately

$$m_3 \simeq \frac{g'^2}{16\pi^2} \frac{m_D^2}{\Lambda^2 + m_D^2} \frac{\Lambda^2}{m_{Z'}^2} \mu' \left(3 \ln \frac{m_{Z'}^2}{\mu'^2} + \ln \frac{m_{\varphi'}^2}{\mu'^2} \right) , \tag{5.3.10}$$

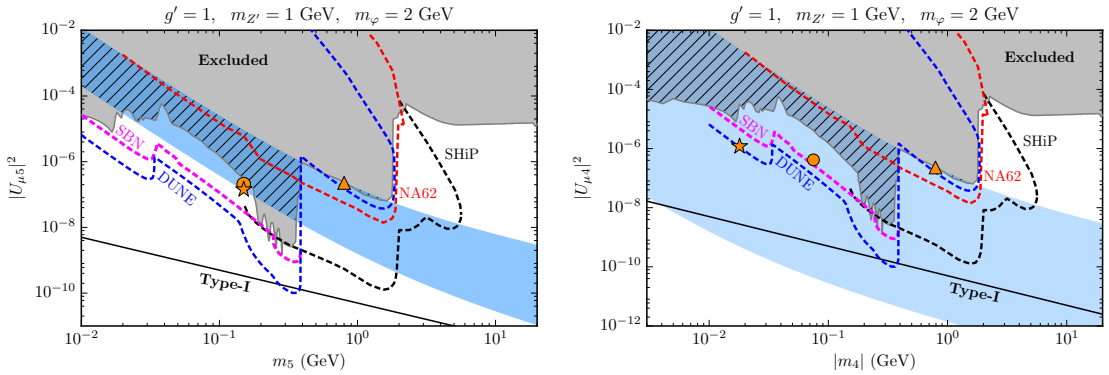

Fig. 5.3. The region of interest for neutrino mass generation in our model in the parameter space of the ν_5 (left) and ν_4 (right) mass states. We require $m_3 = \sqrt{\Delta m^2_{\rm atm}}$ and vary $1\% < m_4/m_5 < 99\%$. Our BPs are $\triangle$) $m_5 = 800$ MeV, $m_4/m_5 = 99\%$, $\circ$) $m_5 = 150$ MeV, $m_4/m_5 = 50\%$ and $\star$) $m_5 = 150$ MeV, $m_4/m_5 = 12\%$. All bounds and projections displayed assume $\chi = \lambda = 0$. The dashed black line shows the equivalent Type-I seesaw contribution to the light neutrino mass.

while for $m_{Z'}, m_{\varphi'} \gg \mu'$, it is

$$m_3 \simeq \frac{g'^2}{8\pi^2} \frac{m_D^2}{\Lambda^2 + m_D^2} \frac{\Lambda^2}{\mu'} \left(3 \ln \frac{m^2_{Z'}}{\Lambda^2} + \ln \frac{m^2_{\varphi'}}{\Lambda^2} - 4 \right). \tag{5.3.11}$$

In this case, the light neutrino masses are controlled mainly by ν_5, and the intermediate state ν_4 can be much lighter.

5.3.2 Searching for the Mass Mechanism

In what follows, we discuss the experimental reach to the heavy neutrinos responsible for neutrino mass generation in our model. Since the vector and scalar portals do not contribute significantly to neutrino masses, we first restrict the study to the case $\chi = \lambda = 0$. For the sake of simplicity and concreteness, we work with a single generation of light neutrinos and focus on the mixing with the muon neutrino. We emphasise that our model predicts

$$\frac{m_4}{m_5} = -\frac{U^2_{\alpha 5}}{U^2_{\alpha 4}}, \tag{5.3.12}$$

implying that both heavy neutrinos should be searched for. For a real mixing matrix one can write $\sum_i^3 U^2_{Di} \sim U^2_{\mu 4}$ and $U^2_{D5} \sim 1$ for small $U_{\mu 4}$. Using these relations and Eq. (5.3.3), we plot the region of interest for neutrino mass generation in Fig. 5.3. We require $m_3 = \sqrt{\Delta m^2_{\rm atm}} \sim 0.05$ eV and vary m_4/m_5 from 1% (ESS-like) to 99% (ISS-like). For the hidden sector parameters, we fix $m_{Z'} = 1$ GeV, $m_{\varphi'} = 2$ GeV and $g' = 1$. By decreasing (increasing) the mass of the Z', it is possible to shift the band to smaller

(larger) values of the mixing angles, although for values smaller than a few hundred MeV, the neutrino masses have a very mild dependence on $m_{Z'}$ (Eqs. 5.3.9 and 5.3.11). Increasing m_4/m_5 to values closer to 100% (*i.e.*, decreasing μ' below $m_5/100$) shifts the top of the band to larger values of mixing angle and asymptotically recovers lepton number as a symmetry. Although this possibility appears excluded for $m_{Z'} = 1$ GeV, it can be achieved by lowering the mass of the mediator particles. For instance, for $m_{Z'} = m_{\varphi'}/2 = 100$ MeV and $m_5 < 100$ MeV, we find that values as small as $\mu' \gtrsim 10^{-3} m_5$ are not covered by the grey region in Fig. 5.3. Values of $m_4/m_5 < 1\%$ have no effect in the parameter space of ν_5, since in that limit the ν_5 state (mostly in the N direction) dominates the loop contribution.

The region labelled as excluded in Fig. 5.3 is composed of bounds from peak searches [278–280], beam dump [281–286] and collider experiments [318–320]. Current and future neutrino experiments can also cover a large region of parameter space with $m_h \lesssim 2$ GeV. For instance, we show the sensitivity of the Short-Baseline Neutrino program (SBN) [287] and of the Deep Underground Neutrino Experiment (DUNE) near detector [321, 322] to heavy neutrinos in decay-in-flight searches. We also show the reach of the NA62 Kaon factory operating in beam dump mode [323], and the dedicated beam dump experiment Search for Hidden Particles (SHiP) [324, 325], which will cover a much larger region of parameter space from 400 MeV to $\lesssim 6$ GeV. All bounds and sensitivities shown do not take into account the new invisible decays of the heavy neutrinos. Searches that rely on the visible decay products of the heavy neutrinos need to be revisited if the ν_h can decay invisibly or if new channels mediated by the vector (and/or scalar) portal dominate. In particular, faster decays of ν_h can shift decay-in-flight bounds to lower values of mixing angles, as discussed in detail in Ref. [287]. Peak searches apply as shown provided ν_h does not decay immediately via neutral-current channels with visible charged particles.

Let us first consider the case of subdominant vector and scalar portals. Compared to the “standard" sterile neutrino case, in which ν_h have only SM interactions suppressed by neutrino mixing, the new neutral-current interaction can enhance the ν_h decays into light and heavy neutrinos. A comprehensive analysis is beyond the scope of this article and we focus on three benchmark points (BP) shown in Fig. 5.3 to exemplify the most characteristic properties. The BP represented as a triangle ($\triangle$) corresponds to $m_5 = 800$

MeV and $m_4/m_5 = 99\%$. In this case, the two heavy states are very degenerate in mass and decay like a "standard" sterile neutrino via $|U_{\mu 4}|^2$-suppressed SM charge- and neutral-current interactions. The channel $\nu_5 \to \nu_4 \nu_\alpha \overline{\nu}_\alpha$ via the Z' is phase space suppressed and becomes relevant only for larger mass splittings. The invisible ν_4 decay mediated by the Z' is subdominant as it scales as $|U_{\mu 4}|^6$ and becomes important only for larger values of the mixing angles.

For the next BPs we fix $m_5 = 150$ MeV. If we take $m_4/m_5 = 50\%$, as we do for the BP represented by the circle ($\circ$), ν_5 will predominantly decay to $\nu_4 \nu_\alpha \overline{\nu}_\alpha$ due to the Z' contribution (provided $|U_{\mu 5}|^2 \gtrsim (m_{Z'}/m_Z)^4$). Consequently, the best candidate for detection is the ν_4 via the SM weak decays $\nu_4 \to \nu_\alpha e^+ e^-$. The values of the mixing angles for this BP, $|U_{\mu 4}|^2 \sim 3 \times 10^{-7}$ and $|U_{\mu 5}|^2 \sim 10^{-7}$, are within reach of the SBN and DUNE experiments. For a larger mass hierarchy, e.g. $m_4/m_5 = 12\%$, see star BP ($\star$), the Z' mediated decay $\nu_5 \to \nu_4 \overline{\nu_4} \nu_4$ dominates, inducing a large ν_4 population in addition to the states already produced in the beam. The intermediate state ν_4 can further decay as in the previous case into $\nu_4 \to \nu_\alpha e^+ e^-$. For the mixing angles we are considering, $|U_{\mu 4}|^2 \sim 10^{-6}$ and $|U_{\mu 5}|^2 \sim 10^{-7}$, DUNE will be able to test this BP. Similar considerations apply to the case where $m_5 > m_4 + m_{Z'}$, where now the Z' can be produced on-shell in the ν_5 decay. The behaviour of ν_4 is as discussed above. If $m_{Z'} < m_4$, then both heavy neutrinos predominantly decay into neutrinos and the Z', which presents a challenge for detection as it produces mainly light neutrinos.

Experimental detection of the Z' and φ' particles in the absence of kinetic and scalar mixing is also daunting. Nevertheless, they can be searched for in the kinematics of charged particles from meson decays [302, 303]. Another strategy is to search for the neutrino byproducts of the decay of a Z' produced at accelerator neutrino facilities [155].

If the vector (and scalar) portals are non-negligible, the phenomenology could be significantly richer. In particular, Z'-mediated decays into $\nu_\alpha e^+ e^-$, and $\nu_\alpha \mu^+ \mu^-$ if kinematically allowed, could dominate even for tiny values of χ^2. For instance, for the circle BP, χ^2 as low as 10^{-8} would make the above decays the main channels. Pseudo-scalar final states are suppressed due to the vector nature of the Z'. The scalar portal is expected to give subdominant contributions due to the small Higgs-electron Yukawa coupling, although decay chains with intermediate ν_4 states may become relevant. Finally, cosmological bounds on

heavy neutrino in the 10 MeV – GeV scale may be weakened as they would decay well before Big Bang Nucleosynthesis [326] (see also the discussion in Refs. [140–143, 146, 257, 304]) The BR would have a very different structure compared to the standard neutrino and vector portals. By looking for the decay channels, one would be able to, at least partially, disentangle the neutrino, vector and scalar contributions.

We have focused on the mixing with muon neutrinos as these provide one of the most sensitive avenue to test the model. In the electron sector, direct bounds on the active-heavy mixing are similar, with peak searches from $\pi^{\pm}$ decay being most relevant below ≈ 100 MeV. For cases with large LNV, heavy neutrinos can dominate neutrinoless double beta decay [72], and this sets the strongest constraints in the parameter space. The tau sector is relatively poorly constrained, so greater freedom exists if such entries are relevant for neutrino mass generation.

Chapter 6

Testing Dark Neutrino Explanations of MiniBooNE

Anomalies in short-baseline accelerator and reactor experiments [258, 259, 261, 327] are yet to have satisfying explanations. Minimal extensions of the three-neutrino framework to explain the anomalies introduce the so-called sterile neutrino states, which do not participate in Standard Model (SM) interactions in order to agree with measurements of the Z-boson invisible decay width [328]. Unfortunately, these minimal scenarios are disfavoured as they fail to explain all data [329–331]. This has led the community to explore non-minimal scenarios. Along this direction, we have already study a well-motivated neutrino-mass model that can also explain the short-baseline anomalies in Chapter 5. In this chapter, we will focus on the phenomenological realisations of dark neutrinos that have been proposed as an explanation of the anomalous observation of ν_e-like events in MiniBooNE [259].

MiniBooNE is a mineral oil Cherenkov detector located in the Booster Neutrino Beam (BNB), at Fermilab [332, 333]. From data collected between 2002 to 2017, the experiment has observed an excess of ν_e-like events that is currently in tension with the standard three-neutrino prediction at a level of 4.7σ [259]. While it is possible that the excess is fully or partially due to systematic uncertainties or SM backgrounds (see, *e.g.*, [334–336]), many Beyond the Standard Model (BSM) explanations have been put forth. These new physics (NP) scenarios typically require the existence of new particles, which can: participate in short-baseline oscillations [337–358], change the neutrino propagation in matter [359–362],

be produced in the beam or in the detector and its surroundings [262–264, 363–367]. These models either increase the conversion of muon- to electron-neutrinos or produce electron-neutrino-like signatures in the detector, where in the latter category one typically exploits the fact that the LSND and MiniBooNE are Cherenkov detectors that cannot distinguish between electrons and photons. Although it is possible to consider MiniBooNE explanations that have little to no theoretical motivation, recent models [148, 149, 368] are motivated by neutrino-mass generation via hidden interactions in the heavy neutrino sector. In particular, the common feature of these models is the upscattering into a heavy neutrino, usually with tens to hundreds of MeV in mass, which subsequently decays into a pair of electrons. If collimated, this pair of electrons can fake a single-electron signature.

Our main contributin is introducing new techniques to probe models that rely on the ambiguity between photons and electrons to explain the MiniBooNE observation, using the dark neutrino model from [148, 368] as a benchmark scenario. Our analysis relies on neutrino-electron scattering measurements [160, 215, 217, 219, 221, 369–373]. This process is currently used to normalize the neutrino fluxes, due to its well-understood cross section, and has been a fertile ground for light NP searches [162,374,375]. Here, however, we expand the capability of these measurements to probe BSM-produced photon-like signatures, by developing a new analysis using previously neglected sideband data. Our technique is complementary to recent searches for coherent single-photon topologies [376]. Since the upscattering process has a threshold of tens to hundreds of MeV, we focus on two high-energy neutrino experiments: MINERνA [160, 215, 370, 371], a scintillator detector in the Neutrinos at the Main Injector (NuMI) beamline at Fermilab, and CHARM-II [217, 372, 373], a segmented calorimeter detector at CERN along the Super Proton Synchrotron (SPS) beamline. These experiments are complementary in the range of neutrino energies they cover and have different background composition. In all cases a relevant sideband measurement exists, allowing us to take advantage of the excellent particle reconstruction capabilities of MINERνA and the precise measurements at CHARM-II to constrain NP.

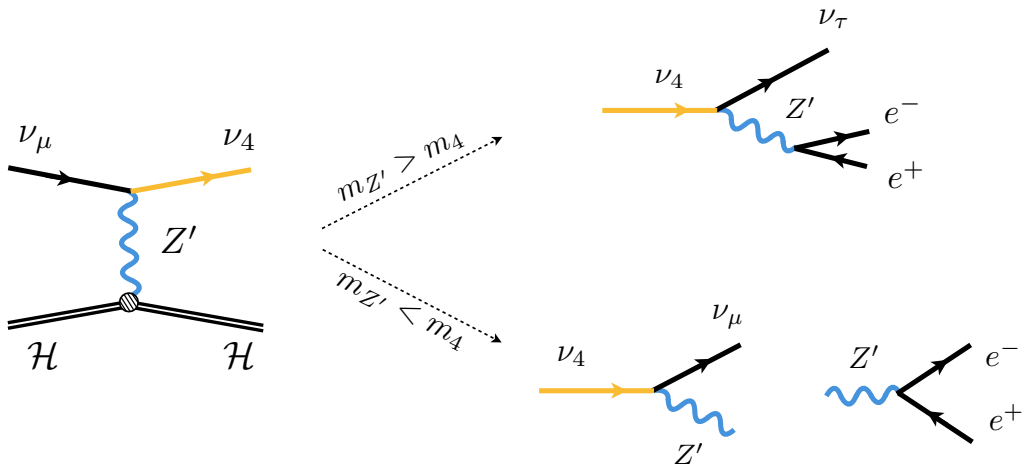

Fig. 6.1. The dark neutrino signal at MiniBooNE. We show the two phenomenological realisations of the dark neutrino model with a heavy (top) and light (bottom) mediator. In the heavy case, large $|U_{\tau 4}|^2$ is required to shorten the ν_4 lifetime.

6.1 Dark Neutrinos at MiniBooNE

We limit our discussion to the minimal version of the model that could explain the MiniBooNE excess. This contains at least one Dirac heavy neutrino[1], ν_D, charged under a new U(1)$'$ gauge group, which is part of the particle content and gauge structure needed for mass generation. The dark sector is connected to the SM in two ways: through kinetic mixing between the new gauge boson and hypercharge, and through neutrino mass mixing. We start by specifying the kinetic part of the NP Lagrangian

$$\mathscr{L}_{\text{kin}} \supset \frac{1}{4}\hat{Z}'_{\mu\nu}\hat{Z}'^{\mu\nu} + \frac{\sin\chi}{2}\hat{Z}'_{\mu\nu}\hat{B}^{\mu\nu} + \frac{m^2_{\hat{Z}'}}{2}\hat{Z}'^{\mu}\hat{Z}'_{\mu}, \tag{6.1.1}$$

where $\hat{Z}'^{\mu}$ stands for the new gauge boson field, $\hat{Z}'^{\mu\nu}$ its field strength, and $\hat{B}^{\mu\nu}$ the hypercharge field strength. After usual field redefinitions [379], we arrive at the physical states of the theory. Working at leading order in χ and assuming $m^2_{Z'}/m^2_Z$ to be small, we can specify the relevant interaction Lagrangian as

$$\mathscr{L}_{\text{int}} \supset g_D \overline{\nu}_D \gamma_\mu \nu_D Z'^{\mu} + e\varepsilon Z'^{\mu} J^{\text{EM}}_{\mu}, \tag{6.1.2}$$

where J^{EM}_{μ} is the SM electromagnetic current, g_D is the U(1)$'$ gauge coupling assumed to be $\mathcal{O}(1)$, and $\varepsilon \equiv c_{\text{w}}\chi$, with c_{w} being the cosine of the weak angle. Additional terms would be present at higher orders in χ and mass mixing with the SM Z is also possible,

[1] Models with the decay of Majorana particles will lead to greater tension with the angular distribution at MiniBooNE due to their isotropic nature [377, 378].

though severely constrained. After electroweak symmetry breaking, the dark neutrino ν_D is a superposition of neutrino mass states. The flavor and mass eigenstates are related via

$$\nu_\alpha = \sum_{i=1}^{4} U_{\alpha i}\nu_i, \quad (\alpha = e, \mu, \tau, D), \tag{6.1.3}$$

where U is a 4×4 unitary matrix. It is expected that $|U_{\alpha 4}|$ is small for $\alpha = e, \mu, \tau$, but $|U_{D4}|$ can be of $\mathcal{O}(1)$ [329,380]. The choice of m_4 and $m_{Z'}$ has important consequences for the allowed decays of the new particle content. We focus on the case in which $m_4 > m_{Z'}$, where the two body $\nu_4 \to \nu_\alpha Z'$ decay is allowed. In addition, the mass of the new gauge boson is kept below ~ 100 MeV, making the decay into e^+e^- pairs the dominant channel. Decay into a pair of neutrinos is possible, but is subdominant provided neutrino mixing is small.

6.1.1 Signature and region of interest

The heavy neutrino is produced from an active flavour state upscattering on a nuclear target A, $\nu_\alpha A \to \nu_4 A$. The upscattering cross section is proportional to $\alpha_D \alpha_{\rm QED} \varepsilon^2 |U_{\alpha 4}|^2$, dominated by $|U_{\mu 4}|$ since all current accelerator neutrino beams are composed mainly of muon neutrinos. This production can happen off the whole nucleus in a coherent way or off individual nucleons. For $m_{Z'} \lesssim 100$ MeV, the production will be mainly coherent, but for heavier masses, such as the ones considered in [149], incoherent upscattering dominates. In Fig. 6.2, we show the NP cross section at the benchmark point of [148] and compare it with the quasi-elastic cross section. By superimposing the cross section on the neutrino fluxes of MINERνA and MiniBooNE, we make it explicit that the larger energies at MINERνA and CHARM-II are ideal to produce ν_4. Once produced, ν_4 predominantly decays into a neutrino and a dielectron pair, $\nu_4 \to \nu_\alpha e^+e^-$, either via an on-shell [148] or off-shell [149] Z' depending on the choice of m_4 and $m_{Z'}$. In this work, we restrict our discussion to the $m_4 > m_{Z'}$ case, where the upscattering is mainly coherent and is followed by a chain of prompt two body decays $\nu_4 \to \nu_\alpha(Z' \to e^+e^-)$. The on-shell Z' is required to decay into an overlapping e^+e^- pair, setting a lower bound on its mass of a few MeV. Experimentally, however, $m_{Z'} > 10$ MeV for $e\epsilon \sim 10^{-4}$ to avoid beam dump constraints [158]. Increasing $m_{Z'}$ increases the ratio of incoherent to coherent events, and makes the electron pair less overlapping. Even though we focus on overlapping e^+e^- pairs, we note that a significant

fraction of events would appear as well-separated showers or as a pair of showers with large energy asymmetry, similarly to neutral current (NC) π^0 events. The asymmetric events also contribute to the MiniBooNE excess and offer a different target for searches in $\nu - e$ scattering data.

A fit to the neutrino energy spectrum at MiniBooNE was performed in [148] and is reproduced in Fig. 6.7. We have performed our own fit to the MiniBooNE energy spectrum using the data release from [259], and our results agree with [148]. This fit leads to preferred values of m_4 close to 100 MeV and $|U_{\mu 4}| \sim 10^{-4}$. Unfortunately, this energy-only fit neglects the distribution of the excess events as a function of their angle θ with respect to the beam. This is important, as the total observed excess contains only $\approx 50\%$ of the events in the most forward bin ($0.8 < \cos\theta < 1.0$), with a statistical uncorrelated uncertainty of 5% on this quantity.

As was recently pointed out in [381], few NP scenarios can reproduce the angular distribution of the MiniBooNE excess. Among these are models where new unstable particles are produced in inelastic collisions in the detector, such as the present case. Here, large θ can be achieved by tweaking the mass of the heavy neutrino; the signal becomes less forward as ν_4 becomes heavier. To show this, we use our dedicated Monte Carlo (MC) simulation to asses the values of m_4 preferred by MiniBooNE data [2]. For $m_{Z'} = 30$ MeV and $m_4 = 100$, 200, and 400 MeV, we find that 98%, 87%, and 70% of the NP events would lie in the most forward bin, respectively. The latter, as expected, is close to the benchmark point of [148]. Thus the relevant region for the MiniBooNE angular distribution is $m_4 \gtrsim 400$ MeV for $m_{Z'} = 30$ MeV.

6.2 Dark Neutrinos in Neutrino-Electron Scattering

Our goal is to develop new techniques to probe dark neutrino models in neutrino-electron scattering measurements. Our analysis showcases a generic way to look for models that rely on the ambiguity between photons and electrons to explain the MiniBooNE observation. Due to the electron-like nature of the excess, neutrino-electron scattering measurements [160, 217, 219, 221, 369] provide the kind of signature one would look for.

[2] Since the released MiniBooNE data do not provide the correlation between angle and energy, and their associated systematics, an energy-angle fit is not possible.

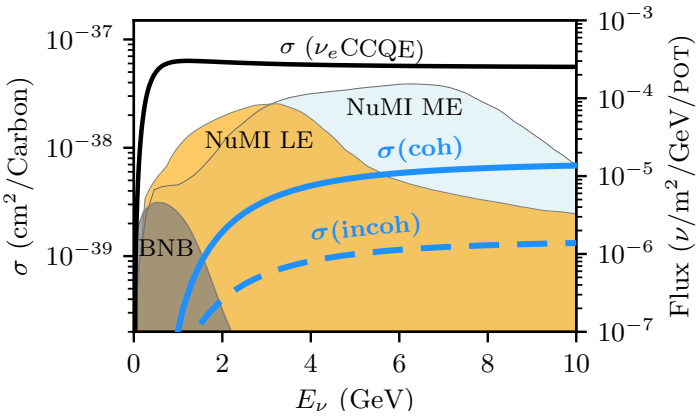

Fig. 6.2. The quasi-elastic cross section on Carbon ($6p^+$) is shown as a function of the neutrino energy (solid black line). The coherent (solid blue) and incoherent (dashed blue) scattering NP cross sections are also shown for the benchmark point of [148]. In the background, we show the BNB flux of ν_μ at MiniBooNE (light gray), and the NuMI beam neutrino flux at MINERνA for the LE (light golden) and ME (light blue) runs in neutrino mode.

Although these measurements have been shown to provide powerful constraints on light NP [162, 374, 375], the unique photon-like topology of the signatures we consider requires us to go beyond the final processed sample quoted by the experiments and make use of sideband measurements to constrain them. Since the typical heavy neutrino mass is in the hundreds-of-MeV regime, we focus on two high-energy neutrino experiments: MINERνA [160, 215, 371] and CHARM-II [217, 372, 373]. These experiments are complementary in neutrino energy and background composition. In both cases we make use of sideband measurements, taking advantage of the excellent particle reconstruction capabilities of MINERνA and the precise measurements at CHARM-II to constrain NP. In Fig. 6.2, we show the cross section at the benchmark point of [368] and compare it with the quasi-elastic cross section. By superimposing the cross section on the neutrino fluxes of MINERνA and MiniBooNE, we make it explicit that the larger energies at MINERνA and CHARM-II are ideal to probe these models.

6.3 Simulation Details

We generate events distributed according to the upscattering cross section for the process $\nu_\mu A \to \nu_4 A$, where A is a nuclear target. Here, we only discuss upscattering on nuclei, as the number of elastic scattering on protons is much smaller at these Z' masses (see Fig. 6.2). We then implement the chain of two-body decays: $\nu_4 \to \nu_\mu Z'$ followed by $Z' \to e^+e^-$. To go

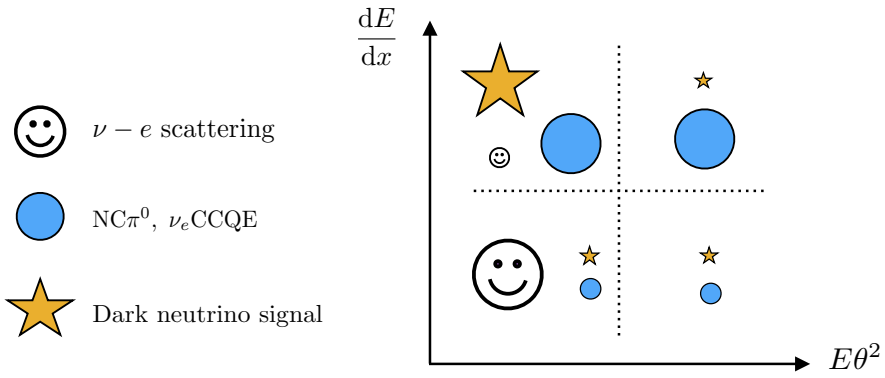

Fig. 6.3. A schematic representation of the relative number of events in sideband regions of neutrino-electron scattering analyses.

from our MC output to the predicted experimental signature, we perform three procedures. First, we smear the energy and angles of the e^+ and e^- originating from the decay of the Z' according to detector dependent Gaussian energy and angular resolutions. Next, we select all events with an overlapping e^+e^- pair, which is assumed to be reconstructed as a single electromagnetic (EM) shower. This guarantees that the events behave like a photon shower inside the detector [3]. Finally, for MINERνA and CHARM-II, these samples are subject to analysis-dependent kinematical cuts to determine if they contribute to the $\nu - e$ scattering sample. Detector resolutions, requirements for the dielectron pair to be overlapping, and analysis-dependent cuts are summarized in Table 6.1. We now list the experimental parameters used in our simulations for each individual detector.

CHARM-II The CHARM-II experiment is simulated using the CERN West Area Neutrino Facility (WANF) wide band beam [382]. The total number of POT is 2.5×10^{19} for the ν and $\overline{\nu}$ run combined. We assume glass to be the main detector material (SiO_2), such that we can treat neutrino scattering off an average target with $\langle Z \rangle = 11$ and $\langle A \rangle = 20.7$ [372,383]. The fiducial volume in our analysis is confined to a transverse area of $320\mathrm{cm}^2$ (corresponding to a fiducial mass of 547t) and the detection efficiency is taken to be 76% (efficiency for π^0 sample is quoted at 82% [384]). We reproduce the total number of $\nu - e$ scattering events with 3 GeV $< E_{\mathrm{vis}} <$ 24 GeV, namely $2677 + 2752$, to within a

[3] For MiniBooNE, we also include events that are highly asymmetric in energy, *i.e.*, $E_{\pm} > 30$ MeV and $E_{\mp} < 30$ MeV, where the most energetic shower defines the angle with respect to the beam.)

few percent level when setting the number of POTs in ν mode to be 1.69 of that in the $\overline{\nu}$ mode [385]. We assume a flux uncertainty of $\sigma_\alpha = 4.7\%$ for neutrino, and $\sigma_\alpha = 5.2\%$ for antineutrino beam [384]. The background uncertainty is constrained to be $\sigma_\beta = 3\%$ using the data with $E_{\rm vis}\theta^2 > 30$ MeV, where the number of new physics events is negligible.

MINERνA For our MINERνA simulation, we use the LE and ME NuMI neutrino fluxes [386]. The total number of POT is 3.43×10^{20} for LE data, and 11.6×10^{20} for ME data. The detector is assumed to be made of CH, with a fiducial mass of 6.10t and detection efficiencies of 73% [370,380]. We assume a flux uncertainty of $\sigma_\alpha = 10\%$ for both the LE and ME modes [91]. Due to the tuning performed in the sideband of interest, the uncertainties on the background rate are much larger. For the LE, we take $\sigma_\beta = 30\%$, while for the ME data $\sigma_\beta = 50\%$. Although tuning is significant for the coherent π^0 production sample, the overall rate of backgrounds in the sideband with large dE/dx does not vary by more than 20% (40%) in the LE (ME) tuning.

MiniBooNE To simulate MiniBooNE, we use the Booster Neutrino Beam (BNB) fluxes from Ref. [332]. Here, we only discuss the neutrino run, although the predictions for the antineutrino run are very similar. We assume a total of 12.84×10^{20} POT in neutrino mode. The fiducial mass of the detector is taken as 450t of CH_2. In order to apply detector efficiencies, we compute the reconstructed neutrino energy under the assumption of CCQE scattering

$$E_\nu^{CCQE} = \frac{E_{\rm vis} m_p}{m_p - E_{\rm vis}(1 - \cos\theta)}, \tag{6.3.1}$$

where $E_{\rm vis} = E_{e^+} + E_{e^-}$ is the total visible energy after smearing. Under this assumption, we can apply the efficiencies provided by the MiniBooNE collaboration [335].

6.4 Kinematics of the Signal

As an important check of our calculation and of the explanation of the MiniBooNE excess within the model of interest, we plot the MiniBooNE neutrino data from 2018 [259] against our MC prediction in Fig. 6.4. We do this for three different new physics parameter choices. We set $m_{Z'} = 30$ MeV, $\alpha\epsilon^2 = 2 \times 10^{-10}$ and $\alpha_D = 1/4$ for all points, but vary $|U_{\mu 4}|^2$ and

Experiment	Detector Resolution	Overlapping	Analysis Cuts
MiniBooNE			
	$\sigma_E/E = 12\%$ $\sigma_\theta = 4^\circ$	$E_+ > 30$ MeV $E_- > 30$ MeV $\Delta\theta_\pm < 13^\circ$	N/A
MINERνA			
	$\sigma_E/E = 6\%/\sqrt{E_e/\text{GeV}} + 3.4\%$ $\sigma_\theta = 1^\circ$	$E_+ > 30$ MeV $E_- > 30$ MeV $\Delta\theta_\pm < 8^\circ$	$E_{\text{vis}} > 0.8$ GeV $E_{\text{vis}}\theta^2 < 3.2$ MeV $Q^2_{\text{rec}} < 0.02$ GeV^2
CHARM-II			
	$\sigma_E/E = 9\%/\sqrt{E/\text{GeV}} + 11\%$ $\sigma_\theta/\text{mrad} = \frac{27(E/\text{GeV})^2+14}{\sqrt{E/\text{GeV}}} + 1$	$E_+ > 30$ MeV $E_- > 30$ MeV $\Delta\theta_\pm < 4^\circ$	$E_{\text{vis}} > 3$ GeV $E_{\text{vis}} < 24$ GeV $E_{\text{vis}}\theta^2 < 28$ MeV

Tab. 6.1. Experimental resolution, condition for dielectrons to be reconstructed as overlapping EM showers and analysis cuts for the detectors studied in this chapter.

m_4 so that the final number of excess events predicted by the model at MiniBooNE equals 334. Then, we repeat this process fixing $m_4 = 100$ and 420 MeV, varying $m_{Z'}$. This shows that the impact of the Z' mass on the angular distribution is minimal.

To verify that the new physics signal is important in neutrino-electron studies, we also plot kinematical distributions for the benchmark point (BP) for different detectors. This corresponds to $m_{Z'} = 30$ MeV, $\alpha\epsilon^2 = 2\times10^{-10}$, $\alpha_D = 1/4$, $|U_{\mu 4}|^2 = 9\times10^{-7}$ and $m_4 = 420$ MeV. The interesting variables are the energy asymmetry of the dielectron pair

$$|E_{\text{asym}}| = \frac{|E_+ - E_-|}{E_+ + E_-}, \tag{6.4.1}$$

as well as the separation angle $\Delta\theta_{e^+e^-}$ between the two electrons. These variables are plotted in Fig. 6.5 at MC truth level, before any smearing or selection takes place. We also plot the total reconstructed energy $E_{\text{vis}} = E_{e^+} + E_{e^-}$ and the quantity $E_{\text{vis}}\theta^2$, where θ stands for the angle formed by the reconstructed EM shower and the neutrino beam. E_{vis} and θ are computed after smearing, but before the selection into overlapping pairs takes place.

6.4.1 MINERνA and CHARM-II Analyses

Neutrino-electron scattering measurements predicate their cuts in the following core ideas: no hadronic activity near the interaction vertex, small opening angle from the beam, $E_e\theta^2 \lesssim 2m_e$, and the requirement that the measured energy deposition, dE/dx, be consistent with

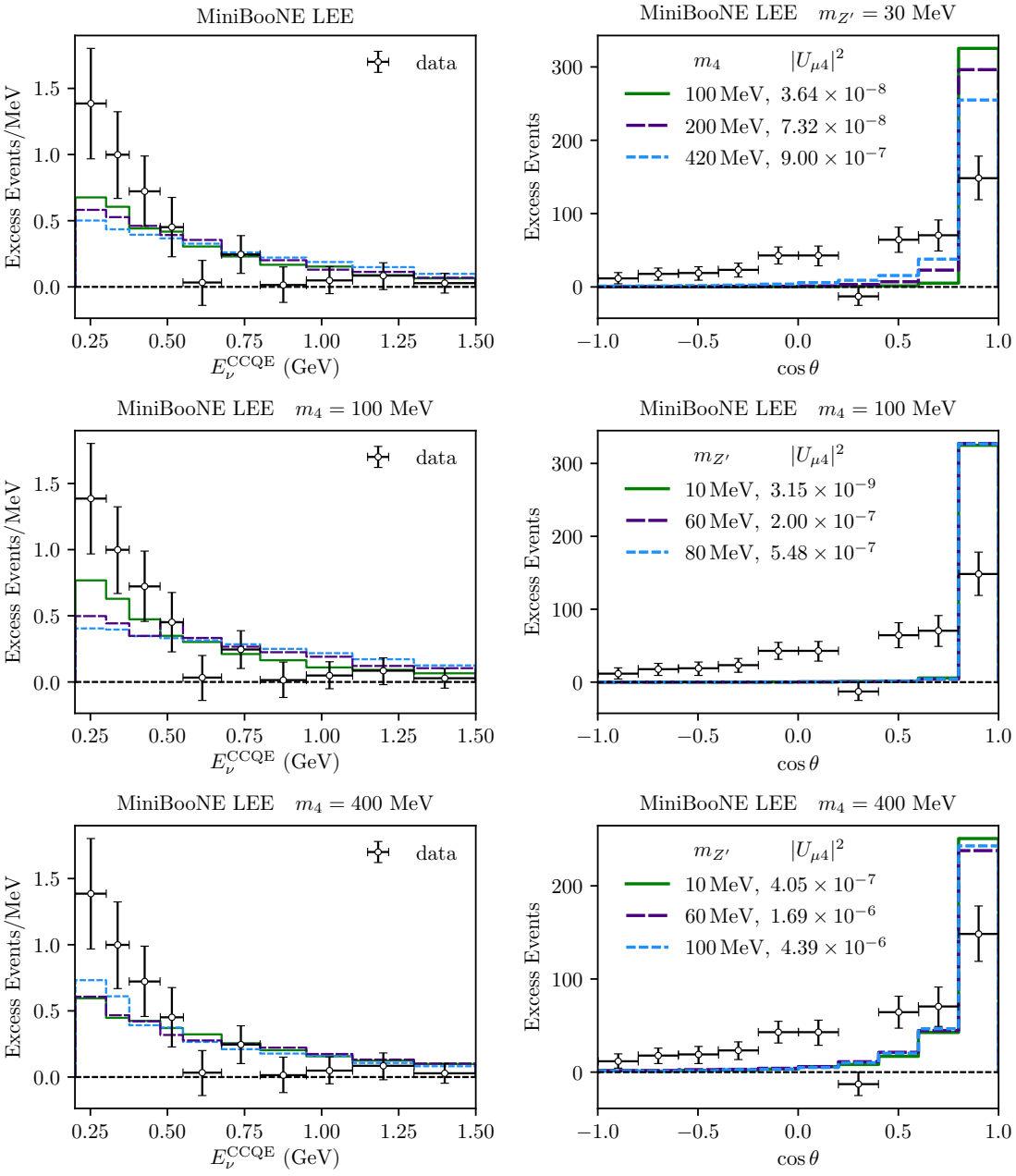

Fig. 6.4. Data and new physics prediction for the reconstructed neutrino energy at MiniBooNE under the assumption of CCQE scattering (**left**), and for the cosine of the angle between the visible EM and the neutrino beam (**right**). We fix couplings so that the total number of events at MiniBooNE equals 334.

that of a single electron. For the NP events, when the coherent process dominates and the mass of the Z' is small, the first two conditions are often satisfied. However, the requirement of a single-electron-like energy deposition removes a significant fraction of the new-physics induced events. This presents a challenge, as the NP events are mostly overlapping electron pairs and will potentially be removed by the dE/dx cut. In order to circumvent this problem, we perform our analysis not at the final-cut level, but at an

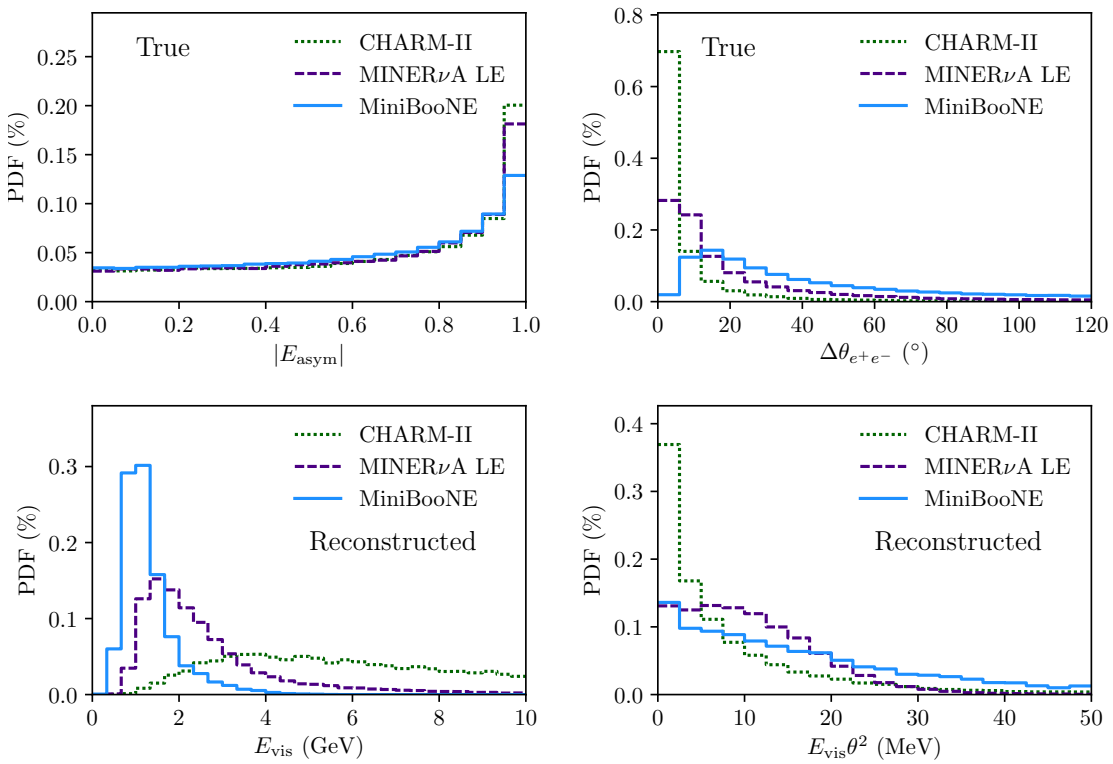

Fig. 6.5. Kinematical distributions for the new physics events at CHARM-II, MINERνA LE and MiniBooNE for the BP. We show the energy asymmetry (**top left**), the electron separation angles (**top right**), both at MC truth level. We also show reconstructed (after smearing) total visible energy E_{vis} (**bottom left**) and $E_{\text{vis}}\theta^2$ (**bottom right**).

intermediate one. This is done differently for CHARM-II and MINERνA: the CHARM-II experiment provides data as a function of $E_e\theta^2$ without the dE/dx cut, and MINERνA provides data as a function of the measured dE/dx after analysis cuts on $E_e\theta^2$.

We have developed our own MC simulation for candidate electron pair events in MiniBooNE, MINERνA and CHARM-II (see the Supplemental Material for more details on detector resolutions, precise signal definition and resulting distributions). We only consider the coherent part of the cross section to avoid hadronic-activity cuts, which is conservative. We also select only events with small energy asymmetries and small opening electron angles. When required, we assume the mean dE/dx in plastic scintillator to follow the same shape as the NC π^0 prediction. Our prediction for new physics events for the BP point is show in Fig. 6.6 on top of the MINERνA ME and CHARM-II data and MC prediction. This includes all analysis cuts, which we describe below.

The CHARM-II analysis is mostly based on Fig. 1 of [217]. This sample is shown as a function of $E\theta^2$ and does not have any cuts on dE/dx. It contains all events with

shower energies between 3 and 24 GeV, and our final cut on $E\theta^2$ is fixed at 28 MeV. For MINERνA , the event selection is identical for the LE and ME analyses [215, 370]. The minimum shower energy required is 0.8 GeV in order to remove the π^0 background and have reliable angular and energy reconstruction. Events are kept only when they meet the following angular separation criterion: $E_e\theta^2 < 3.2 \times 10^{-3}$ GeV rad^2. A final cut is applied, ensuring $dE/dx < 4.5$ MeV/1.7 cm. The MINERνA analyses use the data outside the previous dE/dx cut to constrain backgrounds. This sideband is defined by all events with $E_e\theta^2 > 5 \times 10^{-3}$ GeV rad^2 and $dE/dx < 20$ MeV/1.7 cm. Using this sideband measurement, the collaboration tunes their backgrounds by (0.76, 0.64, 1.0) for (ν_eCCQE, ν_μNC, ν_μCCQE) processes in the LE mode. Our LE analysis uses the data shown in Fig. 3 of [215] where all the cuts are applied except for the final dE/dx cut. In our final event selection, we require that the sum of the energy deposited be more than 4.5 MeV/1.7 cm, compatible with an e^+e^- pair and yielding an efficiency of 90%.

The MINERνA ME data contains an excess in the region of large dE/dx [370], where the NP events would lie. This excess is attributed to NC π^0 events, and grows with the shower energy. With normalization factors as large as 1.7, the collaboration tunes primarily the NC π^0 prediction in an energy dependent way. After tuning, the total NC π^0 sample corresponds to 20% of the total number of events before the dE/dx cut.

To place our limits, we perform a rate-only analysis by means of a χ^2 test statistic (detailed in the Supplemental Material). We incorporate uncertainties in background size and flux normalization as nuisance parameters with Gaussian constraint terms. For the neutrino-electron scattering and BSM signal, we allow the normalization to scale proportionally to the same flux uncertainty parameter. The background term also scales with the flux-uncertainty parameter but has an additional nuisance parameter to account for its unknown size. We obtain our constraint as a function of heavy neutrino mass m_4, and mixing $|U_{\mu 4}|$ assuming a χ^2 with two degrees of freedom [387].

In our nominal MINERνA LE (ME) analysis, we allow for 10% uncertainty on the flux [91], and 30% (40%) uncertainty on the background motivated by the amount of tuning performed on the original backgrounds. Note that the nominal background predictions in the MINERνA LE (ME) analysis overpredicts (underpredicts) the data before tuning, and that tuning parameters are measured at the 3% (5%) level [160, 370]. We also perform a

background-ignorant analysis in which we assume 100% uncertainty for the background normalization, which changes our conclusions by only less than a factor of two. This emphasizes the robustness of our MINERνA bound, since the NP typically overshoots the low number of events in the sideband. For the benchmark point of [148], we predict a total signal of 232 (4240) events for MINERνA LE (ME).

For CHARM-II, the NP signal lies mostly in a region with small $E\theta^2$. Thus, we constrain backgrounds using the data from $28 < E\theta^2 < 60$ MeV rad^2. This sideband measurement constrains the normalization of the backgrounds in the signal region at the level of 3%. The extrapolation of the shape of the background to the signal region introduces the largest uncertainty in our analysis. For this reason, we raise the uncertainty of the background normalization from 3% to a conservative 10% when setting the limits. Flux uncertainties are assumed to be 4.7% and 5.2% for neutrino and antineutrino mode [388], respectively, and are applicable to the new-physics signal, $\nu - e$ scattering prediction, and backgrounds. Uncertainties in the $\nu - e$ scattering cross sections are expected to be sub-dominant and are neglected in the analysis [192]. For CHARM-II, the NP also yields too many events in the signal region, namely $\approx 2.2 \times 10^5$ events for the benchmark point of [148] in antineutrino mode. If we lower $|U_{\mu 4}| = 10^{-4}$ and $m_4 = 100$ MeV, CHARM-II would still have $\approx 3 \times 10^3$ new physics events.

We have performed our own fit to the MiniBooNE energy spectrum using the data release from [259], and our results agree with [148]. The data release, however, only contains information about the neutrino energy and baseline distance. Thus, the re-weighting procedure for the model of interest can only be performed approximately. A proper analysis can be performed only if true and reconstructed electron angles and energies per simulated event are given.

6.5 Results and Prospects

The resulting limits on dark neutrinos in neutrino-electron scattering experiments are shown in the $|U_{\mu 4}|$ vs m_4 plane at 90% confidence level (CL) in Fig. 6.7. The MiniBooNE fit from [148] is shown, together with vertical lines indicating the percentage of events at MiniBooNE that populate the most forward angular bin. We have chosen the same values of ε, α_D, and $m_{Z'}$ as used in [148], and shown their benchmark point ($m_4 = 420$ MeV and

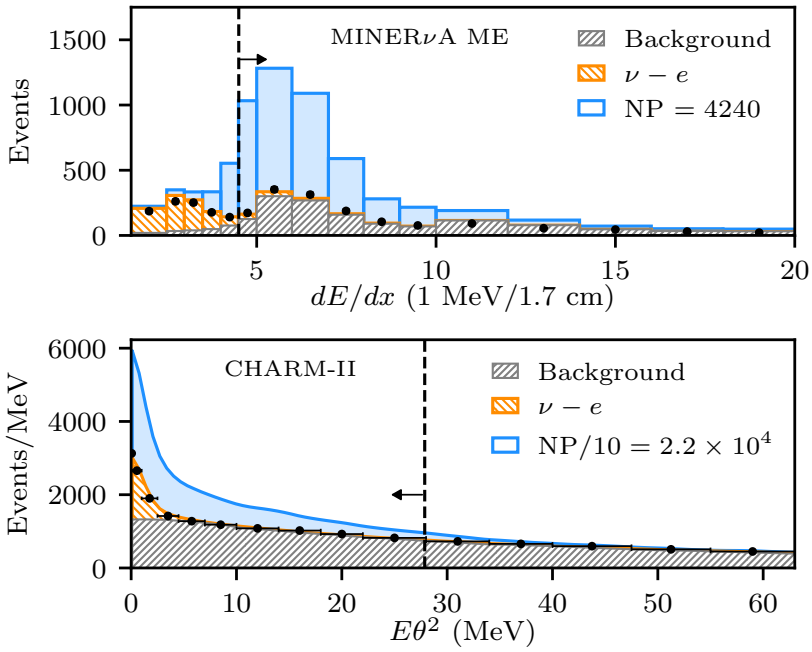

Fig. 6.6. Neutrino-electron scattering data in dE/dx at MINERνA (top) and in $E\theta^2$ at CHARM-II (bottom). Error bars are too small to be seen. For both experiments, we show the $\nu - e$ signal and total background prediction quoted (after tuning at MINERνA), as well as the NP prediction (divided by 10 at CHARM-II). The cuts in our analysis our shown as vertical lines.

$|U_{\mu 4}|^2 = 9 \times 10^{-7}$) as a dotted circle. For these parameters, we can conclude that a good angular distribution at MiniBooNE is in large tension with neutrino-electron scattering data. We note that the MiniBooNE event rate scales identically to our signal rate in all the couplings, and the dependence on $m_{Z'}$ is subleading due to the typical momentum transfer to the nucleus, provided $m_{Z'} \lesssim 100$ MeV . This implies that changing the values of these parameters does not modify the overall conclusions of our work. In addition, for this realization of the model, larger $m_{Z'}$ implies larger values of m_4, increasing the tension between the MiniBooNE fit and our bounds. Our results from MINERνA and CHARM-II are mutually reinforcing given that they impose similar constraints for $m_4 \lesssim 200$ MeV. For larger masses, the kinematics of the signal becomes less forward and the production thresholds start being important. This explains the upturns visible in our bounds, where we observe it first in MINERνA and later in CHARM-II as we increase m_4, since CHARM-II has higher beam energy. Finally, we emphasize that our analysis can be adapted to other models, such as the dark neutrino realisation of [149] and scenarios with heavy neutrinos with dipole interactions [367]. For the former, however, we do not expect our bounds to constrain the region of parameter space where the MiniBooNE explanation is viable, since

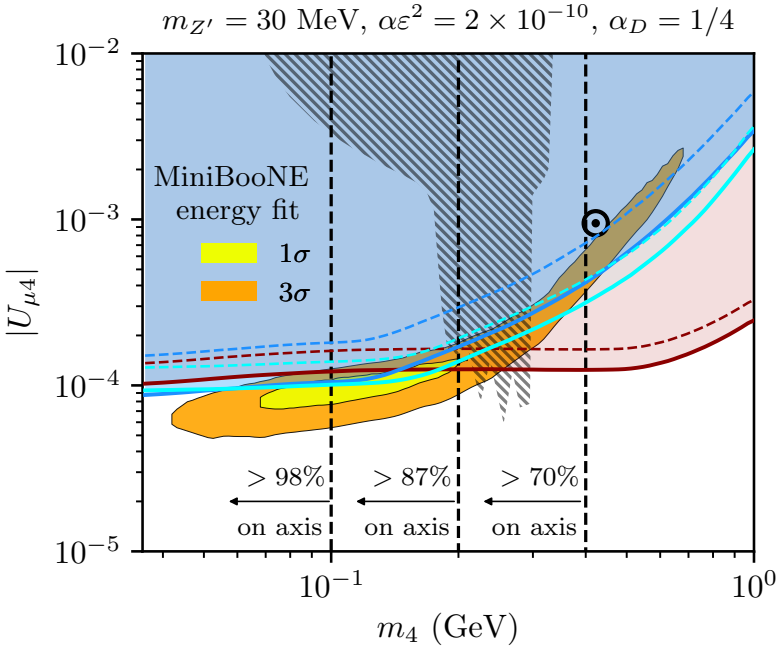

Fig. 6.7. The fit to the MiniBooNE energy distribution from [148] is shown as closed yellow (orange) region for one (three) sigma C.L., together with the benchmark point ($\odot$). Our constraints are shown at 90% C.L. for MINERνA LE in blue (solid – 30% background normalization uncertainty, dashed – conservative 100% case), for MINERνA ME in cyan (solid – 40% background normalization uncertainty, dashed – conservative 100% case), and for CHARM-II in red (solid – 3% background normalization from the sideband constraint, dashed – conservative 10% case). Vertical lines show the percentage of excess events at MiniBooNE that lie in the most forward angular bin. Exclusion from heavy neutrino searches is shown as a hatched background. Other relevant assumed parameters are shown above the plot; changing them does not alter our conclusion.

most of the signal at MiniBooNE contains hadronic activity which would be visible at MINERνA and CHARM-II.

In the near future, our new analysis strategy could be used in the up-coming MINERνA ME results on antineutrino-electron scattering. The NP cross section, being the same for neutrino and antineutrinos, is thus more prominent on top of backgrounds. This class of analyses will also greatly benefit from improved calculations and measurements of coherent π^0 production and single-photon emitting processes. This is particularly important given the excess seen in the MINERνA ME analysis. A complementary result can also be obtained by neutrino-electron scattering measurements at NOνA, which will sample a different kinematic regime as its off-axis beam peaks at lower energies and expects fewer NC π^0 events per ton. Beyond neutrino-electron scattering, the BSM signatures we consider could be lurking in current measurements of π^0 production, *e.g.*, at MINOS [389] and

MINERνA [390] [4], and in analyses like the single photon search performed by T2K [376]. To summarize, a variety of measurements are underway to further lay siege to this explanation of the MiniBooNE observation and, simultaneously, start probing testable neutrino mass generation models, as well as other similar NP signatures. It is clear that understanding neutrino cross sections will be crucial as we move forward.

[4] This ν_eCCQE measurement by MINERνA observes a significant excess of single photon-like showers attributed to diffractive π^0 events. These are abundant in similar realizations of this NP model [149].

Chapter 7

Sterile Neutrinos and Stored Muons

This chapter is dedicated to studying sterile neutrinos in short-baseline oscillations, and discusses two well-known but distinct types of non-unitarity. As a novelty, we investigate these effects with the experimental proposal of Neutrinos from STORed Muons (νSTORM). νSTORM is a proposal for a non-conventional but well-understood neutrino beam from the decay of stored muons. The energy range and the sub-percent uncertainties on the neutrino flux make νSTORM a precision facility with GeV neutrinos. On top of its importance as a first step towards large scale muon facilities (*e.g.*, neutrino factories [391] and muon colliders), the project is very timely as it would provides precise measurements of neutrino-nucleus cross sections. This would serve as an input for long-baseline physic [392], increasing the sensitivity of future experiments to CP violation and other oscillation parameters. The key step ingredient for this project lies in the precise knowledge of the flux, disentangling for the first time the knowledge of the flux from that of the cross sections. In this way, νSTORM also provides a clean and intense environment to search for new physics [135, 393, 394]. In this chapter, we will explore a νSTORM setup with two iron-scintillator detectors, resembling the original proposal for siting at Fermilab, using 60 GeV protons [393] and 3.8 GeV stored muons. At the time of writing, the Fermilab design is currently being reconsidered for siting at CERN instead. While the details of the new proposal are uncertain, it is likely to incorporate larger muon energies (up to $E_\mu \lesssim 6$ GeV) and reviewed detector options [395].

In this chapter we discuss sterile neutrinos in the most minimal extension of the SM by the neutrino portal. Although the scale of the new state is arbitrary, we would like to focus on light states which can be probed in laboratory. We adopt a pure phenomenological approach, and refrain from connecting such steriles to neutrino mass generation. In particular, we consider steriles from sub-eV masses to arbitrarily heavy states. The interest in the eV scale arises from the series of experimental anomalies at short baselines (see Refs. [396] and [331] for a review on this topic). For instance, the excess of ν_e-like events in a beam of predominantly ν_μ states at the Liquid Scintillator Neutrino Detector (LSND) [261] and at the MiniBooNE experiment [259]. Other short-baseline anomalies exist also in the form of a deficit of ν_e and $\overline{\nu}_e$ states in radioactive source experiments [397,398], as well as in reactor experiments [399]. It is intriguing, however, that these results are in severe conflict with null-results from $\nu_\mu \to \nu_\mu$ experiments, such as MINOS [400] and IceCUBE [401]. The tensions between datasets in an eV sterile neutrino interpretation of these anomalies are large. For this reason, we also refrain from connecting our discussion to such anomalies. Nevertheless, searching for steriles and non-unitarity of the PMNS matrix is a worthwhile goal of next generation experiments. This topic may also receive high priority in case of future positive results from the currently running μBooNE [402] experiment, as well as from the full short-baseline program (SBN) currently under construction at Fermilab [403]. νSTORM would offer a robust and unique chance to study eV-scale sterile neutrinos using $\nu_e \to \nu_\mu$ appearance, rather than through $\nu_\mu \to \nu_e$ appearance studied by all other experiments.

7.1 Short-Baseline Oscillations

Standard Model neutrinos produced in charged current interactions are flavour eigenstates ν_α ($\alpha = e, \mu$ or τ). The misalignment between the flavour eigenstates $|\nu_\alpha\rangle$ and the mass eigenstates $|\nu_i\rangle$ in the presence of non-degenrate masses is responsible for neutrino oscillations and mixing. The mixing is described by a matrix U, which in the case of 3 active neutrinos is given by the 3×3 Pontecorvo-Maki-Nakagawa-Sakata (PMNS) matrix. In general, for $3 + N$ flavour and $3 + N$ mass eigenstates, we have

$$|\nu_\alpha\rangle = \sum_i^{3+N} U^*_{\alpha i} |\nu_i\rangle \,. \tag{7.1.1}$$

The invisible decay width of the Z boson as measured at LEP [404] indicates that there are only 3 weakly interacting neutrino states. The N additional flavour eigenstates will be referred to as sterile states, as these are singlets under all SM gauge groups. Similarly, the N additional mass eigenstates are also typically called sterile, since that is their dominant flavour composition.

In general, in a quantum mechanical treatment of neutrino oscillations, the oscillation probability for a neutrino preoduced as a flavour α to be detected as a state β can be written as a function of the baseline L and the neutrino energy E as

$$\begin{aligned} P_{\nu_\alpha \to \nu_\beta} = \delta_{\alpha\beta} &- 2 \sum_{k>j}^{3+N} \mathrm{Re}(U^*_{\alpha k} U_{\beta k} U_{\alpha j} U^*_{\beta j}) \, (1 - \mathrm{Re}\left[I_{kj}(L,E)\right]) \\ &- 2 \sum_{k>j}^{3+N} \mathrm{Im}(U^*_{\alpha k} U_{\beta k} U_{\alpha j} U^*_{\beta j}) \, \mathrm{Im}\left[I_{kj}(L,E)\right], \end{aligned} \tag{7.1.2}$$

where the factor $I_{kj}(L,E)$ satisfies $I_{kk} = 1$ and $I^*_{kj} = I_{jk}$ [405] and will contain any information about the coherence of production, propagation and detection of neutrino mass states. More commonly, under the plane-wave approximation and assuming ultra-relativistic neutrinos with $L = t$, this factor is related to the time evolution of the mass eigenstates and reads

$$I_{kj}(L,E) = \exp\left(-i \frac{\Delta m^2_{kj} L}{2E}\right). \tag{7.1.3}$$

The plane-wave approximation, however, fails to properly accommodate effects due to the finite size of the production or detection region, which might play an important role in oscillations due to steriles with masses above a few eV. In section 7.1.1 we motivate and lay out the necessary formalism developed in [405, 406] for dealing with these issues.

Equation 7.1.1 implies that with the addition of N sterile neutrinos the mixing matrix is enlarged to an $N \times N$ matrix. At the short-baselines we are interested in, however, we can safely ignore any terms in the oscillation probability which contain the active mass-squared differences ($\Delta m^2_{31} \approx 7 \times 10^{-5}$ eV$^2 \ll \Delta m^2_{21} \approx 10^{-3}$ eV$^2 \ll \Delta m^2_{\mathrm{SBL}}$). All oscillations (as a special case of flavour transitions) discussed in this paper will be due to active-sterile mass-squared differences $\Delta m^2_{\mathrm{SBL}}$, which are taken to be in the range 10^{-1} – 10^{3} eV^2. In particular, we will only consider the case where all sterile neutrinos are heavier than the active ones.

In a 3+1 scenario under the short-baseline approximation, equation 7.1.2 gives the following

oscillation probability

$$P^{3+1}_{\nu_\alpha\to\nu_\beta} = 2|U_{\alpha4}|^2|U_{\beta4}|^2(1-\mathrm{Re}(I_{41})) \tag{7.1.4}$$

for appearance, and

$$P^{3+1}_{\nu_\alpha\to\nu_\alpha} = 1-2|U_{\alpha4}|^2(1-|U_{\alpha4}|^2)(1-\mathrm{Re}(I_{41})), \tag{7.1.5}$$

for disappearance. In the 3+1 case, it is customary to write the probabilities in terms of the more phenomenological parameters $\sin^2 2\theta_{\alpha\beta} = 4|U_{\alpha4}|^2|U_{\beta4}|^2$ and $\sin^2 2\theta_{\alpha\alpha} = 4|U_{\alpha4}|^2(1-|U_{\alpha4}|^2)$, and we use these througout the paper.

In the presence of two sterile neutrinos at the eV scale, the oscillation is effectively a 3 neutrino case. This means that the probability formula picks up a complex phase, which will be parametrized by $\eta = \arg\left(U^*_{\alpha5}U_{\beta5}U_{\alpha4}U^*_{\beta4}\right)$. The short baseline approximation to the probability reads

$$\begin{aligned} P^{3+2}_{\nu_\alpha\to\nu_\beta} =& 2\left|U_{\alpha4}\right|^2\left|U_{\beta4}\right|^2\left(1-\mathrm{Re}(I_{41})\right) + 2\left|U_{\alpha5}\right|^2\left|U_{\beta5}\right|^2\left(1-\mathrm{Re}(I_{51})\right) \\ &+2\left|U_{\alpha4}U_{\beta4}U_{\alpha5}U_{\beta5}\right|\mathrm{Re}\left[e^{i\eta}\left(1-I^*_{41}-I_{51}+I_{54}\right)\right], \end{aligned} \tag{7.1.6}$$

for apperance, and

$$\begin{aligned} P^{3+2}_{\nu_\alpha\to\nu_\alpha} =& \ 1-2(1-|U_{\alpha4}|^2-|U_{\alpha5}|^2)\times\left[|U_{\alpha4}|^2(1-\mathrm{Re}(I_{41}))+|U_{\alpha5}|^2(1-\mathrm{Re}(I_{51}))\right] \\ &-2|U_{\alpha4}|^2|U_{\alpha5}|^2\left(1-\mathrm{Re}(I_{54})\right), \end{aligned} \tag{7.1.7}$$

for disappearance. Note how the CP complex phase only appears in the appearance formulae since CPT invariance implies CP conservation for the disappearance channel. Full expressions for the oscillation probability in the plane wave approximation can be obtained by using Eq. (7.1.3), and for production decoherence assuming point-like parent particles one can use the expressions for I_{kj} we discuss below.

7.1.1 Localization at Production

The presence of light sterile neutrinos with masses above the eV scale can realise the interesting scenario where the localization at production might be broken. For a neutrino to be created as a coherent superposition of different mass eigenstates we should not be able to resolve what mass eigenstate was produced, *i.e.* $\sigma_{m^2} \gg \Delta m^2$ for all the involved mass-

splittings is a condition for production coherence [406]. Using the relativistic expression for the neutrino energy, the condition for the uncertainty on the neutrino momentum σ_P can be written as

$$\sigma_P \gg \frac{\Delta m^2}{2P}. \tag{7.1.8}$$

If we assume that σ_P is related to the uncertainty in the spatial coordinate of the neutrino as $\sigma_P \sim min(1/\sigma_{x_S}, 1/\sigma_{x_D})$, we arrive at the well known condition for neutrino oscillations not to be washed-out [405]

$$\sigma_{x_S} \ll L_{\rm osc}, \quad \sigma_{x_D} \ll L_{\rm osc}, \tag{7.1.9}$$

where $L_{\rm osc} = 4\pi P/\Delta m^2$ and factors of 2 and π were ignored. This condition says that the production or detection decoherence effects are equivalent to the averaging of the oscillations due to finite size of sources and detectors.

The production region at νSTORM, for example, is given by the size of the decay pipeline $\ell_p = 180$ m. This is only an order of magnitude smaller than the far detector baseline (≈ 2 km) and, more importantly for higher mass sterile searches, it is larger than the near detector distance from the end of the decay pipeline. For instance, if a sterile neutrino with a mass larger than 10 eV is present, the near detector would only see flavour transitions constant in energy.

The probabilities derived in the previous section have been derived for a general factor I_{kj}, which under the plane-wave approximation is given by equation 7.1.3. In the wavepacket treatment for neutrino oscillations, I_{kj} is corrected by production, detection and propagation coherence factors [405]:

$$I_{kj} = \exp\left(-i\frac{\Delta m^2_{kj} L}{2P}\right) S_{\rm prop}(L/L^{\rm coh}_{kj}) S_{\rm P/D}(\sigma_x/L^{\rm osc}_{kj}), \tag{7.1.10}$$

where the S damping factors are due to propagation coherence, and localization at production and detection. The quantity $L^{\rm coh}_{kj} = 4\sqrt{2}E^2\sigma_x/|\Delta m^2_{kj}|$ is the coherence lenght of a pair of mass eigenstates, *i.e.* the lenght in which the two states continue to have a significant overlap of their coordinate wave packets. The S factors are equal to unity for zero arguments and quickly decrease for increasing arguments. In this study, we ignore any propagation and detection effects and focus only on the production localization S_P. We choose to work with the formalism developed in references [406, 407], where oscillation probabilities were derived in the quantum mechanical wavepacket approach. This approach

is in contrast with the incoherent summation of the probability along the production region, where the straight averaged neutrino flux is given by a convolution of the plane wave probability formula and the neutrino flux at different points of the decay straight. The equivalence of the two approaches is discussed in Ref. [406], and for all our purposes they lead to the same results as long as the neutrino parent particles can be treated as pointlike, *i.e.* have vanishingly small wavepacket spatial width. It should be emphasized, however, that the wavepacket formalism is more general than the incoherent probability summation. Moreover, the available neutrino fluxes for νSTORM already take the finite size of the production region into account [408], and cannot be convolved with the oscillation probability over the production region once more.

Finally, let us emphasize our results are robust against different estimates for the neutrino wavepacket. If it turns out to be smaller than the production region, due to collisions of the parent partcles with the residual gas in the decay pipe, for instance, then our results remain unchanged. This is because even in this scenario, the production region is large, and the classical avereging of the probability over it leads to the washing out of the oscillation. This is, again, a reflection of the fact that our formalism is analogous to the incoherent summation of the probability over the production region. If, instead, the wavepacket is larger, due to large parent particle wavepacket size, for instance, then corrections to our method are in place. In this case, additional averaging effects would be at play, suppressing oscillations with large Δm^2.

Expressions for the S_P factors as well as the full oscillation probabilities for some channels are given below. For completeness, we show the I_{kj} factors that have been used in our calculations, corresponding to the case of pointlike parent particles and pontlike detection approximations derived in [405]. For clarity, we omit all $k\,j$ mass subscripts in our expression, leaving only indices corresponding to the neutrino parent particle $X = \mu, \pi$. We write it in two forms: a compact formula, and one in which the real and imaginary parts are explicitly separated:

$$\begin{aligned} I_{kj} &= \frac{1}{1-e^{-\Delta_p/\xi_X}}\frac{1}{1-i\xi_X}\left[1-e^{-\Delta_p/\xi_X}e^{i\Delta_p}\right]e^{-i\Delta} \\ &= \frac{1}{1-e^{-\Delta_p/\xi_X}}\frac{1}{1+\xi_X^2}\Big\{\cos\Delta+\xi_X\sin\Delta-e^{-\Delta_p/\xi_X}\left(\cos\left(\Delta-\Delta_p\right)+\xi_X\sin\left(\Delta-\Delta_p\right)\right)+ \\ &\qquad i\left[\xi_X\cos\Delta-\sin\Delta-e^{-\Delta_p/\xi_X}\left(\xi_X\cos\left(\Delta-\Delta_p\right)-\sin\left(\Delta-\Delta_p\right)\right)\right]\Big\}. \end{aligned} \tag{7.1.11}$$

In the expression above we denote the lenght of the decay pipeline by ℓ_p and use the following definitions:

$$\Delta = \frac{\Delta m^2_{kj}}{2P} L, \quad \Delta_p = \frac{\Delta m^2_{kj}}{2P} \ell_p, \quad \xi_X = v_X \frac{\Delta m^2_{kj}}{2P} \ell_{\mathrm{dec}_X}, \tag{7.1.12}$$

where the parent particle properties enter our probability formulas via ξ_X with the velocity v_X and the decay lenght $\ell_{\mathrm{dec}_X} = 1/\Gamma_X$.

Using the definitions above and the I_{kj} factor in Eq. (7.1.11), we can write the probability formulas for our 3+N models. As an example, we show the 3+1 apperance and disapperance formulas of interest, choosing $\sin^2 2\theta_{e\mu} = 4|U_{e\mu}|^2|U_{\mu\mu}|^2$ and $\sin^2 2\theta_{\mu\mu} = 4|U_{e\mu}|^2(1-|U_{\mu\mu}|^2)$. For appearance, it reads

$$P^{3+1}_{\nu_e\to\nu_\mu} = \sin 2\theta_{e\mu}\Big\{1 - \frac{1}{1-e^{-\Delta_p/\xi_X}}\frac{1}{1+\xi_X^2}\Big[\cos\Delta + \xi_X \sin\Delta \\ - e^{-\Delta_p/\xi_X}\big(\cos(\Delta-\Delta_p) + \xi_X \sin(\Delta-\Delta_p)\big)\Big]\Big\}, \tag{7.1.13}$$

while for disappearance,

$$P^{3+1}_{\nu_\mu\to\nu_\mu} = \sin^4\theta_{\mu\mu} + \cos^4\theta_{\mu\mu} + \frac{\sin^2 2\theta_{\mu\mu}}{1-e^{-\Delta_p/\xi_X}}\frac{1}{1+\xi_X^2}\Big[\cos\Delta + \xi_X\sin\Delta \\ - e^{-\Delta_p/\xi_X}\big(\cos(\Delta-\Delta_p) + \xi_X\sin(\Delta-\Delta_p)\big)\Big]. \tag{7.1.14}$$

7.1.2 Non-Unitarity from Light and Heavy Sterile Neutrinos

The scale of the new sterile state is completely arbitrary from a theoretical point of view, each one with its own distinct phenomenology. At most oscillation experiments, however, any sterile neutrino with a mass above $\mathcal{O}(10)$ eV leads to what we call an effective *zero-distance* effect, whether through its averaged-out oscillations or due to integrating out the heavy states. In the following, we will have a glimpse these two regimes. In all our discussion we will neglect the decay of the heavy states, although we note that extra interactions of the new states trying to reconcile cosmology and sterile neutrinos might decrease its lifetime [409–412].

It is instructive to divide the parameter space into three regions.

- The sterile neutrino is kinematically accessible and can be produced in muon or pion decays, but its oscillation lenght is too small to be seen at any reasonable experiment.

- The sterile mass is close to but still smaller than the parent particle mass and impacts the neutrino production and detection rate due to kinematical factors. This intermediate region is relevant for meson decay peak searches, but less important for oscillation experiments.
- The sterile is much heavier than the parent particle and cannot be produced at the oscillation experiments. This is effectively identical to integrating out the heavy state.

There is no fundamental difference between the first two scenarios, except that in the first one the effects due to the mass of the sterile are too small to be relevant. The third case concerns masses above the electroweak scale, and is typically studied under the minimal unitarity violation (MUV) formalism [413]. In an effective field theory, one can parametrize the effects of these large mass steriles via the non-unitarity of the PMNS matrix. One can show that this arises from the non-orthonormality of the low-scale flavour states at oscillation experiments.

We will aim at connecting the high-scale non-unitarity and the averaged out oscillations of light steriles. First, however, we will explore where the zero-distance effects are coming from in the two cases. Later, by trying to be as general as possible in the derivation of the event rates, we will attempt to develop a formalism that explicitly shows how these effects change at different mass scales.

Averaged-Out Steriles

First, we will explore the phenomenology of sterile neutrinos above the eV scale but lighter than their parent particles. Once the sterile mass is too large to allow for oscillation with active neutrinos to happen (*e.g.*, due to production localization effects) the sterile states contribute to the oscillation probability only through a constant term. This contribution stems from the fact that even in the absence of oscillations, flavour transitions are still possible. This regimes comprises masses of $10\,\text{eV} \lesssim m_4 < m_\mu(m_\pi)$.

If we neglect any effects on the neutrino production due to the sterile mass, and take the limit of $L \ll L_{kj}^{\text{osc}}$ (or $\sigma_x \ll L_{kj}^{\text{osc}}$), we get

$$P_{\nu_\alpha \to \nu_\beta} = \sum_{k}^{3+N} |U_{\alpha k}|^2 |U_{\beta k}|^2 + 2 \sum_{k>j}^{3} \text{Re}\Big\{ \Big(U_{\alpha k}^* U_{\alpha j} U_{\beta k} U_{\beta j}^* \Big) \Big\},$$

$$= \left| \sum_{k}^{3} U^*_{\alpha k} U_{\beta k} \right|^2 + \sum_{k=3+1}^{3+N} |U_{\alpha k}|^2 |U_{\beta k}|^2, \tag{7.1.15}$$

where we averaged out active-sterile phases to zero and kept all active terms for which $L \ll L^{\rm osc}_{kj} = 4\pi E/\Delta m^2_{kj}$. In a 3+1 model, for instance, one can reduce this expression using the unitarity of the mixing matrix $\sum_k^{3+1} U_{\alpha k} U^*_{\beta k} = \delta_{\alpha\beta}$ to

$$P_{\nu_\alpha \to \nu_\beta} = 2|U_{\alpha 4}|^2 |U_{\beta 4}|^2, \quad P_{\nu_\alpha \to \nu_\alpha} = 1 - 2|U_{\alpha 4}|^2 + 2|U_{\alpha 4}|^4, \tag{7.1.16}$$

for appearance and disappearance, respectively. The interpretation of the appearance formula is clear: the constant oscillation probability only provides the mixing factor required to obtain the flux of sterile states from the flux of ν_α at production and another mixing factor to obtain the probability that such a state interacts as a neutrino of flavour β. The zero-distance effects in this case is given by the possibility that the sterile state is produced, propagates ballistically to the detector and scatters off a nuclei creating another flavour lepton.

Integrated-Out Steriles

In this section we summarize the main results of Ref. [413]. The mixing amongst active neutrinos is given by the sub-block N of the neutrino mixing matrix U, such that the flavour neutrino fields are given by

$$\nu_\alpha = \sum_{i}^{3} N_{\alpha i}\, \nu_i, \quad \text{where} \quad U = \begin{pmatrix} N & \Theta \\ R & S \end{pmatrix}. \tag{7.1.17}$$

Here, U is the full unitary mixing matrix of neutral leptons, and N the non-unitary PMNS matrix describing the mixing of active-light states. R, S and Θ contain the mixing between active-heavy, sterile-heavy and sterile-light states, respectively, and are also not unitary in general. Note that the orthonormality of the neutrino mass states still holds, but the quantum states associated to neutrinos of a specific flavour (like the state produced from the decay of a pion or a muon) are no longer formed by a complete basis, and are no longer orthonormal. The true flavour states are orthonormal, but they require the presence of the heavy neutrino state, which is not produced in terrestrial oscillation experiments.

Additional normalization factors are then necessary for the flavour state produced

$$|\nu_\alpha\rangle = \frac{1}{\sqrt{(NN^\dagger)_{\alpha\alpha}}} \sum_i^3 N^*_{\alpha i} |\nu_i\rangle \,, \tag{7.1.18}$$

where for a 3+1 model, for example, would yield $(NN^\dagger)_{\alpha\alpha} = 1 - |U_{\alpha 4}|^2$. This normalization factor appears in the calculation of the oscillation probability as

$$P_{\nu_\alpha \to \nu_\beta} = \frac{\left| \sum_i^3 N^*_{\alpha i} e^{-iP_i L} N_{\beta i} \right|^2}{(NN^\dagger)_{\alpha\alpha}(NN^\dagger)_{\beta\beta}}, \tag{7.1.19}$$

which at zero-distance ($L = 0$, before active oscillations take place) is

$$P_{\nu_\alpha \to \nu_\beta} = \frac{\left| (NN^\dagger)_{\beta\alpha} \right|^2}{(NN^\dagger)_{\alpha\alpha}(NN^\dagger)_{\beta\beta}}. \tag{7.1.20}$$

This is not the end of the story, however, as the neutrino production and detection also receive corrections due to the non-unitarity of the mixing matrix. In particular, the following relations are valid for charged current processes (CC) with a single neutrino involved

$$\sigma_\alpha^{\rm CC} = \sigma_\alpha^{\rm CC\ (SM)} (NN^\dagger)_{\alpha\alpha}, \quad \frac{d\Phi_\beta^{\rm CC}}{dE} = \frac{d\Phi_\beta^{\rm CC\ (SM)}}{dE} (NN^\dagger)_{\beta\beta}, \tag{7.1.21}$$

whilst for CC processes with two neutrino flavours (*e.g.*, muon decay) receive additional corrections

$$\sigma_\alpha^{\rm CC} = \sigma_\alpha^{\rm CC\ (SM)} (NN^\dagger)_{\alpha\alpha}(NN^\dagger)_{\beta\beta}, \quad \frac{d\Phi_\beta^{\rm CC}}{dE} = \frac{d\Phi_\beta^{\rm CC\ (SM)}}{dE} (NN^\dagger)_{\alpha\alpha}(NN^\dagger)_{\beta\beta}. \tag{7.1.22}$$

Neutral current processes also receive corrections, but of the type $|(NN^\dagger)_{ij}|^2$. The previous expressions hint at a cancellation between the normalization factors in the probability and the corrections to the production and detection. This means that at an oscillation experiment neutrinos from pion decay would not be affected by the normalization factors, whilst neutrinos from muons could. In addition, the oscillation probability differs from the averaged out one, even when the cancellations are in place. We can see that by comparing the quartic term in the following 3+1 probability with the one in the previous section (Eq. (7.1.16))

$$P_{\nu_\alpha \to \nu_\beta} = \frac{|\delta_{\alpha\beta} - U^*_{\alpha 4} U_{\beta 4}|^2}{(1 - |U_{\alpha 4}|^2)(1 - |U_{\beta 4}|^2)} = \frac{\delta_{\alpha\beta} - 2\delta_{\alpha\beta}|U_{\alpha 4}|^2 + |U_{\alpha 4}|^2 |U_{\beta 4}|^2}{(1 - |U_{\alpha 4}|^2)(1 - |U_{\beta 4}|^2)}. \tag{7.1.23}$$

For completeness, we also show the parameterizations for the non-unitarity of the mixing matrix N used in the literature. For instance, Ref. [139] chooses to use a lower triangular

matrix $\boldsymbol{\alpha}$ as in

$$N = (\mathbf{1} - \boldsymbol{\alpha})U, \tag{7.1.24}$$

where U is the analogue of the PMNS matrix and unitary and

$$\boldsymbol{\alpha} = \begin{pmatrix} \alpha_{ee} & 0 & 0 \\ \alpha_{\mu e} & \alpha_{\mu\mu} & 0 \\ \alpha_{\tau e} & \alpha_{\tau\mu} & \alpha_{\tau\tau} \end{pmatrix},$$

with real diagonal entries. Using the previous parametrization one can then write the quantity of interest $NN^\dagger$ (omitting the tau entries) as

$$NN^\dagger = \mathbf{1} - \boldsymbol{\alpha} - \boldsymbol{\alpha}^\dagger + \boldsymbol{\alpha}\boldsymbol{\alpha}^\dagger = \begin{pmatrix} 1 - 2\alpha_{ee} + \alpha_{ee}^2 & \alpha_{\mu e}^*(\alpha_{ee} - 1) & * \\ \alpha_{\mu e}(\alpha_{ee} - 1) & 1 - 2\alpha_{\mu\mu} + \alpha_{\mu\mu}^2 + |\alpha_{\mu e}|^2 & * \\ * & * & * \end{pmatrix}. \tag{7.1.25}$$

Alternatively, one can parametrize N as $N = \boldsymbol{T}U$, where we use the matrix $\boldsymbol{T}$ from Ref. [414], which is written as

$$\boldsymbol{T} = \begin{pmatrix} \alpha_{11} & 0 & 0 \\ \alpha_{21} & \alpha_{22} & 0 \\ \alpha_{31} & \alpha_{32} & \alpha_{33} \end{pmatrix}. \tag{7.1.26}$$

In this parametrization, the quantity of interest $NN^\dagger$ is slightly simpler

$$NN^\dagger = \begin{pmatrix} \alpha_{11}^2 & \alpha_{11}\alpha_{21}^* & * \\ \alpha_{11}\alpha_{21} & \alpha_{22}^2 + |\alpha_{21}|^2 & * \\ * & * & * \end{pmatrix}, \tag{7.1.27}$$

and the relation between the two parametrizations is clear: $\alpha_{\alpha\beta} \to \delta_{ij} - \alpha_{ij}$, with $e \to 1, \mu \to 2$ and $\tau \to 3$. Bounds on the non-unitarity parameters can be derived from a variety of processes and have been collected in Refs. [415], for instance.

Understanding the Gap

In this section we will connect the two regimes described above at the level of oscillation probabilities. For the sake of our argument, a plane wave treatment is sufficient. We begin

with a neutrino flavour state produced in the interaction $P_I \to P_F\, \ell_\alpha^+\, \nu_\alpha$, written as

$$|\nu_\alpha\rangle = \frac{1}{\sqrt{\sum_i |A_{\alpha i}|^2}} \sum_k^{3+N} A_{\alpha k}\, |\nu_k\rangle\,, \tag{7.1.28}$$

where the amplitude for producing a neutrino mass eigenstate is given by

$$A_{\alpha k} = \left\langle \nu_k, \ell_\alpha^+, P_F \right| \hat{S}\, |P_I\rangle = U_{\alpha k}^* \mathcal{F}_k M_\alpha. \tag{7.1.29}$$

Here we factorised the amplitude for neutrino production into a mixing matrix element $U_{\alpha k}$, a factor $\mathcal{F}_k$ containing all the dependence on the neutrino mass m_k, and the remaining flavour-dependent factor M_α. Just remains an *assumption* in what follows. More concretely, the factor $\mathcal{F}$ can be thought of as a kinematical factor in the calculation of the neutrino production and detection, and carries information about the heavy neutrino mass and its ratio to the other scales involved. In writing the equation above, we are assuming that the matrix element M_α has no dependence on the neutrino mass [1]. Within our assumptions, $\mathcal{F}_k = 1$ when $m_k \ll M_P$, where M_P is the mass of the parent particle of the neutrino, and $\mathcal{F}_k = 0$ when $m_k > M_P$. The amplitude for the production of a neutrino of specific flavour is then

$$|A_\alpha|^2 = \sum_k |U_{\alpha k}|^2\, |\mathcal{F}_k|^2\, |M_\alpha|^2\,. \tag{7.1.30}$$

When only one heavy neutrino is present and all light states have $\mathcal{F}_k = 1$ for $k < 4$, we can write

$$|A_\alpha|^2 = \left(\sum_k^3 |U_{\alpha k}|^2 + |U_{\alpha 4}|^2\, |\mathcal{F}_4|^2 \right) |M_\alpha|^2 = \left(1 + \left(|\mathcal{F}_4|^2 - 1 \right) |U_{\alpha 4}|^2 \right) |M_\alpha|^2 \tag{7.1.31}$$

reducing to

$$|A_\alpha|^2 = |M_\alpha|^2, \tag{7.1.32}$$

for averaged-out steriles, and

$$|A_\alpha|^2 = \left(1 - |U_{\alpha 4}|^2 \right) |M_\alpha|^2, \tag{7.1.33}$$

for integrated-out steriles. The neutrino flux, which is proportional to $|A_\alpha|^2$, receives similar corrections. A very similar discussion can be made for the amplitude of detection, where we will now call $\mathcal{F}_k^P$ and $\mathcal{F}_k^D$ the kinematical factor for the production and detection

[1] While this is customary for $\mathcal{F}^P$, which can be thought of as a Shrock factor [416] in meson decay processes, $\mathcal{F}^D$ requires more care due to the more complex nature of the scattering process.

state, respectively.

We will now calculate the flavour transition probability assuming that the fourth mass eigenstate is heavy enough that it will not oscillate, allowing only for zero-distance effects. We start by defining general flavour states as in Eq. (7.1.28) for production and detection, $\left|\nu_\alpha^P\right\rangle$ and $\left|\nu_\beta^D\right\rangle$. Expanding the amplitude as in Eq. (7.1.29), we obtain the production state

$$\left|\nu_\alpha^P\right\rangle = N_\alpha^P \, \hat{M}_\alpha^P \sum_i^{3+N} U_{\alpha i}^* \mathcal{F}_i^P \left|\nu_i\right\rangle , \tag{7.1.34}$$

where $\hat{M}_\alpha^P = M_\alpha^P/|M_\alpha^P|$ and $\left(N_\alpha^P\right)^{-2} = \sum_i^{3+N} \left|U_{\alpha i}\mathcal{F}_i^P\right|^2$. An analogous expression is valid for the detection state. When calculating the oscillation probability, we will need the transition amplitude

$$\mathcal{A}_{\alpha\to\beta} = \left\langle \nu_\beta^D \right| e^{-i\hat{E}T + i\hat{p}L} \left|\nu_\alpha^P\right\rangle = N_\alpha^P N_\beta^D \, \hat{M}_\alpha^P \hat{M}_\beta^{D*} \sum_k^{3+N} U_{\alpha k}^* \mathcal{F}_k^P U_{\beta k} \mathcal{F}_k^{D*} e^{-i\phi_{kj}} . \tag{7.1.35}$$

Squaring it, we get the oscillation probability

$$P_{\alpha\to\beta} = \left(N_\alpha^P \, N_\beta^D\right)^2 \sum_{k,j}^{3+N} U_{\alpha k}^* U_{\alpha j} U_{\beta k} U_{\beta j}^* \, \mathcal{F}_k^P \mathcal{F}_j^{P*} \mathcal{F}_k^{D*} \mathcal{F}_j^D e^{-i\phi_{kj}} . \tag{7.1.36}$$

The oscillation phase $\phi_{kj} = (E_k - E_j)T - (p_k - p_j)L$ was obtained under the plane-wave assumption, so only the oscillation term L/L_{kj}^{osc} is relevant here. The following two extreme cases are important: $e^{-i\phi_{kj}}$ goes to one for undeveloped oscillations ($L/L_{kj}^{\text{osc}} \to 0$), and $e^{-i\phi_{kj}}$ gets averaged out to zero for oscillations developed too early compared to the experimental baselines ($L/L_{kj}^{\text{osc}} \to \infty$). In the presence of N sterile neutrinos (with $L_{kj} \ll L_{\text{detector}}$, where $k > 3$ and $j \leq 3$), we can write

$$P_{\alpha\to\beta} = \left(N_\alpha^P \, N_\beta^D\right)^2 \left(\left| \sum_k^3 U_{\alpha k}^* U_{\beta k} \mathcal{F}_k^P \mathcal{F}_k^{D*} \right|^2 + \sum_{k=3+1}^{3+N} |U_{\alpha k}|^2 |U_{\beta k}|^2 |\mathcal{F}_k^P|^2 |\mathcal{F}_k^D|^2 \right) . \tag{7.1.37}$$

Using the unitarity of the whole mixing matrix and assuming $\mathcal{F}_i = 1$ for $i = 1, 2$ and 3, we can rewrite the previous expression more simply for a 3+1 model as

$$\begin{aligned} P_{\alpha\to\beta} = &\left(1 + (|\mathcal{F}_4^P|^2 - 1)|U_{\alpha 4}|^2\right)^{-1} \left(1 + (|\mathcal{F}_4^D|^2 - 1)|U_{\beta 4}|^2\right)^{-1} \\ &\times \left[\delta_{\alpha\beta} - 2\delta_{\alpha\beta}|U_{\alpha 4}|^2 + |U_{\alpha 4}|^2 |U_{\beta 4}|^2 \left(|\mathcal{F}_4^P|^2 |\mathcal{F}_4^D|^2 + 1\right)\right] . \end{aligned} \tag{7.1.38}$$

To check we recover the known expressions for an averaged-out sterile ($|\mathcal{F}_k| = 1$) and an integrated-out sterile ($|\mathcal{F}_k| = 0$) in a 3+1 model, we rewrite the previous expression for

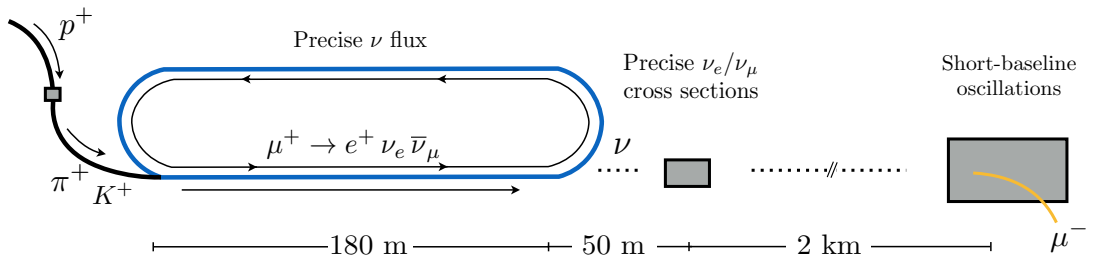

Fig. 7.1. νSTORM in a diagram.

each case.

$$\text{Averaged-out sterile:} \quad P_{\alpha\to\beta} = \delta_{\alpha\beta} - 2\delta_{\alpha\beta}|U_{\alpha4}|^2 + 2|U_{\alpha4}|^2|U_{\beta4}|^2. \tag{7.1.39}$$

$$\text{Integrated-out sterile:} \quad P_{\alpha\to\beta} = \frac{\delta_{\alpha\beta} - 2\delta_{\alpha\beta}|U_{\alpha4}|^2 + |U_{\alpha4}|^2|U_{\beta4}|^2}{(1-|U_{\alpha4}|^2)\,(1-|U_{\beta4}|^2)}. \tag{7.1.40}$$

We see that even with the two regimes being fundamentally different, one with a sterile neutrino propagating from source to detector and the other with a completely decoupled sterile, their effect on neutrino oscillation experiments is very similar. If we assume that the two factors in the denominator of expression 7.1.40 cancel with the production and detection factors discussed in the previous section, then the only difference between the two regimes is a factor of 2 in the term of order $\mathcal{O}(|U|^4)$. Finally, the wave packet version of our argument is more involved, but one can show that the averaged out wave packet probability is indentical to the averaged out plane-wave probability, making our result very general in that sense.

7.2 νSTORM

The neutrino beam at νSTORM is derived from the decay of pions and stored muons. νSTORM is an accelerator neutrino experiment, and so relies on meson production in the usual way: high-energy protons colliding onto a solid target. A magnetic horn then collects 5.0 ± 0.5 GeV charged pions of the desired polarity, and inject them in the first straight of a racetrack like storage ring, where 52% of the collected charged pions are expected to decay before being stopped at the end of the straight. Muons with an energy of 3.8 ± 0.38 GeV are then collected and stored in the ring, where they are expected to circulate for a mean number of 50 turns. The first straight section of the ring, the decay pipeline, is

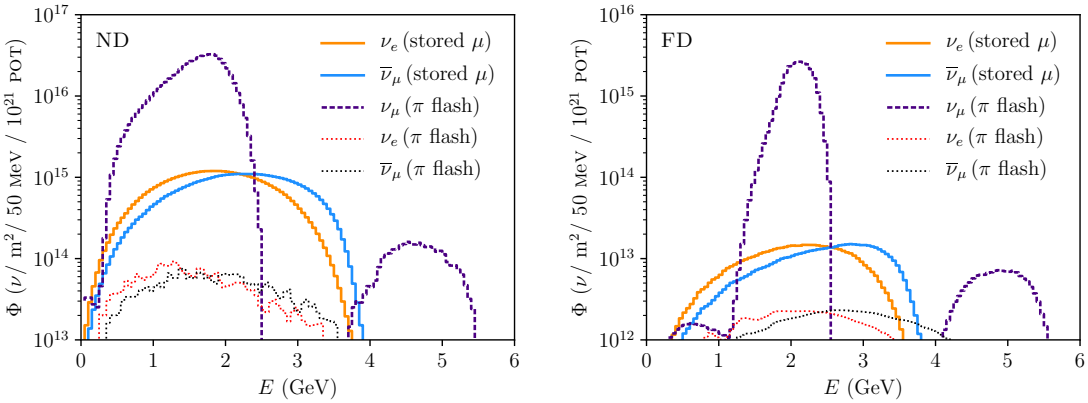

Fig. 7.2. The neutrino flux at the near (left) and far (right) detectors of νSTORM. Note that the neutrinos from stored muons are separated from the ones generated in the pion flash through timing.

estimated to be 180 m long [417], which will determine the size of the neutrino production region. In this setup, one obtains a beam of ν_μ ($\overline{\nu}_\mu$) from the decays of the injected π^+ (π^-) in what we call the *pion flash*. The useful decays of the stored μ^+ (μ^-) then yield a beam of $\overline{\nu}_\mu$ (ν_μ) and ν_e ($\overline{\nu}_e$). The injection of pions into the ring is assumed to happen at large enough time intervals to allow for a discrimination between the neutrinos coming from the pion flash and the ones coming from the useful muon decays (a timing cut of the order of $180/c = 600$ ns or greater is needed to account for all pion decays before the muon data collection [408]). This allows us, for example, to completely separate the oscillations channels involving ν_e and $\overline{\nu}_\mu$ from the ones involving ν_μ as initial states, for the π^+ polarity. It is clear, however, that a small contamination of muon decays happens during the pion flash. This is a small number of the neutrinos produced, and is taken into account by including 1% of the muon decay flux into the pion flash neutrino flux. Kaons also contribute to the pion flash flux, albeit at larger energies. Fig. 7.2 shows the neutrino flux at the near and far site, considered here.

For the remainder of this section we present the results of our sensitivity studies for νSTORM. We used the GLoBES package [418], and implementing our own oscillation engine as well as our own treatment of the systematics. We start by noting that in an experiment like νSTORM, the charge identification of muons is extremely important to separate neutrino and antineutrino events in the detectors. This is true independently of whether we are interested in oscillation analyses or cross section measurements. For instance, in an $\nu_e \to \nu_\mu$ appearance experiment, the greatest source of background comes

from the misidentified intrinsic antineutrinos in the $\overline{\nu}_\mu \to \overline{\nu}_\mu$ channel. This, however, can be circumvented with large enough magnetic fields at the detectors and curvature analyses of the muon tracks. In all our simulations we assume that both the near and far detectors are magnetised. More specifically, we implement migration matrices for the SuperBIND style iron-scintillator detector, which have kindly been provided to us by the collaboration [2]. The far detector is assumed to have a fiducial mass of 1.3 kt, while the near detector is taken to be an identical but smaller version of the far detector with 0.2 kt of fiducial mass.

Sample	Channel	Sensitivity
π^+ flash	$\nu_\mu \to \nu_\mu$	$\sin^2 2\theta_{\mu\mu}$
	$\nu_\mu \to \nu_e$	$\sin^2 2\theta_{e\mu}$
Stored μ^+	$\nu_e \to \nu_e$	$\sin^2 2\theta_{ee}$
	$\overline{\nu}_\mu \to \overline{\nu}_\mu$	$\sin^2 2\theta_{\mu\mu}$
	$\nu_e \to \nu_\mu$	$\sin^2 2\theta_{e\mu}$

Tab. 7.1. The oscillation channels at νSTORM, indicating to what phenomenological parameter they are sensitive to.

We study various channels simultaneously at νSTORM, however, only $\nu_\mu(\overline{\nu}_\mu)$ disappearance and $\nu_e \to \nu_\mu$ appearance count with existing migration matrices. For illustration, we also include oscillation channels involving electrons flavour in the final state. These will, of course, be challenging for iron detectors, but can become an additional goal if the detector are made of liquid Argon (LAr), for instance. For the current purposes, we take the analogous migration matrix with a muon in the final state, reduce the signal efficiency by a factor of 1/2 and increase backgrounds by a factor of 400. Table 7.1 contains a summary of the signal channels we consider, and to which of the following phenomenological parameters they are sensitive to:

$$\sin^2 2\theta_{e\mu} = 4|U_{e4}|^2|U_{\mu 4}|^2,$$
$$\sin^2 2\theta_{ee} = 4|U_{e4}|^2(1-|U_{e4}|^2), \qquad \sin^2 2\theta_{\mu\mu} = 4|U_{\mu 4}|^2(1-|U_{\mu 4}|^2). \tag{7.2.1}$$

[2] Ryan Bayes, private communication

7.2.1 Treatment of Systematics

Here, we detail our methodology for dealing with systematics errors at νSTORM. We choose to use the pull method, which adds penalties to the best-fit parameter when deviating the parameters that control the systematics away from their central values. We work with a χ^2 test which can be written as

$$\chi^2_{\text{TOT}} = \sum_D \sum_C \chi^2_{D,C} + \chi^2_{\text{Pull}}. \tag{7.2.2}$$

The $\chi^2_{D,C}$ for each detector D and channel C is a sum over the energy bins E_i and a function of theoretical event rate $T^i_{D,C}$ and the simulated observed rate $O^i_{D,C}$:

$$\chi^2_{D,C} = 2 \sum_i^{n_{\text{bins}}} \Big(T^i_{D,C} - O^i_{D,C} + O^i_{D,C} \ln \frac{O^i_{D,C}}{T^i_{D,C}} \Big). \tag{7.2.3}$$

The set of systematical errors for the signal and the background are represented by auxiliary parameters α and β, respectively, and are to be profiled over when calculating the theoretical event rates

$$T^i_{D,C} = (1 + \alpha^C_{\text{Flux}} + \alpha^D_{\text{Det}} + \alpha^{i,C}_{\text{Xsec}}) S^i_{D,C} + (1 + \beta^{D,C}) B^i_{D,C}, \tag{7.2.4}$$

where $S^i_{D,C}$ and $B^i_{D,C}$ are the signal and background in the i-th energy bin, respectively. The error α^C_{Flux} is the total flux normalization error, correlated between near and far detector, α^D_{Det} are the uncorrelated detector specific systematics and $\alpha^i_{\sigma_C}$ are the bin dependent cross sections and efficiency errors, which take shape uncertainties into account. We emphasize that the total flux normalization for the channels of interest is only uncorrelated between the two flux components. For examaple, for a π^+ polarity run, we have:

$$\alpha^{\nu_e \to \nu_\mu}_{\text{Flux}} = \alpha^{\overline{\nu}_\mu \to \overline{\nu}_\mu}_{\text{Flux}} = \alpha^{\mu^+}_{\text{Flux}}, \quad \alpha^{\nu_\mu \to \nu_\mu}_{\text{Flux}} = \alpha^{\pi^+}_{\text{Flux}}. \tag{7.2.5}$$

The background systematics take into account an overall normalization factor uncorrelated amongst all channels and detectors with $\beta^{D,C}_{BG}$ and shape effects with β^i_{BG}, also uncorrelated for all channels and detectors. Depending on what channel we are considering, there will be cross section uncertainties in the charge misidentificiation component of the background, which are taken into account in our analysis but not included in this discussion. In total, for our 4 channels of interest, 16 energy bins and one beam polarity, we have 52 signal systematic errors and 8 for the background.

In all our results, except when explicitly stated otherwise, we include 0.5% flux normalisation uncertainties correlated between near and far detectors, and 0.5% for detector specific uncertainties. Bin dependent cross section times efficiency uncertainties are taken to be 20% at the time of the measurement, and overall background normalisation uncertainties 35%. We also include an energy calibration error of 0.5%. Finally, we point out that the χ^2 analysis is done for the far and near detectors datasets separately, without resorting to near to far ratios.

7.3 Sensitivity Results

In the following sections we present our results for the sensitivity of νSTORM to different physical scenarios.

3+1 Oscillations

In a 3+1 model, it is customary to present results in terms of the phenomenological parameters $\sin^2 2\theta_{\alpha\beta} = 4|U_{\alpha 4}|^2|U_{\beta 4}|^2$ and $\sin^2 2\theta_{\alpha\alpha} = 4|U_{\alpha 4}|^2(1 - |U_{\alpha 4}|^2)$. Fig. 7.3 shows the sensitivity of νSTORM to the phenomenological parameters in the 3+1 model, where the parametrization allows for a clear separation between appearance, ν_μ disappearance and ν_e disappearance channels. We also show curves for single detector fits with and without systematics. For the combinations of both near and far detectors, we show the curve that would be obtained with a plane-wave treatment of oscillations, as well as the full localized oscillation probabilities. The latter represent our final results.

The interplay between the near and far detectors in this study is pivotal and has been discussed in the literature before in the context of the very low energy neutrino factory (VLENF) [419]. For low Δm^2_{41}, the near detector is not affected by oscillations and can safely measure cross sections and detector efficiencies, while the far detector measures the oscillation parameters. The detector roles are swapped for larger Δm^2_{41}, however, where oscillations now develop at the near detector and are washed out at the far detector. In fact, due to localization effects, if $\Delta m^2_{41} \gtrsim 10$ eV^2, the oscillations are typically washed out at the near detector as well as at the far detector. In this case, the total effect is a constant shift of normalisation common between the near and far sites. This effect is less dramatic

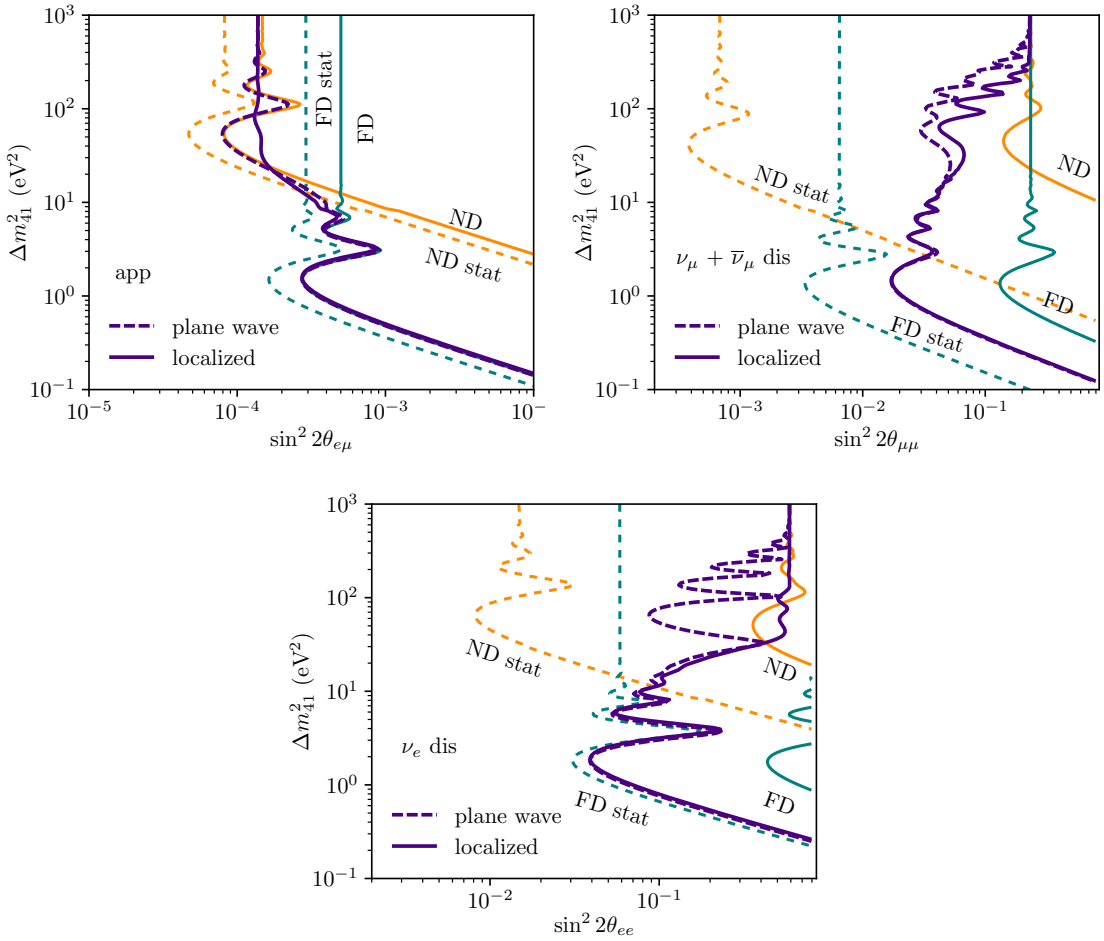

Fig. 7.3. The 99% C.L. sensitivities of νSTORM to the phenomenological parameters $\theta_{e\mu}$ (top left), $\theta_{\mu\mu}$ (top right), and θ_{ee} (bottom). The orange (cyan) curves assume only a single near (far) detector, respectively, and do not take localization into account. For those, dashed lines are the statistical limit. The dashed purple curves assume the presence of both detectors. Solid purple curves take localization into account.

for ν_μ disappearance as the pions are much shorter-lived. The production region, in this case, is $\ell_{\mathrm{dec}_\pi} \ll \ell_p = 180$ m, and so oscillations are localized for larger values of Δm^2_{41}. This effect is visible in Fig. 7.4, where we show the ν_μ disappearance sensitivity curves for the muon sample separately from that of the full sample (using neutrinos from pions as well as muon decays). Fig. 7.4 also shows the sensitivity obtained with our standard choice for systematics (20% cross section $\times$ efficiencies, and 0.5% correlated and uncorrelated flux uncertainties), as well as with a more pessimistic choice (35% cross section $\times$ efficiencies, and 1% correlated and uncorrelated flux uncertainties).

In Fig. 7.5, we compare νSTORM sensitivity curves to expected sensitivities for the SBN program [403], and overlay the existing bounds on the different active-heavy neutrino

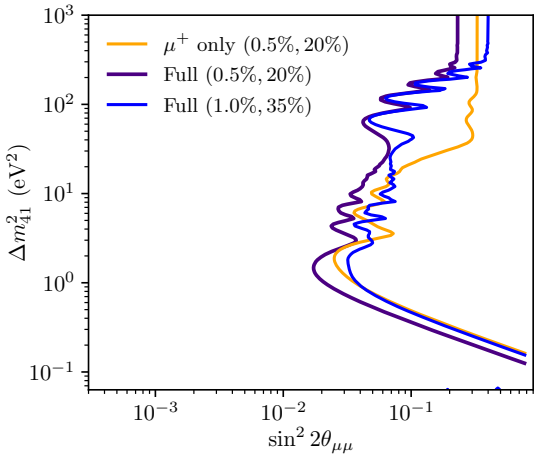

Fig. 7.4. Variations of the ν_μ disappearance sensitivity at 99% C.L.. In purple, we show the main curve from Fig. 7.3 and in blue we increase all flux related systematic uncertainties to 1% and cross sections $\times$ efficiencies uncertainties to 35%. With the standard systematics, in orange we use only the events from stored muons (larger decay length).

mixing. When plotting our results, we disregard bounds coming from astrophysical and cosmological observations (although these can be severe, especially at larger masses [420,421]). We also omit bounds from neutrinoless double-beta decay, which are model dependent and apply only if neutrinos are Majorana particles. In short, we display the strongest direct constraints on the existence of a fourth heavy neutrino from laboratory experiments.

While an experiment like νSTORM is to test lower mass regions, it does perform much better than any other accelerator experiment for larger masses, where the measurement is essentially one of the zero-distance flavour transitions. As well as bounds from oscillation experiments, Fig. 7.5 also shows bounds coming from β-decay experiments. These are obtained by searching for kinks in the kinematics of the outgoing electrons in beta decay. The curves shown are from Ref. [422] and correspond to the following radioactive isotopes: 1 – ^{3}H, 2 – ^{3}H, 3 – ^{187}Re, 4 – ^{3}H, 5 – ^{3}H, 6 – ^{63}Ni, 7 – ^{63}Ni, 8 – ^{35}S, 9 – ^{64}Cu, 10 – ^{20}F. The bound labelled 11 is from the Troitsk nu-mass experiment as reported in Ref. [423]. Bounds on $|U_\mu 4|^2$ come mainy from searches at IceCube [401], MINOS and MINOS+ [400] [3]. For $|U_{e4}||U_{\mu 4}|$, we show bounds obtained from appearance experiments (electron-muon or muon-electron channels), where the NOMAD and CCFR curves were taken from Ref. [425], and the NuTEV and KARMEN ones from Ref. [426]. Another way to bound the product of mixing elements is through the unitarity of the full mixing matrix. In fact, in any $3+N$

[3] This bound has generated debates in the literature and has been claimed to be too aggressive at large masses [396, 424]. In view of that, we hatch the relevant region in our plot.

model, one can show that

$$P_{\alpha\to\beta} \leq \frac{1}{2}(1 - P_{\alpha\to\alpha})(1 - P_{\beta\to\beta}), \tag{7.3.1}$$

or in terms of mixing matrix elements

$$\left(\sum_k 4|U_{\alpha k}|^2|U_{\beta k}|^2\right)^2 \leq \left(\sum_j 4|U_{\alpha j}|^2(1-|U_{\alpha j}|^2)\right)^2 \left(\sum_i 4|U_{\beta i}|^2(1-|U_{\beta i}|^2)\right)^2. \tag{7.3.2}$$

This allows us to translate the bounds on $|U_{e4}|$ and $|U_{\mu 4}|$ into bounds on the product $|U_{e4}U_{\mu 4}|$, as we do in the bottom axes of Fig. 7.5.

3+2 Oscillations

We now present our results for the 3+2 model. In this case, the ordering of the two sterile neutrinos is not physical, hence $\Delta m^2_{54} > 0$ without any loss of generality. Note that now the presence of two oscillation frequencies complicates the interplay of the near and far detectors. If Δm^2_{41} is in the $\mathcal{O}(1)$ ev^2 region and Δm^2_{51} in the $\mathcal{O}(10^2)$ ev^2 region, then both the near and the far detectors are affected by flavour transitions and the systematics cannot be disentangled from the new physics effects in all cases.

A selected number of sensitivity curves in the 3+2 model are shown in figure 7.6. We do not marginalise over the parameters that do not compose the axes, but rather set them to specific values. These are shown in the axes and were chosen based on the global-fit of Ref. [427], where the best fit is given by $\Delta m^2_{41} = 0.47$ eV^2, $|U_{e4}| = 0.13$, $|U_{e5}| = 0.14$, $|U_{\mu 4}| = 0.15$, $|U_{\mu 5}| = 0.13$ and $\eta = -0.15\pi$.

Now, we assess the sensitivity of νSTORM to the effective short-baseline CP violation phase η for a few choices of the 3+2 parameters. We repeat this study for different combinations of injected π^+ (stored μ^+) and π^- (stored μ^-) modes, assuming the same efficiencies and fluxes for the CP conjugated channels. Assuming a precision of 10% and 20% in the measurement of the 3+2 model parameters, we evaluate the sensitivity to η in figure 7.7, showing that νSTORM could be sensitive to maximally CP violating phases at the 3 and 4 σ level. This is to be contrasted with the study in Ref. [428], where the CP violation arises from the interference between the Δm^2_{31} and Δm^2_{41} mass differences. Here, CP violation arises exclusively due to the interference between the two large oscillation frequencies.

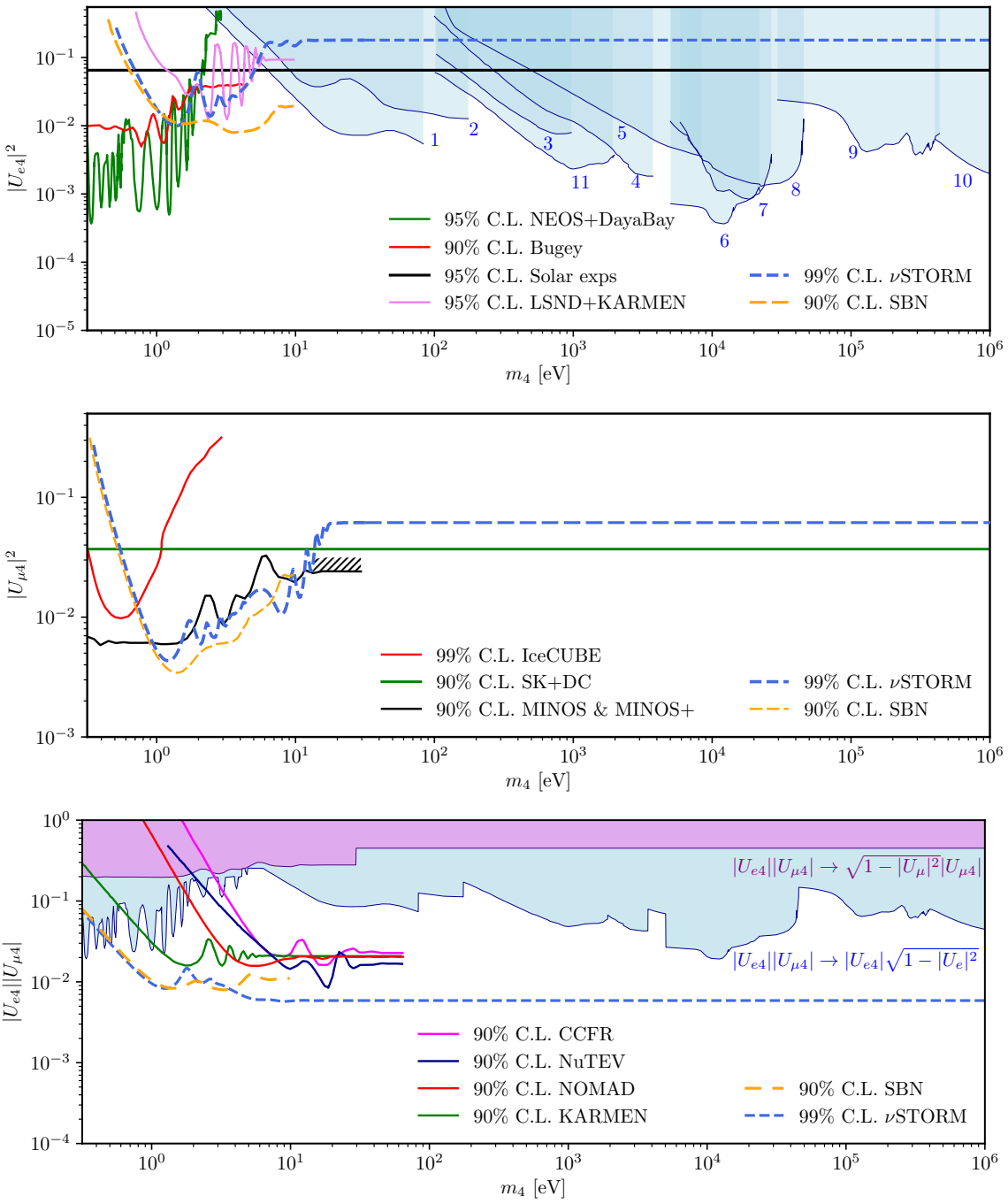

Fig. 7.5. Laboratory bounds on the active-heavy mixing for the 3+1 model with $m_4 \approx \Delta m^2_{41}$. Constraints on mixing with electron flavour (top), muon flavour (middle), and the product of the two (bottom) are shown. The numbered bounds on $|U_{e4}|$ come from kink searches in β-decay and are all at 95% C.L., except 2 and 9, which are at 90% C.L. The projected sensitivities for SBN [403] and νSTORM shown as orange and blue dashed lines, respectively.

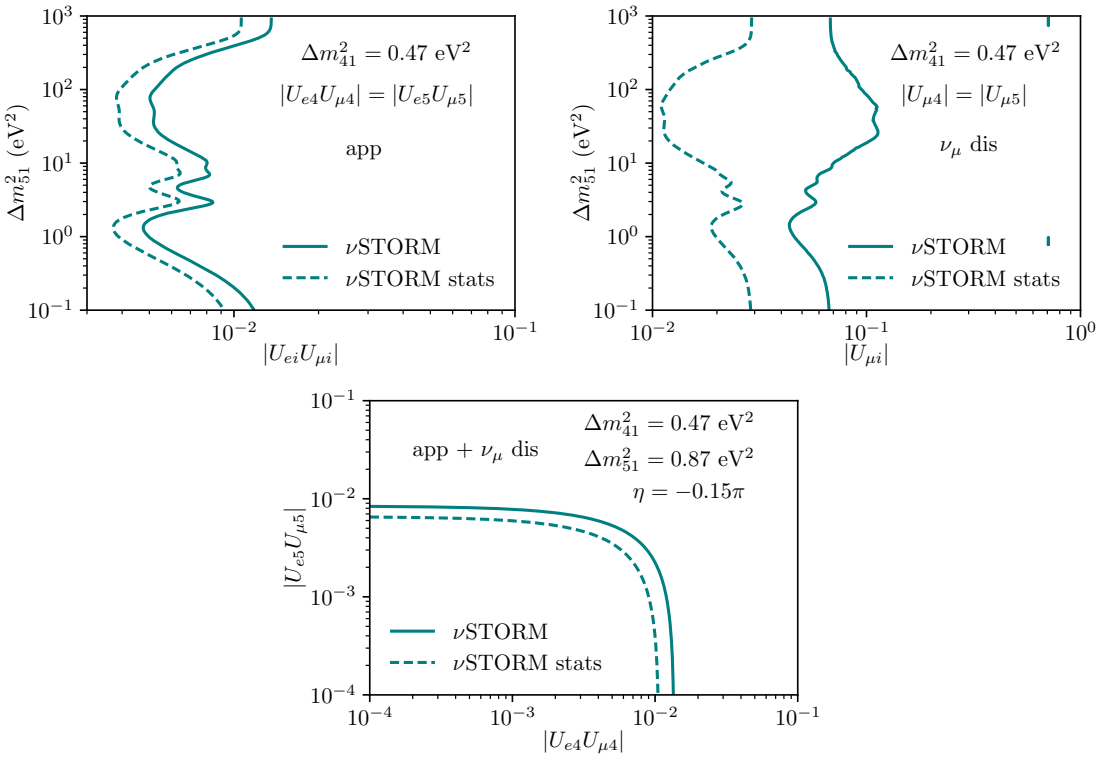

Fig. 7.6. The sensitivity of νSTORM to short-baseline oscillations in a 3+2 model at 99% C.L. Top left shows the result of an appearance experiment, top right of a muon-disappearance experiment, and bottom of both channels combined.

Averaged-out steriles

Having discussed oscillations, we now focus on the flux normalization effects from averaged-out sterile neutrinos. This regime is already visible at large sterile masses in Fig. 7.5. Those bounds can be translated into model independent bounds on the sum of active-light neutrino mixing, as we do in this section.

The zero-distance effects present in this averaged-out regime are hard to constrain in disappearance channels given the large cross section uncertainties, assumed to be 20% here [4]. For the $\nu_e \to \nu_\mu$ appearance channels, sensitivity is limited by backgrounds. These are typically small at νSTORM , since the final states contain muons, much easier to identify than electrons, and due to the presence a magnetic field to differentiate μ^+ and μ^-.

The results shown in Fig. 7.8 for νSTORM are plotted compared with an existing study for MiniBoone [429] and SBN. We also show the bounds from a global-fit to this type of

[4] Improvements may come from restricting the analysis to well-known cross sections, such as $\nu - e$ scattering and neutrino-nucleus scattering with low $\nu = E_\nu - E_\ell$ values.

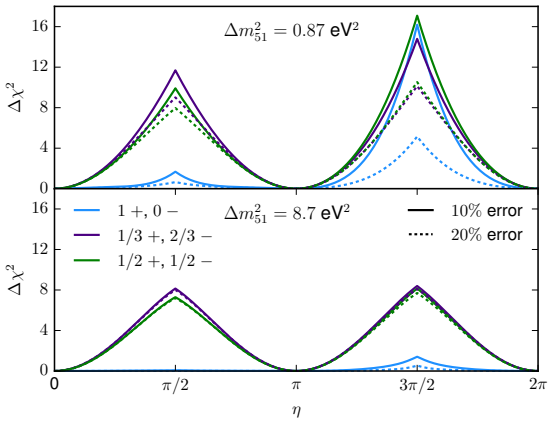

Fig. 7.7. The sensitivity of νSTORM to the CP violating phase η when giving all other parameters 10% and 20% gaussian priors. The top axes show the choice of $\Delta m^2_{51} = 0.87$ eV^2, while the bottom axes show a ten times larger value. We use three different configurations: 100% μ^+ runtime, 66% μ^- and 33% μ^+ runtime, and 50% runtime each. The other parameters in the 3+2 model are assumed to be $\Delta m^2_{41} = 0.47$ eV^2, $|U_{e4}| = 0.13$, $|U_{e5}| = 0.14$, $|U_{\mu 4}| = 0.15$ and $|U_{\mu 5}| = 0.13$.

non-unitarity in neutrino oscillations [430].

Integrated-out steriles

Now we show results for the integrated-out sterile at νSTORM. For simplicity, we show our results in terms of a 3+1 parametrization, but the constraints can easily be translated into constraints on non-unitarity parameters (*e.g.*, the α parameters). This is very similar to the averaged-out regime, however, different normalization factors appear in the oscillation probabilities depending on the production process of the intial neutrino. Let us emphasize that in the integrated-out regime, the different oscillation channels are now dependent on mixing matrix elements that may not even involve the neutrino (low energy) flavours. In fact, the channels $\nu_\mu \to \nu_\mu$ and $\overline{\nu}_\mu \to \overline{\nu}_\mu$ depend on different mixings, since they involve neutrinos with different parent particles. In our implementation, we define an effective flavour transition probability $\hat{P}$ which absorbs any factors due to non-unitarity at production and detection

$$\hat{P}_{\nu_\alpha \to \nu_\beta} = \frac{\sigma_\alpha^{\mathrm{CC}}}{\sigma_\alpha^{\mathrm{CC\ (SM)}}} P_{\nu_\alpha \to \nu_\beta} \frac{d\Phi_\alpha^{\mathrm{CC}}/dE}{d\Phi_\alpha^{\mathrm{CC\ (SM)}}/dE}, \tag{7.3.3}$$

where $P_{\nu_\alpha \to \nu_\beta}$ is the standard probability. The explicit expressions we use in this analysis are shown below for the different samples.

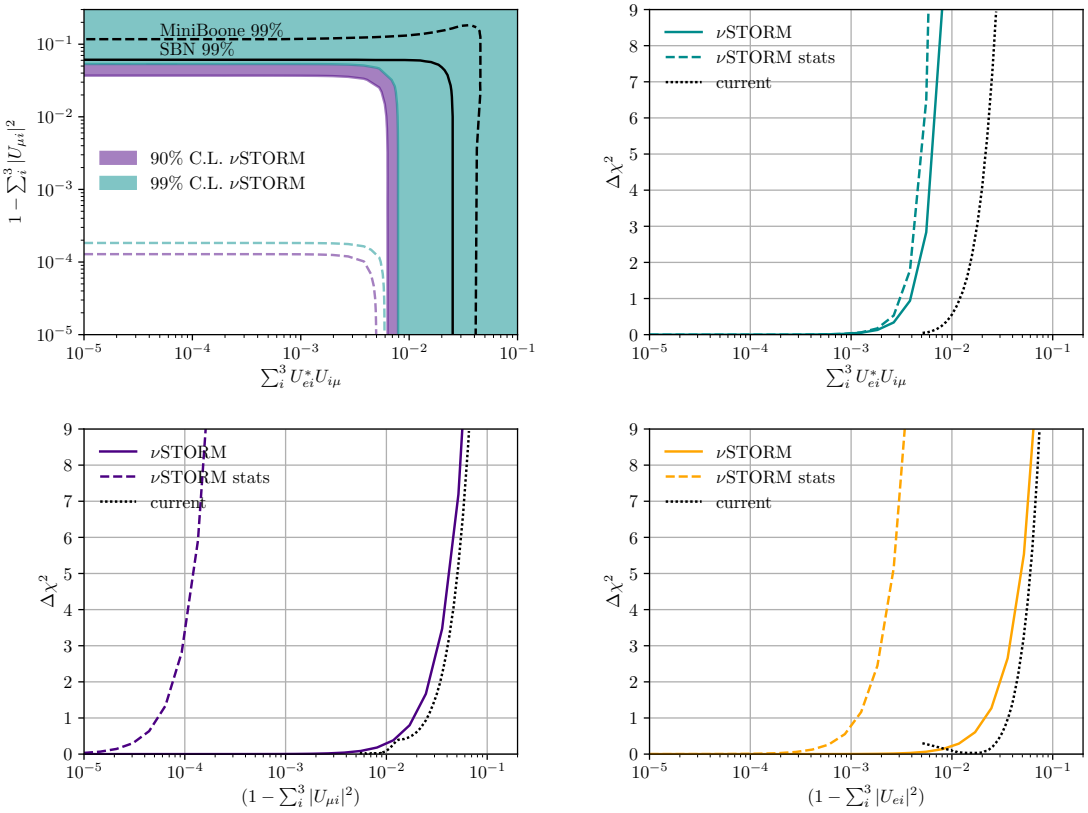

Fig. 7.8. Bounds on the non-unitarity of the mixing matrix in the averaged-out sterile case. Top left shows the two dimensional plane to which ν_μ disappearance and $\nu_e \to \nu_\mu$ apperance experiments are sensitive to. We then show the one-dimensional $\Delta\chi^2$ profile for appearance (top right), ν_μ disappearance (bottom left) and ν_e disappearance (bottom right). All colorful dashed lines stand for the statistical limit at νSTORM.

- $\underline{\pi^+(k^+) \to \mu^+\nu_\mu}$:

$$\hat{P}_{\nu_\mu\to\nu_\mu} = 1 - 2|U_{\mu 4}|^2 + |U_{\mu 4}|^4, \tag{7.3.4}$$

$$\hat{P}_{\nu_\mu\to\nu_e} = |U_{e4}|^2|U_{\mu 4}|^2. \tag{7.3.5}$$

- $\underline{\mu^+ \to e^+\nu_e\overline{\nu}_\mu}$:

$$\hat{P}_{\nu_e\to\nu_e} = \left(1 - 2|U_{e4}|^2 + |U_{e4}|^4\right)\left(1 - |U_{\mu 4}|^2\right), \tag{7.3.6}$$

$$\hat{P}_{\overline{\nu}_\mu\to\overline{\nu}_\mu} = \left(1 - 2|U_{\mu 4}|^2 + |U_{\mu 4}|^4\right)\left(1 - |U_{e4}|^2\right), \tag{7.3.7}$$

$$\hat{P}_{\nu_e\to\nu_\mu} = |U_{e4}|^2|U_{\mu 4}|^2\left(1 - |U_{\mu 4}|^2\right). \tag{7.3.8}$$

The bounds that νSTORM could place on neutrino mixing in this regime are shown in Fig. 7.9. Although νSTORM possesses the advantage of a precise flux, the bound in this regime are much less competitive with bounds obtained from the charged-lepton sector.

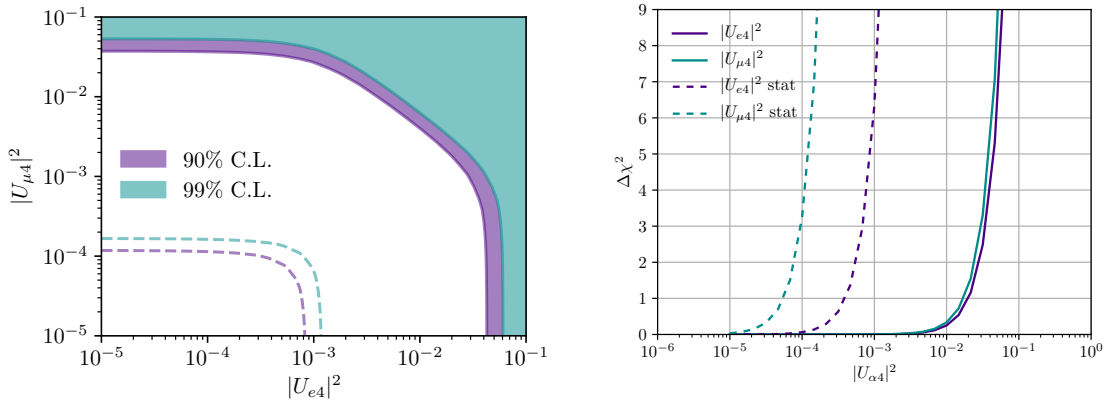

Fig. 7.9. Sensitivity to non-unitarity in the integrated-out sterile case. Dashed lines stand for the statistical limit at νSTORM.

For instance, precision measurements in the charged-lepton and quark sectors yield a bound on $|U_{\mu 4}| < 0.021$ at 2σ [415]. This is to be contrasted with the νSTORM sensitivity to $|U_{\mu 4}| > 0.19$ at 2σ. The situation is much worse for the product $|U_{e4}U_{\mu 4}|$. There, $|U_{e4}U_{\mu 4}| < 2.4 \times 10^{-5}$ due to lepton flavour violation bounds (dominated by $\mu \to e\gamma$ searches), while νSTORM is only sensitive to $|U_{e4}U_{\mu 4}| > 6.4 \times 10^{-3}$.

7.4 Overview

The novel neutrino beam at νSTORM allows for interesting possibilities in the search for short-baseline oscillations. Despite the precise flux, cross section and efficiency uncertainties still greatly limit the power of any disappearance search, especially for constant flavour transitions. The possibilities considered here, however, are not exhaustive. In view of the redesign of the proposal for siting at CERN, this work can be adapted to higher neutrino energies and different detector materials. In particular, opting for (magnetized) LAr detectors, would allow to explore all oscillation channels available at νSTORM to the fullest. Other great improvements on searching for new physics can be achieved by combining well-known cross sections with the well-known flux at νSTORM. As a next step, we envisage applying the same study to neutrino-electron scattering for different detector choices. Measuring this process is currently a method to obtain information on the neutrino flux at accelerator experiments, since its cross sections is well known. At νSTORM, it can be used to constrain new physics since the cross section uncertainties would be reduced from tens of a percent to the few percent level. Sterile neutrinos and non-unitarity need

not be the only goal of such analyses. Precision measurements of electroweak parameters, such as θ_{W}, can also be achieved through these methods. The limitation, however, lies mainly on the statistics and detector performance.

Other avenues to precise GeV neutrino beams also exist. For instance, the ENUBET proposal [431, 432], where a well-understood ν_e beam is obtained from decays of the type $K^+ \to \pi^0 e^+ \nu_e$. In this way, the proposal aims to tag each neutrino interaction in the detector with a particular daughter lepton at production, promising the first tagged neutrino beam. At higher energies, above tens of GeV, the neutrino DIS cross sections offer better precision and higher rates, although also relying on our ability to understand the flux.

Chapter 8

Conclusions

Particle physics is at a very important moment of its history. The Standard Model (SM) provides unprecedented accuracy when describing particle physics data, but it provides no explanation for neutrino masses and the existence of dark matter (DM). It is tempting to think that these phenomena are to the Standard Model what blackbody radiation was to classical physics in the beginning of the 20th century, a scientific revolution on the wait. While we cannot be sure, we continue to devise new theoretical explanations and new methods to test them. In particular, the experimental efforts in neutrino physics open new possibilities to test the connections between neutrinos and beyond the SM physics. New detector technologies, such as liquid Argon (LAr), and more powerful neutrino beams, allow us to study neutrino interactions in great detail and mimic conditions of high intensity fixed-target and beam-dump facilities.

Rare and well-understood neutrino scattering processes offer a unique tool to test the SM weak interactions. We have shown that measuring the neutrino trident production ($\nu A \to \nu \ell \ell A$) cross section at GeV energies will be an attainable goal of near future experiments such as the Deep Underground Neutrino Experiment (DUNE). The backgrounds in LAr are expected to be manageable within our assumptions for particle identification capabilities. Our calculation for the cross section makes it explicit the poor performance of the Equivalent Photon Approximation for this process, and provides an estimate for trident rates at various current and future neutrino facilities. In Chapter 4, we assess the sensitivity of DUNE to new anomaly-free leptophilic $U(1)_{L_\alpha - L_\beta}$ groups. The new Z' gauge bosons can be searched for in leptonic and semi-leptonic neutrino scattering processes,

such as neutrino trident and neutrino-electron scattering ($\nu\, e \to \nu\, e$). We showed that for $L_e - L_\mu$, the new boson may be searched for in neutrino-electron scattering measurements, provided the neutrino flux uncertainties are kept under control. For $L_\mu - L_\tau$, neutrino trident production of dimuon pairs can set strong bounds on the coupling and masses of the Z' boson, otherwise much harder to constrain since it does not couple to the first SM generation of particles. We show that if the number of non-trident background events exceeds that of the number of SM tridents, then DUNE starts to lose its ability to probe the entire parameter space able to explain the muon $(g-2)_\mu$.

A new set of models for low energy phenomenology in neutrino experiments has been developed in Chapter 5. The model contains a new dark neutrino state ν_D, charged under a hidden $U(1)'$ local gauge symmetry, which in turn is broken by the vev of a new scalar Φ. The setup realises all three neutral and renormalizable portals to hidden sectors: the scalar, vector and neutrino portals. With the presence of a completely neutral state N, this closely resembles other low-scale seesaw models like the inverse and extended seesaw. We show how the phenomenology is very different from having each portal taken individually, opening up parameter space to explain experimental anomalies such as the muon $(g-2)$, and the MiniBooNE low energy anomaly. As it turns out, the model also radiatively generates light neutrino masses, while remaining testable at the MeV scale.

Phenomenological realizations of the dark neutrino model had already been put forward as explanations of the excess of electron-like events at MiniBooNE. As shown in Chapter 6, light Z' scenarios are severely constrained by neutrino-electron scattering measurements at accelerator neutrino experiments. We proposed a new technique to constrain these models by investigating sideband data in the MINERνA low energy measurement, as well as in the past measurements performed by CHARM-II. By using simplified rate analysis in sideband regions of MINERνA and CHARM-II, as well as computing the MiniBooNE angular spectrum, we showed that the region where both energy and angular distributions at MiniBooNE can be explained in this model are in severe tension with neutrino-electron scattering data. Although not all parameter space is excluded, our work highlights the importance of the coherent photon-like sidebands in neutrino-electron scattering measurements and paves the way for future analyses at MINERνA, NOνA, and DUNE, eventually.

Neutrino beams from stored muons can bring great improvements to laboratory neutrino experiments. The νSTORM project is a first step towards neutrino factories and muon colliders, and may provide a definite test of whether short-baseline oscillations due to eV sterile neutrinos exist. Beyond testing existing anomalies, it could provide the most stringent limits on non-unitarity of the PMNS matrix due to light sterile neutrinos. Our analysis also highlighted the peculiarities of the beam, with implications for production localisation, short-baseline CP violation, and displaying a variety of oscillation channels in a single experiment.

Neutrino physics is a field full of exciting and unexpected results. Neutrino oscillations have marked the beginning of our exploration of beyond the SM physics, but much more is yet to be learned. Beyond studying the physics of neutrino flavour, neutrino oscillation and scattering experiments are a unique tool to probe the weak interactions and to search for new particles. The theoretical models, novel measurements, and analyses techniques we have proposed in this thesis are intimately connected to the unique properties of neutrinos. Whether neutrinos are indeed a gateway to dark sectors, or just what we need to rule this possibility out, we are confident that the bright future of neutrino physics will shine light on what lies beyond the SM.

Appendices

Appendix A

Phase Space

In this appendix we derive some key results for the phase space treatment we use in calculating cross sections and decay rates. We begin with the factorization of N-final state phase-space factors into $N-2$ two-body ones. In general, the N-body phase space can be written as

$$\mathrm{d}\Phi_N(P,\{p_i\}) = (2\pi)^4\delta^4(P-\sum_i^N p_i)\prod_i^N \frac{\mathrm{d}^3p_i}{(2\pi)^3 2E_i}, \tag{A.0.1}$$

where $\{p_i\} = p_1,\ldots,p_N$. Focusing on the 1-2 subsystem with total momentum $p_{12} = p_1+p_2$, we can write

$$\begin{aligned}
\mathrm{d}\Phi_N(P,\{p_i\}) &= \int \mathrm{d}^4p_{12}\,\delta^4(p_{12}-p_1-p_2)\,(2\pi)^4\delta^4(P-\sum_i^N p_i)\prod_i^N \frac{\mathrm{d}^3p_i}{(2\pi)^3 2E_i} \\
&= \int \mathrm{d}^4p_{12}\,\mathrm{d}\Phi_2(p_{12},p_1,p_2)\,(2\pi)^4\delta^4(P-p_{12}-\sum_{i=3}^N p_i)\prod_{i=3}^N \frac{\mathrm{d}^3p_i}{(2\pi)^3 2E_i} \\
&= \int \mathrm{d}^4p_{12}\,\mathrm{d}m_{12}^2\,\delta(p_{12}^2-m_{12}^2)\,\mathrm{d}\Phi_2(p_{12},p_1,p_2) \\
&\qquad\qquad \times (2\pi)^4\delta^4(P-p_{12}-\sum_{i=3}^N p_i)\prod_{i=3}^N \frac{\mathrm{d}^3p_i}{(2\pi)^3 2E_i},
\end{aligned} \tag{A.0.2}$$

which from

$$\int \mathrm{d}^4p_{12}\,\delta(p_{12}^2-m_{12}^2) = \int \mathrm{d}^4p_{12}\,\frac{\delta(E_{12}-\sqrt{m_{12}^2+|\vec{p}_{12}|^2})}{2\sqrt{m_{12}^2+|\vec{p}_{12}|^2}} = \int \frac{\mathrm{d}^3p_{12}}{2E_{12}},$$

yields the final results

$$\mathrm{d}\Phi_N(P, p_1, \ldots, p_N) = \frac{\mathrm{d}m_{12}^2}{2\pi}\mathrm{d}\Phi_2(p_{12}, p_1, p_2)\mathrm{d}\Phi_N(P, p_{12}, p_3, \ldots, p_N). \tag{A.0.3}$$

This result not only lets us factorize any resonant features in phase space, but also provides a recipe to tackle the kinematics of any process in terms of a series of 2-body problems, which are much simpler. The 2-body phase-space factors and associated four-momenta in the respective center-of-mass (CM) frame can always be written as

$$\begin{aligned}
\mathrm{d}\Phi_2(p_{12}, p_1, p_2) &= \frac{\lambda^{1/2}\left(1, m_1^2/E_{12}^{\mathrm{CM}\,2}, m_2^2/E_{12}^{\mathrm{CM}\,2}\right)}{32\pi^2}\mathrm{d}\Omega^{\mathrm{CM}}, \\
p_{12} &= \left(E_{12}^{\mathrm{CM}}, \vec{0}\right), \\
p_1 &= \left(\frac{E_{12}^{\mathrm{CM}\,2} + m_1^2 - m_2^2}{2E_{12}^{\mathrm{CM}\,2}}, |\vec{p}_1|\sin\theta\cos\phi, |\vec{p}_1|\sin\theta\sin\phi, |\vec{p}_1|\cos\theta\right), \\
p_2 &= \left(\frac{E_{12}^{\mathrm{CM}\,2} + m_2^2 - m_1^2}{2E_{12}^{\mathrm{CM}\,2}}, -\vec{p}_1\right),
\end{aligned} \tag{A.0.4}$$

where $\lambda(a, b, c) = (a - b - c)^2 - 4bc$ is the Källén function. Now, the problem is reduced to finding the CM frame of every p_{ij} subsystem, and the transformation between all such frames, if necessary. Of course, the dependence of the matrix element on the kinematics makes certain phase space parametrization better than others, making each problem unique. Lab variables, for instance, are the standard parametrization for DIS scattering as they preserve crucial physical intuition of the process at hand.

Neutrino trident production Now we derive a phase space parametrization for neutrino trident production in terms of the momentum transfer $K^2 = 2p_1 \cdot p_2$. This is important if one wants to change variables to smooth out the integrand at low $M_{Z'}$ masses. We follow the calculation in [188] and [1], and proceed to define K^2 as one of the integration variables. The relevant Lorentz invariant phase space for the $2 \to 3$ leptonic part of the cross section is given by

$$\begin{aligned}
\int \mathrm{d}^3\Pi_{\mathrm{LIPS}} = \int \frac{\mathrm{d}\vec{p_2}}{(2\pi)^3 2E_2}\frac{\mathrm{d}\vec{p_3}}{(2\pi)^3 2E_3}\frac{\mathrm{d}\vec{p_4}}{(2\pi)^3 2E_4} \\
(2\pi)^4\delta^{(4)}(p_1 + q - p_2 - p_3 - p_4).
\end{aligned} \tag{A.0.5}$$

Following [188] we start by working in the frame $\vec{p_1} + \vec{q} - \vec{p_3} = 0$, putting $\vec{p_1}$ along the $\hat{z}$ direction instead. The delta function can be integrated with the $\vec{p_4}$ and $|\vec{p_2}|$ integrals, such that

$$\int \frac{\mathrm{d}\vec{p_2}}{2E_2}\frac{\mathrm{d}\vec{p_4}}{2E_4}\,\delta^{(4)}(p_1 + q - p_2 - p_3 - p_4) = \int \frac{|\vec{p_2}|}{4W_c}\,\frac{1}{E_1E_2}\mathrm{d}K^2\,\mathrm{d}\phi_2, \tag{A.0.6}$$

where we defined

$$\begin{aligned} |\vec{p_2}| &= (W_c^2 - m_1^2)/2W_c, \\ W_c &= q^0 + E_1 - E_3, \\ K^2 &= 2E_1E_2(1 - \cos\theta_2). \end{aligned} \tag{A.0.7}$$

Since we conserve energy and momentum in this frame, we can take $-1 \leq \cos\theta_2 \leq 1$ and $0 \leq \phi_2 \leq 2\pi$. The remaining $\vec{p_3}$ integral can be performed with the variables defined in [188] to yield

$$\int \frac{\mathrm{d}\vec{p_3}}{2E_3} = \int \frac{2\pi}{\hat{s}}\,\mathrm{d}x_5\,\mathrm{d}x_3, \tag{A.0.8}$$

where a trivial azimuthal angle was integrated over. Their limits are more easily found in the frame $\vec{p_1} + \vec{q} = 0$, with $\vec{q}$ along the $\hat{z}$ direction. Finally, our main result is given by

$$\int \mathrm{d}^3\Pi_{\mathrm{LIPS}} = \frac{1}{(2\pi)^4}\int \frac{|\vec{p_2}|}{4W_c}\,\frac{1}{\hat{s}}\,\frac{1}{E_1E_2}\,\mathrm{d}x_5\,\mathrm{d}x_3\,\mathrm{d}K^2\,\mathrm{d}\phi_2. \tag{A.0.9}$$

There remains two non-trivial integrations to be performed to obtain the full 4-body phase space cross section, namely the ones over q^2 and $\hat{s}$. The substitutions suggested in [189] for these two invariants are still convenient, and we make use of them in our numerical integrations.

Appendix B

Form Factors

Electromagnetic form factors In the coherent regime, we use a Woods-Saxon (WS) form factor due to its success in reproducing the experimental data [433, 434]. The WS form factor is the Fourier transform of the nuclear charge distribution, defined as

$$\rho(r) = \frac{\rho_0}{1 + \exp\left(\dfrac{r - r_0}{a}\right)}\,, \tag{B.0.1}$$

where we take $r_0 = 1.126\,A^{1/3}$ fm and $a = 0.523$ fm. One can then calculate the WS form factor as

$$F(Q^2) = \frac{1}{\int \rho(r)\,\mathrm{d}^3 r} \int \rho(r)\, \exp\left(-i\vec{q}\cdot\vec{r}\right) d^3 r\,. \tag{B.0.2}$$

Here we use an analytic expression for the symmetrized Fermi function [435, 436] instead of calculating the WS form factor numerically. This symmetrized form is found to agree very well with the full calculation and reads

$$F(Q^2) = \frac{3\pi a}{r_0^2 + \pi^2 a^2} \frac{\pi a \coth\left(\pi Q a\right) \sin\left(Q r_0\right) - r_0 \cos\left(Q r_0\right)}{Q r_0 \sinh\left(\pi Q a\right)}\,. \tag{B.0.3}$$

In the incoherent regime, we work with the functions $H_1^{\mathrm{N}}(Q^2)$ and $H_2^{\mathrm{N}}(Q^2)$, which depend on the Dirac and Pauli form factors of the nucleon N as follows

$$H_1^{\mathrm{N}}(Q^2) = |F_1^{\mathrm{N}}(Q^2)|^2 - \tau |F_2^{\mathrm{N}}(Q^2)|^2\,, \quad \text{and} \quad H_2^{\mathrm{N}}(Q^2) = \left|F_1^{\mathrm{N}}(Q^2) + F_2^{\mathrm{N}}(Q^2)\right|^2\,, \tag{B.0.4}$$

where $\tau = -Q^2/4M^2$. The form factors $F_1^{\mathrm{N}}(Q^2)$ and $F_2^{\mathrm{N}}(Q^2)$ can be related to the usual Sachs electric G_{E} and magnetic G_{M} form factors. These have a simple dipole

parametrization

$$G_E^{\mathrm{N}}(Q^2) = F_1^{\mathrm{N}}(Q^2) + \tau F_2^{\mathrm{N}}(Q^2) = \begin{cases} 0, & \text{if N} = n, \\ G_D(Q^2), & \text{if N} = p, \end{cases} \tag{B.0.5}$$

$$G_M^{\mathrm{N}}(Q^2) = F_1^{\mathrm{N}}(Q^2) + F_2^{\mathrm{N}}(Q^2) = \begin{cases} \mu_n\, G_D(Q^2), & \text{if N} = n, \\ \mu_p\, G_D(Q^2), & \text{if N} = p, \end{cases} \tag{B.0.6}$$

where $\mu_{p,n}$ is the nucleon magnetic moment in units of the nuclear magneton and $G_D(Q^2) = (1 + Q^2/M_V^2)^{-2}$ is a simple dipole form factor with $M_V = 0.84$ GeV.

Neutral current form factor Here we show our weak hadronic current used in the dark-bremsstrahlung calculation. Similarly to the electromagnetic case, we write the weak hadronic current for a spin-0 nucleus with Z protons and N neutrons as

$$\begin{aligned} \mathrm{H}_{\mathrm{W}}^{\mu} &= \langle \mathcal{H}(k_3)|\, J_{\mathrm{W}}^{\mu}(Q^2)\, |\mathcal{H}(k_b)\rangle \\ &= Q_{\mathrm{W}}(k_b + k_3)^{\mu} F_{\mathrm{W}}(Q^2), \end{aligned} \tag{B.0.7}$$

% where $Q_{\mathrm{W}} = (1 - 4s_{\mathrm{w}}^2)Z - N$ and $F_{\mathrm{W}}(Q^2)$ stands for the weak form factor of the nucleus. We implement the Helm form factor as in [437], defined as

$$|F(Q^2)|^2 = \left(\frac{3j_1(QR)}{QR}\right)^2 e^{-Q^2 s^2}, \tag{B.0.8}$$

where $j_1(x)$ stands for the spherical Bessel function of the first kind, $s = 0.9$ fm and $R = 3.9$ fm for ^{40}Ar.

Appendix C

Trident Distributions

In this appendix we explore the trident signal in more detail, showing some relevant kinematical distributions for coherent and diffractive events. For concreteness, and due to its large number of events, we choose to focus on the DUNE ND, only commenting slightly on the signal at the lower energies of SBN and νSTORM. The observables we calculate are the invariant mass of the charged leptons $m^2_{\ell^+\ell^-}$, their separation angle $\Delta\theta$ and their individual energies $E_\pm$. The flux convolved distributions of these observables are shown for the DUNE ND in neutrino mode in Fig. C.1. In these plots, we sum all trident channels with a given undistinguishable final-state proportionally to their rates, although ν_μ initiated processes always dominate. The coherent and diffractive contributions are shown separately and on the same axes, but we do not worry about their relative normalization. Other potentially interesting quantities are the angle between the cone formed by the two charged leptons and the beam, α_C, and the angle of each charged lepton with respect to the beam direction, $\theta_\pm$. We also report the distributions of the momentum transfer to the hadronic system, Q^2. Although this is not a directly measurable quantity, it is a strong discriminant between the coherent and diffractive processes. We do not present the antineutrino distributions here, but they are qualitatively similar.

Perhaps one of the most valuable tools for background suppression in the measurement of the $\mu^+\mu^-$ trident signal at CHARM II, CCFR and NuTeV [107–109] was the smallness of the invariant mass $m^2_{\ell^+\ell^-}$. This feature, shown here on the top row of Fig. C.1, is also present at lower energies, where the distributions become even more peaked at lower values; although, the diffractive events tend to be have a more uniform distribution in this variable.

This is also true for the angular separation $\Delta\theta$, where coherent dimuon tridents tends to be quite collimated, with 90% of events having $\Delta\theta < 20°$, whilst diffractive ones are less so, with only 47% of events surviving the cut. This difference is much less pronounced for mixed and dielectron channels, where only half of our coherent events obey $\Delta\theta < 20°$, when 37% of diffractive events do so.

An interesting feature of same flavour tridents induced by a neutrino (antineutrino) is that the negative (positive) charged lepton tends to be slightly more energetic than its counterpart, whilst for mixed tridents muons tend to carry away most of the energy. These considerations are also reflected in the angular distributions. The most energetic particle is also the more forward one. For instance, in mixed neutrino induced tridents, $\sim 80\%$ of the μ^- are expected to be within 10° of the beam direction, whilst only $\sim 35\%$ of their e^+ counterparts do so.

Finally, we mention that detection thresholds can also be important for trident channels with electrons in the final-state. Assuming, for example, a detection threshold for muons and electromagnetic (EM) showers of 30 MeV in LAr, we end up with efficiencies of (99%, 71%, 77%, 86%) for ($\mu^+\mu^-$, e^+e^-, $e^+\mu^-$, $e^-\mu^+$) coherent tridents. These efficiencies become (96%, 91%, 93%, 96%) for incoherent tridents, dropping for $\mu^+\mu^-$ and increasing for all others. For comparison, at the lower neutrino energies of SBND and assuming the same detection thresholds, the efficiencies for coherent and incoherent tridents are slightly lower, (97%, 57%, 67%, 77%) and (90%, 81%, 85%, 90%) respectively.

While trident events are generally quite forward going, their angular behaviour is quite interesting. We consider here the angle between the charged lepton cone and the neutrino beam, α_C, defined as

$$\cos\alpha_C = \frac{(\vec{p}_3 + \vec{p}_4)\cdot\vec{p}_1}{|\vec{p}_3 + \vec{p}_4||\vec{p}_1|}\,,$$

and in the individual angle of the charged lepton to the neutrino beam, θ. For same flavour tridents we define θ for each charge of the visible final-state, whilst for mixed tridents we use their flavour. We also show the distribution in $Q^2 = -q^2$, where $q = (P - P')$, which is of particular interest when considering coherency and the impact of form factors.

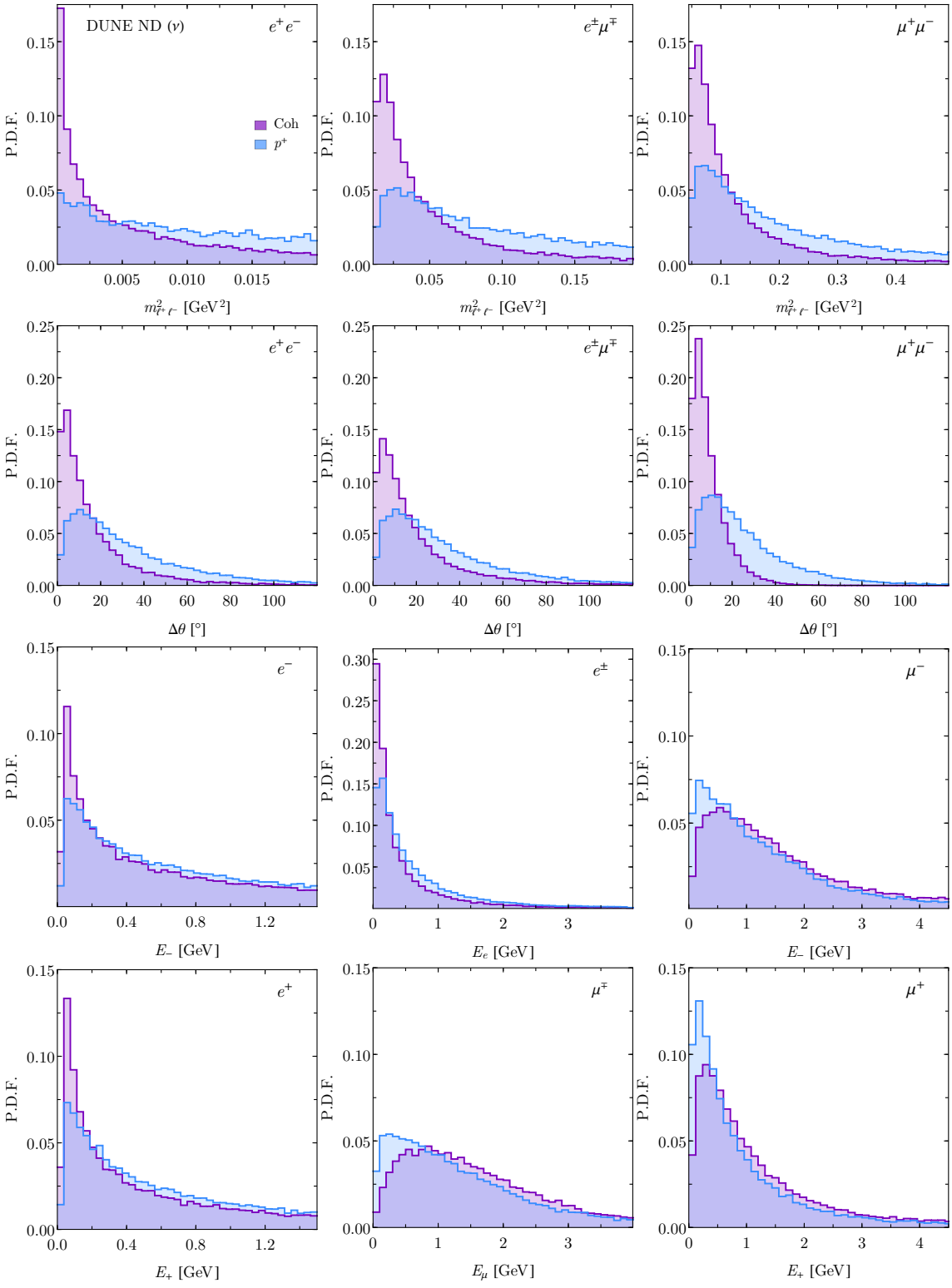

Fig. C.1. Flux convolved neutrino trident production distributions for DUNE ND in neutrino mode. In purple we show the coherent contribution in ^{40}Ar and in blue the incoherent contribution from protons as targets only (including Pauli blocking). The coherent and incoherent distributions are normalized independently. The relative importance of each contribution as a function of E_ν can be seen in Fig. 3.6.

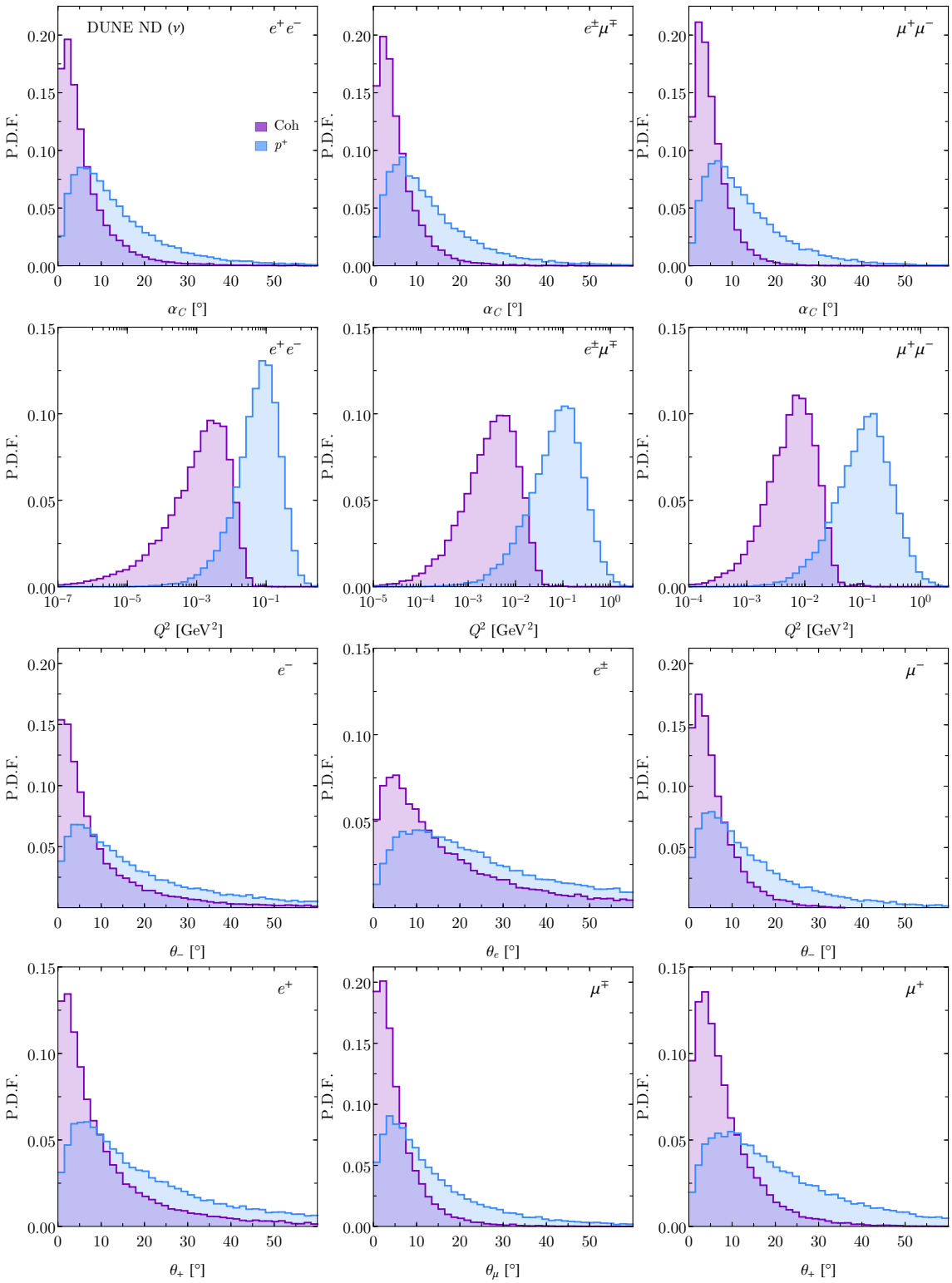

Fig. C.2. Flux convolved neutrino trident production distributions for DUNE ND in neutrino mode in additional variables. In purple we show the coherent contribution in ^{40}Ar and in blue the incoherent contribution from protons as targets only (including Pauli blocking). The coherent and incoherent distributions are normalized independently.

Appendix D

Dark Neutrino Self-Energies

In this appendix, we compute the one-loop corrections to the light neutrino masses in our dark neutrino model, following Refs. [317, 438, 439].

We work with the on-shell (OS) renormalization scheme. This is ensured by requiring that the off-diagonal elements of the self-energy be diagonal when the external particles are on their mass shell, and that the residue of the renormalized propagator are equal to one. Note this is only applicable to the off-diagonal entries that involve at least one heavy neutrino, and that the light-light entries are all non-zero and finite at one-loop.

Assuming Majorana neutrino fields, one can write the self-energy tensor in its most general form:

$$\Sigma_{ij}(\not{q}) = \not{q}\mathrm{P}_L\Sigma^L_{ij}(q^2) + \not{q}\mathrm{P}_R\Sigma^R_{ij}(q^2) + \mathrm{P}_L\Sigma^M_{ij}(q^2) + \mathrm{P}_R\Sigma^{M*}_{ij}(q^2), \tag{D.0.1}$$

where by virtue of the Majorana nature the previous terms obey

$$\Sigma^L_{ij}(q^2) = \Sigma^{R*}_{ij}(q^2), \qquad \Sigma^M_{ij}(q^2) = \Sigma^M_{ji}(q^2).$$

The contribution from the scalar fields $s = h^0, \varphi^0$, the goldstones $G = G_h, G_\varphi$ and the vector bosons $V = Z, Z'$ are

$$-i\,\Sigma^s_{ij}(p^2) = (-i)^2\,(\Delta_s P_R + \Delta^*_s P_L)_{ik} \times \int \frac{d^dk}{(2\pi)^d}\,\frac{i(\not{p}+\not{k}+m_k)}{(p+k)^2-m_k^2}\,\frac{i}{k^2-m_s^2}\,(\Delta_s P_R + \Delta^*_s P_L)_{kj}\,,$$

$$-i\,\Sigma^{G_s}_{ij}(p^2) = (-i)^2\,(i\,\Delta_s P_R - i\,\Delta^*_s P_L)_{ik} \times$$

$$\int \frac{d^dk}{(2\pi)^d}\frac{i(\not{p}+\not{k}+m_k)}{(p+k)^2-m_k^2}\frac{i}{k^2-\xi_V m_V^2}\left(i\,\Delta_s P_R - i\,\Delta_s^* P_L\right)_{kj},$$

$$-i\,\Sigma_{ij}^V(p^2) = -(-i)^2\gamma^\mu\left(C_V P_L - C_V^T P_R\right)_{ik}\times$$
$$\int \frac{d^dk}{(2\pi)^d}\frac{i(\not{p}+\not{k}+m_k)}{(p+k)^2-m_k^2}\frac{iP_{\mu\nu}}{k^2-m_V^2}\gamma^\nu\left(C_V P_L - C_V^T P_R\right)_{kj},$$

with no index summation notation. In the latter term, we defined the vector boson propagator numerator, which we rewrite as

$$\begin{aligned}\gamma^\mu P_{\mu\nu}\gamma^\nu &= \gamma^\mu\left[g_{\mu\nu}-(1-\xi_V)\frac{k_\mu k_\nu}{k^2-\xi_V m_V^2}\right]\gamma^\nu \\ &= d-(1-\xi_V)\frac{k^2-m_k^2}{k^2-\xi_V m_V^2}-\frac{m_k^2}{m_V^2}\frac{(k^2-\xi_V m_V^2)-(k^2-m_V^2)}{k^2-\xi_V m_V^2}.\end{aligned}$$

This allows us to write the relevant part of the self-energy as functions of the scalar two-point loop function

$$B_0(l,m_a^2,m_c^2) = \mu^{2\epsilon}\int\frac{d^dk}{(2\pi)^d}\frac{1}{(k^2-m_a^2)((l+k)^2-m_c^2)}, \tag{D.0.2}$$

such that

$$\Sigma_{ij}^s(0)\,P_R = -\frac{\pi^2}{(2\pi)^4}\mu^{d-4}\left[(\Delta_s)_{ik}m_k B_0(0,m_k^2,m_s^2)(\Delta_s)_{kj}\right]P_R \tag{D.0.3}$$

$$\Sigma_{ij}^G(0)\,P_R = \frac{\pi^2}{(2\pi)^4}\mu^{d-4}\left[(\Delta_G)_{ik}m_k B_0(0,m_k^2,\xi_V m_V^2)(\Delta_G)_{kj}\right]P_R \tag{D.0.4}$$

$$\Sigma_{ij}^V(0)\,P_R = -\frac{\pi^2}{(2\pi)^4}\mu^{d-4}\left[(C_V)_{ik}m_k\, f(m_k^2,m_V^2,\xi m_V^2)(C_V^*)_{kj}\right]P_R, \tag{D.0.5}$$

where the rearrangement of the boson propagator allowed us to write $f(m_k^2,m_V^2,\xi m_V^2)$ as

$$\begin{aligned}f(m_k^2,m_V^2,\xi m_V^2) = {}& d\,B_0(0,m_k^2,m_V^2)-(1-\xi_V)B_0(0,m_V^2,\xi_V m_V^2)+ \\ & \frac{m_k^2}{m_V^2}B_0(0,m_k^2,\xi_V m_V^2)-\frac{m_k^2}{m_V^2}B_0(0,m_k^2,m_V^2).\end{aligned}$$

Finally, the scalar loop function is given by

$$\begin{aligned}B_0(0,m_a^2,m_b^2) &= \frac{1}{\epsilon}-\gamma_E+\ln 4\pi-\int_0^1 dx\ln\frac{m_a^2-x(m_a^2-m_b^2)}{\mu^2} \\ &= \frac{1}{\epsilon}-\gamma_E+\ln 4\pi-\frac{m_a^2}{m_b^2-m_a^2}\left[\ln\frac{m_a^2}{\mu^2}-1\right]+\frac{m_b^2}{m_b^2-m_a^2}\left[\ln\frac{m_b^2}{\mu^2}-1\right].\end{aligned}$$

The finiteness of our final result and its gauge invariance are a consequence of the identities in Eqs. 5.2.24 and 5.2.26. For light neutrinos ($i,j=1,2,3$), the final result reads

$$\Sigma_{ij} P_R = -\frac{\pi^2}{(2\pi)^4} C_V \hat{m} \left[d\, B_0(0, \hat{m}^2, m_V^2) + \frac{\hat{m}^2}{m_V^2} \Big(B_0(0, \hat{m}^2, m_S^2) - B_0(0, \hat{m}^2, m_V^2) \Big) \right] C_V^T P_R. \tag{D.0.6}$$

After significant algebra, and checking the cancellation of divergencies, we arrive at

$$m_{ij} = \frac{1}{4\pi^2} \sum_{k=4}^{5} \Big[(C_Z)_{ik} (C_Z)_{jk} \frac{m_k^3}{m_Z^2} F(m_k^2, m_Z^2, m_h^2) \; + \; (C_{Z'})_{ik} (C_{Z'})_{jk} \frac{m_k^3}{m_{Z'}^2} F(m_k^2, m_{Z'}^2, m_{\varphi'}^2) \Big], \tag{D.0.7}$$

where

$$F(a, b, c) \equiv \frac{3 \, \ln(a/b)}{a/b - 1} + \frac{\ln(a/c)}{a/c - 1}. \tag{D.0.8}$$

For the full expression, involving mixing, we find ($B_0(x^2) \equiv B_0(0, \hat{m}^2, x^2)$)

$$\begin{aligned}
\Sigma^M(0) = {} & C_Z \hat{m} \left\{ 4B_0(m_Z^2) - \frac{\hat{m}^2}{m_Z^2} \Big[B_0(m_Z^2) - c_{\omega'}^2 B_0(m_{h'}^2) - s_{\omega'}^2 B_0(m_{\varphi'}^2) \Big] \right\} C_Z^{\mathrm{T}} \\
& + C_{Z'} \hat{m} \left\{ 4B_0(m_{Z'}^2) - \frac{\hat{m}^2}{m_{Z'}^2} \Big[B_0(m_{Z'}^2) - c_{\omega'}^2 B_0(m_{\varphi'}^2) - s_{\omega'}^2 B_0(m_{h'}^2) \Big] \right\} C_{Z'}^{\mathrm{T}} \\
& + s_{\omega'} c_{\omega'} \left\{ C_Z \hat{m} \Big[B_0(m_{h'}^2) - B_0(m_{\varphi'}^2) \Big] C_{Z'}^{\mathrm{T}} + C_{Z'} \hat{m} \Big[B_0(m_{h'}^2) - B_0(m_{\varphi'}^2) \Big] C_Z^{\mathrm{T}} \right\}.
\end{aligned}$$

Bibliography

[1] P. Ballett, M. Hostert, S. Pascoli, Y. F. Perez-Gonzalez, Z. Tabrizi and R. Zukanovich Funchal, *Neutrino Trident Scattering at Near Detectors*, *JHEP* **01** (2019) 119, [1807.10973].

[2] P. Ballett, M. Hostert and S. Pascoli, *Neutrino Masses from a Dark Neutrino Sector below the Electroweak Scale*, 1903.07590.

[3] P. Ballett, M. Hostert and S. Pascoli, *Dark Neutrinos and a Three Portal Connection to the Standard Model*, 1903.07589.

[4] P. Ballett, M. Hostert, S. Pascoli, Y. F. Perez-Gonzalez and Z. Tabrizi, *$Z's$ in neutrino scattering at DUNE*, 1902.08579.

[5] C. A. Argüelles, M. Hostert and Y.-D. Tsai, *Testing New Physics Explanations of MiniBooNE Anomaly at Neutrino Scattering Experiments*, 1812.08768.

[6] DUNE collaboration, R. Acciarri et al., *Long-Baseline Neutrino Facility (LBNF) and Deep Underground Neutrino Experiment (DUNE)*, 1512.06148.

[7] Hyper-Kamiokande collaboration, K. Abe et al., *Hyper-Kamiokande Design Report*, 1805.04163.

[8] C.-N. Yang and R. L. Mills, *Conservation of Isotopic Spin and Isotopic Gauge Invariance*, *Phys. Rev.* **96** (1954) 191–195.

[9] S. L. Glashow, *Partial Symmetries of Weak Interactions*, *Nucl. Phys.* **22** (1961) 579–588.

[10] S. Weinberg, *A Model of Leptons*, *Phys. Rev. Lett.* **19** (1967) 1264–1266.

[11] A. Salam, *Weak and Electromagnetic Interactions*, *Conf. Proc.* **C680519** (1968) 367–377.

[12] P. W. Higgs, *Broken symmetries, massless particles and gauge fields*, *Phys. Lett.* **12** (1964) 132–133.

[13] P. W. Higgs, *Broken Symmetries and the Masses of Gauge Bosons*, *Phys. Rev. Lett.* **13** (1964) 508–509.

[14] F. Englert and R. Brout, *Broken Symmetry and the Mass of Gauge Vector Mesons*, *Phys. Rev. Lett.* **13** (1964) 321–323.

[15] CMS collaboration, S. Chatrchyan et al., *Observation of a new boson at a mass of 125 GeV with the CMS experiment at the LHC*, *Phys. Lett.* **B716** (2012) 30–61, [1207.7235].

[16] ATLAS collaboration, G. Aad et al., *Observation of a new particle in the search for the Standard Model Higgs boson with the ATLAS detector at the LHC*, *Phys. Lett.* **B716** (2012) 1–29, [1207.7214].

[17] G. Zweig, *An SU(3) model for strong interaction symmetry and its breaking. Version 1*, .

[18] M. Gell-Mann, *A Schematic Model of Baryons and Mesons*, *Phys. Lett.* **8** (1964) 214–215.

[19] D. J. Gross and F. Wilczek, *Ultraviolet Behavior of Nonabelian Gauge Theories*, *Phys. Rev. Lett.* **30** (1973) 1343–1346.

[20] H. D. Politzer, *Reliable Perturbative Results for Strong Interactions?*, *Phys. Rev. Lett.* **30** (1973) 1346–1349.

[21] T. Nakano and K. Nishijima, *Charge Independence for V-particles*, *Prog. Theor. Phys.* **10** (1953) 581–582.

[22] M. Gell-Mann, *The interpretation of the new particles as displaced charge multiplets*, *Nuovo Cim.* **4** (1956) 848–866.

[23] Gargamelle Neutrino collaboration, F. J. Hasert et al., *Observation of Neutrino Like Interactions Without Muon Or Electron in the Gargamelle Neutrino Experiment*, *Phys. Lett.* **B46** (1973) 138–140.

[24] Particle Data Group collaboration, M. Tanabashi et al., *Review of Particle Physics*, *Phys. Rev.* **D98** (2018) 030001.

[25] ALEPH, DELPHI, L3, OPAL, SLD, LEP Electroweak Working Group, SLD Electroweak Group, SLD Heavy Flavour Group collaboration, S. Schael et al., *Precision electroweak measurements on the Z resonance*, *Phys. Rept.* **427** (2006) 257–454, [hep-ex/0509008].

[26] L. D. Faddeev and V. N. Popov, *Feynman Diagrams for the Yang-Mills Field*, *Phys. Lett.* **B25** (1967) 29–30.

[27] J. M. Cornwall, D. N. Levin and G. Tiktopoulos, *Derivation of Gauge Invariance from High-Energy Unitarity Bounds on the s Matrix*, *Phys. Rev.* **D10** (1974) 1145.

[28] C. H. Llewellyn Smith, *High-Energy Behavior and Gauge Symmetry*, *Phys. Lett.* **46B** (1973) 233–236.

[29] N. Cabibbo, *Unitary Symmetry and Leptonic Decays*, *Phys. Rev. Lett.* **10** (1963) 531–533.

[30] M. Kobayashi and T. Maskawa, *CP Violation in the Renormalizable Theory of Weak Interaction*, *Prog. Theor. Phys.* **49** (1973) 652–657.

[31] D. A. Kirzhnits and A. D. Linde, *Macroscopic Consequences of the Weinberg Model*, *Phys. Lett.* **42B** (1972) 471–474.

[32] L. Dolan and R. Jackiw, *Symmetry Behavior at Finite Temperature*, *Phys. Rev.* **D9** (1974) 3320–3341.

[33] S. Weinberg, *Gauge and Global Symmetries at High Temperature*, *Phys. Rev.* **D9** (1974) 3357–3378.

[34] N. Cabibbo, L. Maiani, G. Parisi and R. Petronzio, *Bounds on the Fermions and Higgs Boson Masses in Grand Unified Theories*, *Nucl. Phys.* **B158** (1979) 295–305.

[35] G. Degrassi, S. Di Vita, J. Elias-Miro, J. R. Espinosa, G. F. Giudice, G. Isidori et al., *Higgs mass and vacuum stability in the Standard Model at NNLO*, *JHEP* **08** (2012) 098, [1205.6497].

[36] R. J. Crewther, P. Di Vecchia, G. Veneziano and E. Witten, *Chiral Estimate of the Electric Dipole Moment of the Neutron in Quantum Chromodynamics*, *Phys. Lett.* **88B** (1979) 123.

[37] J. M. Pendlebury et al., *Revised experimental upper limit on the electric dipole moment of the neutron*, *Phys. Rev.* **D92** (2015) 092003, [1509.04411].

[38] R. D. Peccei and H. R. Quinn, *Constraints Imposed by CP Conservation in the Presence of Instantons*, *Phys. Rev.* **D16** (1977) 1791–1797.

[39] F. Zwicky, *Die Rotverschiebung von extragalaktischen Nebeln*, *Helv. Phys. Acta* **6** (1933) 110–127.

[40] V. C. Rubin and W. K. Ford, Jr., *Rotation of the Andromeda Nebula from a Spectroscopic Survey of Emission Regions*, *Astrophys. J.* **159** (1970) 379–403.

[41] Planck collaboration, Y. Akrami et al., *Planck 2018 results. I. Overview and the cosmological legacy of Planck*, 1807.06205.

[42] D. Clowe, M. Bradac, A. H. Gonzalez, M. Markevitch, S. W. Randall, C. Jones et al., *A direct empirical proof of the existence of dark matter*, *Astrophys. J.* **648** (2006) L109–L113, [astro-ph/0608407].

[43] G. R. Blumenthal, S. M. Faber, J. R. Primack and M. J. Rees, *Formation of Galaxies and Large Scale Structure with Cold Dark Matter*, *Nature* **311** (1984) 517–525.

[44] R. Cooke, M. Pettini, R. A. Jorgenson, M. T. Murphy and C. C. Steidel, *Precision measures of the primordial abundance of deuterium*, *Astrophys. J.* **781** (2014) 31, [1308.3240].

[45] B. Famaey and S. McGaugh, *Modified Newtonian Dynamics (MOND): Observational Phenomenology and Relativistic Extensions*, *Living Rev. Rel.* **15** (2012) 10, [1112.3960].

[46] L. Barack et al., *Black holes, gravitational waves and fundamental physics: a roadmap*, *Class. Quant. Grav.* **36** (2019) 143001, [1806.05195].

[47] C. Boehm and P. Fayet, *Scalar dark matter candidates*, *Nucl. Phys.* **B683** (2004) 219–263, [hep-ph/0305261].

[48] C. Boehm, P. Fayet and J. Silk, *Light and heavy dark matter particles*, *Phys. Rev.* **D69** (2004) 101302, [hep-ph/0311143].

[49] J. Alexander et al., *Dark Sectors 2016 Workshop: Community Report*, 2016, 1608.08632, http://lss.fnal.gov/archive/2016/conf/fermilab-conf-16-421.pdf.

[50] N. Craig, C. Englert and M. McCullough, *New Probe of Naturalness*, *Phys. Rev. Lett.* **111** (2013) 121803, [1305.5251].

[51] J. Heeck, *Unbroken B – L symmetry*, *Phys. Lett.* **B739** (2014) 256–262, [1408.6845].

[52] P. Minkowski, $\mu \to e\gamma$ *at a Rate of One Out of* 10^9 *Muon Decays?*, *Phys. Lett.* **67B** (1977) 421–428.

[53] R. N. Mohapatra and G. Senjanovic, *Neutrino Mass and Spontaneous Parity Violation*, *Phys. Rev. Lett.* **44** (1980) 912.

[54] T. Yanagida, *HORIZONTAL SYMMETRY AND MASSES OF NEUTRINOS*, *Conf. Proc.* **C7902131** (1979) 95–99.

[55] M. Gell-Mann, P. Ramond and R. Slansky, *Complex Spinors and Unified Theories*, *Conf. Proc.* **C790927** (1979) 315–321, [1306.4669].

[56] W. Konetschny and W. Kummer, *Nonconservation of Total Lepton Number with Scalar Bosons*, *Phys. Lett.* **70B** (1977) 433–435.

[57] T. P. Cheng and L.-F. Li, *Neutrino Masses, Mixings and Oscillations in SU(2) x U(1) Models of Electroweak Interactions*, *Phys. Rev.* **D22** (1980) 2860.

[58] G. Lazarides, Q. Shafi and C. Wetterich, *Proton Lifetime and Fermion Masses in an SO(10) Model*, *Nucl. Phys.* **B181** (1981) 287–300.

[59] J. Schechter and J. W. F. Valle, *Neutrino Masses in SU(2) x U(1) Theories*, *Phys. Rev.* **D22** (1980) 2227.

[60] R. N. Mohapatra and G. Senjanovic, *Neutrino Masses and Mixings in Gauge Models with Spontaneous Parity Violation*, *Phys. Rev.* **D23** (1981) 165.

[61] R. Foot, H. Lew, X. G. He and G. C. Joshi, *Seesaw Neutrino Masses Induced by a Triplet of Leptons*, *Z. Phys.* **C44** (1989) 441.

[62] J. A. Casas and A. Ibarra, *Oscillating neutrinos and muon —> e, gamma*, *Nucl. Phys.* **B618** (2001) 171–204, [hep-ph/0103065].

[63] A. Arhrib, R. Benbrik, M. Chabab, G. Moultaka, M. C. Peyranere, L. Rahili et al., *The Higgs Potential in the Type II Seesaw Model*, *Phys. Rev.* **D84** (2011) 095005, [1105.1925].

[64] R. N. Mohapatra and J. W. F. Valle, *Neutrino Mass and Baryon Number Nonconservation in Superstring Models*, *Phys. Rev.* **D34** (1986) 1642.

[65] M. C. Gonzalez-Garcia and J. W. F. Valle, *Fast Decaying Neutrinos and Observable Flavor Violation in a New Class of Majoron Models*, *Phys. Lett.* **B216** (1989) 360–366.

[66] D. Wyler and L. Wolfenstein, *Massless Neutrinos in Left-Right Symmetric Models*, *Nucl. Phys.* **B218** (1983) 205–214.

[67] E. K. Akhmedov, M. Lindner, E. Schnapka and J. W. F. Valle, *Left-right symmetry breaking in NJL approach*, *Phys. Lett.* **B368** (1996) 270–280, [hep-ph/9507275].

[68] E. K. Akhmedov, M. Lindner, E. Schnapka and J. W. F. Valle, *Dynamical left-right symmetry breaking*, *Phys. Rev.* **D53** (1996) 2752–2780, [hep-ph/9509255].

[69] S. K. Kang and C. S. Kim, *Extended double seesaw model for neutrino mass spectrum and low scale leptogenesis*, *Phys. Lett.* **B646** (2007) 248–252, [hep-ph/0607072].

[70] J. Barry, W. Rodejohann and H. Zhang, *Light Sterile Neutrinos: Models and Phenomenology*, *JHEP* **07** (2011) 091, [1105.3911].

[71] H. Zhang, *Light Sterile Neutrino in the Minimal Extended Seesaw*, *Phys. Lett.* **B714** (2012) 262–266, [1110.6838].

[72] J. Lopez-Pavon, S. Pascoli and C.-f. Wong, *Can heavy neutrinos dominate neutrinoless double beta decay?*, *Phys. Rev.* **D87** (2013) 093007, [1209.5342].

[73] E. Ma, *Verifiable radiative seesaw mechanism of neutrino mass and dark matter*, *Phys. Rev.* **D73** (2006) 077301, [hep-ph/0601225].

[74] L. M. Krauss, S. Nasri and M. Trodden, *A Model for neutrino masses and dark matter*, *Phys. Rev.* **D67** (2003) 085002, [hep-ph/0210389].

[75] B. Pontecorvo, *Inverse beta processes and nonconservation of lepton charge*, *Sov. Phys. JETP* **7** (1958) 172–173.

[76] Z. Maki, M. Nakagawa and S. Sakata, *Remarks on the unified model of elementary particles*, *Prog. Theor. Phys.* **28** (1962) 870–880.

[77] T. Schwetz, M. Tortola and J. W. F. Valle, *Global neutrino data and recent reactor fluxes: status of three-flavour oscillation parameters*, *New J. Phys.* **13** (2011) 063004, [1103.0734].

[78] M. C. Gonzalez-Garcia, M. Maltoni and T. Schwetz, *Updated fit to three neutrino mixing: status of leptonic CP violation*, *JHEP* **11** (2014) 052, [1409.5439].

[79] I. Esteban, M. C. Gonzalez-Garcia, A. Hernandez-Cabezudo, M. Maltoni and T. Schwetz, *Global analysis of three-flavour neutrino oscillations: synergies and tensions in the determination of $\theta_2 3, \delta_C P$, and the mass ordering*, *JHEP* **01** (2019) 106, [1811.05487].

[80] C. Y. Cardall, *Coherence of neutrino flavor mixing in quantum field theory*, *Phys. Rev.* **D61** (2000) 073006, [hep-ph/9909332].

[81] M. Beuthe, *Oscillations of neutrinos and mesons in quantum field theory*, *Phys. Rept.* **375** (2003) 105–218, [hep-ph/0109119].

[82] C. Giunti, *Neutrino wave packets in quantum field theory*, *JHEP* **11** (2002) 017, [hep-ph/0205014].

[83] E. K. Akhmedov and J. Kopp, *Neutrino Oscillations: Quantum Mechanics vs. Quantum Field Theory*, *JHEP* **04** (2010) 008, [1001.4815].

[84] A. Kobach, A. V. Manohar and J. McGreevy, *Neutrino Oscillation Measurements Computed in Quantum Field Theory*, *Phys. Lett.* **B783** (2018) 59–75, [1711.07491].

[85] G. Cozzella and C. Giunti, *Mixed states for mixing neutrinos*, *Phys. Rev.* **D98** (2018) 096010, [1804.00184].

[86] D. Notzold and G. Raffelt, *Neutrino Dispersion at Finite Temperature and Density*, *Nucl. Phys.* **B307** (1988) 924–936.

[87] J. F. Nieves, *Neutrinos in a Medium*, *Phys. Rev.* **D40** (1989) 866.

[88] H. A. Weldon, *Covariant Calculations at Finite Temperature: The Relativistic Plasma*, *Phys. Rev.* **D26** (1982) 1394.

[89] J. C. D'Olivo, J. F. Nieves and M. Torres, *Finite temperature corrections to the effective potential of neutrinos in a medium*, *Phys. Rev.* **D46** (1992) 1172–1179.

[90] F. J. Botella, C. S. Lim and W. J. Marciano, *Radiative Corrections to Neutrino Indices of Refraction*, *Phys. Rev.* **D35** (1987) 896.

[91] MINERvA collaboration, L. Aliaga et al., *Neutrino Flux Predictions for the NuMI Beam*, *Phys. Rev.* **D94** (2016) 092005, [1607.00704].

[92] M. Betancourt et al., *Comparisons and Challenges of Modern Neutrino Scattering Experiments (TENSIONS2016 Report)*, *Phys. Rept.* **773-774** (2018) 1–28, [1805.07378].

[93] MiniBooNE collaboration, A. A. Aguilar-Arevalo et al., *First Measurement of the Muon Neutrino Charged Current Quasielastic Double Differential Cross Section*, *Phys. Rev.* **D81** (2010) 092005, [1002.2680].

[94] J. Nieves, I. Ruiz Simo and M. J. Vicente Vacas, *The nucleon axial mass and the MiniBooNE Quasielastic Neutrino-Nucleus Scattering problem*, *Phys. Lett.* **B707** (2012) 72–75, [1106.5374].

[95] E. Hernandez, J. Nieves and M. J. Vicente-Vacas, *Neutrino Induced Coherent Pion Production off Nuclei and PCAC*, *Phys. Rev.* **D80** (2009) 013003, [0903.5285].

[96] MINERvA collaboration, J. Mousseau et al., *Measurement of Partonic Nuclear Effects in Deep-Inelastic Neutrino Scattering using MINERvA*, *Phys. Rev.* **D93** (2016) 071101, [1601.06313].

[97] C. Andreopoulos et al., *The GENIE Neutrino Monte Carlo Generator*, *Nucl. Instrum. Meth.* **A614** (2010) 87–104, [0905.2517].

[98] O. Buss, T. Gaitanos, K. Gallmeister, H. van Hees, M. Kaskulov, O. Lalakulich et al., *Transport-theoretical Description of Nuclear Reactions*, *Phys. Rept.* **512** (2012) 1–124, [1106.1344].

[99] Y. Hayato, *NEUT*, *Nucl. Phys. Proc. Suppl.* **112** (2002) 171–176.

[100] C. Juszczak, J. A. Nowak and J. T. Sobczyk, *Simulations from a new neutrino event generator*, *Nucl. Phys. Proc. Suppl.* **159** (2006) 211–216, [hep-ph/0512365].

[101] W. Czyz, G. C. Sheppey and J. D. Walecka, *Neutrino production of lepton pairs through the point four-fermion interaction*, *Nuovo Cim.* **34** (1964) 404–435.

[102] J. Lovseth and M. Radomiski, *Kinematical distributions of neutrino-produced lepton triplets*, *Phys. Rev.* **D3** (1971) 2686–2706.

[103] K. Fujikawa, *The self-coupling of weak lepton currents in high-energy neutrino and muon reactions*, *Annals Phys.* **68** (1971) 102–162.

[104] R. W. Brown, *Intermediate boson. i. theoretical production cross-sections in high-energy neutrino and muon experiments*, *Phys. Rev.* **D3** (1971) 207–223.

[105] K. Koike, M. Konuma, K. Kurata and K. Sugano, *Neutrino production of lepton pairs. 1. -*, *Prog. Theor. Phys.* **46** (1971) 1150–1169.

[106] G. Magill and R. Plestid, *Neutrino Trident Production at the Intensity Frontier*, *Phys. Rev.* **D95** (2017) 073004, [1612.05642].

[107] CHARM-II collaboration, D. Geiregat et al., *First observation of neutrino trident production*, *Phys. Lett.* **B245** (1990) 271–275.

[108] CCFR collaboration, S. R. Mishra et al., *Neutrino tridents and W Z interference*, *Phys. Rev. Lett.* **66** (1991) 3117–3120.

[109] NuTeV collaboration, T. Adams et al., *Neutrino trident production from NuTeV*, in *High-energy physics. Proceedings, 29th International Conference, ICHEP'98, Vancouver, Canada, July 23-29, 1998. Vol. 1, 2*, pp. 631–634, 1998, hep-ex/9811012.

[110] R. W. Brown, R. H. Hobbs, J. Smith and N. Stanko, *Intermediate boson. iii. virtual-boson effects in neutrino trident production*, *Phys. Rev.* **D6** (1972) 3273–3292.

[111] I. V. Gaidaenko, V. A. Novikov and M. I. Vysotsky, *On the production of a lepton pair in the collision of ultrarelativistic neutral particle with nonzero magnetic moment with nuclei*, *Phys. Lett.* **B497** (2001) 49–54, [hep-ph/0007204].

[112] W. Altmannshofer, S. Gori, M. Pospelov and I. Yavin, *Neutrino Trident Production: A Powerful Probe of New Physics with Neutrino Beams*, *Phys. Rev. Lett.* **113** (2014) 091801, [1406.2332].

[113] Y. Kaneta and T. Shimomura, *On the possibility of a search for the $L_\mu - L_\tau$ gauge boson at Belle-II and neutrino beam experiments*, *PTEP* **2017** (2017) 053B04, [1701.00156].

[114] S.-F. Ge, M. Lindner and W. Rodejohann, *New Physics and Atmospheric Neutrino Trident Production with PINGU and ORCA*, 1702.02617.

[115] G. Magill and R. Plestid, *Probing new charged scalars with neutrino trident production*, *Phys. Rev.* **D97** (2018) 055003, [1710.08431].

[116] A. Falkowski, G. Grilli di Cortona and Z. Tabrizi, *Future DUNE constraints on EFT*, *JHEP* **04** (2018) 101, [1802.08296].

[117] R. Belusevic and J. Smith, *W - Z Interference in Neutrino - Nucleus Scattering*, *Phys. Rev.* **D37** (1988) 2419.

[118] M. A. Kozhushner and E. P. Shabalin, *Production of lepton particle pairs on a Coulomb center*, *Sov. Phys. JETP* **14** (1962) 676.

[119] E. P. Shabalin, *The $\mu^+\mu^-$ and e^+e^- pair production cross sections for neutrinos scattered by nuclei*, *Sov. Phys. JETP* **16** (1963) 125.

[120] L. N. Hand, *Experimental investigation of pion electroproduction*, *Phys. Rev.* **129** (1963) 1834–1846.

[121] T. W. Donnelly and J. D. Walecka, *Electron Scattering and Nuclear Structure*, *Ann. Rev. Nucl. Part. Sci.* **25** (1975) 329–405.

[122] W. Altmannshofer, S. Gori, J. Martín-Albo, A. Sousa and M. Wallbank, *Neutrino Tridents at DUNE*, 1902.06765.

[123] B. A. Kniehl, *Elastic e p scattering and the Weizsacker-Williams approximation*, *Phys. Lett.* **B254** (1991) 267–273.

[124] C. F. von Weizsacker, *Radiation emitted in collisions of very fast electrons*, *Z. Phys.* **88** (1934) 612–625.

[125] E. J. Williams, *Nature of the high-energy particles of penetrating radiation and status of ionization and radiation formulae*, *Phys. Rev.* **45** (1934) 729–730.

[126] E. Fermi, *On the Theory of the impact between atoms and electrically charged particles*, *Z. Phys.* **29** (1924) 315–327.

[127] S. Frixione, M. L. Mangano, P. Nason and G. Ridolfi, *Improving the Weizsacker-Williams approximation in electron - proton collisions*, *Phys. Lett.* **B319** (1993) 339–345, [hep-ph/9310350].

[128] R. Acciarri et al., *A Proposal for a Three Detector Short-Baseline Neutrino Oscillation Program in the Fermilab Booster Neutrino Beam*, 1503.01520.

[129] DUNE collaboration, R. Acciarri et al., *Long-Baseline Neutrino Facility (LBNF) and Deep Underground Neutrino Experiment (DUNE)*, 1601.02984.

[130] D. DUNE Collaboration, R. Acciarri et al., *Long-Baseline Neutrino Facility (LBNF) and Deep Underground Neutrino Experiment (DUNE) Conceptual Design Report Volume 2: The Physics Program for DUNE at LBNF*, 1512.06148.

[131] A. Weber, "ND(s) for DUNE." May, 2018.

[132] DUNE collaboration, V. Papadimitriou, "Design of the LBNF Beamline." 2016.

[133] F. J. P. Soler, *nuSTORM: Neutrinos from Stored Muons*, in *Proceedings, Topical Research Meeting on Prospects in Neutrino Physics (NuPhys2014): London, UK, December 15-17, 2014*, 2015, 1507.08836.

[134] D. Adey, R. Appleby, R. Bayes, A. Bogacz, A. Bross, J.-B. Lagrange et al., *Overview of the neutrinos from stored muons facility - nustorm*, *Journal of Instrumentation* **12** (2017) P07020.

[135] νSTORM collaboration, D. Adey et al., *Light sterile neutrino sensitivity at the nuSTORM facility*, *Phys. Rev.* **D89** (2014) 071301, [1402.5250].

[136] C. Andreopoulos et al., *The GENIE Neutrino Monte Carlo Generator*, *Nucl. Instrum. Meth.* **A614** (2010) 87–104, [0905.2517].

[137] J. Smith and J. A. M. Vermaseren, *Electromagnetic Backgrounds in Neutrino Produced Trimuon Events*, *Phys. Rev.* **D17** (1978) 2288.

[138] C. H. Albright, J. Smith and J. A. M. Vermaseren, *A Comparison of Trimuon Production Mechanisms*, *Phys. Rev.* **D18** (1978) 108.

[139] M. Blennow, P. Coloma, E. Fernandez-Martinez, J. Hernandez-Garcia and J. Lopez-Pavon, *Non-Unitarity, sterile neutrinos, and Non-Standard neutrino Interactions*, *JHEP* **04** (2017) 153, [1609.08637].

[140] S. Hannestad, R. S. Hansen and T. Tram, *How Self-Interactions can Reconcile Sterile Neutrinos with Cosmology*, *Phys. Rev. Lett.* **112** (2014) 031802, [1310.5926].

[141] B. Dasgupta and J. Kopp, *Cosmologically Safe eV-Scale Sterile Neutrinos and Improved Dark Matter Structure*, *Phys. Rev. Lett.* **112** (2014) 031803, [1310.6337].

[142] A. Mirizzi, G. Mangano, O. Pisanti and N. Saviano, *Collisional production of sterile neutrinos via secret interactions and cosmological implications*, *Phys. Rev.* **D91** (2015) 025019, [1410.1385].

[143] J. F. Cherry, A. Friedland and I. M. Shoemaker, *Short-baseline neutrino oscillations, Planck, and IceCube*, 1605.06506.

[144] F. Capozzi, I. M. Shoemaker and L. Vecchi, *Solar Neutrinos as a Probe of Dark Matter-Neutrino Interactions*, *JCAP* **1707** (2017) 021, [1702.08464].

[145] P. B. Denton, Y. Farzan and I. M. Shoemaker, *Activating the fourth neutrino of the 3+1 scheme*, *Phys. Rev.* **D99** (2019) 035003, [1811.01310].

[146] X. Chu, B. Dasgupta, M. Dentler, J. Kopp and N. Saviano, *Sterile neutrinos with secret interactions—cosmological discord?*, *JCAP* **1811** (2018) 049, [1806.10629].

[147] A. Esmaili and H. Nunokawa, *On the robustness of IceCube's bound on sterile neutrinos in the presence of non-standard interactions*, *Eur. Phys. J.* **C79** (2019) 70, [1810.11940].

[148] E. Bertuzzo, S. Jana, P. A. N. Machado and R. Zukanovich Funchal, *Dark Neutrino Portal to Explain MiniBooNE excess*, *Phys. Rev. Lett.* **121** (2018) 241801, [1807.09877].

[149] P. Ballett, S. Pascoli and M. Ross-Lonergan, *U(1)' mediated decays of heavy sterile neutrinos in MiniBooNE*, 1808.02915.

[150] C. Boehm, *Implications of a new light gauge boson for neutrino physics*, *Phys. Rev.* **D70** (2004) 055007, [hep-ph/0405240].

[151] D. G. Cerdeño, M. Fairbairn, T. Jubb, P. A. N. Machado, A. C. Vincent and C. Bœhm, *Physics from solar neutrinos in dark matter direct detection experiments*, *JHEP* **05** (2016) 118, [1604.01025].

[152] P. B. Denton, Y. Farzan and I. M. Shoemaker, *Testing large non-standard neutrino interactions with arbitrary mediator mass after COHERENT data*, *JHEP* **07** (2018) 037, [1804.03660].

[153] A. Falkowski, M. González-Alonso and Z. Tabrizi, *Reactor neutrino oscillations as constraints on Effective Field Theory*, 1901.04553.

[154] Y. Farzan, *A model for large non-standard interactions of neutrinos leading to the LMA-Dark solution*, *Phys. Lett.* **B748** (2015) 311–315, [1505.06906].

[155] P. Bakhti, Y. Farzan and M. Rajaee, *Secret interactions of neutrinos with light gauge boson at the DUNE near detector*, *Phys. Rev.* **D99** (2019) 055019, [1810.04441].

[156] X.-G. He, G. C. Joshi, H. Lew and R. R. Volkas, *Simplest Z-prime model*, *Phys. Rev.* **D44** (1991) 2118–2132.

[157] X. G. He, G. C. Joshi, H. Lew and R. R. Volkas, *NEW Z-prime PHENOMENOLOGY*, *Phys. Rev.* **D43** (1991) 22–24.

[158] M. Bauer, P. Foldenauer and J. Jaeckel, *Hunting All the Hidden Photons*, *JHEP* **07** (2018) 094, [1803.05466].

[159] W. Altmannshofer, S. Gori, M. Pospelov and I. Yavin, *Neutrino Trident Production: A Powerful Probe of New Physics with Neutrino Beams*, *Phys. Rev. Lett.* **113** (2014) 091801, [1406.2332].

[160] J. Park, *Neutrino-Electron Scattering in MINERvA for Constraining the NuMI Neutrino Flux*, Ph.D. thesis, U. Rochester, 2013. 10.2172/1248363.

[161] J. Bian, *Measurement of Neutrino-Electron Elastic Scattering at NOvA Near Detector*, in *Proceedings, Meeting of the APS Division of Particles and Fields (DPF 2017): Fermilab, Batavia, Illinois, USA, July 31 - August 4, 2017*, 2017, 1710.03428.

[162] M. Lindner, F. S. Queiroz, W. Rodejohann and X.-J. Xu, *Neutrino-electron scattering: general constraints on Z' and dark photon models*, *JHEP* **05** (2018) 098, [1803.00060].

[163] T. Araki, S. Hoshino, T. Ota, J. Sato and T. Shimomura, *Detecting the $L_\mu - L_\tau$ gauge boson at Belle II*, *Phys. Rev.* **D95** (2017) 055006, [1702.01497].

[164] S.-F. Ge, M. Lindner and W. Rodejohann, *Atmospheric Trident Production for Probing New Physics*, *Phys. Lett.* **B772** (2017) 164–168, [1702.02617].

[165] P. Batra, B. A. Dobrescu and D. Spivak, *Anomaly-free sets of fermions*, *J. Math. Phys.* **47** (2006) 082301, [hep-ph/0510181].

[166] J. A. Dror, R. Lasenby and M. Pospelov, *New constraints on light vectors coupled to anomalous currents*, *Phys. Rev. Lett.* **119** (2017) 141803, [1705.06726].

[167] V. D. Barger, E. Ma and K. Whisnant, *General Analysis of a Possible Second Weak Neutral Current in Gauge Models*, *Phys. Rev.* **D26** (1982) 2378.

[168] S. M. Barr, B. Bednarz and C. Benesh, *Anomaly Constraints and New U(1) Gauge Bosons*, *Phys. Rev.* **D34** (1986) 235.

[169] B. C. Allanach, J. Davighi and S. Melville, *An Anomaly-free Atlas: charting the space of flavour-dependent gauged $U(1)$ extensions of the Standard Model*, 1812.04602.

[170] J. Ellis, M. Fairbairn and P. Tunney, *Anomaly-Free Models for Flavour Anomalies*, *Eur. Phys. J.* **C78** (2018) 238, [1705.03447].

[171] B. C. Allanach, J. Davighi and S. Melville, *Anomaly-free, flavour-dependent U(1) charge assignments for Standard Model/Standard Model plus three right-handed neutrino fermionic content*, Dec., 2018. 10.5281/zenodo.1478085.

[172] A. Ismail, W.-Y. Keung, K.-H. Tsao and J. Unwin, *Axial vector Z' and anomaly cancellation*, *Nucl. Phys.* **B918** (2017) 220–244, [1609.02188].

[173] Y. Kahn, G. Krnjaic, S. Mishra-Sharma and T. M. P. Tait, *Light Weakly Coupled Axial Forces: Models, Constraints, and Projections*, *JHEP* **05** (2017) 002, [1609.09072].

[174] J. A. Dror, R. Lasenby and M. Pospelov, *Dark forces coupled to nonconserved currents*, *Phys. Rev.* **D96** (2017) 075036, [1707.01503].

[175] B. Holdom, *Two U(1)'s and Epsilon Charge Shifts*, *Phys. Lett.* **166B** (1986) 196–198.

[176] A. Kamada and H.-B. Yu, *Coherent Propagation of PeV Neutrinos and the Dip in the Neutrino Spectrum at IceCube*, *Phys. Rev.* **D92** (2015) 113004, [1504.00711].

[177] M. Ibe, W. Nakano and M. Suzuki, *Constraints on $L_\mu - L_\tau$ gauge interactions from rare kaon decay*, *Phys. Rev.* **D95** (2017) 055022, [1611.08460].

[178] M. Escudero, D. Hooper, G. Krnjaic and M. Pierre, *Cosmology With a Very Light $L_\mu - L_\tau$ Gauge Boson*, 1901.02010.

[179] T. Araki, F. Kaneko, T. Ota, J. Sato and T. Shimomura, *MeV scale leptonic force for cosmic neutrino spectrum and muon anomalous magnetic moment*, *Phys. Rev.* **D93** (2016) 013014, [1508.07471].

[180] J. Heeck and W. Rodejohann, *Gauged $L_\mu - L_\tau$ Symmetry at the Electroweak Scale*, *Phys. Rev.* **D84** (2011) 075007, [1107.5238].

[181] K. J. Kelly and Y. Zhang, *Mono-Neutrino at DUNE: New Signals From Neutrinophilic Thermal Dark Matter*, 1901.01259.

[182] M. Holder et al., *Observation of Trimuon Events Produced in Neutrino and anti-neutrino Interactions*, *Phys. Lett.* **70B** (1977) 393–395.

[183] CHORUS collaboration, A. Kayis-Topaksu et al., *Experimental study of trimuon events in neutrino charged-current interactions*, *Phys. Lett.* **B596** (2004) 44–53.

[184] A. Benvenuti et al., *Observation of a new process with trimuon production by high-energy neutrinos*, *Physical Review Letters* **38** (may, 1977) 1110–1113.

[185] B. C. Barish, J. F. Bartlett, A. Bodek, K. W. Brown, D. Buchholz, Y. K. Chu et al., *Observation of Trimuon Production by Neutrinos*, *Physical Review Letters* **38** (mar, 1977) 577–580.

[186] J. Smith and J. A. M. Vermaseren, *PH YSICAL RE VIE% 0 Electromagnetic backgrounds in neutrino-produced trimuon events*, .

[187] NuTeV collaboration, M. Goncharov et al., *Precise Measurement of Dimuon Production Cross-Sections in ν_μ Fe and $\bar{\nu}_\mu$ Fe Deep Inelastic Scattering at the Tevatron.*, *Phys. Rev.* **D64** (2001) 112006, [hep-ex/0102049].

[188] W. Czyz, G. C. Sheppey and J. D. Walecka, *Neutrino production of lepton pairs through the point four-fermion interaction*, *Il Nuovo Cimento* **34** (oct, 1964) 404–435.

[189] J. Løvseth and M. Radomski, *Kinematical distributions of neutrino-produced lepton triplets*, *Physical Review D* **3** (1971) 2686–2706.

[190] C. F. Uhlemann and N. Kauer, *Narrow-width approximation accuracy*, *Nucl. Phys.* **B814** (2009) 195–211, [0807.4112].

[191] W. J. Marciano and Z. Parsa, *Neutrino electron scattering theory*, *J. Phys.* **G29** (2003) 2629–2645, [hep-ph/0403168].

[192] A. de Gouvea and J. Jenkins, *What can we learn from neutrino electron scattering?*, *Phys. Rev.* **D74** (2006) 033004, [hep-ph/0603036].

[193] A. N. Khan, *Global analysis of the source and detector nonstandard interactions using the short baseline $\nu - e$ and $\overline{\nu} - e$ scattering data*, *Phys. Rev. D* **93** (May, 2016) 093019.

[194] J. N. Bahcall, M. Kamionkowski and A. Sirlin, *Solar neutrinos: Radiative corrections in neutrino - electron scattering experiments*, *Phys. Rev.* **D51** (1995) 6146–6158, [astro-ph/9502003].

[195] M. Passera, *QED corrections to neutrino electron scattering*, *Phys. Rev.* **D64** (2001) 113002, [hep-ph/0011190].

[196] R. W. Brown, R. H. Hobbs, J. Smith and N. Stanko, *Intermediate boson. iii. virtual-boson effects in neutrino trident production*, *Phys. Rev.* **D6** (1972) 3273–3292.

[197] DUNE collaboration, R. Acciarri et al., *Long-Baseline Neutrino Facility (LBNF) and Deep Underground Neutrino Experiment (DUNE)*, 1601.05471.

[198] D. R. Albert, "The DUNE Near Detector." Aug., 2018.

[199] M. Steven, "Status of DUNE Near Detector." Oct., 2018.

[200] DUNE collaboration, "2016 DUNE fluxes." 2016.

[201] DUNE collaboration, "2016 DUNE fluxes." 2017.

[202] DUNE collaboration, "High-Pressure Argon gas TPC Option for the DUNE Near Detector." 2019.

[203] MINOS collaboration, D. G. Michael et al., *The Magnetized steel and scintillator calorimeters of the MINOS experiment*, *Nucl. Instrum. Meth.* **A596** (2008) 190–228, [0805.3170].

[204] MINERvA collaboration, L. Aliaga et al., *Design, Calibration, and Performance of the MINERvA Detector*, *Nucl. Instrum. Meth.* **A743** (2014) 130–159, [1305.5199].

[205] A. G. Abramov, N. A. Galyaev, V. I. Garkusha, J. Hylen, F. N. Novoskoltsev, A. D. Ryabov et al., *Beam optics and target conceptual designs for the NuMI project*, *Nucl. Instrum. Meth.* **A485** (2002) 209–227.

[206] A. Bodek, U. Sarica, D. Naples and L. Ren, *Methods to Determine Neutrino Flux at Low Energies:Investigation of the Low ν Method*, *Eur. Phys. J.* **C72** (2012) 1973, [1201.3025].

[207] J. M. Conrad, M. H. Shaevitz and T. Bolton, *Precision measurements with high-energy neutrino beams*, *Rev. Mod. Phys.* **70** (1998) 1341–1392, [hep-ex/9707015].

[208] NOMAD collaboration, P. Astier et al., *Neutrino production of opposite sign dimuons in the NOMAD experiment*, *Phys. Lett.* **B486** (2000) 35–48.

[209] NuTeV collaboration, T. Adams et al., *Evidence for diffractive charm production in muon-neutrino Fe and anti-muon-neutrino Fe scattering at the Tevatron*, *Phys. Rev.* **D61** (2000) 092001, [hep-ex/9909041].

[210] N. J. Baker, S. A. Kahn, M. J. Murtagh, N. P. Samios, M. Tanaka, C. Baltay et al., *$\mu^- e^+$ dilepton production in charged-current ν_μ interactions*, *Phys. Rev. D* **43** (May, 1991) 2765–2777.

[211] MINERvA collaboration, A. Higuera et al., *Measurement of Coherent Production of $\pi^\pm$ in Neutrino and Antineutrino Beams on Carbon from E_ν of* 1.5 *to* 20 *GeV*, *Phys. Rev. Lett.* **113** (2014) 261802, [1409.3835].

[212] MINERvA collaboration, A. Mislivec et al., *Measurement of total and differential cross sections of neutrino and antineutrino coherent $\pi^\pm$ production on carbon*, *Phys. Rev.* **D97** (2018) 032014, [1711.01178].

[213] ArgoNeuT collaboration, R. Acciarri et al., *First Measurement of Neutrino and Antineutrino Coherent Charged Pion Production on Argon*, *Phys. Rev. Lett.* **113** (2014) 261801, [1408.0598].

[214] ArgoNeuT collaboration, R. Acciarri et al., *Measurement of ν_μ and $\bar{\nu}_\mu$ neutral current $\pi^0 \to \gamma\gamma$ production in the ArgoNeuT detector*, *Phys. Rev.* **D96** (2017) 012006, [1511.00941].

[215] MINERvA collaboration, J. Park et al., *Measurement of Neutrino Flux from Neutrino-Electron Elastic Scattering*, *Phys. Rev.* **D93** (2016) 112007, [1512.07699].

[216] S. Bilmis, I. Turan, T. M. Aliev, M. Deniz, L. Singh and H. T. Wong, *Constraints on Dark Photon from Neutrino-Electron Scattering Experiments*, *Phys. Rev.* **D92** (2015) 033009, [1502.07763].

[217] CHARM-II collaboration, P. Vilain et al., *Precision measurement of electroweak parameters from the scattering of muon-neutrinos on electrons*, *Phys. Lett.* **B335** (1994) 246–252.

[218] TEXONO collaboration, H. T. Wong et al., *A Search of Neutrino Magnetic Moments with a High-Purity Germanium Detector at the Kuo-Sheng Nuclear Power Station*, *Phys. Rev.* **D75** (2007) 012001, [hep-ex/0605006].

[219] TEXONO collaboration, M. Deniz et al., *Measurement of Nu(e)-bar -Electron Scattering Cross-Section with a CsI(Tl) Scintillating Crystal Array at the Kuo-Sheng Nuclear Power Reactor*, *Phys. Rev.* **D81** (2010) 072001, [0911.1597].

[220] J.-W. Chen, H.-C. Chi, H.-B. Li, C. P. Liu, L. Singh, H. T. Wong et al., *Constraints on millicharged neutrinos via analysis of data from atomic ionizations with germanium detectors at sub-keV sensitivities*, *Phys. Rev.* **D90** (2014) 011301, [1405.7168].

[221] G. Bellini et al., *Precision measurement of the 7Be solar neutrino interaction rate in Borexino*, *Phys. Rev. Lett.* **107** (2011) 141302, [1104.1816].

[222] BaBar collaboration, J. P. Lees et al., *Search for a Dark Photon in e^+e^- Collisions at BaBar*, *Phys. Rev. Lett.* **113** (2014) 201801, [1406.2980].

[223] BaBar collaboration, J. P. Lees et al., *Search for Invisible Decays of a Dark Photon Produced in e^+e^- Collisions at BaBar*, *Phys. Rev. Lett.* **119** (2017) 131804, [1702.03327].

[224] M. B. Wise and Y. Zhang, *Lepton Flavorful Fifth Force and Depth-dependent Neutrino Matter Interactions*, *JHEP* **06** (2018) 053, [1803.00591].

[225] M. Bustamante and S. K. Agarwalla, *Universe's Worth of Electrons to Probe Long-Range Interactions of High-Energy Astrophysical Neutrinos*, *Phys. Rev. Lett.* **122** (2019) 061103, [1808.02042].

[226] S. Baek, N. G. Deshpande, X. G. He and P. Ko, *Muon anomalous g-2 and gauged L(muon) - L(tau) models*, *Phys. Rev.* **D64** (2001) 055006, [hep-ph/0104141].

[227] M. Pospelov, *Secluded U(1) below the weak scale*, *Phys. Rev.* **D80** (2009) 095002, [0811.1030].

[228] A. Kamada, K. Kaneta, K. Yanagi and H.-B. Yu, *Self-interacting dark matter and muon $g-2$ in a gauged $U(1)_{L_\mu - L_\tau}$ model*, *JHEP* **06** (2018) 117, [1805.00651].

[229] Muon g-2 collaboration, G. W. Bennett et al., *Final Report of the Muon E821 Anomalous Magnetic Moment Measurement at BNL*, *Phys. Rev.* **D73** (2006) 072003, [hep-ex/0602035].

[230] RBC, UKQCD collaboration, T. Blum, P. A. Boyle, V. Gülpers, T. Izubuchi, L. Jin, C. Jung et al., *Calculation of the hadronic vacuum polarization contribution to the muon anomalous magnetic moment*, *Phys. Rev. Lett.* **121** (2018) 022003, [1801.07224].

[231] A. Keshavarzi, D. Nomura and T. Teubner, *Muon $g-2$ and $\alpha(M_Z^2)$: a new data-based analysis*, *Phys. Rev.* **D97** (2018) 114025, [1802.02995].

[232] Muon g-2 collaboration, J. Grange et al., *Muon (g-2) Technical Design Report*, 1501.06858.

[233] BaBar collaboration, J. P. Lees et al., *Search for a muonic dark force at BABAR*, *Phys. Rev.* **D94** (2016) 011102, [1606.03501].

[234] ATLAS collaboration, G. Aad et al., *Measurements of Four-Lepton Production at the Z Resonance in pp Collisions at $\sqrt{s}$ =7 and 8 TeV with ATLAS*, *Phys. Rev. Lett.* **112** (2014) 231806, [1403.5657].

[235] CMS collaboration, A. M. Sirunyan et al., *Search for an $L_\mu - L_\tau$ gauge boson using $Z \to 4\mu$ events in proton-proton collisions at $\sqrt{s} = 13$ TeV*, *Phys. Lett.* **B792** (2019) 345–368, [1808.03684].

[236] R. Petti, ""Precision measurements of fundamental interactions in the ND(s)." 2018.

[237] H. Duyang, B. Guo, S. R. Mishra and R. Petti, *A Novel Approach to Neutrino-Hydrogen Measurements*, 1809.08752.

[238] W. Buchmuller, C. Greub and P. Minkowski, *Neutrino masses, neutral vector bosons and the scale of B-L breaking*, *Phys. Lett.* **B267** (1991) 395–399.

[239] S. Khalil, *Low scale B - L extension of the Standard Model at the LHC*, *J. Phys.* **G35** (2008) 055001, [hep-ph/0611205].

[240] P. Fileviez Perez, T. Han and T. Li, *Testability of Type I Seesaw at the CERN LHC: Revealing the Existence of the B-L Symmetry*, *Phys. Rev.* **D80** (2009) 073015, [0907.4186].

[241] S. Khalil, *TeV-scale gauged B-L symmetry with inverse seesaw mechanism*, *Phys. Rev.* **D82** (2010) 077702, [1004.0013].

[242] C. O. Dib, G. R. Moreno and N. A. Neill, *Neutrinos with a linear seesaw mechanism in a scenario of gauged B-L symmetry*, *Phys. Rev.* **D90** (2014) 113003, [1409.1868].

[243] S. Baek, H. Okada and K. Yagyu, *Flavour Dependent Gauged Radiative Neutrino Mass Model*, *JHEP* **04** (2015) 049, [1501.01530].

[244] V. De Romeri, E. Fernandez-Martinez, J. Gehrlein, P. A. N. Machado and V. Niro, *Dark Matter and the elusive Z' in a dynamical Inverse Seesaw scenario*, *JHEP* **10** (2017) 169, [1707.08606].

[245] T. Nomura and H. Okada, *An inverse seesaw model with $U(1)_R$ gauge symmetry*, *LHEP* **1** (2018) 10–13, [1806.01714].

[246] V. Brdar and A. Y. Smirnov, *Low Scale Left-Right Symmetry and Naturally Small Neutrino Mass*, *JHEP* **02** (2019) 045, [1809.09115].

[247] H. Okada and K. Yagyu, *Radiative generation of lepton masses with the $U(1)'$ gauge symmetry*, *Phys. Rev.* **D90** (2014) 035019, [1405.2368].

[248] C. E. Diaz, S. F. Mantilla and R. Martinez, *Radiative neutrino masses with forbidden seesaw mechanism in an abelian extension of the Standard Model*, 1712.05433.

[249] T. Nomura and H. Okada, *A Linear seesaw model with hidden gauge symmetry*, 1806.07182.

[250] M. Pospelov, *Neutrino Physics with Dark Matter Experiments and the Signature of New Baryonic Neutral Currents*, *Phys. Rev.* **D84** (2011) 085008, [1103.3261].

[251] B. Batell, M. Pospelov and B. Shuve, *Shedding Light on Neutrino Masses with Dark Forces*, *JHEP* **08** (2016) 052, [1604.06099].

[252] Y. Farzan and J. Heeck, *Neutrinophilic nonstandard interactions*, *Phys. Rev.* **D94** (2016) 053010, [1607.07616].

[253] M. Pospelov and J. Pradler, *Elastic scattering signals of solar neutrinos with enhanced baryonic currents*, *Phys. Rev.* **D85** (2012) 113016, [1203.0545].

[254] M. Pospelov and J. Pradler, *Dark Matter or Neutrino recoil? Interpretation of Recent Experimental Results*, *Phys. Rev.* **D89** (2014) 055012, [1311.5764].

[255] R. Harnik, J. Kopp and P. A. N. Machado, *Exploring nu Signals in Dark Matter Detectors*, *JCAP* **1207** (2012) 026, [1202.6073].

[256] D. McKeen and N. Raj, *Monochromatic dark neutrinos and boosted dark matter in noble liquid direct detection*, 1812.05102.

[257] X. Chu, B. Dasgupta and J. Kopp, *Sterile neutrinos with secret interactions—lasting friendship with cosmology*, *JCAP* **1510** (2015) 011, [1505.02795].

[258] MiniBooNE collaboration, A. A. Aguilar-Arevalo et al., *A Search for electron neutrino appearance at the $\Delta m^2 \sim 1eV^2$ scale*, *Phys. Rev. Lett.* **98** (2007) 231801, [0704.1500].

[259] MiniBooNE collaboration, A. A. Aguilar-Arevalo et al., *Significant Excess of ElectronLike Events in the MiniBooNE Short-Baseline Neutrino Experiment*, *Phys. Rev. Lett.* **121** (2018) 221801, [1805.12028].

[260] LSND Collaboration collaboration, C. Athanassopoulos, L. B. Auerbach, R. L. Burman, I. Cohen, D. O. Caldwell, B. D. Dieterle et al., *Evidence for $\overline{\nu}_\mu \to \overline{\nu}_e$*

oscillations from the lsnd experiment at the los alamos meson physics facility, *Phys. Rev. Lett.* **77** (Oct, 1996) 3082–3085.

[261] LSND collaboration, A. Aguilar-Arevalo et al., *Evidence for neutrino oscillations from the observation of anti-neutrino(electron) appearance in a anti-neutrino(muon) beam*, *Phys. Rev.* **D64** (2001) 112007, [hep-ex/0104049].

[262] S. N. Gninenko, *The MiniBooNE anomaly and heavy neutrino decay*, *Phys. Rev. Lett.* **103** (2009) 241802, [0902.3802].

[263] S. N. Gninenko, *A resolution of puzzles from the LSND, KARMEN, and MiniBooNE experiments*, *Phys. Rev.* **D83** (2011) 015015, [1009.5536].

[264] M. Masip, P. Masjuan and D. Meloni, *Heavy neutrino decays at MiniBooNE*, *JHEP* **01** (2013) 106, [1210.1519].

[265] A. Radionov, *Constraints on electromagnetic properties of sterile neutrinos from MiniBooNE results*, *Phys. Rev.* **D88** (2013) 015016, [1303.4587].

[266] P. Fayet, *U-boson production in e+ e- annihilations, psi and Upsilon decays, and Light Dark Matter*, *Phys. Rev.* **D75** (2007) 115017, [hep-ph/0702176].

[267] Y. Farzan, *A Minimal model linking two great mysteries: neutrino mass and dark matter*, *Phys. Rev.* **D80** (2009) 073009, [0908.3729].

[268] Y. Farzan, S. Pascoli and M. A. Schmidt, *AMEND: A model explaining neutrino masses and dark matter testable at the LHC and MEG*, *JHEP* **10** (2010) 111, [1005.5323].

[269] A. Arhrib, C. Bœhm, E. Ma and T.-C. Yuan, *Radiative Model of Neutrino Mass with Neutrino Interacting MeV Dark Matter*, *JCAP* **1604** (2016) 049, [1512.08796].

[270] J. F. Cherry, A. Friedland and I. M. Shoemaker, *Neutrino Portal Dark Matter: From Dwarf Galaxies to IceCube*, 1411.1071.

[271] M. Escudero, N. Rius and V. Sanz, *Sterile neutrino portal to Dark Matter I: The $U(1)_{B-L}$ case*, *JHEP* **02** (2017) 045, [1606.01258].

[272] M. Escudero, N. Rius and V. Sanz, *Sterile Neutrino portal to Dark Matter II: Exact Dark symmetry*, *Eur. Phys. J.* **C77** (2017) 397, [1607.02373].

[273] B. Batell, T. Han, D. McKeen and B. Shams Es Haghi, *Thermal Dark Matter Through the Dirac Neutrino Portal*, *Phys. Rev.* **D97** (2018) 075016, [1709.07001].

[274] A. Olivares-Del Campo, C. Bœhm, S. Palomares-Ruiz and S. Pascoli, *Dark matter-neutrino interactions through the lens of their cosmological implications*, *Phys. Rev.* **D97** (2018) 075039, [1711.05283].

[275] M. Blennow, E. Fernandez-Martinez, A. O.-D. Campo, S. Pascoli, S. Rosauro-Alcaraz and A. V. Titov, *Neutrino Portals to Dark Matter*, 1903.00006.

[276] P. S. B. Dev and A. Pilaftsis, *Minimal Radiative Neutrino Mass Mechanism for Inverse Seesaw Models*, *Phys. Rev.* **D86** (2012) 113001, [1209.4051].

[277] V. Barger, P. Langacker, M. McCaskey, M. Ramsey-Musolf and G. Shaughnessy, *Complex Singlet Extension of the Standard Model*, *Phys. Rev.* **D79** (2009) 015018, [0811.0393].

[278] T. Yamazaki et al., *Search for Heavy Neutrinos in Kaon Decay*, .

[279] E949 collaboration, A. V. Artamonov et al., *Search for heavy neutrinos in $K^+ \to \mu^+ \nu_H$ decays*, *Phys. Rev.* **D91** (2015) 052001, [1411.3963].

[280] NA48/2 collaboration, J. R. Batley et al., *Searches for lepton number violation and resonances in $K^\pm \to \pi\mu\mu$ decays*, *Phys. Lett.* **B769** (2017) 67–76, [1612.04723].

[281] G. Bernardi et al., *Search for Neutrino Decay*, *Phys. Lett.* **166B** (1986) 479–483.

[282] CHARM collaboration, F. Bergsma et al., *A Search for Decays of Heavy Neutrinos*, *Phys. Lett.* **128B** (1983) 361.

[283] NA3 collaboration, J. Badier et al., *Mass and Lifetime Limits on New Longlived Particles in 300-GeV/cπ^- Interactions*, *Z. Phys.* **C31** (1986) 21.

[284] NuTeV, E815 collaboration, A. Vaitaitis et al., *Search for neutral heavy leptons in a high-energy neutrino beam*, *Phys. Rev. Lett.* **83** (1999) 4943–4946, [hep-ex/9908011].

[285] WA66 collaboration, A. M. Cooper-Sarkar et al., *Search for Heavy Neutrino Decays in the BEBC Beam Dump Experiment*, *Phys. Lett.* **160B** (1985) 207–211.

[286] NOMAD collaboration, P. Astier et al., *Search for heavy neutrinos mixing with tau neutrinos*, *Phys. Lett.* **B506** (2001) 27–38, [hep-ex/0101041].

[287] P. Ballett, S. Pascoli and M. Ross-Lonergan, *MeV-scale sterile neutrino decays at the Fermilab Short-Baseline Neutrino program*, *JHEP* **04** (2017) 102, [1610.08512].

[288] P. Ilten, Y. Soreq, M. Williams and W. Xue, *Serendipity in dark photon searches*, *JHEP* **06** (2018) 004, [1801.04847].

[289] A. Atre, T. Han, S. Pascoli and B. Zhang, *The Search for Heavy Majorana Neutrinos*, *JHEP* **05** (2009) 030, [0901.3589].

[290] A. Abada, V. De Romeri, M. Lucente, A. M. Teixeira and T. Toma, *Effective Majorana mass matrix from tau and pseudoscalar meson lepton number violating decays*, *JHEP* **02** (2018) 169, [1712.03984].

[291] D. Curtin, R. Essig, S. Gori and J. Shelton, *Illuminating Dark Photons with High-Energy Colliders*, *JHEP* **02** (2015) 157, [1412.0018].

[292] A. Hook, E. Izaguirre and J. G. Wacker, *Model Independent Bounds on Kinetic Mixing*, *Adv. High Energy Phys.* **2011** (2011) 859762, [1006.0973].

[293] G. Mohlabeng, *Revisiting the Dark Photon Explanation of the Muon g-2 Anomaly*, 1902.05075.

[294] SINDRUM collaboration, S. Egli et al., *First Observation of the Decay $\pi^+ \to e^+$ Neutrino e^+e^- and a Determination of the Form-factors F(V), F(a), R*, *Phys. Lett.* **B175** (1986) 97.

[295] SINDRUM collaboration, C. Grab, *FIRST OBSERVATION OF THE DECAY $\pi^+ \to e^+e^-e^+$ neutrino AND A DETERMINATION OF THE FORM-FACTORS F(V), F(A) AND R*, in *Proceedings, 23RD International Conference on High Energy Physics, JULY 16-23, 1986, Berkeley, CA*, 1986.

[296] A. A. Poblaguev et al., *Experimental study of the radiative decays K+ —> mu+ nu e+ e- and K+ —> e+ nu e+ e-*, *Phys. Rev. Lett.* **89** (2002) 061803, [hep-ex/0204006].

[297] H. Ma et al., *First observation of the decay K+ —> e+ nu(e) mu+ mu-*, *Phys. Rev.* **D73** (2006) 037101, [hep-ex/0505011].

[298] NA48/2 collaboration, L. Peruzzo, *Model independent measurement of the leptonic kaon decay $K^{\pm} \to \mu^{\pm}\nu_{\mu}e^{+}e^{-}$*, *J. Phys. Conf. Ser.* **873** (2017) 012020.

[299] SINDRUM collaboration, W. H. Bertl et al., *Search for the Decay $\mu^{+} \to e^{+}e^{+}e^{-}$*, *Nucl. Phys.* **B260** (1985) 1–31.

[300] CLEO collaboration, M. S. Alam et al., *Tau decays into three charged leptons and two neutrinos*, *Phys. Rev. Lett.* **76** (1996) 2637–2641.

[301] CMS collaboration, A. M. Sirunyan et al., *Search for invisible decays of a Higgs boson produced through vector boson fusion in proton-proton collisions at $\sqrt{s} = 13$ TeV*, 1809.05937.

[302] R. Laha, B. Dasgupta and J. F. Beacom, *Constraints on New Neutrino Interactions via Light Abelian Vector Bosons*, *Phys. Rev.* **D89** (2014) 093025, [1304.3460].

[303] P. Bakhti and Y. Farzan, *Constraining secret gauge interactions of neutrinos by meson decays*, *Phys. Rev.* **D95** (2017) 095008, [1702.04187].

[304] N. Song, M. C. Gonzalez-Garcia and J. Salvado, *Cosmological constraints with self-interacting sterile neutrinos*, *JCAP* **1810** (2018) 055, [1805.08218].

[305] J. F. Beacom, N. F. Bell and G. D. Mack, *General Upper Bound on the Dark Matter Total Annihilation Cross Section*, *Phys. Rev. Lett.* **99** (2007) 231301, [astro-ph/0608090].

[306] S. Palomares-Ruiz and S. Pascoli, *Testing MeV dark matter with neutrino detectors*, *Phys. Rev.* **D77** (2008) 025025, [0710.5420].

[307] M. Pospelov, A. Ritz and M. B. Voloshin, *Secluded WIMP Dark Matter*, *Phys. Lett.* **B662** (2008) 53–61, [0711.4866].

[308] G. Mangano, A. Melchiorri, P. Serra, A. Cooray and M. Kamionkowski, *Cosmological bounds on dark matter-neutrino interactions*, *Phys. Rev.* **D74** (2006) 043517, [astro-ph/0606190].

[309] R. J. Wilkinson, C. Boehm and J. Lesgourgues, *Constraining Dark Matter-Neutrino Interactions using the CMB and Large-Scale Structure*, *JCAP* **1405** (2014) 011, [1401.7597].

[310] Y. Farzan and S. Palomares-Ruiz, *Dips in the Diffuse Supernova Neutrino Background*, *JCAP* **1406** (2014) 014, [1401.7019].

[311] C. A. Argüelles, A. Kheirandish and A. C. Vincent, *Imaging Galactic Dark Matter with High-Energy Cosmic Neutrinos*, *Phys. Rev. Lett.* **119** (2017) 201801, [1703.00451].

[312] Y. Zhang, X. Ji and R. N. Mohapatra, *A Naturally Light Sterile neutrino in an Asymmetric Dark Matter Model*, *JHEP* **10** (2013) 104, [1307.6178].

[313] W. Grimus and L. Lavoura, *The Seesaw mechanism at arbitrary order: Disentangling the small scale from the large scale*, *JHEP* **11** (2000) 042, [hep-ph/0008179].

[314] R. Adhikari and A. Raychaudhuri, *Light neutrinos from massless texture and below TeV seesaw scale*, *Phys. Rev.* **D84** (2011) 033002, [1004.5111].

[315] Y. Cai, J. Herrero-García, M. A. Schmidt, A. Vicente and R. R. Volkas, *From the trees to the forest: a review of radiative neutrino mass models*, *Front.in Phys.* **5** (2017) 63, [1706.08524].

[316] A. Pilaftsis, *Radiatively induced neutrino masses and large Higgs neutrino couplings in the standard model with Majorana fields*, *Z. Phys.* **C55** (1992) 275–282, [hep-ph/9901206].

[317] B. A. Kniehl and A. Pilaftsis, *Mixing renormalization in Majorana neutrino theories*, *Nucl. Phys.* **B474** (1996) 286–308, [hep-ph/9601390].

[318] DELPHI collaboration, P. Abreu et al., *Search for neutral heavy leptons produced in Z decays*, *Z. Phys.* **C74** (1997) 57–71.

[319] OPAL collaboration, M. Z. Akrawy et al., *Limits on neutral heavy lepton production from Z0 decay*, *Phys. Lett.* **B247** (1990) 448–457.

[320] CMS collaboration, A. M. Sirunyan et al., *Search for heavy neutral leptons in events with three charged leptons in proton-proton collisions at $\sqrt{s} = 13$ TeV*, *Phys. Rev. Lett.* **120** (2018) 221801, [1802.02965].

[321] P. Ballett, T. Boschi and S. Pascoli, *Searching for MeV-scale Neutrinos with the DUNE Near Detector*, in *Proceedings, Prospects in Neutrino Physics (NuPhys2017): London, UK, December 20-22, 2017*, pp. 124–128, 2018, 1803.10824.

[322] P. Ballett, T. Boschi and S. Pascoli, *Heavy Neutral Leptons from low-scale seesaws at the DUNE Near Detector*, 1905.00284.

[323] M. Drewes, J. Hajer, J. Klaric and G. Lanfranchi, *Perspectives to find heavy neutrinos with NA62*, in *53rd Rencontres de Moriond on Electroweak Interactions and Unified Theories (Moriond EW 2018) La Thuile, Italy, March 10-17, 2018*, 2018, 1806.00100.

[324] W. Bonivento et al., *Proposal to Search for Heavy Neutral Leptons at the SPS*, 1310.1762.

[325] S. Alekhin et al., *A facility to Search for Hidden Particles at the CERN SPS: the SHiP physics case*, *Rept. Prog. Phys.* **79** (2016) 124201, [1504.04855].

[326] A. D. Dolgov, S. H. Hansen, G. Raffelt and D. V. Semikoz, *Heavy sterile neutrinos: Bounds from big bang nucleosynthesis and SN1987A*, *Nucl. Phys.* **B590** (2000) 562–574, [hep-ph/0008138].

[327] LSND collaboration, C. Athanassopoulos et al., *Evidence for anti-muon-neutrino —> anti-electron-neutrino oscillations from the LSND experiment at LAMPF*, *Phys. Rev. Lett.* **77** (1996) 3082–3085, [nucl-ex/9605003].

[328] ALEPH, CDF, D0, DELPHI, L3, OPAL, SLD, LEP Electroweak Working Group, Tevatron Electroweak Working Group, SLD Electroweak and Heavy Flavour Groups collaboration, L. E. W. Group, *Precision Electroweak Measurements and Constraints on the Standard Model*, 1012.2367.

[329] Collin, G. H. and Argüelles, C. A. and Conrad, J. M. and Shaevitz, M. H., *First Constraints on the Complete Neutrino Mixing Matrix with a Sterile Neutrino*, 1607.00011.

[330] F. Capozzi, C. Giunti, M. Laveder and A. Palazzo, *Joint short- and long-baseline constraints on light sterile neutrinos*, *Phys. Rev.* **D95** (2017) 033006, [1612.07764].

[331] M. Dentler, Hernández-Cabezudo, J. Kopp, P. A. N. Machado, M. Maltoni, I. Martinez-Soler et al., *Updated Global Analysis of Neutrino Oscillations in the Presence of eV-Scale Sterile Neutrinos*, *JHEP* **08** (2018) 010, [1803.10661].

[332] MiniBooNE collaboration, A. A. Aguilar-Arevalo et al., *The Neutrino Flux prediction at MiniBooNE*, *Phys. Rev.* **D79** (2009) 072002, [0806.1449].

[333] MiniBooNE collaboration, A. A. Aguilar-Arevalo et al., *The MiniBooNE Detector*, *Nucl. Instrum. Meth.* **A599** (2009) 28–46, [0806.4201].

[334] MiniBooNE collaboration, A. A. Aguilar-Arevalo et al., *Unexplained Excess of Electron-Like Events From a 1-GeV Neutrino Beam*, *Phys. Rev. Lett.* **102** (2009) 101802, [0812.2243].

[335] MiniBooNE collaboration, A. A. Aguilar-Arevalo et al., *A Combined $\nu_\mu \to \nu_e$ and $\bar{\nu}_\mu \to \bar{\nu}_e$ Oscillation Analysis of the MiniBooNE Excesses*, 2012, 1207.4809, http://lss.fnal.gov/archive/2012/pub/fermilab-pub-12-394-ad-ppd.pdf.

[336] R. J. Hill, *On the single photon background to ν_e appearance at MiniBooNE*, *Phys. Rev.* **D84** (2011) 017501, [1002.4215].

[337] H. Murayama and T. Yanagida, *LSND, SN1987A, and CPT violation*, *Phys. Lett.* **B520** (2001) 263–268, [hep-ph/0010178].

[338] A. Strumia, *Interpreting the LSND anomaly: Sterile neutrinos or CPT violation or...?*, *Phys. Lett.* **B539** (2002) 91–101, [hep-ph/0201134].

[339] G. Barenboim, L. Borissov and J. D. Lykken, *CPT violating neutrinos in the light of KamLAND*, hep-ph/0212116.

[340] M. C. Gonzalez-Garcia, M. Maltoni and T. Schwetz, *Status of the CPT violating interpretations of the LSND signal*, *Phys. Rev.* **D68** (2003) 053007, [hep-ph/0306226].

[341] V. Barger, D. Marfatia and K. Whisnant, *LSND anomaly from CPT violation in four neutrino models*, *Phys. Lett.* **B576** (2003) 303–308, [hep-ph/0308299].

[342] M. Sorel, J. M. Conrad and M. H. Shaevitz, *A Combined analysis of short baseline neutrino experiments in the (3+1) and (3+2) sterile neutrino oscillation hypotheses*, *Phys. Rev.* **D70** (2004) 073004, [hep-ph/0305255].

[343] G. Barenboim and N. E. Mavromatos, *CPT violating decoherence and LSND: A Possible window to Planck scale physics*, *JHEP* **01** (2005) 034, [hep-ph/0404014].

[344] K. M. Zurek, *New matter effects in neutrino oscillation experiments*, *JHEP* **10** (2004) 058, [hep-ph/0405141].

[345] D. B. Kaplan, A. E. Nelson and N. Weiner, *Neutrino oscillations as a probe of dark energy*, *Phys. Rev. Lett.* **93** (2004) 091801, [hep-ph/0401099].

[346] H. Pas, S. Pakvasa and T. J. Weiler, *Sterile-active neutrino oscillations and shortcuts in the extra dimension*, *Phys. Rev.* **D72** (2005) 095017, [hep-ph/0504096].

[347] A. de Gouvêa and Y. Grossman, *A Three-flavor, Lorentz-violating solution to the LSND anomaly*, *Phys. Rev.* **D74** (2006) 093008, [hep-ph/0602237].

[348] T. Schwetz, *LSND versus MiniBooNE: Sterile neutrinos with energy dependent masses and mixing?*, *JHEP* **02** (2008) 011, [0710.2985].

[349] Y. Farzan, T. Schwetz and A. Y. Smirnov, *Reconciling results of LSND, MiniBooNE and other experiments with soft decoherence*, *JHEP* **07** (2008) 067, [0805.2098].

[350] S. Hollenberg, O. Micu, H. Pas and T. J. Weiler, *Baseline-dependent neutrino oscillations with extra-dimensional shortcuts*, *Phys. Rev.* **D80** (2009) 093005, [0906.0150].

[351] A. E. Nelson, *Effects of CP Violation from Neutral Heavy Fermions on Neutrino Oscillations, and the LSND/MiniBooNE Anomalies*, *Phys. Rev.* **D84** (2011) 053001, [1010.3970].

[352] E. Akhmedov and T. Schwetz, *MiniBooNE and LSND data: Non-standard neutrino interactions in a (3+1) scheme versus (3+2) oscillations*, *JHEP* **10** (2010) 115, [1007.4171].

[353] J. S. Diaz and V. A. Kostelecky, *Three-parameter Lorentz-violating texture for neutrino mixing*, *Phys. Lett.* **B700** (2011) 25–28, [1012.5985].

[354] Y. Bai, R. Lu, S. Lu, J. Salvado and B. A. Stefanek, *Three Twin Neutrinos: Evidence from LSND and MiniBooNE*, *Phys. Rev.* **D93** (2016) 073004, [1512.05357].

[355] C. Giunti and E. M. Zavanin, *Appearance–disappearance relation in* $3 + N_s$ *short-baseline neutrino oscillations*, *Mod. Phys. Lett.* **A31** (2015) 1650003, [1508.03172].

[356] D. K. Papoulias and T. S. Kosmas, *Impact of Nonstandard Interactions on Neutrino-Nucleon Scattering*, *Adv. High Energy Phys.* **2016** (2016) 1490860, [1611.05069].

[357] Moss, Zander and Moulai, Marjon H. and Argüelles, Carlos A. and Conrad, Janet M., *Exploring a nonminimal sterile neutrino model involving decay at IceCube*, *Phys. Rev.* **D97** (2018) 055017, [1711.05921].

[358] M. Carena, Y.-Y. Li, C. S. Machado, P. A. N. Machado and C. E. M. Wagner, *Neutrinos in Large Extra Dimensions and Short-Baseline* ν_e *Appearance*, 1708.09548.

[359] J. Liao and D. Marfatia, *Impact of nonstandard interactions on sterile neutrino searches at IceCube*, *Phys. Rev. Lett.* **117** (2016) 071802, [1602.08766].

[360] J. Liao, D. Marfatia and K. Whisnant, *MiniBooNE, MINOS+ and IceCube data imply a baroque neutrino sector*, 1810.01000.

[361] J. Asaadi, E. Church, R. Guenette, B. J. P. Jones and A. M. Szelc, *New light Higgs boson and short-baseline neutrino anomalies*, *Phys. Rev.* **D97** (2018) 075021, [1712.08019].

[362] D. Döring, H. Päs, P. Sicking and T. J. Weiler, *Sterile Neutrinos with Altered Dispersion Relations as an Explanation for the MiniBooNE, LSND, Gallium and Reactor Anomalies*, 1808.07460.

[363] C. Dib, J. C. Helo, S. Kovalenko and I. Schmidt, *Sterile neutrino decay explanation of LSND and MiniBooNE anomalies*, *Phys. Rev.* **D84** (2011) 071301, [1105.4664].

[364] D. McKeen and M. Pospelov, *Muon Capture Constraints on Sterile Neutrino Properties*, *Phys. Rev.* **D82** (2010) 113018, [1011.3046].

[365] M. Masip and P. Masjuan, *Heavy-neutrino decays at neutrino telescopes*, *Phys. Rev.* **D83** (2011) 091301, [1103.0689].

[366] S. N. Gninenko, *New limits on radiative sterile neutrino decays from a search for single photons in neutrino interactions*, *Phys. Lett.* **B710** (2012) 86–90, [1201.5194].

[367] G. Magill, R. Plestid, M. Pospelov and Y.-D. Tsai, *Dipole portal to heavy neutral leptons*, 1803.03262.

[368] E. Bertuzzo, S. Jana, P. A. N. Machado and R. Zukanovich Funchal, *Neutrino Masses and Mixings Dynamically Generated by a Light Dark Sector*, *Phys. Lett.* **B791** (2019) 210–214, [1808.02500].

[369] LSND collaboration, L. B. Auerbach et al., *Measurement of electron - neutrino - electron elastic scattering*, *Phys. Rev.* **D63** (2001) 112001, [hep-ex/0101039].

[370] MINERvA collaboration, E. Valencia et al., *Constraint of the MINERvA Medium Energy Neutrino Flux using Neutrino-Electron Elastic Scattering*, 1906.00111.

[371] E. Valencia-Rodriguez, *Neutrino - Electron Scattering in MINERνA for Constraint NuMI Flux at Medium*, Ph.D. thesis, Guanajuato U., 2016. 10.2172/1341804.

[372] CHARM-II collaboration, K. De Winter et al., *A Detector for the Study of Neutrino - Electron Scattering*, *Nucl. Instrum. Meth.* **A278** (1989) 670.

[373] CHARM-II collaboration, D. Geiregat et al., *Calibration and performance of the CHARM-II detector*, *Nucl. Instrum. Meth.* **A325** (1993) 92–108.

[374] M. Pospelov and Y.-D. Tsai, *Light scalars and dark photons in Borexino and LSND experiments*, *Phys. Lett.* **B785** (2018) 288–295, [1706.00424].

[375] G. Magill, R. Plestid, M. Pospelov and Y.-D. Tsai, *Millicharged particles in neutrino experiments*, 1806.03310.

[376] T2K collaboration, K. Abe et al., *Search for neutral-current induced single photon production at the ND280 near detector in T2K*, 1902.03848.

[377] J. A. Formaggio, J. M. Conrad, M. Shaevitz, A. Vaitaitis and R. Drucker, *Helicity effects in neutral heavy lepton decays*, *Phys. Rev.* **D57** (1998) 7037–7040.

[378] A. B. Balantekin, A. de Gouvêa and B. Kayser, *Addressing the Majorana vs. Dirac Question with Neutrino Decays*, 1808.10518.

[379] E. J. Chun, J.-C. Park and S. Scopel, *Dark matter and a new gauge boson through kinetic mixing*, *JHEP* **02** (2011) 100, [1011.3300].

[380] S. Parke and M. Ross-Lonergan, *Unitarity and the Three Flavour Neutrino Mixing Matrix*, 1508.05095.

[381] J. R. Jordan, Y. Kahn, G. Krnjaic, M. Moschella and J. Spitz, *Severe Constraints on New Physics Explanations of the MiniBooNE Excess*, 1810.07185.

[382] CHARM II collaboration, P. Vilain et al., *Leading order QCD analysis of neutrino induced dimuon events*, *Eur. Phys. J.* **C11** (1999) 19–34.

[383] CHARM-II collaboration, P. Vilain et al., *Coherent single charged pion production by neutrinos*, *Phys. Lett.* **B313** (1993) 267–275.

[384] CHARM-II collaboration, P. Vilain et al., *Neutral current coupling constants from neutrino and anti-neutrino - electron scattering*, *Phys. Lett.* **B281** (1992) 159–166.

[385] CHARM-II collaboration, D. Geiregat et al., *An Improved determination of the electroweak mixing angle from muon-neutrino electron scattering*, *Phys. Lett.* **B259** (1991) 499–507.

[386] L. Aliaga Soplin, *Neutrino Flux Prediction for the NuMI Beamline*, Ph.D. thesis, William-Mary Coll., 2016. 10.2172/1250884.

[387] Particle Data Group collaboration, M. Tanabashi et al., *Review of Particle Physics*, *Phys. Rev.* **D98** (2018) 030001.

[388] CHARM collaboration, J. V. Allaby et al., *Total Cross-sections of Charged Current Neutrino and Anti-neutrino Interactions on Isoscalar Nuclei*, *Z. Phys.* **C38** (1988) 403–410.

[389] MINOS collaboration, P. Adamson et al., *Measurement of single π^0 production by coherent neutral-current ν Fe interactions in the MINOS Near Detector*, *Phys. Rev.* **D94** (2016) 072006, [1608.05702].

[390] MINERvA collaboration, J. Wolcott et al., *Evidence for Neutral-Current Diffractive π^0 Production from Hydrogen in Neutrino Interactions on Hydrocarbon*, *Phys. Rev. Lett.* **117** (2016) 111801, [1604.01728].

[391] IDS-NF collaboration, S. Choubey et al., *International Design Study for the Neutrino Factory, Interim Design Report*, 1112.2853.

[392] F. J. P. Soler, *nuSTORM: Neutrinos from Stored Muons*, in *Proceedings, Topical Research Meeting on Prospects in Neutrino Physics (NuPhys2014): London, UK, December 15-17, 2014*, 2015, 1507.08836, https://inspirehep.net/record/1385878/files/arXiv:1507.08836.pdf.

[393] nuSTORM collaboration, D. Adey et al., *nuSTORM - Neutrinos from STORed Muons: Proposal to the Fermilab PAC*, 1308.6822.

[394] P. Ballett, M. Hostert and S. Pascoli, *Light Sterile Neutrinos at νSTORM: Decoherence and CP violation*, in *Proceedings, Prospects in Neutrino Physics (NuPhys2016): London, UK, December 12-14, 2016*, 2017, 1705.09214.

[395] K. Long, *The nuSTORM experiment*, *J. Phys. Conf. Ser.* **1056** (2018) 012033.

[396] A. Diaz, C. A. Argüelles, G. H. Collin, J. M. Conrad and M. H. Shaevitz, *Where Are We With Light Sterile Neutrinos?*, 1906.00045.

[397] GALLEX collaboration, W. Hampel et al., *Final results of the Cr-51 neutrino source experiments in GALLEX*, *Phys. Lett.* **B420** (1998) 114–126.

[398] J. N. Abdurashitov et al., *Measurement of the response of a Ga solar neutrino experiment to neutrinos from an Ar-37 source*, *Phys. Rev.* **C73** (2006) 045805, [nucl-ex/0512041].

[399] G. Mention, M. Fechner, T. Lasserre, T. A. Mueller, D. Lhuillier, M. Cribier et al., *The Reactor Antineutrino Anomaly*, *Phys. Rev.* **D83** (2011) 073006, [1101.2755].

[400] MINOS+ collaboration, P. Adamson et al., *Search for sterile neutrinos in MINOS and MINOS+ using a two-detector fit*, *Phys. Rev. Lett.* **122** (2019) 091803, [1710.06488].

[401] IceCube collaboration, M. G. Aartsen et al., *Searches for Sterile Neutrinos with the IceCube Detector*, *Phys. Rev. Lett.* **117** (2016) 071801, [1605.01990].

[402] MicroBooNE collaboration, C. Adams et al., *First Measurement of Inclusive Muon Neutrino Charged Current Differential Cross Sections on Argon at $E_\nu \sim 0.8$ GeV with the MicroBooNE Detector*, 1905.09694.

[403] D. Cianci, A. Furmanski, G. Karagiorgi and M. Ross-Lonergan, *Prospects of Light Sterile Neutrino Oscillation and CP Violation Searches at the Fermilab Short Baseline Neutrino Facility*, *Phys. Rev.* **D96** (2017) 055001, [1702.01758].

[404] SLD Electroweak Group, DELPHI, ALEPH, SLD, SLD Heavy Flavour Group, OPAL, LEP Electroweak Working Group, L3 collaboration, S. Schael et al., *Precision electroweak measurements on the Z resonance*, *Phys. Rept.* **427** (2006) 257–454, [hep-ex/0509008].

[405] E. K. Akhmedov and A. Yu. Smirnov, *Paradoxes of neutrino oscillations*, *Phys. Atom. Nucl.* **72** (2009) 1363–1381, [0905.1903].

[406] E. Akhmedov, D. Hernandez and A. Smirnov, *Neutrino production coherence and oscillation experiments*, *JHEP* **04** (2012) 052, [1201.4128].

[407] D. Hernandez and A. Yu. Smirnov, *Active to sterile neutrino oscillations: Coherence and MINOS results*, *Phys. Lett.* **B706** (2012) 360–366, [1105.5946].

[408] C. D. Tunnell, *Designing a 3.8-GeV/c muon-decay ring and experiment sensitive to electronvolt-scale sterile neutrinos*, doctor of philosophy thesis, University of Oxford, 2013.

[409] A. Mirizzi, G. Mangano, O. Pisanti and N. Saviano, *Collisional production of sterile neutrinos via secret interactions and cosmological implications*, *Phys. Rev.* **D91** (2015) 025019, [1410.1385].

[410] X. Chu, B. Dasgupta and J. Kopp, *Sterile neutrinos with secret interactions—lasting friendship with cosmology*, *JCAP* **1510** (2015) 011, [1505.02795].

[411] M. Archidiacono, S. Hannestad, R. S. Hansen and T. Tram, *Cosmology with self-interacting sterile neutrinos and dark matter - A pseudoscalar model*, *Phys. Rev.* **D91** (2015) 065021, [1404.5915].

[412] M. Archidiacono, S. Gariazzo, C. Giunti, S. Hannestad, R. Hansen, M. Laveder et al., *Pseudoscalar—sterile neutrino interactions: reconciling the cosmos with neutrino oscillations*, *JCAP* **1608** (2016) 067, [1606.07673].

[413] S. Antusch, C. Biggio, E. Fernandez-Martinez, M. B. Gavela and J. Lopez-Pavon, *Unitarity of the Leptonic Mixing Matrix*, *JHEP* **10** (2006) 084, [hep-ph/0607020].

[414] F. J. Escrihuela, D. V. Forero, O. G. Miranda, M. Tortola and J. W. F. Valle, *On the description of nonunitary neutrino mixing*, *Phys. Rev.* **D92** (2015) 053009, [1503.08879].

[415] E. Fernandez-Martinez, J. Hernandez-Garcia and J. Lopez-Pavon, *Global constraints on heavy neutrino mixing*, *JHEP* **08** (2016) 033, [1605.08774].

[416] R. E. Shrock, *General Theory of Weak Leptonic and Semileptonic Decays. 1. Leptonic Pseudoscalar Meson Decays, with Associated Tests For, and Bounds on, Neutrino Masses and Lepton Mixing*, *Phys. Rev.* **D24** (1981) 1232.

[417] D. Neuffer, A. Liu and A. Bross, *NuSTORM μ Ring – Design and Injection Optimization*, *PoS* **NUFACT2014** (2014) 068, [1502.03751].

[418] P. Huber, M. Lindner and W. Winter, *Simulation of long-baseline neutrino oscillation experiments with GLoBES (General Long Baseline Experiment Simulator)*, *Comput. Phys. Commun.* **167** (2005) 195, [hep-ph/0407333].

[419] W. Winter, *Optimization of a Very Low Energy Neutrino Factory for the Disappearance Into Sterile Neutrinos*, *Phys. Rev.* **D85** (2012) 113005, [1204.2671].

[420] K. N. Abazajian, *Sterile neutrinos in cosmology*, *Phys. Rept.* **711-712** (2017) 1–28, [1705.01837].

[421] S. Bridle, J. Elvin-Poole, J. Evans, S. Fernandez, P. Guzowski and S. Soldner-Rembold, *A Combined View of Sterile-Neutrino Constraints from CMB and Neutrino Oscillation Measurements*, *Phys. Lett.* **B764** (2017) 322–327, [1607.00032].

[422] O. Dragoun and D. Vénos, *Constraints on the Active and Sterile Neutrino Masses from Beta-Ray Spectra: Past, Present and Future*, *J. Phys.* **3** (2016) 77–113, [1504.07496].

[423] J. N. Abdurashitov et al., *First measeurements in search for keV-sterile neutrino in tritium beta-decay by Troitsk nu-mass experiment*, *Pisma Zh. Eksp. Teor. Fiz.* **105** (2017) 723–724, [1703.10779].

[424] W. C. Louis, *Problems With the MINOS/MINOS+ Sterile Neutrino ν_μ Result*, 1803.11488.

[425] NOMAD collaboration, P. Astier et al., *Search for nu(mu) —> nu(e) oscillations in the NOMAD experiment*, *Phys. Lett.* **B570** (2003) 19–31, [hep-ex/0306037].

[426] NuTeV collaboration, S. Avvakumov et al., *A Search for muon-neutrino —> electron-neutrino and muon-anti-neutrino —> electron-anti-neutrino oscillations at NuTeV*, *Phys. Rev. Lett.* **89** (2002) 011804, [hep-ex/0203018].

[427] G. H. Collin, C. A. Argüelles, J. M. Conrad and M. H. Shaevitz, *Sterile Neutrino Fits to Short Baseline Data*, *Nucl. Phys.* **B908** (2016) 354–365, [1602.00671].

[428] A. de Gouvêa, K. J. Kelly and A. Kobach, *CP-invariance violation at short-baseline experiments in 3+1 neutrino scenarios*, *Phys. Rev.* **D91** (2015) 053005, [1412.1479].

[429] G. S. Karagiorgi, *Searches for New Physics at MiniBooNE: Sterile Neutrinos and Mixing Freedom*, 2010.

[430] M. Ross-Lonergan, *Constraining Non-Unitarity in the Neutrino Sector using the SBN Facility*, .

[431] ENUBET Collaboration collaboration, F. Acerbi, G. Ballerini, M. Bonesini, C. Brizzolari, G. Brunetti, M. Calviani et al., *The ENUBET project*, Tech. Rep. CERN-SPSC-2018-034. SPSC-I-248, CERN, Geneva, Oct, 2018.

[432] F. Acerbi et al., *A high precision neutrino beam for a new generation of short baseline experiments*, 1901.04768.

[433] G. Fricke, C. Bernhardt, K. Heilig, L. A. Schaller, L. Schellenberg, E. B. Shera et al., *Nuclear Ground State Charge Radii from Electromagnetic Interactions*, *Atom. Data Nucl. Data Tabl.* **60** (1995) 177–285.

[434] U. D. Jentschura and V. G. Serbo, *Nuclear form factor, validity of the equivalent photon approximation and Coulomb corrections to muon pair production in photon-nucleus and nucleus-nucleus collisions*, *European Physical Journal C* **64** (aug, 2009) 309–317, [0908.3853].

[435] R. Anni, G. Co and P. Pellegrino, *Nuclear charge density distributions from elastic electron scattering data*, *Nucl. Phys.* **A584** (1995) 35–59, [nucl-th/9410023].

[436] D. W. L. Sprung and J. Martorell, *The symmetrized fermi function and its transforms*, *Journal of Physics A: Mathematical and General* **30** (1997) 6525.

[437] G. Duda, A. Kemper and P. Gondolo, *Model Independent Form Factors for Spin Independent Neutralino-Nucleon Scattering from Elastic Electron Scattering Data*, *JCAP* **0704** (2007) 012, [hep-ph/0608035].

[438] W. Grimus and L. Lavoura, *One-loop corrections to the seesaw mechanism in the multi-Higgs-doublet standard model*, *Phys. Lett.* **B546** (2002) 86–95, [hep-ph/0207229].

[439] D. Aristizabal Sierra and C. E. Yaguna, *On the importance of the 1-loop finite corrections to seesaw neutrino masses*, *JHEP* **08** (2011) 013, [1106.3587].